



HAL
open science

Multiscale and Multiphysics analysis of the deformation of cellular arrangements under an electric-field excitation: application to electroporation

Danish Shamoon

► To cite this version:

Danish Shamoon. Multiscale and Multiphysics analysis of the deformation of cellular arrangements under an electric-field excitation: application to electroporation. Physics [physics]. Université de Bretagne occidentale - Brest, 2020. English. NNT : 2020BRES0028 . tel-03274239

HAL Id: tel-03274239

<https://theses.hal.science/tel-03274239>

Submitted on 29 Jun 2021

HAL is a multi-disciplinary open access archive for the deposit and dissemination of scientific research documents, whether they are published or not. The documents may come from teaching and research institutions in France or abroad, or from public or private research centers.

L'archive ouverte pluridisciplinaire **HAL**, est destinée au dépôt et à la diffusion de documents scientifiques de niveau recherche, publiés ou non, émanant des établissements d'enseignement et de recherche français ou étrangers, des laboratoires publics ou privés.

THESE DE DOCTORAT DE

L'UNIVERSITE
DE BRETAGNE OCCIDENTALE

ECOLE DOCTORALE N° 596
Matière Molécules et Matériaux
Spécialité : Physique

Par

Danish SHAMOON

Analyse multi-échelle et multi-physique de la déformation d'arrangements cellulaires soumis à un champ électrique : Application à l'électroporation

Thèse présentée et soutenue à Brest, le 17 Juin 2020
Unité de recherche : Lab-STICC

Rapporteurs avant soutenance :

Abderrahmane BEROUAL, Professeur, EEA/Ampère, 36 Av
Guy de Collongue, 69134 ÉCULLY CEDEX

Marie FRENEA-ROBIN, Maître de Conférences, HDR,
Département Ingénierie, Ecole Centrale de Lyon, 36 Av Guy de
Collongue, 69134 ÉCULLY CEDEX

Composition du Jury :

Abderrahmane BEROUAL, Professeur, EEA/Ampère, 36 Av
Guy de Collongue, 69134 ÉCULLY CEDEX (rapporteur)

Marie FRENEA-ROBIN, Maître de Conférences, HDR,
Département Ingénierie, Ecole Centrale de Lyon, 36 Av Guy
de Collongue, 69134 ÉCULLY CEDEX (rapporteur)

Tristan MONTIER, Professeur, Faculté de médecine et
des sciences de la santé, UBO, CS 93837, 29238 BREST
CEDEX 3 (Président du Jury)

Christian BROSSEAU, Professeur, UBO – Labsticc, CS
93837, 6 Av Le Gorgeu, 29238 BREST CEDEX 3
(Directeur de thèse)

Sophie LASQUELLEC, Maître de Conférences, UBO –
Labsticc, CS 93837, 6 Av Le Gorgeu, 29238 BREST
CEDEX 3 (Co-encadrante)

Preface

All praise be to The Almighty.

I wholeheartedly thank my research advisor Prof. Christian Brosseau for giving me the opportunity to work on this highly interdisciplinary PhD project that involved working at the interface of Physics, Mathematics and Biology. Due to the richness of the subjects, I worked hard to avoid being distracted from pursuing multiple directions that the project could advance in. But given the three years duration of this PhD, Christian made sure that the attention is restricted to a few important topics only and who also identified that the obtained results or analyses were ready to be submitted for publishing. Without his regular support and guidance, this work would not have progressed as much.

I thank my co-advisor Asst. Prof. Sophie Lasquellec for critically examining and guiding the work. Her insightful discussions and assistance helped a lot in improving the quality of work. I also thank Sophie and Tomo for initializing my COMSOL experience. Previous models from Tomo and Melvin were also utilized for enhancing skills in COMSOL.

I thank the collaborating team from Slovenia, at Laboratory of Biocybernetics where I spent three months (April-June 2018) as part of UBO's International Mobility Program. I thank Prof. Damijan Miklavčič for giving me the opportunity to work in his Lab. I thank Janja for mentorship with insightful discussions and Lea for further guidance. The learning experience there added a new dimension to the work. I thank Melvin whose previous work preserved at that Lab was also beneficial in context of enhancing skills in COMSOL. I also attended a week-long workshop titled Electroporation Based Treatments and Technologies, EBTT (November 2017) earlier there which gave me an exposure to the ongoing research in Electroporation across Europe and the US. I thank all other members of the Lab for their generosity.

This PhD, the International Mobility and EBTT workshop were all funded by UBO which is gratefully acknowledged. Part of the work during the stay in Slovenia was also supported by Slovenian Research Agency.

I thank the annual thesis examining committee (CSI) which was composed of Prof. Abderrahman Beroual and Prof. Dr. Tristan Montier for giving motivation, valuable comments and suggestions while finding my work satisfactory to be continued.

I came to France without any level of French language. On my first arrival in Brest, Sophie drove me from the airport to the student's residence and helped me with the registration at university and opening of the bank account. I am very grateful to her. I thank all the people at the workplace with whom I had the chance to interact. Vinod for pre-arrival queries. Narasimha for showing the markets in my first few days. Nha, David, Norbert and Elyas for their helpful and friendly company in the office. I thank Michelle, Anne, Alain, Bernadette and Mr. Corouge for their respective affairs. Mme. Le Borgne and M. Karfaoui from Crous and Marjolaine and Béatrice from CMI were very kind. I thank all the people whom I met during the French language classes, the fellow students (especially Aakosh, Feng and Xia) and the teachers (Cyril, François, Marion, Adeline) who made the learning experience more meaningful. Special thanks to Prof. Jean-Alban and Loic who gave their time for home tutoring French as well. I thank all the people for their generous company with whom I had the chance to go on excursions or do some sports activities.

Last, but not the least, I thank my old friends, relatives and especially the dear family members for their unconditional and continuous support throughout my life.

Brest, France, January 2020

Danish Shamoon

List of publications

I. Low-order statistics of effective permittivity and electric field fluctuations in two-phase heterostructures

D. Shamon, S. Lasquellec and C. Brosseau

Journal of Applied Physics, 122 (4), (2017) 044106

DOI: 10.1063/1.4985799

II. Perspective: Towards understanding the multiscale description of cells and tissues by electromechanobiology

D. Shamon, S. Lasquellec and C. Brosseau

Journal of Applied Physics, 123 (24), (2018) 240902

DOI: 10.1063/1.5018723

III. Assessing the electro-deformation and electro-poration of biological cells using a three-dimensional finite element model

D. Shamon, J. Dermol-Černe, L. Rems, M. Reberšek, T. Kotnik, S. Lasquellec, C. Brosseau, and D. Miklavčič

Applied Physics Letters, 114 (6), (2019) 063701

DOI: 10.1063/1.5079292

IV. A multiphysics analysis of the strain energy in multicellular environments

D. Shamon, S. Lasquellec and C. Brosseau

Applied Physics Letters, 115 (4), (2019) 043701

DOI: 10.1063/1.5109533

Impact factors (Clarivate Analytics, 2019):

Journal of Applied Physics – 2.328

Applied Physics Letters – 3.521

Overview of publications

Publication I: “Low-order statistics of effective permittivity and electric field fluctuations in two-phase heterostructures”

Understanding the collective, low-frequency dielectric properties of heterostructures is a major goal in condensed matter. An effective medium approximation (EMA) involves a decoupling between the low-order statistics of the electric field fluctuations and the characteristic length scales. We report and characterize, via finite element studies, the low-order statistics effective permittivity of two phase 2D and 3D random and deterministic heterostructures as geometry, phase permittivity contrast, and inclusion content are varied. Since EMA analytical expressions become cumbersome even for simple shapes and arrangements, numerical approaches are more suitable for studying heterostructures with complex shapes and topologies. Our numerical study verifies the EMA analytic predictions when the scales are well-separated. Our numerical study compares two approaches for calculating the effective permittivity by explicit calculations of local average fields and energy. We study the conditions under which these approaches give a reliable estimate of permittivity by comparing with 2D/3D EMA analytical models and duality relation. It is found that local average fields give more accurate results. By considering 2D checkerboards which consist of a multitude of contiguous $N \times N$ square cells, the influence of the internal length scale (i.e., N) on permittivity is discussed.

Publication II: “Perspective: Towards understanding the multiscale description of cells and tissues by electromechanobiology”

Almost all biological cells in living tissues exert and experience forces that influence biological function. When subjected to an exogenous electric field, mechanical forces operate on cells, its constituents, and interfaces with the environment. Many issues about force generation and dynamics, the distance over which a force exerts its influence and how cells

convert an electrical excitation into a mechanical deformation, are not well understood from general first-principles physics. The electric field at the interface between cells is not only the driving force for the polarization and conduction phenomena but also induces simultaneously a mechanical stress field. Within the extremely heterogeneous multicellular structure of biological materials (BM), theoretical models and experimental techniques to understand and control their local electromechanical response in BM grow space. In recent years, biophysicists have begun to uncover the important time and length scales that mediate force propagation in BM. In this perspective review, the multiscale modelling approaches and experimental probes for the application of an electromagnetic field to exert mechanical forces upon polarizable BM are reported with special emphasis on the control of forces at the cell and tissue levels. Modelling is based on a multicellular assembly exchanging charges and stresses with the environment. Here, we shall restrict to coarse-graining models since the resulting computational complexity quickly becomes overwhelming. Such work can pave the way for a deeper understanding of how physical forces influence biological functions.

Publication III: “Assessing the electro-deformation and electro-poration of biological cells using a three-dimensional finite element model”

In this Letter, we explore how cell electro-deformation and electro-poration are connected. We build a time-domain model of layered concentric shells (a model of biological cells) including their dielectric and elastic properties. We simulate delivery of one trapezoidal voltage pulse to either a single spherical cell or an assembly of three neighboring cells in a specific configuration and calculate cell deformation and pore formation. We describe the qualitative features of the electric field, surface charge density, transmembrane voltage, cell elongation, and pore density distribution at specific times i.e., before, during and after the application of the electric pulse and explore the correlations between them. Our results show that (1) the polarization charge redistribution plays a significant role in the spatial distribution

of electrical stresses at 1s time scales and (2) the cell deformation and pore density can be correlated with regions of high surface charge density. In future work, our model could be used for understanding basic mechanisms of electro-deformation and electro-poration with high-frequency short bipolar pulses of biological cells in suspension or tissues.

Publication IV: “A multiphysics analysis of the strain energy in multicellular environments”

This Letter considers the strain energy distribution in cell assemblies. Our scalable model consists of N-core-shell spherical structures modeling biological cells with assumptions based on two fundamental premises. First, we use a finite element in the framework of time-domain to solve for the electrodeformation and cell electroporation when a well-defined electrical stimulus is delivered to a multicellular environment. Second, the strain-stress response of the cell assemblies is characterized by a relaxation time which is much larger than the time constant of the membrane charging. A “switch off” (corresponding to times after electrical pulsing) phenomenon observed in the strain energy signal might provide an interesting discriminant test capable of providing different information on the proximity (coupling) effect between cell and assembly anisotropy depending on the type of electrical stimulus employed. In the explicit examples we study, we learn how the local enhancement of the electric field, deformation of the cell, strain energy, and relative area occupied by the pores are modified by varying the intercellular distance distribution.

Contents

Preface.....	3
List of publications	5
Overview of publications	6
Contents	9
1. Introduction	11
2. State-of-the-art and current issues of ED and EP	19
2.1 Prior to application of electrical stimulus.....	20
2.2 After application of electrical stimulus	20
Shamoon et al. (2018)	27
2.3 A closer context on ED and EP.....	46
3. Modelling cells and tissues.....	51
3.1 Introduction.....	51
3.2 Finite Element Method.....	52
3.3 COMSOL Multiphysics and computational resources.....	55
3.4 Electric field fluctuations.....	56
Shamoon et al. (2017)	59
3.5 Numerical protocol.....	70
3.6 Geometry and meshing.....	71
3.7 Modelling coupled physics.....	74

3.7.1 Electrical model	75
3.7.2 Structural model.....	77
3.7.3 Pore model.....	80
3.8 Problem size and solver techniques	81
4. Results and discussion: ED and EP of cell assemblies.....	83
4.1 Time-dependent analyses	83
4.1.1 Small number of deforming cells.....	84
Shamoon et al. (2019-a)	93
Shamoon et al. (2019-b).....	103
4.1.2 Large number of deforming cells (unpublished work).....	112
4.2 Frequency analyses	116
4.2.1 Effect of relative orientation among two cells on total force	119
4.2.2 Effect of introducing next-nearest neighbors	123
5. Conclusion and Perspectives	129
References	133
Appendix A: Geometry conception using algorithms	139
A1. Random 2D checkerboard generation	139
A2. Randomly distributed spherical N-Cells generation	140

1. Introduction

Human beings can be viewed as extremely sophisticated biological machines that are composed of several functional systems which coordinate with each other to perform life. From breathing to eating food, being healthy or sick, even feeling emotions is full of physical and chemical processes that continue to be investigated in terms of fundamental research. One of the major differences between man-made machines and biological machines is that the latter are often composed of flexible components that are made of soft materials involving biochemical functionality. Focusing more on the physical aspects, consider the breathing of air – the lungs expand while inhalation and contract while exhalation. The effective elastic behavior of organs is indeed connected to the elastic behavior of its composing parts and any unusual change in the elasticity of media will affect the bodily functions leading to sickness or even fatal diseases. This is why the subject of mechanical behavior in biology has eventually attracted a lot of attention through the last two decades [1-2]. Though the subject is being and has been explored at several length scales [3-6], this work is particularly concerned to build simple biological tissue models in order to characterize their deformation when they are stimulated by an electric field. Several basic questions are still open for studying biological cells under an applied electric field – (1) How mechanical stress appears in biological media affecting biological functions? (2) How multicellular structures emerge or organize themselves at large scale in a mechanical context? (3) How tiny components at small scales that make up a cell affect its mechanical behavior? Numerical modelling and experimental validation based on a recent study [7] has shown that cellular level mechanical stresses in epithelial tissue can induce cell death that essentially prevents accumulation of unwanted or pathological cells. In order to study the mechanical behavior and response of biological media to internal or external stimuli, a basic introduction to its composition and underlying processes is needed.

Biological media are extremely heterogeneous and complex in terms of material composition. Physical processes occur at several length scales naturally [8-9] or in response to an external stimuli [10-12] Guo et al. (2016)].

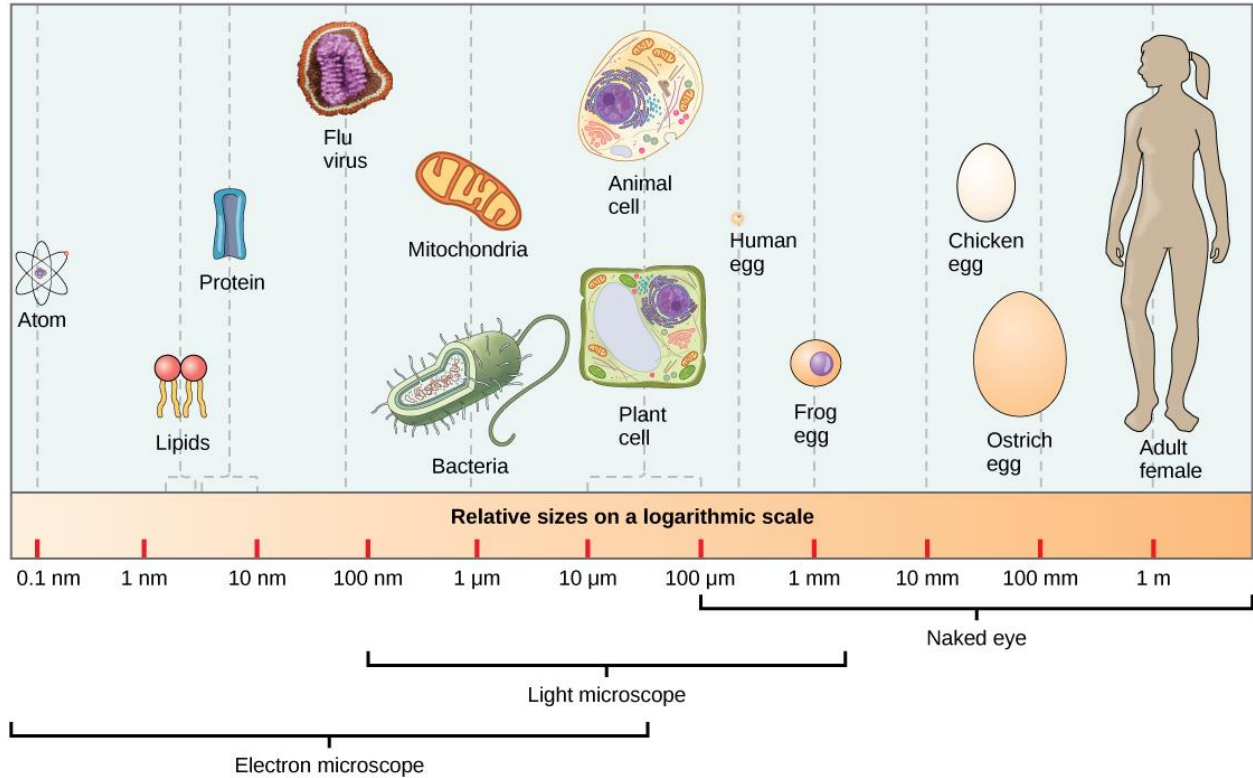


Fig.1.1: A basic comparison of relative length scales in a biological context. (Adapted from [13])

All living species are made up of tiny microscale structural units known as biological cells that possess nano-structured features as well. From a physical standpoint, a simple picture is to consider that the cells sitting next to each other compose a tissue, the tissues of different type compose organs which further coordinate with each other to perform functions of a living organism. Most animal cells fall in the size range of 5-30 μm while most plant cells fall in the range of 10-100 μm. The smallest scale includes ions and biomolecules such as proteins, carbohydrates, lipids and nucleic acids in the range of few nanometers. The major constituent in the entire biological media is water that can be thought of as a host medium in which all the mentioned entities flow or move. In fact, ions and small biomolecules are usually more mobile to flow around in the fluid regions whereas lipids and proteins can form aggregates or more

complex structures like membranes, cytoskeleton or other intracellular or extracellular entities which are less mobile. The medium can be roughly described as a dispersion of particle-like entities (ions & small molecules) and elastic or viscoelastic super-structures (membranes & cytoskeleton) in a liquid host medium (interior and exterior of the cells). The central idea is the separation of cell interior from cell exterior by the cell membrane.

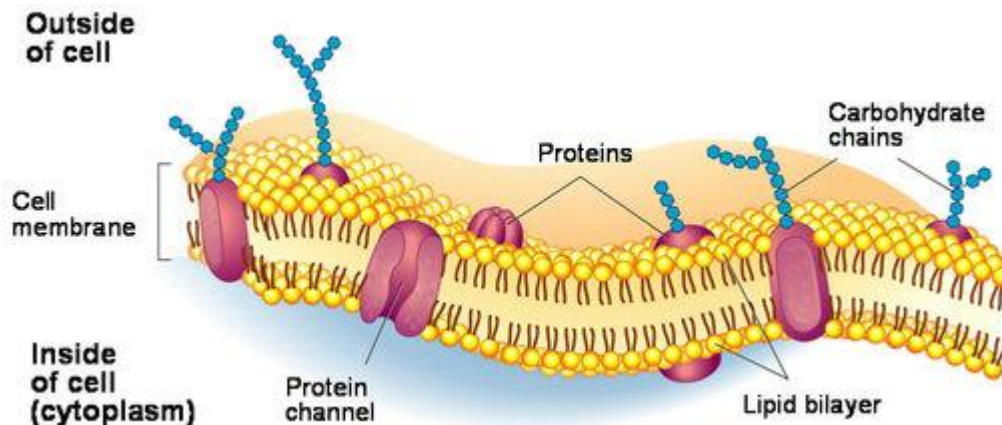


Fig.1.2: An illustration of the cell membrane (5-10 nm thick) composed of lipid molecules forming a bilayer that is embedded with proteins and ion channels (Public domain image)

While biological cells perform their usual functions in their natural surroundings, one can broadly distinguish between their physical and chemical processes. This work is mainly concerned with physical aspects such as the electrical and mechanical behavior of the involved entities. The usual functions of cells can be manipulated by various external stimuli such as electrical, mechanical and fluidic or a combination of these. Here, attention is focused to those studies involving an electric stimulus to generate electrical and mechanical responses in the cells. An externally applied electric field can disrupt the cell membranes by exerting an electric stress distribution over their surfaces. This arises because the applied electric field essentially polarizes the individual cells by accumulating the bound charges at the cell membrane which behave as an insulating material. As a result, an electric stress is induced that tends to deform the cell shape and when the fields are strong enough, it leads to formation of nano-pores into the cell membrane thereby altering its insulating behavior to partially conducting. If the pores

last long enough to kill the cells, the process is irreversible, otherwise it is reversible. These two phenomena (also depicted in Fig.1.3) are referred to as electrodeformation (ED) and electroporation (EP), respectively. As a matter of fact, the mechanisms of ED and EP are crucial for understanding the biophysical description of cells and tissues. Experimentally, ED and EP of cells were first observed nearly four decades ago [14-15].

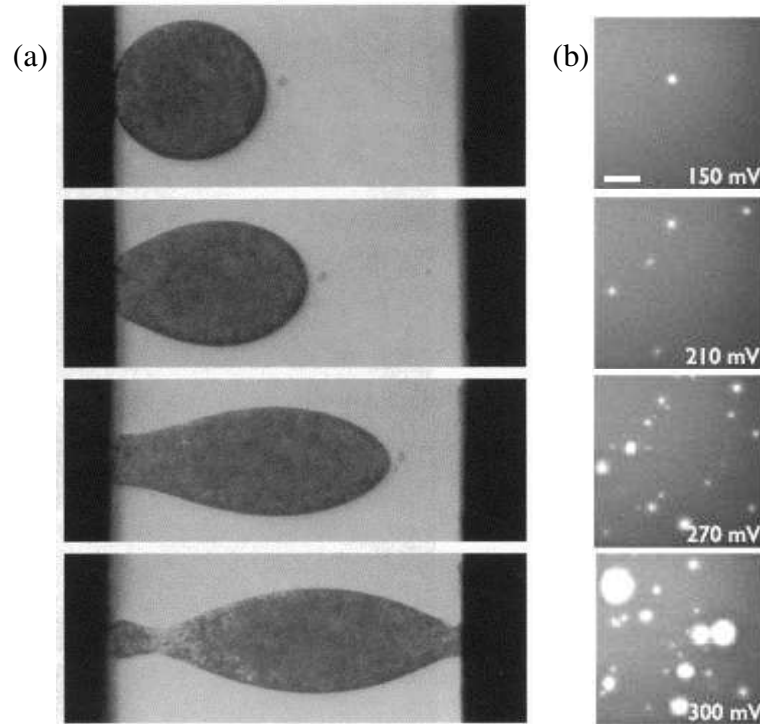


Fig.1.3: Microscopic images showing (a) electrodeformation (Fig.1 of [16]) and (b) electroporation (Fig.3A of [17]). Left image shows global deformation of *Arbacia Puntulata* egg under an AC electric field of 2 MHz. The egg diameter = 75 μm , the space between electrodes = 175 μm , electric field strength at electrode surface was gradually increased from 0 to 1095 V/cm, cell deformation was recorded at a time interval of about 30 s. Right image (using TIRF) shows pore formations over a patch of lipid bilayer (DPhPC) across which the transmembrane potential is being varied by applying a DC voltage. The scale bar is 25 μm in (b).

Historically, the major issues in developmental biology (e.g. morphological changes) and wound-healing (repair of damaged tissue) are explained through mechanisms involving chemical gradients and reaction-diffusion processes. In the same context, the idea of naturally existing electrical gradients and electromechanical processes have also been explored [18-19]. The electric fields can also exist naturally in the biological media and guide cells to move or

deform. In the same fashion, an external electric field can trigger an electrical or mechanical response in the media and thus affect the usual biological functions or processes.

It is worth noting that ED and EP phenomena have not been studied simultaneously in the archival literature with a few notable exceptions [20-21]. Additionally, there is a larger number of studies dealing with electrical and EP modelling of cells or tissues than those concerned with ED modelling.

Since a decade, Brosseau's group has expertise in finite element modelling for many purposes: analyze the fraction of electroporated cells in a random distribution of numerous cells and determine the anisotropy in its conductivity by time-dependent analysis [22]; evaluate the electric field enhancement using plasmonic nano-particles near cell membrane surface by steady-state analysis [23]; study the electrostatic force and surface charge redistribution over conducting objects maintained at fixed electric potentials by steady-state analysis [24-25]; analyze the electrical interaction among polarizable cells and surface charge redistribution by frequency analysis under an applied electric field [26]; and determine the electric potential across the cell membranes of arbitrary shaped cells in the context of EP [27].

What has not been studied so far is the electromechanical response of cell assemblies modelling a biological tissue. This topic forms the core subject of this work. It has been shown in the case of phospholipid bilayers that EP is affected by ED [21]. Phospholipid bilayers offer a much simpler system to study in comparison to real biological cells which are way more complex. The important point to note here is that the length and time scales involved for the two phenomena are not necessarily the same for simple phospholipid bilayers as compared to those for complex cell membranes based on a few simple arguments. For instance – (1) ED of phospholipid bilayer can be expected to be much more pronounced than that for cell membrane because the latter is also strengthened by the cytoskeleton; (2) electropores of up to 25 μm

diameter can be formed on phospholipid bilayers whereas on cell membranes they are supposedly of up to a few tens of nm diameter as predicted by models [10].

This work is motivated by the presumption that a multicellular description within the framework of continuum physics is useful to predict the electromechanical collective response of numerous cells in a suspension or arranged as a tissue. The continuum description of the media employed here leaves out the complexity of the intracellular organelles and the finer structural details of the cytoskeleton or even the extra-cellular matrix. Thus, the spirit of this work is different from molecular dynamics approach as well as the homogeneous tissue approach and lies in between the two by virtue of modelling multiple (3-5) distinct phases.

This work attempts to answer the following questions. How do cell-cell proximity and asymmetry in the arrangement of cells affect the ED and EP phenomena? How do closely spaced multiple cells behave differently from the single cell situation under an externally applied electric field? How does random positioning in cellular arrangements modelling a suspension or tissue contribute to the effective mechanical response under an externally applied electric field?

At the very outset of this work, it is worth noting that the innovation of this work compared to the state-of-the-art dealing with electrical and EP modelling of cells is that it considers elasticity of biological media and predicts time-dependent small deformations of numerous biological cells and calculates strain energy for a global quantification of the deformation. Importantly, it deals with both symmetric and non-symmetric configurations of cells in 3D. Time domain coupling of electrical and mechanical response under the continuum approach using finite element numerical analysis offers an improved platform for further scrutiny of applied electric field effects on biological media. These effects may be linked and validated by the recent advances in experimental measurements of force, displacements over cells and their perforation efficiency.

The organization of this work is as follows: Chapter 2 gives a short account the state-of-the-art and current issues in the field of electromechanobiology. Chapter 3 gives an introduction of the numerical methods employed in this work. Chapter 4 discusses the results of ED and EP for deformable cells under an applied electric field. Chapter 5 presents the conclusions and perspectives while invoking a brief discussion on the scope and limitations of our results.

2. State-of-the-art and current issues of ED and EP

In this chapter, a brief analysis of scientific reports dealing with an electric stimulation of single (or multiple) cell(s) (or vesicles) is presented. Firstly, an overview of ED and EP scenarios is put forward. The publication Shamooun et al, (2018) [28] is then presented that provides a short review of the state-of-the-art and current issues in electromechanobiology. Experiments or theoretical analyses of ED and EP scenarios are very diverse owing to the differences of biological media and specific methods used. Therefore, our bibliographic analysis offers a broad classification of the literature in terms of the consequence of the application of electric field on biological media i.e. motion, deformation and perforation of individual cells. We note that this hinders a precise comparative analysis of results emerging from different studies unless very similar methods or conditions are employed.

The literature discussed in the publication Shamooun et al, (2018) [28] portrays an important aspect of the field of electromechanobiology i.e. its diversity in terms of particular cells, cellular environment and specific devices used. Table 2.1 provides a glimpse along these differences. Biological cells are extracted from living organisms and stocked, which are regrown in the lab by one of the two cell-culture techniques - ‘adherent’ culture where they occur as monolayers on an artificial substrate or as ‘suspension’ culture where they are in a free-floating condition. On a substrate, cells assume a flattened shape whereas in suspension, they are mostly spherical (exception for Red Blood Cells (RBCs) which are discoidal).

Cell name (References in Shamooun et al, 2018 [28])	Cell environment	Device electrodes
Human Bone Marrow Mesenchymal stem cells [42]	Adhering	Parallel facing
Human Embryonic Kidney cells [39]	Free-floating	Coplanar
JURKAT (Human T Lymphocyte cells) {WBCs} [39]	Free-floating	Coplanar
PC3 (Human Prostate Cancer cells) [39]	Free-floating	Coplanar
Red blood cells {RBCs} [45]	Free-floating	None + optics
PC12 (Mouse Neuronal cells) [38]	Adhering	Coplanar
Human Melanoma cells (Skin Cancer cells) [48]	Adhering	None + optics
NIH/3T3 cells (Mouse Embryonic cells) [44]	Free-floating	Parallel facing + optics

Table 2.1: Some cells in diverse scenarios of examination for mechanical response studies.

2.1 Prior to application of electrical stimulus

The cell membrane is the basic component for ED and EP studies. It serves as the boundary separating the cell interior (also known as cytoplasm) from the cell exterior (also known as extracellular fluid or matrix). The major structural component of the cell membrane is the lipid bilayer over which membrane proteins and ion-channels are embedded (Fig.1.2). It gives shape to the cell which is also re-enforced by the underlying cytoskeleton. It facilitates the transport of mobile biomolecules in and out of the cell by natural biological processes such as endocytosis, exocytosis and ionic flow through ion-channels.

The naturally occurring differences of the ionic charge concentration across the membrane renders the cytoplasm to be slightly negative with respect to the extracellular fluid, thereby leading to a 'resting membrane potential' across the cell membrane. This potential across the membrane is actually measured by an experimental technique called 'patch-clamp' and found to be in the range of -100 mV to -10 mV depending on the type of cells. Typical average numbers can be -95 mV for skeletal muscle cells, -70 mV for neurons, -50 mV for smooth muscle cells and -12 mV for erythrocytes (or Red Blood Cells (RBCs)). The relative permittivity of cell membrane is reported in the range of 2-9. From an electrical point of view, the membrane acts as a good insulator. The capacitance of the cell membrane is on the order of 10^{-6} F/cm². Overall, all parts of the biological media can behave partly as conductors (due to mobility of charges) and partly as capacitors (due to storage of charges).

2.2 After application of electrical stimulus

The biological media can also be viewed as a network of resistors and capacitors through which a current flows under an applied electric field. Under an externally applied pulsed field for a duration larger than the charging time of the membrane (which is on the order of 1 μ s), charge redistribution takes place that leads to an increase in the membrane potential

in addition to the resting potential. The application of AC field affects this interfacial charge distribution in an interesting way that has been well studied both theoretically [29] and experimentally. At low frequencies ($\nu < \text{MHz}$), the cell membrane does not allow the current to pass through it, while at higher frequencies ($\nu > \text{MHz}$), the current passes through the cell membrane. The consequence of this behavior appears in the effective dielectric response of the biological cells in the form of β -relaxation related to classical Maxwell-Wagner interfacial polarization charges. A theoretical study for calculating the dielectric spectra over a broad range of frequencies was performed by Biasio et al. (2010) [30] that considers core-shell structures of prolate and oblate spheroidal cell suspensions. The results not only show the β -dispersion but also the α -dispersion that occurs at much lower frequencies ($\nu < \text{kHz}$). This study is distinguished by the fact that it not only corroborates the interfacial polarization effect arising from the heterogeneity of the system but it also adds the effect of additional surface charge distribution leading to α -dispersion. The surface charge distribution generates superficial current densities which are accounted by $J = -\gamma_k \nabla V - D_k \nabla \rho_k$ where γ_k and D_k are surface conductivity and ion diffusion coefficient while k refers to the outer or inner side of the membrane. Under the assumption of small electric fields, the conductivity is proportional to charge distribution through mobilities, μ_k of the bound charges such that $\gamma_k = \mu_k \rho_k$. Figure 2.1 shows the dielectric relaxation for prolate and oblate spheroids as membrane conductivity is varied between 10^{-7} to 10^{-5} S/m. The study shows several other parameter variations such as the effect of changing aspect ratio of the spheroids, surface conductivities or ion diffusion coefficients etc. Dielectric properties of biological materials have been well characterized by Schwan and Takashima, (1991) [31] stating that the various plateaus observed in the response are due to ionic processes (α -relaxation), charging-up of the membrane or orientation of the permanent dipoles (β -relaxation) and orientational relaxation of water (γ -relaxation).

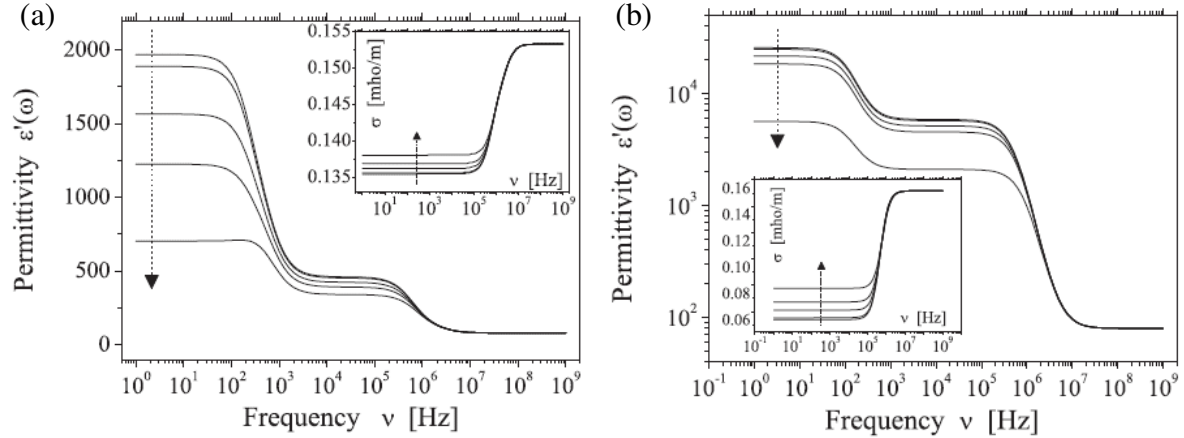


Fig.2.1: Effect of changing membrane conductivity (10^{-7} , 10^{-6} , 5×10^{-6} , 10^{-5} , 2×10^{-5} S/m, the arrow marks the ascending order) for dielectric spectra of (a) prolate and (b) oblate spheroidal cell suspensions. Insets show the corresponding conductivity spectra. The conductivity and relative permittivity for cell suspension media is set to 0.15 S/m & 78.5 while that for cytoplasm is set to 0.2 S/m & 100. Membrane relative permittivity is set to 2.5. The volume of the spheroids is the same $65.4 \mu\text{m}^3$ while the major and minor semi-axes for prolate shape are $5 \mu\text{m}$ & $1.8 \mu\text{m}$ and that for oblate shape are $4 \mu\text{m}$ and $1.98 \mu\text{m}$. Surface conductivities and ion diffusion coefficients are set to 10^{-9} C/Vs and 10^{-8} m^2/s . (Adapted from Fig.5 and Fig.6 of [30]).

The redistributed charge exerts a force on the membrane which has been evaluated for Chinese Hamster Ovary (CHO) cells using co-planar electrodes with AC electric field to be 0.8-21 Pa [32]. Force and stress measurement techniques used to study biological media have been reviewed by Sugimura et al, (2016) [3], listed in Table 2.2.

	Measured quantities	Measurable range	Time scale*	Size scale‡	Advantages	Disadvantages	Cost
Indentation/ Microplates/ AFM	Cell or aggregate surface tension	0.1 Pa	s-h	1-100 μm	Absolute measurements	Contact method	€€- €€€€
Pipette aspiration	Cell or aggregate surface tension	$\mu\text{N}/\text{m}$ - mN/m	> 10 s	1-100 μm	Absolute measurements	Contact method	€€
Optical/ Magnetic tweezers	Cell junction tension	pN-nN	ms-min	0.1-10 μm	Non-contact; Absolute measurements	Delicate calibration	€€€
Subcellular laser ablation	Cell junction tension to viscous drag ratio	NA	0.1 s-min	0.1-10 μm	Non-contact	Possible collateral damage	€€- €€€
Tissue scale laser ablation	Tissue stress to viscosity ratio	NA	s-min	10 μm - 1 mm	Non-contact	Requires sample and laser alignment, few experiments per sample	€€- €€€
FRET force probe	Intramolecular tension	pN	Video rate	nm	Molecular measurements	Requires different control constructs, delicate calibration	€
Liquid drops	Cell-scale stress	~0.1-60 kPa	0.1 s-h	>5 μm	Absolute measurements	Requires surface chemistry of droplets	€€
Birefringence	Tissue-scale stress	> 10 kPa	Video rate	> μm	Global	Requires flat, transparent sample, delicate calibration	€
Force inference	Relative cell junction tension, cell pressure	NA	Video rate	> μm	Image based; Global	Requires image segmentation	€

*Time scale of the mechanical processes that can be probed; ‡Size scale of the mechanical processes or mechanical elements that can be probed; NA, not applicable because only relative measurements; Costs excluding the microscopes: € (<€10,000); €€ (€10,000-50,000); €€€ (€50,000-1,00,000); €€€€ (€1,00,000-2,00,000)

Table 2.2: Ways and benefits of several force measurement methods in living tissue for various time and length scales. (Adapted from [3])

Once, the force is exerted, the resulting deformation depends on the rheological (elastic or viscoelastic) properties of the cell membrane and the region locally surrounding it. Estimation of elastic properties is usually performed by mechanical testing schemes. Atomic Force Microscope (AFM) tip is used to exert a known force, the deformation is observed and the properties estimated based on analytical models. Elastic properties of many different types of mammalian cells measured by AFM reviewed by Kuznetsova et al. (2007) [33] are listed in Table 2.3. The wide variability of the values indicate not only the realistic variety but also the imperfections in the measurement.

Cell type	Young's modulus (kPa)
Endothelial cells	
BPAEC	0.2-2.0
HUVEC	10-11
Leukocytes	
HL60	0.2-1.4
JURKAT	0.02-0.08
Neutrophils	0.07-0.2
Corti organ's cells	
Outer hair cells	300-400
Mouse outer hair cells	2-4
Hensen's cells	0.3-1.1
Skeletal muscle cells	
Murine C ₂ C ₁₂ myoblasts	11-45
Murine C ₂ C ₁₂ myotubes	8-14
Myofibrils	40-45
Osteoblasts	0.3-20
Epidermal keratocytes	10-55
Platelets	1-50
Erythrocytes	14-33

Table 2.3: Young's modulus of some mammalian cells probed using AFM. (Adapted from [33])

The elasticity of cerebral endothelial (D3) cells, which constitute the structural basis of blood-brain barrier, have been analyzed by AFM indentation [34], the average value of Young's modulus is found to be close to 5 kPa. ED has also been used for estimating elastic properties [32]. The reported values for Young's modulus (including those for extracellular matrix on the right extremum) vary from 0.02 kPa to 1.2 GPa. The wide range is due to the fact

that different types of cells in a tissue vary in internal structural composition. For instance, cells from the muscular tissue have stiffness in between those from the blood (softer) and bone (stiffer).

Transmembrane potential (*TMP* or also noted as *ITV* in the literature) refers to the potential across the membrane which is the sum of the resting and induced potentials. Once, this potential exceeds a few hundred millivolts, some structural changes appear in the cell membrane that lead to formation of new electrical conduction pathways in the otherwise insulating membrane. In the context of Fig.1.3b, where electropores (of several micrometers in diameter) over a phospholipid bilayer are imaged, it is interesting to observe how several pores appear as function of the *TMP* (values of which are marked in the inset of the figure). It is worth emphasizing that such electropores have not been yet imaged over real cell membranes but their presence is inferred by the observed increased transport of small and large molecules across the membrane also leading to an increase in the measured conductance of the membrane. Ionic currents are studied using the patch-clamp techniques for isolated cells, tissue sections or even patches of membrane. Use of fluorescence microscopy additionally corroborates the entry of certain florescent molecules such as Propidium Iodide into the cell cytoplasm. Figure 2.2 highlights several methods and indicators of EP. Cell viability and transfection efficiency are consequently calculated as well to further quantify EP in cell populations. Cell viability is defined as the ratio of initial cell number minus the dead cell number to the initial cell number. The living and dead cells are labelled with a mixture of two florescent dyes that render the cell green or red based on whether it is living or dead. Transfection efficiency is defined as the percentage of the cells transfected with a desired ‘cargo’ as compared to the entire population. While the experimental aspects were briefly put forward, the theoretical aspects are briefly introduced next.

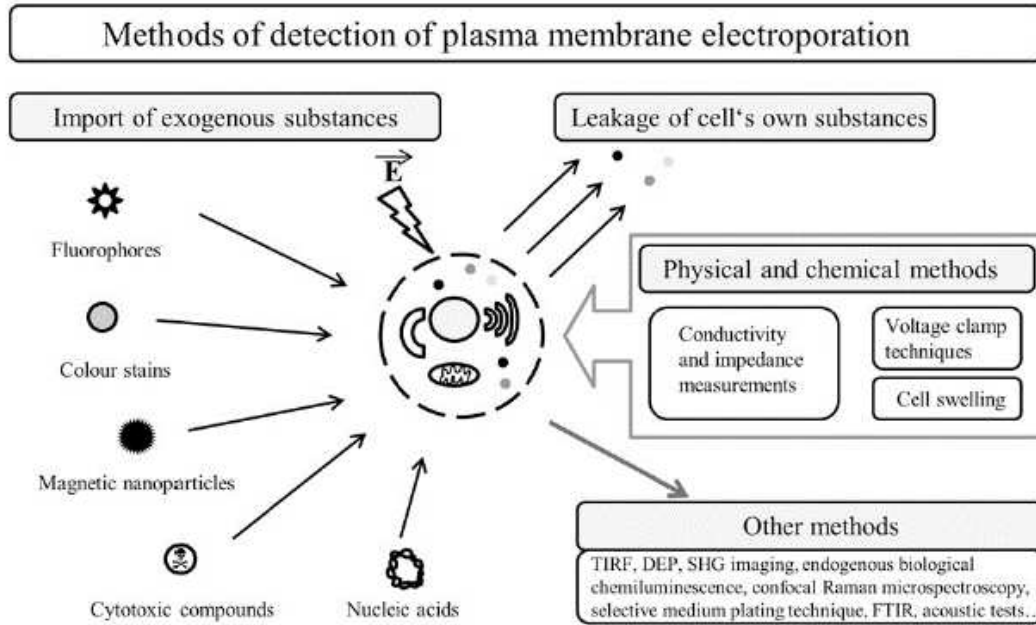


Fig.2.2: Several methods that are used to infer electroporation of cells. (Adapted from [35]).

The dielectric breakdown of cell membranes was known even before the term ‘electroporation’ was coined down. Under high field strengths, the usual insulating behavior of the membrane changes to conducting, highlighting a critical threshold in terms of either the applied field strength or the voltage induced across the membrane. Initial theoretical studies (also reviewed in [36]) began with analytically describing the induced voltage across the membrane of an isolated spherical cell in terms of field strength E_{app} and cell radius R as $TMP = 1.5RE_{app} \cos \theta$, where θ is angle between the field line and a normal from the center of the cell to its membrane. This equation is known as Schwan’s equation and used for steady-state description of TMP which was derived by Schwan in 1957 by solving Laplace equation (see also [37]). To describe the transient behavior during initial microseconds, the first order Schwan’s equation is written as $TMP = 1.5RE_{app} \cos \theta (1 - \exp(-t/\tau_m))$, where τ_m is membrane charging time constant ($\sim 1 \mu s$) given by $\tau_m = \frac{R\epsilon_m}{2d_m(\frac{\sigma_2\sigma_1}{\sigma_2+2\sigma_1})+R\sigma_m}$, where d_m denotes membrane thickness, σ and ϵ denote conductivity and relative permittivity. ‘1’ and ‘2’ refers to the outside and inside of the cell. Under an oscillating field with frequency ν , the TMP varies

with frequency as $TMP = \frac{1.5RE_{app} \cos \theta}{\sqrt{1+(\omega\tau_m)^2}}$, where $\omega = 2\pi\nu$. When the period of oscillating field or the duration of pulsed field becomes comparable or smaller than the charging constant, the induced voltage is diminished. Thus, high frequency stimuli (GHz) and ultra-short duration pulses (ns) lead to diminished values of induced TMP . The experimentally determined threshold voltage for murine myeloma cells was reported in the same study in the range of 0.33-0.53 V. The threshold value is usually assumed to be constant (0.258 V) in an advanced theoretical model (to be discussed next), but this study reports variations in it with changing conductivity of the suspension media and applied frequency. A parallel RC circuit is also a simple representation that is employed to calculate the response current flowing through the overall tissue under the application of a voltage pulse. A larger network of RC circuits has been employed by Gowrishankar and Weaver, (2002) [38] for single as well as multiple cells.

The theory of EP progressed further [10, 39] which assumes an appearance of nanopores over cell membrane affects the membrane conductivity. This model is described in more detail in the next chapter. The size of the pores is assumed to be fixed in this work but as it will be discussed shortly that it can increase or decrease depending on the pore energy dynamics.

The following publication Shamooun et al. (2018) [28] gives significant details on the progress of understanding the concept and general results dealing with electromechanobiology of cells and tissue.

Shamoon et al. (2018)

Perspective: Towards understanding the multiscale description of cells and tissues

by electromechanobiology

D. Shamoon, S. Lasquellec and C. Brosseau

Journal of Applied Physics, 123 (24), (2018) 240902

DOI: 10.1063/1.5018723

Perspective: Towards understanding the multiscale description of cells and tissues by electromechanobiology

D. Shamoon, S. Lasquellec, and C. Brosseau^{a)}

Université de Brest, Lab-STICC, CS 93837, 6 Avenue Le Gorgeu, 29238 Brest Cedex 3, France

(Received 8 December 2017; accepted 1 June 2018; published online 25 June 2018)

Almost all biological cells in living tissues exert and experience forces that influence biological function. When subjected to an exogenous electric field, mechanical forces operate on cells, its constituents, and interfaces with the environment. Many issues about force generation and dynamics, the distance over which a force exerts its influence and how cells convert an electrical excitation into a mechanical deformation, are not well understood from general first-principles physics. The electric field at the interface between cells is not only the driving force for the polarization and conduction phenomena but also induces simultaneously a mechanical stress field. Within the extremely heterogeneous multicellular structure of biological materials (BM), theoretical models and experimental techniques to understand and control their local electromechanical response in BM grow space. In recent years, biophysicists have begun to uncover the important time and length scales that mediate force propagation in BM. In this perspective review, the multi-scale modelling approaches and experimental probes for the application of an electromagnetic field to exert mechanical forces upon polarizable BM are reported with special emphasis on the control of forces at the cell and tissue levels. Modelling is based on a multicellular assembly exchanging charges and stresses with the environment. Here, we shall restrict to coarse-graining models since the resulting computational complexity quickly becomes overwhelming. Such work can pave the way for a deeper understanding of how physical forces influence biological functions. *Published by AIP Publishing.* <https://doi.org/10.1063/1.5018723>

I. INTRODUCTION AND MOTIVATION

A. Context and motivation

Biological materials (BM) such as eukaryotic cells and tissues are extremely heterogeneous and structured at many length scales. Such materials are easily deformable by external stresses, electric or magnetic fields, or even by thermal fluctuations which can be described from a soft condensed matter perspective. The physical and physiological functions of composite BM are highly dependent on the structural, spatial, and chemical interactions of its subcellular components: the extremely thin dielectric membrane and the highly conducting cytoplasm. Previous studies have indicated hierarchical and highly ordered structures in BM based on small-angle x-ray and neutron scattering, transmission electron microscopy, and atomic force microscopy, see, e.g., Ref. 1. As sketched in Fig. 1, several configurations (in schematic forms) of BM will be under discussion in this report. Individual cells are the building blocks of tissues. In most BM, our knowledge of cellular diversity is incomplete.

To understand how complex tissues work, it is important to learn the functional capacities of each cell type and to understand how any physical information may be inferred by locally probing an extremely heterogeneous material. As illustrated in Fig. 1, cell shape is also affected by cell-substrate, cell-cell, and cell-extracellular medium (ECM) interactions, apart from its intrinsic cytoskeletal architecture and organelles.

One of the most intriguing issues in biophysics is how to describe the ability of cells to respond to electric fields and how the forces derived from these propagate on the characteristic length scales of their local microenvironment.¹ As polarizable physical objects, the expression of the total force acting on a cell which is subjected to an electric field can be calculated by Maxwell's stress tensor.² The precise control of forces between cells and those acting across individual molecules in cells is crucial to maintain the characteristic shape and size of tissues.³ In this capacity, the mechanical properties of cells are largely determined by the actin cytoskeleton network, a hybrid polymer gel consisting of several kinds of filamentous proteins, such as filamentous actin (F-actin), microtubules, and intermediate filaments. Cells generate forces by contracting the cytoskeleton.⁴ The cytoskeletal network is predominantly under tension; its stiffness increases with tension and thereby increases the forces it can support.⁵⁻⁷

Almost all living cells and tissues exert and experience physical forces that influence biological function.¹ One of the ultimate goals of biology is aimed at understanding and controlling biochemical reaction systems. Mechanical properties and forces are important in health as well, i.e., there are many examples showing that numerous human pathologies are strongly linked to changes in the mechanical properties of tissues, e.g., arteriosclerosis and liver fibrosis.^{8,9} Translating this research into the clinic may also help us create innovative ways of treating certain diseases using electric- and mechanics-based tools. Despite the great deal of effort that has been devoted to these materials, however,

^{a)}brosseau@univ-brest.fr

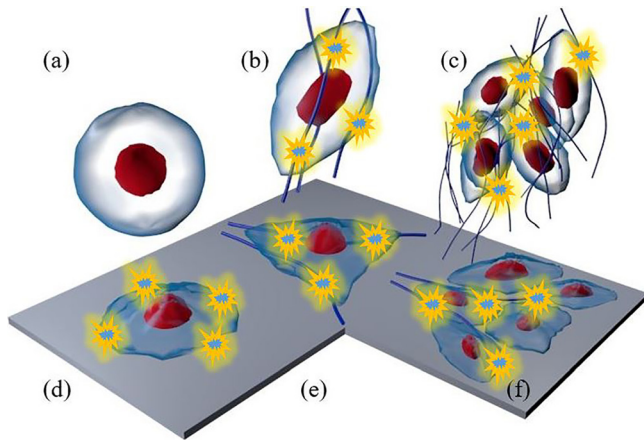


FIG. 1. Schematics of several examples of BM considered in this report. (a) Most mammalian cells assume a spherical shape. A biological cell is a material with complex properties consisting of an extremely heterogeneous, dynamic, and non-equilibrium intracellular biopolymer network (cytoskeleton). (b) A cell within the extracellular medium (ECM) which serves as the physical scaffolding within which cells live and move (shown here as blue threads). Cell-cell interactions and intracellular protein complexes (adhesion) between cells and ECM drive the stability and/or reconstruction of multicellular structures. Focal adhesions (yellow stars) mediate mechanical forces transmission to the cytoskeletons. Furthermore, they also transmit forces generated inside the cell by molecular motors such as myosin. (c) Spatial aggregation of cells forming a tissue with cell-cell and cell-ECM interactions that drive the stability and/or reconstruction of multicellular structures. (d)–(f) Cells adhering on a flat substrate assume nearly planar shapes.

understanding the local properties of the forces transmitted between cells of arbitrary shape and size in tissues still presents challenges for theory, simulation, and experiment. However, a local description is insufficient to disclose fundamental physical mechanisms of electromechanobiology. BM are intrinsically complex because they are influenced by variables that are outside a single level of space-time description. Thus, the collective behavior of BM cannot be simply inferred from the behavior of its elements. This has encouraged researchers to look into more sophisticated models integrating stochastic fluctuations and spatial inhomogeneity using experimental observations as guidelines during the formulation of these models.

Although the molecular details of BM are complex, in the past decade or so, numerical techniques allow quantitative coarse-grained-level three-dimensional core-shell (CS) models of biological cells.^{10–12} Some of the benefits and challenges of finite element (FE) modelling of the frequency response in an external electric field of dynamic multicellular structures (nonthermal effects) are discussed in Refs. 13–15. Despite these studies, however, electromechanobiology studies of BM combining physical modelling and experiment are still lacking and continue to be a major scientific challenge.

A partial motivation for this report is to summarize and highlight recent major advances in electromechanobiology that have paved the way for new phenomena and technologies useful for manipulation of BM at cellular and tissue levels. Throughout this perspective at the interfaces of applied physics and biology, we will highlight the importance and benefits of multiscale models of multicellular force in BM as leverage to be used for manipulating and engineering

synthetic BM, both for therapeutic applications and basic biological studies.

B. Plan

We have divided our presentation into three sections. First, to set the stage for the presentation of modelling and experimental results in Secs. II–IV, we introduce and define useful concepts. We take the point of view of analytical formulations of the mechanical response that a CS model of biological cells must experience when they are stimulated by an electric field. Second, we provide several illustrating examples of how a variety of recent developments of experimental techniques add to the characterization toolbox for describing the electromechanical response in living cells and controlling the remote manipulation of BM. Third, after exploring the insights provided by these examples, we discuss some of the most recent multiphysics coarse-graining approaches that are opening up opportunities in achieving great sensitivity of relaxation, electric field induced transmembrane voltage (ITV), electroporation (EP), and membrane disruption consequent on the variation of the operating frequency, shape, and surface charge, and we briefly offer perspective comments and describe relevant challenges on the current trends in this field of research.

II. ANALYTICAL FORMULATIONS OF FORCES

The purpose of this section is to briefly consider analytical formulations which can be used to describe how cells sense and respond mechanically to an electric field excitation. Although most of the concepts have been around in various forms for about 50 years, they seem to have recently gained serious traction and acceptance in the general field of biophysics. Many theoretical studies have demonstrated that BM exhibit rich macroscopic electromechanical behavior, depending sensitively on network connectivity of cells, field excitation (i.e., dc, ac), and frequency.

A. Background

One way to think about electrostatic forces (EFs) between two polarized objects is based on the Maxwell stress tensor (MST). If T is a contraction of the latter $\mathbf{n}T = -\frac{1}{2}\mathbf{n}(\mathbf{E}\cdot\mathbf{D}) + (\mathbf{n}\cdot\mathbf{E})\mathbf{D}'$, where \mathbf{E} is the electric field and \mathbf{D} is the electric displacement. This is integrated over the surface of the particle on which force acts, i.e., $F = \oint_S \mathbf{n}\cdot T dS$, where dS is a surface element, \mathbf{n} is the outward normal from the particle, and t means the transpose of a column vector.^{16–18} In frequency domain studies, the instantaneous electrostatic force is calculated by taking the real part of all the variables involved. The cycle averaged Maxwell's stress tensor can be computed as $\mathbf{n}\langle T \rangle = \frac{1}{2}\text{Re}[-\frac{1}{2}\mathbf{n}(\mathbf{E}^*\cdot\mathbf{D}) + (\mathbf{n}\cdot\mathbf{E}^*)\mathbf{D}']$, where $*$ is the symbol of complex conjugation. The second is relevant to non-uniform applied electric fields \mathbf{E} and involves considering dipole or multipole moments, e.g., $F = \mathbf{p}\cdot\nabla\mathbf{E}$ for the lowest-order (dipole) approximation, where \mathbf{p} is the dipole moment. Several authors^{18–20} have shown that the differences observed in the EF calculations between the two different simulation methods arise because

the approximations in the two methods are taken to different orders. Biological cells stressed by an external electrical field undergo mechanical deformation and remodelling caused by electro-mechanical Maxwell stresses. These stresses appear at the internal and external biomembrane interfaces due to the differences in electrical properties of the membrane and the surrounding and internal fluids. The Maxwell forces exerted on the interface between two dielectrics are directed from the dielectric with a higher permittivity towards the dielectric with a lower permittivity. For a spherical cell, the polarization charge density on the internal membrane/cytoplasm interface is higher than the charge density on the external membrane/extracellular medium (ECM). ECM that surrounds and supports cells possesses a gel-like structure composed of several kinds of biopolymers such as collagen, elastin, hyaluronic acid, fibronectin, and proteoglycans. More importantly, ECM serves also as a dynamic roadmap for cellular signalling molecules such as cytokines and chemokines. The difference in the polarization charge densities is accompanied by differences in the magnitude of the electro-mechanical stresses on either side of the membrane. This leads to the appearance of a net radial force.

Based on a surface charge method, Doerr and Yu calculated the EF between an arbitrary number of charged dielectric spheres.^{21–23} These authors noted that the magnitude (relative to point charges in an infinite solvent) of attractive EFs decreased while the magnitude of repulsive EFs is increased (again, relative to point charges in an infinite solvent). These results raised the question of why a dense system of charged cells does not simply aggregate. Recently, Tian and co-workers used an analytical approach to address the problem of evaluating the EF between two polarized inhomogeneous particles.²⁴ Their study points towards the importance of the inhomogeneities as key factors for determining crossover frequencies (CFs) at which the EF changes from attraction to repulsion or vice versa (i.e., defined also by a vanishing EFs). Within the dipolar approximation, CFs correspond to an angular frequency $\omega_{CF} = \frac{1}{\epsilon_0} \sqrt{\frac{(\sigma_1 - \sigma_2)(\sigma_2 + 2\sigma_1)}{(\epsilon_2 - \epsilon_1)(\epsilon_2 + 2\epsilon_1)}} = \tau_{MWS}^{-1/2} \sqrt{\frac{(\sigma_1 - \sigma_2)}{\epsilon_0(\epsilon_2 - \epsilon_1)}}$, where a homogeneous dielectric sphere (relative permittivity ϵ_2 and

conductivity σ_2) is embedded in a host medium (relative permittivity ϵ_1 and conductivity σ_1) submitted to an electric field with a harmonic time dependence, and $\tau_{MWS} = \frac{(\epsilon_2 + 2\epsilon_1)\epsilon_0}{\sigma_2 + 2\sigma_1}$ is the Maxwell-Wagner-Sillars relaxation time.

It is also worth noting that cell modelling in terms of undeformable particles can be useful for analytical studies of biological cells since such objects are fairly simple enough to handle and yet provide rich insights by incorporating several physical factors within a single theory. Recently, several synthetic systems which capture the ability of cells (considered as magnetic microparticles) to move and interact through viscoelastic materials in response to external stimuli have been proposed.^{25,26} Consideration of the fundamental forces that capture the essential features of the response of a particle to an electric field excitation includes the dielectrophoretic (DEP) and electrothermal (ET) forces. Since the present report considers particles of $\sim 1 - 10 \mu\text{m}$ size, the effects of gravity can be neglected. Additionally, Castellanos and coworkers predicted that ac electroosmosis is not observable for frequencies greater than 100 kHz when medium electrical conductivity²⁷ is 0.002 S/m. DEP results in a force on a dielectric particle subjected to a non-uniform voltage gradient (where the particle is much smaller than the electric field nonuniformities).¹⁸ ET force is the volume force exhibited on the fluid medium due to the thermal gradients generated by ac electric fields. The ac nonuniform electrical fields in the system generate Joule heating at the electrodes leading to changes in the conductivity and permittivity of the medium, thus exerting an electrical force on the medium.²⁸ The (time-averaged) forces acting on a particle in suspension under the influence of an ac electric field are of several kinds (Table I).

B. CS modelling

Although the details of the constituents of even a single cell are complex, it is natural to ask how the electrical and mechanical properties of biological cells can be described in terms of an effective (continuum) CS model since it represents a minimal model of reduced complexity.^{29,30} To this way of thinking, the cytoplasm can be approximated as a

TABLE I. DEP is a phenomenon in which a force is exerted on uncharged particles because of the polarization effects that occur in nonuniform electric fields. Usually this force arises on all types of particles, charged or uncharged. The strength of the DEP force depends mainly on electrical properties of the particles, medium, shape (here assumed to be spherical of radius r), and size of the particles, field magnitude E_{rms} , angular frequency ω , and phase φ the applied AC signal; f_{CM} defines the Clausius-Mossotti factor which depends on the applied frequency, cell shape, and relative polarizability of the particle with respect to the host medium. For a homogeneous dielectric sphere,¹⁸ $f_{CM} = \frac{\epsilon_2 - \epsilon_1}{\epsilon_2 + 2\epsilon_1}$. ET flow is typically observed at frequencies greater than 100 kHz. When an external electric field is applied across the electrode, Joule heating creates temperature gradients near the electrode. The temperature gradient induces permittivity and conductivity gradients. The interaction between the electric field and the gradients, as a result, creates a bulk electrical force causing fluid motion.

Force	Analytical formulation
DEP	$\langle F \rangle = 2\pi\epsilon_1 r^3 \left[\text{Re}(f_{CM}) \nabla E_{rms}^2 + \text{Im}(f_{CM}) \sum_{x,y,z} E_{rms}^2 \nabla \varphi \right] \quad (1)$
ET	$\langle F \rangle = \frac{1}{2} \epsilon_1 \nabla T E_{rms}^2 \left[\frac{(1/\epsilon_1)(d\epsilon_1/dT) - (1/\sigma_1)(d\sigma_1/dT)}{1 + (\omega\epsilon_1/\sigma_1)^2} - \frac{(1/\epsilon_1)(d\epsilon_1/dT)}{2} \right] \quad (2)$

highly conducting salt solution with a large concentration of dissolved organic material. From a physicochemical point of view, the cell membrane constitutes a region of low polarizability that can act as either a barrier to the passage of ions between two aqueous electrolyte solutions or more likely can act to slow down diffusion near cell boundaries by trapping diffusing particles. The membrane surrounding the cell has a lipid bilayer structure [Fig. 2(a)]. It is very thin, typically 4–10 nm in thickness, and has incorporated into it large amounts of proteins and discrete domains (less than tens of nm).

The ITV, caused by low membrane permittivity and conductivity, as well as the rearrangement of interfacial charges, gives rise to field changes on the order of 1 kVcm^{-1} across the membrane thickness, for $\approx 1 \text{ V cm}^{-1}$ field strength. In these analytical models, the inner medium exhibits the same dielectric properties of the ECM, and the surface of the cell is negatively charged for nearly all cells because of the predominance there of negatively charged groups, e.g., carboxylates and phosphates. This results in positive ions being attracted from the ECM to the surface to form double layers.³¹

CS modelling is of course a gross simplification because it relies on a reductionist approach. It turns out that one of the simplest single spherical CS models³² of the effective complex permittivity is $\varepsilon_2 = \frac{r\varepsilon_{\text{cyt}}C_{\text{mem}}}{\varepsilon_{\text{cyt}} + rC_{\text{mem}}}$, where r is the radius of the rigid sphere, ε_{cyt} is the permittivity of cytoplasm, and C_{mem} is the membrane capacitance that includes the effect of membrane thickness and permittivity or conductivity. This effective permittivity can then be used to estimate the total EF on the dielectric object under an applied electric field as the object gets polarized. Derived from MST calculations, the dielectric force³² can be written as $F_{\text{DEP}} = \frac{Re(\varepsilon_1)}{4} \left(\left| \frac{\varepsilon_2 - \varepsilon_1}{\varepsilon_1} \mathbf{E} \cdot \mathbf{n} \right|^2 + Re \left(\frac{\varepsilon_2 - \varepsilon_1}{\varepsilon_1} \right) |\mathbf{E}|^2 \right) \mathbf{n}$, where ε_1 is the permittivity of ECM.

The shape of the object and its polarizability (relative to the host medium) dictate the distribution of the bound charges and hence the distribution of the electric force. Analytically, the shapes are often limited to spherical or ellipsoidal, and the applied field is usually taken to be uniform (with the notable exception of Ref. 27). However, the induced polarization alters the original distribution of the applied field which becomes significant either with increased polarization or number density of objects considered. The EF can be accounted for by superimposing the induced dipolar fields but the field distribution becomes highly non-uniform depending on position and polarization of each object.

For modelling the membrane elasticity, a strain energy density function is often employed. A typical expression for the deformation force derived from such an energy function is $\mathbf{F}_{\text{mec}} = \left[E_s \frac{d\xi}{ds} + \kappa E_B \frac{d(\kappa - \kappa_0)}{ds} \right] \mathbf{t} + \left[E_B \frac{d^2(\kappa - \kappa_0)}{ds^2} - E_s \xi \kappa \right] \mathbf{n}$, where ξ is the strain, E_s and E_B are elastic shear and bending modulus, \mathbf{t} and \mathbf{n} denote tangential and normal components, s is infinitesimal segment of the membrane, and κ and κ_0 are current and resting curvatures. The electrical and mechanical forces can thus be added to get the total force and thereby the overall electromechanical response.

C. Cell electropermeabilization

Since the discovery of EP, the question of the physical mechanisms that temporarily disturb the phospholipid bilayer of the plasma membrane has been a forefront topic in the field of EP. EP results in the significant increase in the electrical conductivity and diffusive permeability of the cell membrane caused by a series of short-duration, high-intensity electric pulses through tissue,^{33–37} i.e., typically a few kV cm^{-1} lasting from few ns to $1 \mu\text{s}$ to few ms. Under specific conditions, the pulses produce temporary structural changes in the cell membranes and the rearrangement of its components leads to the formation of aqueous hydrophilic pores allowing an increased transport of molecules through the normally impermeable membrane. A number of studies have reported that EP depends on the local induced transmembrane voltage (ITV) induced by the external electric field. It has also been shown that a specific ITV threshold exists for the manifestation of the EP phenomenon (typically from 0.2 V to 1 V, depending on the cell type), i.e., only the cells within areas where $\text{ITV} \geq \text{ITV}_{\text{th}}$ are electroporated. If the field is too strong or lasts too long a time, the viability of the cells is compromised and EP is said to be irreversible.

Based on a simple analytical electrostatic model³⁷ of a single cell, under the assumptions that the external dc applied field is uniform, infinitely far from the cell and the membrane is passive, it is relatively straightforward to show that the ITV scales as $V = 1.5ER \cos \theta (1 - \exp(-t/\tau_m) + U_{\text{rest}})$. Here θ denotes the polar angle which is measured from the center of the spherical cell with respect to the direction of the electric field, E is the field magnitude, R is the cell radius, τ_m is the membrane charging time constant, and U_{rest} is the resting potential $\approx -40 \text{ mV}$. The exponential term describes the return to equilibrium via relaxation. More advanced methods take into account the concentration of ions at the membrane surface based on Poisson-Boltzmann or Poisson-Nernst-Planck equations, e.g., Ref. 38. Over the last two decades, biophysical models have been developed to explain and predict the conditions for cell electroporation, in particular those dealing with the influence of the repetition rate of microsecond and nanosecond electric pulses.

Although these analytical studies have begun to characterize the electromechanical response of BM, a theoretical understanding of how local mechanics are determined by the heterogeneous structure is still lacking. Facing many issues which cannot be tackled analytically, the communities of biophysicists and applied physicists have developed experimental approaches and numerical models used to simulate the electrical and mechanical responses at different time and length scales which will be reported in Secs. III and IV.

III. RECENT ADVANCES AND HIGHLIGHTS IN FORCE MEASUREMENT IN THE LAB

There is a long record of experimental studies dealing with cell response to a wide variety of electric fields for decades but how the corresponding forces act on various length and time scales in the biological media continues to be investigated due to lack of clarity. As a result, electrical stimuli can create movement, deformation, and/or poration of a cell.

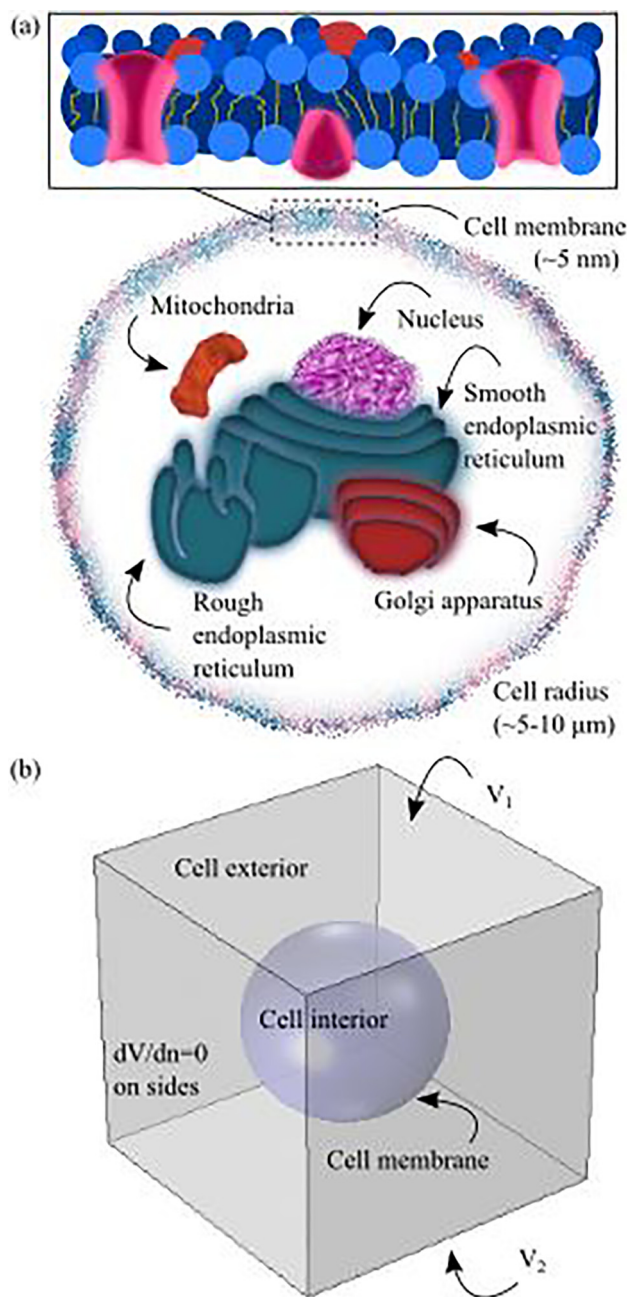


FIG. 2. (a) Illustrating a typical animal cell with various organelles (cytoskeleton is not shown); the colored cell membrane denotes the different membrane proteins and a lipid bilayer structure (close-up shown in the inset). (b) Computational domain for a single cell model where the cell membrane is modelled with a contact impedance boundary condition relating the normal component of current density on either side of the cell with membrane conductivity and thickness.

All these responses can be harnessed for biological and biomedical applications.

A. Introduction

As an example for the purpose of illustration, Ref. 39 examines what kind of movement a non-uniform ac electric field generates for lines of several human cells. Depending of field intensity, frequency, and conductivity, different types of motion can be observed. Additionally, the authors in Ref. 39 demonstrate the competing nature of dielectrophoretic (DEP) and electrohydrodynamic (EHD) forces in an ac

stimulated electromicrofluidic chip. The device has coplanar electrodes which delivered a field magnitude between 0.022 and 0.067 V/micron at a frequency range of 1 kHz and 200 kHz. EHD forces, i.e., ac electro-osmotic and electrothermal, are suggested to explain the observed clockwise and anti-clockwise rotation by creating vortices or swirls in the fluid that drag or rotate the cell along. The resulting overall motion is recorded and an estimate of speed obtained from image analysis that ranges from $\mu\text{m/s}$ to cm/s in the case of translational motion. The rotational speed is in the range of 10–40 rpm. The role of intracellular Ca distribution, its importance in field-directed cell shape changes, and movement is also described in Ref. 40. In this study, it is shown that the electrostatic and electro-osmotic forces apply mechanical forces on the cell triggering the initial signal of electrotactic movement of cells. The asymmetric membrane potential, due to the charge redistribution in the membrane components eventually, is also evidenced to affect electrotaxis. The motion of individual cells in electromicrofluidic platforms is mainly governed by DEP and EHD forces. An elaborate review for dielectrophoretic platforms has been given by Khoshmanesh.⁴¹

Several platforms have recently proved to be powerful tools to stimulate electrically and optically for different kinds of *in vivo* and *in vitro* BM. For example, Ref. 42 describes a device capable of simultaneously providing mechanical, electrical, and biochemical stimulation in order to investigate cellular responses in the fields of stem cell biology and regenerative medicine. Values of electrical field gradients of 5 V/cm can be easily attainable and are comparable to those found *in vivo*. The experiments demonstrate the ability for inducing changes in cell morphology, cytoskeletal fiber orientation, and changes in gene expression under physiological stimuli. Morphological rearrangements of the actin cytoskeleton can be observed, and cellular shapes (Fig. 3), characterized with image segmentation, produce a percentage orientation of the actin fibers in the range of 180°.

A recent report highlighted a large variety of methods dedicated to measuring forces and stresses in living tissues, some of which are summarized in Table II.

Other force-reporting techniques require the investigator to isolate cells and tissues and surround or embed them with non-biological markers that allow the force to be sensed as displacement or deformation. Two most commonly used force sensors to characterize BM are AFM and optically trapped microbeads. These tools are coupled to ultrasensitive displacement detection systems based on opto-electric, acousto-opto-electric, or piezoelectric phenomena. While AFM can effectively measure pN forces, it makes use of a tip sharpened at the nanometer scale, and thus can be considered invasive and moreover it is difficult to scale up to multi-tip probing.⁴³ Moreover, the probed forces can be a mix of contributions which must be carefully deconvolved or inferred. For instance, the AFM tip interacts with the sample surface and can sense long range as well as short range forces dealing with electrostatic, van der Waals, and adhesive forces, respectively. Thus, care must be taken when interpreting the force maps. The long range non-contact mode of AFM is used for electrostatic force mapping (EFM). Furthermore, the calibration of these force probes, based on

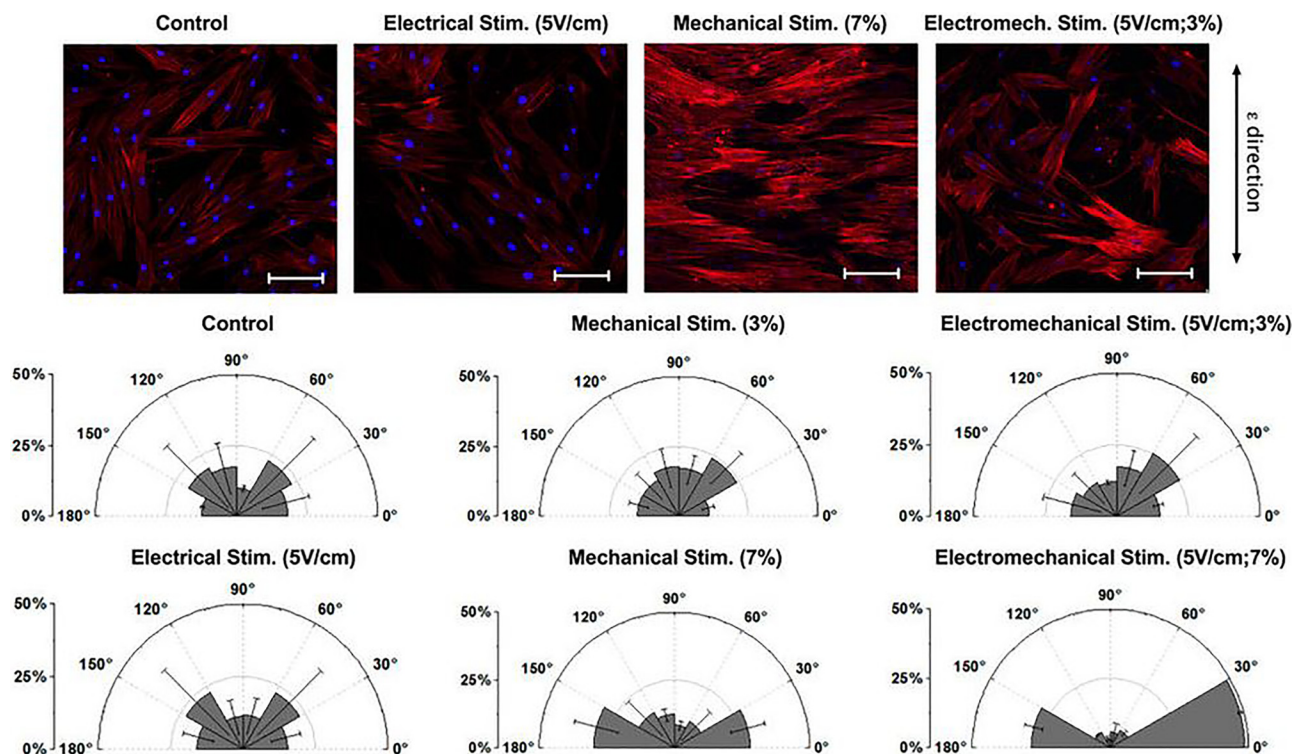


FIG. 3. Human bone marrow mesenchymal stem cells (top row) stained with blue color for nucleus and red color for actin fibers (top) showing a control image (no stimulation) and selected images from controlled electrical stimulation (biphasic square-wave pulse of ± 1.2 V for 1 ms at 1 Hz repetition is applied that delivers an average electric field of 5 V/cm), mechanical stimulation (the entire base is stretched along the y axis as shown on right by double arrow), and electromechanical stimulation; scale bars are $100 \mu\text{m}$ each. Subsequent orientation analysis (bottom) for selected stimulation scenarios: In each image, several actin fibers are identified along with their orientation angle and a histogram of percentage orientation is plotted [Reproduced with permission Pavese *et al.*, *Sci. Rep.* **5**, 11800 (2015). Copyright 2014 Author(s), licensed under a Creative Commons Attribution 4.0 License].⁴²

simple theoretical models of elasticity or viscoelasticity under conventional mechanical testing schemes, can be delicate. On the other hand, optically trapped microbeads can attach themselves to the cell surface or proteins over it thereby sensing the forces associated with its displacements with very high spatial resolution. However, one cannot consider this effect as an electromechanical response because forces due to the electric field act on the bead rather than the BM. The beads, in fact, transfer an external force profile to the BM which is used to move the optical trap from the manipulation point of view. We end with a note of caution. Separating the different contributions to the probed force is a challenging task. In particular, measuring only electromechanical forces requires that an ideal force probe should be able to differentiate between electric field induced forces and mechanical ones which remains a formidable challenge within the context of the coupled active dynamics existing inside the living and heterogeneous BM that include biochemical reactions, diffusion, growth, and development. Apart from experimentally sensing the forces as previously discussed, live motion of cell can be recorded by imaging continuously as the stimulation is effective. An example of cytoskeleton rearrangement is shown in Fig. 3 and other cases for translation and rotation at cellular level are shown in Figs. 4 and 5.

B. Measurement of cell and tissue deformation

Two approaches are worth highlighting because they have already had some success and are providing

experimental ways to manipulating biological cells. On the one hand, several authors propose using nanoribbons made of piezoelectric lead zirconate titanate (PZT) for electrical stimulation of cell membrane and detection of cellular deformation.³⁸ The aim is to characterize the mechanical response of neuronal cells to applied voltages. Depolarization caused by an applied voltage induces a change in membrane tension. Charges on opposing sides of a membrane repel to each other laterally, creating a local pressure, thus changing the net surface tension. This has the effect of altering the cell radius so that the pressure remains constant across the membrane. A preliminary setup calibration (without cells) by making use of AFM is required. Then, neuronal cells are cultured on PZT nanoribbons and a standard whole-cell patch-clamp technique is used to stimulate membrane voltages in cells while recording the electrical response in PZT nanoribbons. The generated electrical response was characterized by a whole-cell patch clamp technique using 1 micron diameter micropipette through which a current is supplied to the membrane to evoke a sharp increase in membrane potential after a certain threshold. This suggests the presence of voltage gated ion channels and cell perforation. A current pulse of up to 200 pA was used which raised the membrane potential up to 20 mV from a resting potential of -50 mV for roughly about the duration of the pulse and thereafter relaxing gradually. The electrical response was accompanied with a change in surface tension of cell and a small change in shape. Correspondingly, the altered force exerted by the cell on the suspended piezoelectric nano-ribbon produced a detectable

TABLE II. Ways and benefits of several force measurement methods in living tissue for various time and length scales [Reproduced with permission from Sugimura *et al.*, Development **143**, 186 (2016). Copyright 2016. The Company of Biologists Ltd.].⁴³ NA, not applicable because only relative measurements. Costs excluding the microscopes: €(<€10 000); €€(€10 000–50 000); €€€(€50 000–1 00 000); €€€€(€1 00 000–2 00 000).

	Measured quantities	Measurable range	Time scale ^a	Size scale ^b	Advantages	Disadvantages	Cost
Indentation/microplates/AFM	Cell or aggregate surface tension	0.1 Pa	s-h	1–100 μm	Absolute measurements	Contact method	€€-€€€€
Pipette aspiration	Cell or aggregate surface tension	$\mu\text{N/m-mN/m}$	>10 s	1–100 μm	Absolute measurements	Contact method	€€
Optical/magnetic tweezers	Cell junction tension	pN-nN	ms-min	0.1–10 μm	Non-contact; absolute measurements	Delicate calibration	€€€
Subcellular laser ablation	Cell junction tension to viscous drag ratio	NA	0.1 s-min	0.1–10 μm	Non-contact	Possible collateral damage	€€-€€€
Tissue scale laser ablation	Tissue stress to viscosity ratio	NA	s-min	10 μm –1 mm	Non-contact	Requires sample and laser alignment, few experiments per sample	€€-€€€
FRET force probe	Intramolecular tension	pN	Video rate	nm	Molecular measurements	Requires different control constructs, delicate calibration	€
Liquid drops	Cell-scale stress	~0.1–60 kPa	0.1 s-h	>5 μm	Absolute measurements	Requires surface chemistry of droplets	€€
Birefringence	Tissue-scale stress	>10 kPa	Video rate	> μm	Global	Requires flat, transparent sample, delicate calibration	€
Force inference	Relative cell junction tension, cell pressure	NA	Video rate	> μm	Image based; Global	Requires image segmentation	€

^aTime scale of the mechanical processes that can be probed.

^bSize scale of the mechanical processes or mechanical elements that can be probed.

deflection. From the analytical model relating the cell radius to the magnitude of the force, the authors are able to show that a change of 120 mV of the cell membrane voltage induces a force of about 1.6 nN on the suspended nanoribbons corresponding to a 1 nm deflection (Fig. 6). Several benefits of this method are worthy to note. Firstly, it turns out that PZT nanoribbons are thin and flat and can therefore conform to or even buckle onto curvilinear surfaces. Secondly, they can be fabricated using standard microfabrication techniques and are easily scaled. They can be bio-interfaced directly with tissues for measuring macroscopic electromechanical properties.

On the other hand, optical techniques have become available for studying the electromechanical response of cells, and large initiatives are emphasizing the newly accessible physical data sets they produce. In Ref. 45, the authors presented a single beam near-field laser trapping technique under focused evanescent wave illumination. The device is able to stretch, hold, and rotate a red blood cell (RBC): it depends on the trapping power used. Since RBCs play an important role in drug therapy and disease an understanding of their fundamental mechanical and viscoelastic properties is important. This system is compared to laser tweezers used to pull on bead-handles attached to a RBC for introducing deformations in the range 15%–50%. Due to its highly confined nature, the strength of the evanescent focal spot is so strong that a non-linear near-field excitation becomes possible. In the near-field trapping case, the axial trapping volume is only a few tens of nanometers. Force calibration is rather difficult to perform because the object under stress can exhibit a variety of deformation profiles (Fig. 7). As a consequence, the response is often reported as a function of the power (typically ~15–20 mW) rather than the force or stress in the plane of the trap. Stretching, rotation, and even folding of RBC were reported using these traps that have a spatial extent of only a few tens of nm.⁴⁵ RBC rotation was reported on the order of 1 rpm, deformation of up to 25% by stretching and squeezing. Folding up to 60° was also reported as the power in the plane is increased.

C. Cell perforation

In recent years, several technological advances have emerged revolutionizing the field of EP. In Ref. 46, the authors proposed a specific platform for intracellular delivery which can be scalable from single cell–suspension experiments. It enables the delivery of well-defined molecular content to the selected cell or group of cells in an arbitrary time-window. Cell perforation by electrical stimulation has been recently reviewed.⁴⁷ In this study, various platforms from bulk electroporation (BEP) to micro- (MEP) and nano-electroporation (NEP) are compared. BEP experiments in millimeter-to-centimeter-sized chambers allow handling millions of cells but lead to non-uniformly distributed electric fields at the single cell level. It can lead to highly stochastic transfection profiles and cell lysis in most cases. High voltage is needed (>1000 V) and can cause a significant decrease in cell viability due to joule heating, pH changes, and bubble formation. For *in vivo* applications, several groups demonstrated

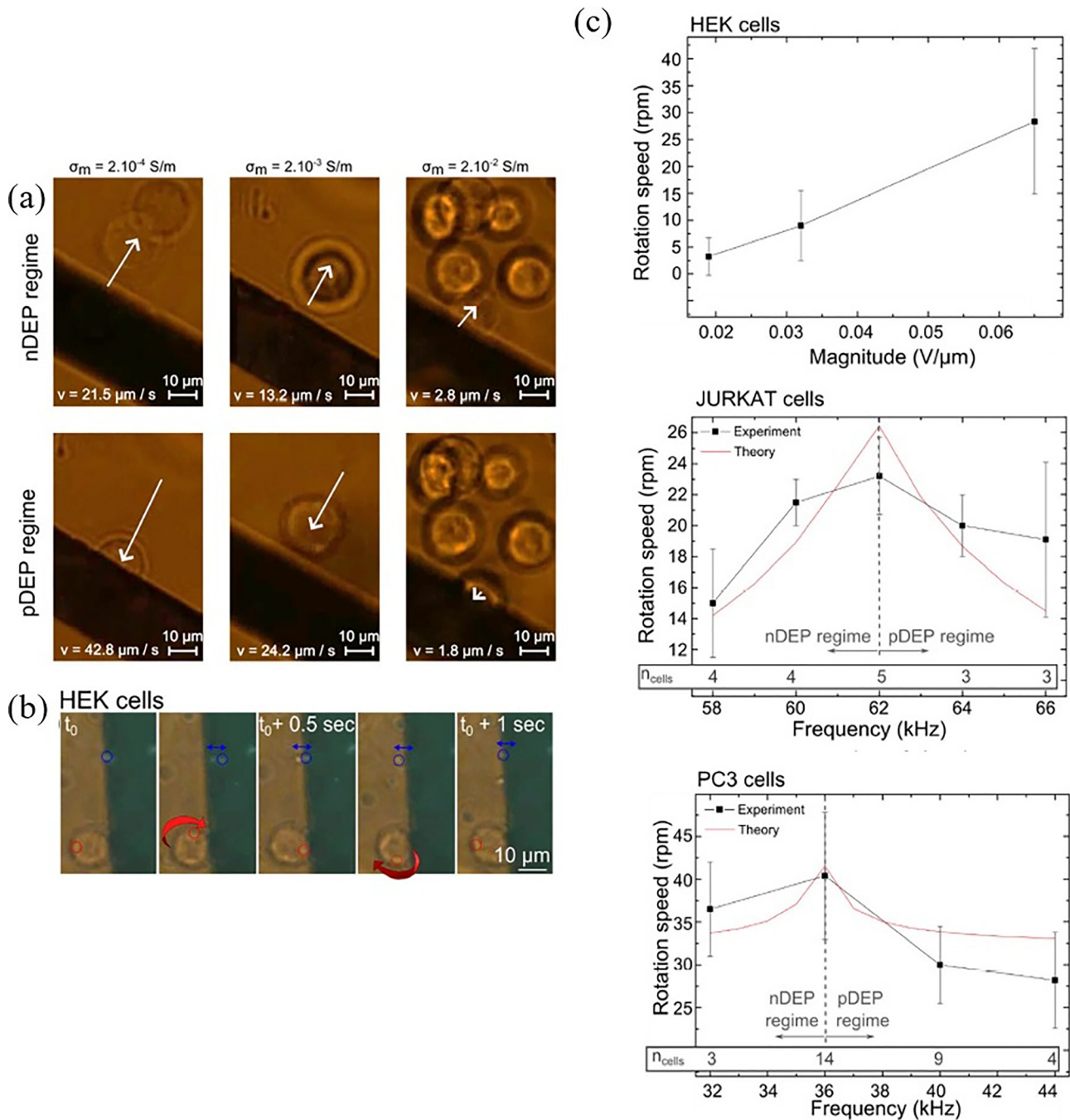


FIG. 4. Cellular motion for human cells (HEK, JURKAT, and PC3) in AC electrofluidic chip. (a) Translational motion of HEK cells away from (top row, negative-DEP) and towards the coplanar electrodes shown as dark patch (bottom row, positive-DEP) indicated by arrows. (b) Rotational motion of HEK cells near the edge of coplanar electrodes. (c) Rotational speed of cells as magnitude or frequency of stimulation is varied. The rotational speed and its variance both increase with magnitude of applied voltage and the former exhibits a broad peak behavior at a particular frequency. Theoretically, n-DEP and p-DEP regimes depend on the real part of the CM factor being negative and positive, respectively. n_{cells} denote the number of cells used for mean value calculation. The nonlinear fits to the experimental data were performed using Origin, and the theoretical curve was also plotted based on the model equations used in Ref. 39 [Reproduced with permission from Vaillier *et al.*, PLoS One **9**, e95231 (2014). Copyright 2014 Author(s), licensed under a Creative Commons Attribution 3.0 License.].³⁹

that the adding of gold nanoparticles (AuNPs) in the cell buffer improves the cell transfection efficiency. Miniaturized (MEP and NEP) electroporation systems are used for biomedical applications, including adoptive immunotherapy, gene/RNA-based therapies, cell reprogramming, and intracellular bio-interrogation of living cells. Electrodes are far away from most of the cells in BEP as the generated fields act over all cell surfaces, while MEP and NEP are focused on reducing this area to small regions on the surface. Perforation is

inferred from the movement of fluorescent chemical markers into the cells. These markers are processed from the image based on which transfection efficiency is evaluated [Fig. 8]. Reversible or irreversible perforation can be performed as evidenced by viability markers. It must be noted that transfection efficiency is cargo dependent. The number of perforated cells in a single shot is always better in BEP but transfection efficiency and viability are better in MEP and NEP.⁴⁷ From the electric stimulation point of view, it must be noted that the

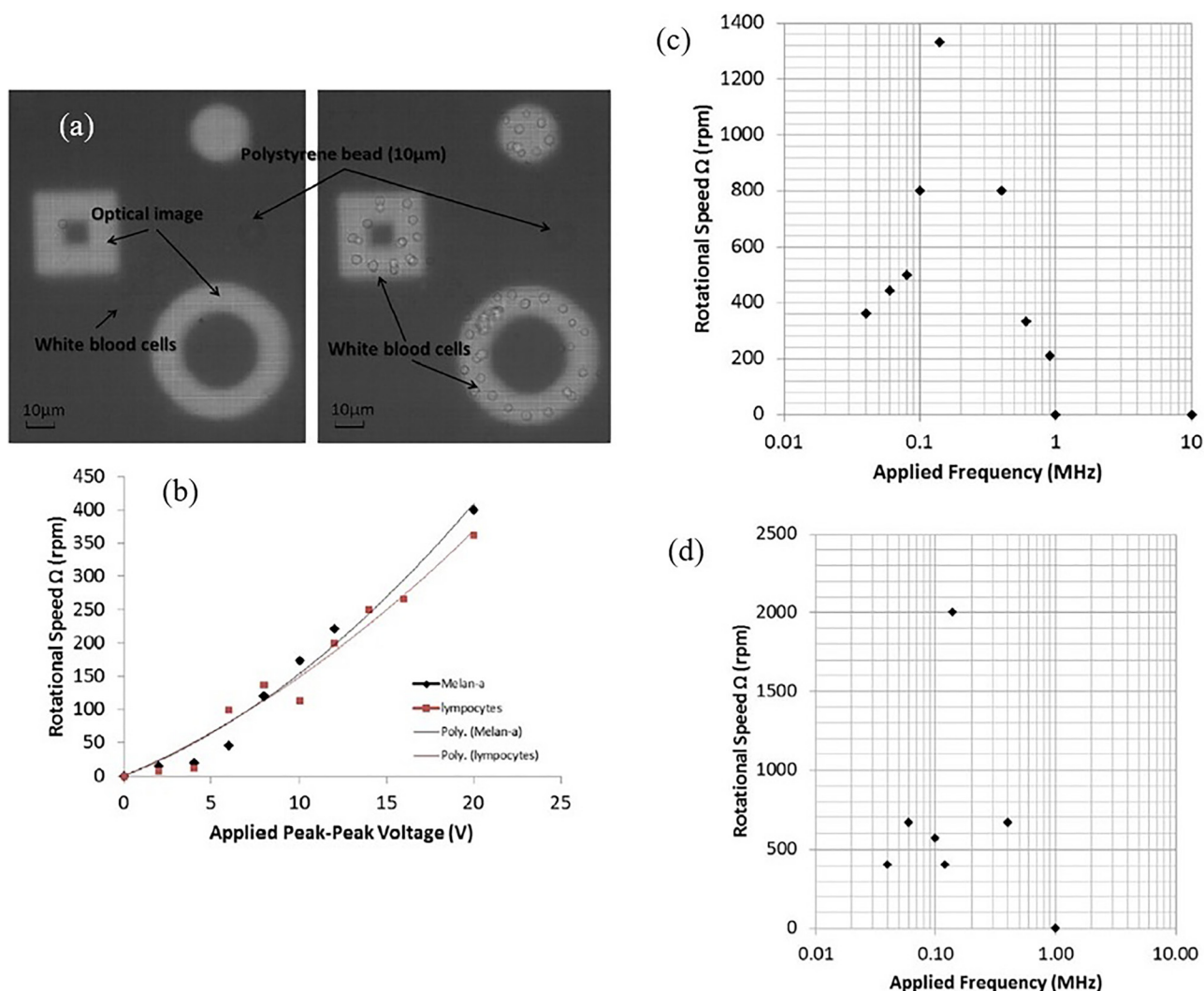


FIG. 5. Cellular motion for mouse cells in opto-electro-microfluidic chip, (a) WBCs moving away from the light pattern (negative-DEP) at one frequency (left image) and into it (positive-DEP) at another (right image); rotational motion near the edge of the light spot as (b) applied voltage and (c, d) frequency is varied. Rotational speed varies quadratically with applied voltage and exhibits sharp peak behavior with frequency [Reproduced with permission from Chau *et al.*, PLoS One **8**, e51577 (2013). Copyright 2013 Author(s), licensed under a Creative Commons Attribution 3.0 License.].⁴⁴

bias voltage applied to the device and the voltage across the cell can be very different when BEP systems are used. BEP requires bias voltage to the order of 1 kV whereas it can be as low as 100 to 1 V for MEPs and NEPs depending on the designs. MEP system miniaturization results in more localized/enhanced implementation of the electric field on individual cells, leading to successful transfection at relatively low voltages and improved cell viability and transfection efficiencies. In NEP, only a nanosized portion of the cell membrane is considered. One unique advantage of NEP-based transfection is that cytosolic cargo delivery is entirely modulated by electrophoretic forces. Such systems can achieve 90% transfection efficiency and 100% cell viabilities. Additionally, electrophoretic forces are enhanced within the nano-channel due to the high voltage drop, which allow cargo delivery to occur within microseconds compared to diffusion-dominated processes, which can take a much longer time (BEP, MEP).

Cell perforation by ultrafast optical fields can also be achieved using plasmonics, which has paved the way for new phenomena and technologies useful for manipulation of light. There are broadly two ways of doing this. One way is

to deposit metal nanoparticles in the substrate on which the cell membrane is attached. Another way is to have nanostructured or unstructured metal coatings on the substrate over which the cells are brought into contact. Either way, a metal-dielectric interface is established that allows plasmonic resonance to be excited by an incident optical field. In this context, three recent studies that achieve plasmonic optoporation by short laser pulses in the durations of ns-ps-fs can be highlighted. In Ref. 48, 15 ns (pulse duration), laser pulses of 532 nm (on resonance) and 75 ns pulses of 1064 nm (off resonance) with 10 Hz repetition frequency are used to excite 100 nm gold nanoparticles (AuNPs) deposited on the membrane of melanoma cells that lead to their perforation [Fig. 9(a)]. Likewise, in Ref. 49 the authors deposited 100–200 nm Au nanoparticles on breast cancer cells and used 45 fs laser pulse centered at 800 nm with 3 Hz repetition frequency for excitation. Cells perforate due to the formation of submicrometer cavitation bubbles around the nanoparticles. Transfection efficiency of 77% and a viability of 90% are reported [Figs. 8(c) and 9(b)]. In addition, for bubbles of large sizes (above 5 μm) cells die. In Ref. 46, another kind

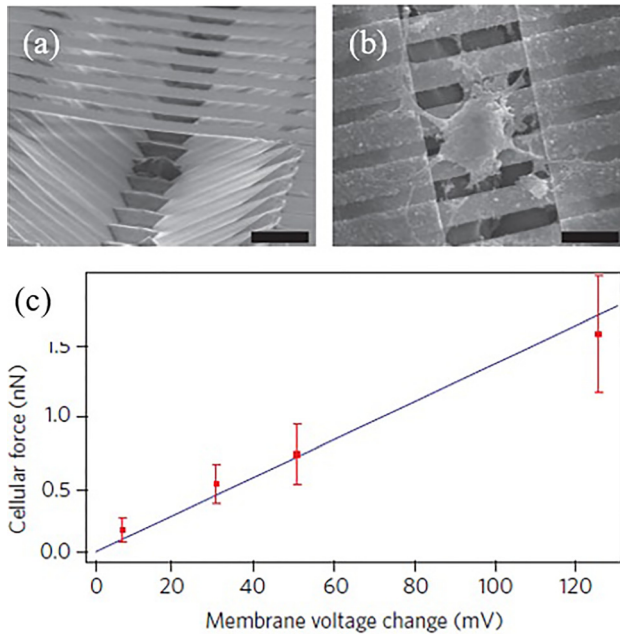


FIG. 6. Sensing nanometer scale deformations in excitable cells on a scalable substrate: SEM image of the device showing (a) piezoelectric nanoribbons as part of the substrate and (b) a neuronal cell adhering over it; scale bars are 15 μm . (c) Calculated force (blue line) as a function of membrane voltage based on the model presented in Ref. 38 and measured membrane voltage (red data points, error bars include variance of data and fitting errors from the AFM calibration) which increases along with its variance as the voltage across the membrane is increased [Reproduced with permission from Nguyen *et al.*, Nat. Nanotechnol. **7**, 587 (2012). Copyright 2012 Macmillan Publishers Ltd.].³⁸

of experiment is performed using gold nanotubes of 180 nm diameter over a substrate. Mouse fibroblast cells spread over the nanostructured substrate. Excitation was done with an 8 ps laser pulse of 1064 nm with a repetition frequency of 80 MHz during 10 ms. Cells are perforated by shockwaves generated around each nanotube. Lifetime of the pores is estimated with chemical markers and is close to 10 min (Fig. 11).

IV. MULTISCALE PHYSICS OF INTERCELLULAR FORCES IN TISSUES

It has been established above that the mechanical forces between cells generated by an electric field are so far poorly appreciated and consequently under-exploited. Over the past few years, a variety of numerical modelling techniques have been designed to overcome the severe limitations of analytical models used to quantify intercellular forces, such as the inclusion of arbitrary shape for cell and the distribution of material properties, and offer much more versatile analysis. One of the major goals of such theoretical modelling is to predict quantities which are physically measurable at cellular and subcellular levels. However, due to the mismatch between theoretical assumptions and experimental realities, disagreements are quite common. *Ab initio* classical molecular dynamics (MD) of biomolecules which can simulate the coupling between electrical and mechanical properties have not yet been published in the archival literature. On the other hand, continuum (homogenized) medium approaches such as

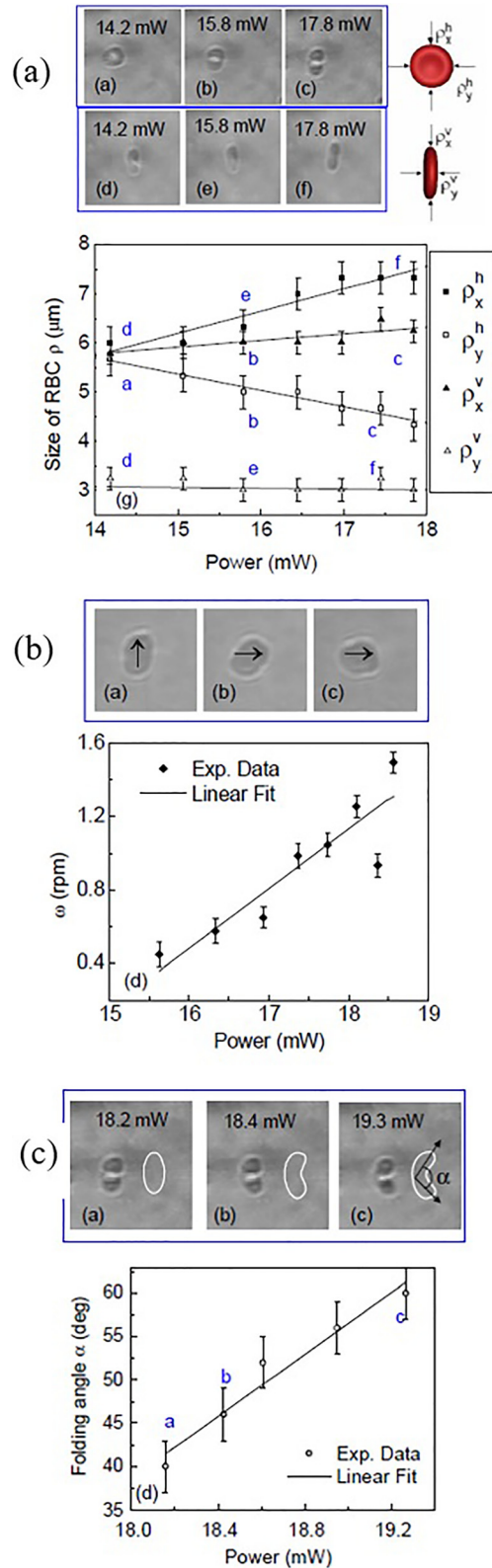


FIG. 7. Near-field optical manipulation of RBC on a substrate as a function of power in the focal plane: (a) stretching is denoted by size $\rho_{x,y}^{h,v}$ (μm), where the superscript h-v corresponds to RBC trapped in horizontal or vertical plane on substrate, subscript x-y corresponds to x and y axes; (b) rotation of RBC trapped in horizontal plane, arrows indicate change in the direction of incident laser polarization; (c) folding of RBC trapped in the horizontal plane. The response is reported to be mainly linear in all cases and thus a linear fit is performed [Reproduced with permission from Gu *et al.*, Opt. Express **15**, 1369 (2007). Copyright 2007 Optical Society of America].⁴⁵

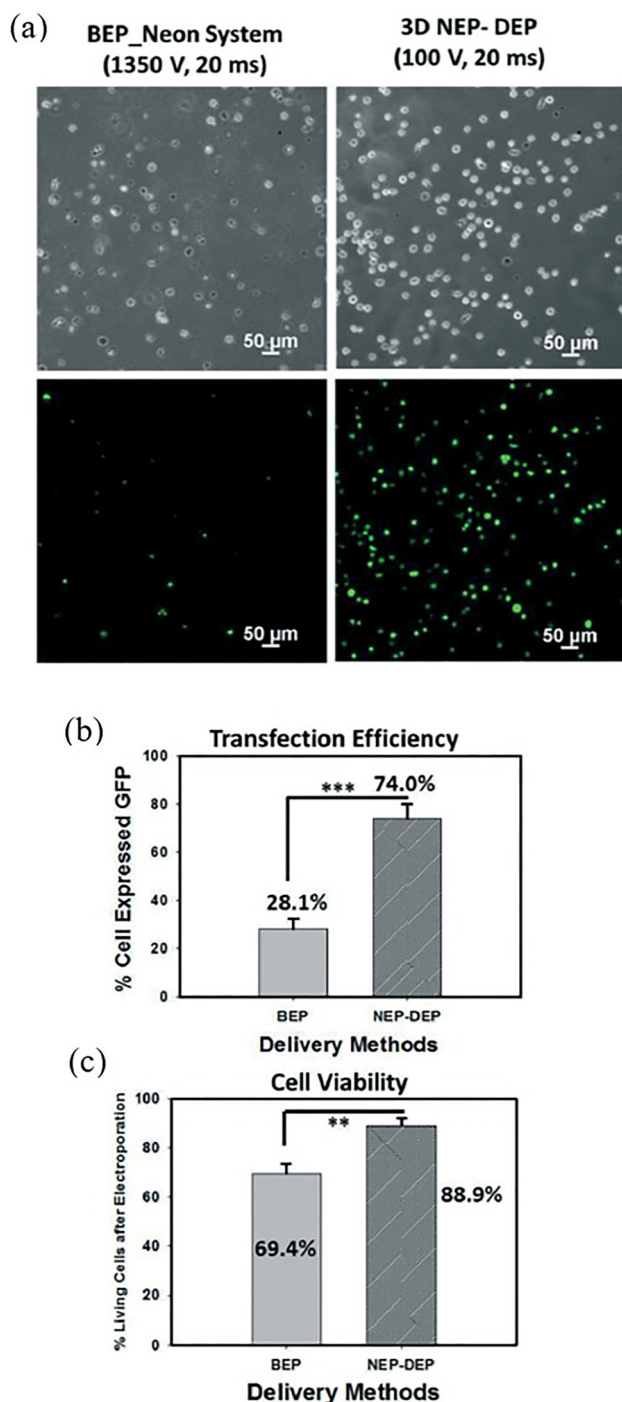


FIG. 8. Comparison of bulk electroporation and nano-electroporation of genetically engineered immune cells (NK cells): (a) Phase contrast (top row) and epifluorescence (bottom row) images, the latter indicating the delivery of target substance into the cells, (b) transfection efficiency, (c) cell viability [Reproduced with permission from Chang *et al.*, Lab Chip **16**, 4047 (2016). Copyright 2016 Royal Society of Chemistry].⁴⁷

finite element (FE) and finite difference time domain computations are valid because the cell size is sufficiently large for the molecular details of the membrane to be ignored. Typically, many simplifications are made to a cell's morphology in order to more easily represent it computationally, which include simple shapes in the form of, e.g., spheres, and a limited amount of physical phenomena. However, biological cells are complex structures with ever-changing geometry and physics that span many length and time scales.

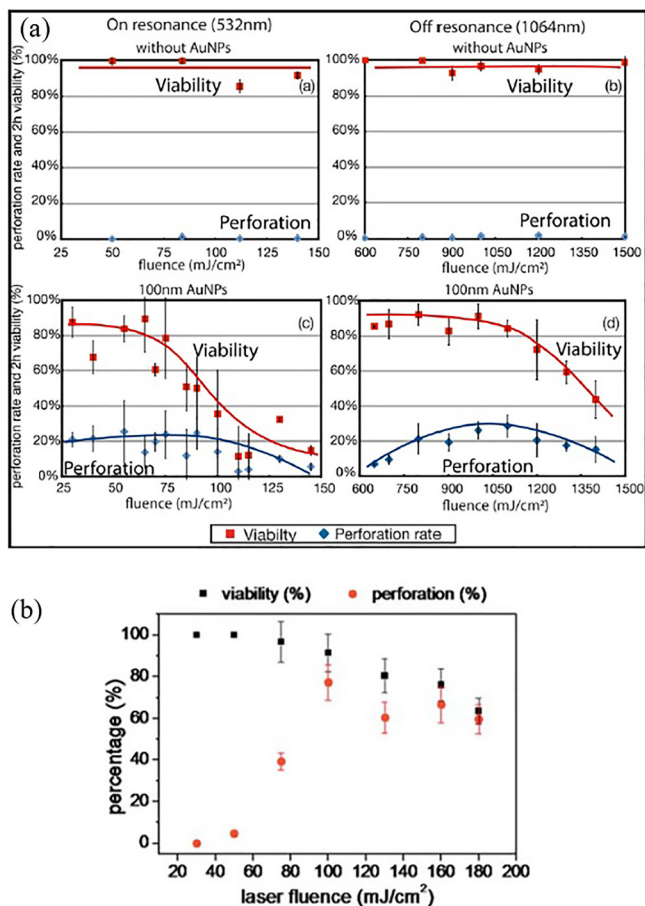


FIG. 9. Plasmonic gold nanoparticle enhanced electroporation of: (a) melanoma cells using ns laser pulses in on-resonance (532 nm) and off-resonance (1064 nm) conditions and (b) cancer cells treated with fs laser pulses (45 fs, 800 nm) as a function of laser fluence [(a) and (b) are reproduced with permission from Lalonde *et al.*, Biomed. Opt. Express **4**, 490 (2013). Copyright 2013 Optical Society of America⁴⁸ and Boutopoulos *et al.*, J. Biophot. **9**, 26 (2016). Copyright 2016 Wiley,⁴⁹ respectively).

Recent developments have shown that arbitrary shaped and structured cells can be incorporated into models (Fig. 10), either by parameterizing volumes and surfaces for distributing spherical CS¹⁴ or discoidal structures³² in a given computational space or by using microscopic images of a densely packed tissue.⁵⁰ For the specific application reported in Fig. 10(b), the geometries of biological cells are described in 2D using triangles that are refined around high-aspect ratio features, such as at the cell and nuclear membranes.

A. Stress distribution dependence on material distribution and properties

Several approaches are worth highlighting because they have already had some success and are providing a constructive path forward to electromechanobiology. For example, Ye and coworkers³² use a numerical modelling approach of the effective complex permittivity of a spherical CS structure and applied it for RBC to calculate the DEP force resulting from the application of a non-uniform electric field. These authors found that the DEP force is nonzero only at the boundary of 2D biconcave shapes as other regions were considered homogeneous. They obtained the DEP force

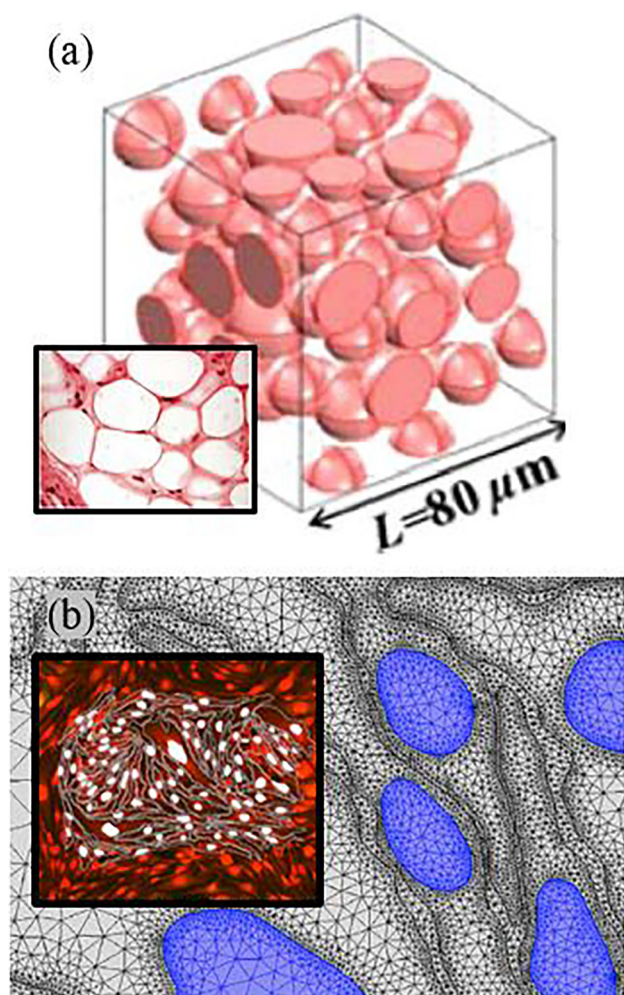


FIG. 10. Modeling geometries of random configurations of cells which may closely resemble *in vivo* cellular environments in living tissues (insets), where cells form a loosely connected, disordered network [(a) and (b) are reproduced with permission from Appl. Phys. Lett. **100**, 143701 (2012). Copyright 2012 AIP Publishing¹⁴ and Murovec *et al.*, Biophys. J. **111**, 2286 (2016). Copyright 2016 Elsevier.⁵⁰ respectively).

distribution as illustrated in Fig. 12(d). Using a FE analysis, Yu and Sheng analyzed the response of three differently shaped CS (sphere, cylinder and biconcave disc) structures under electric field stimulation. This study informs us about the effect of shape and material distribution in a CS model on the mechanical response Figs. 12(a)–12(c).

Numerically calculated MST spatial distribution at the boundaries of homogeneous dielectric spheres modelling undeformable cells under an applied uniform electric field clearly show a bidirectional stretching force due to the induced dipole.² The frequency dependence of MST distribution is shown as medium conductivities and inter-particle distances are varied. Frequency-domain finite element (FE) simulations provide numerical evidence that the time-averaged electrostatic force changes from repulsion to attraction as the drive frequency of the electric field is varied. The simulations published so far strongly suggest that the repulsion to attraction (RTA) transition phenomenon is largely associated with an asymmetric screening at very small separation between cells (Fig. 13). This observation has direct application to the problem of electrostatics in biomolecular

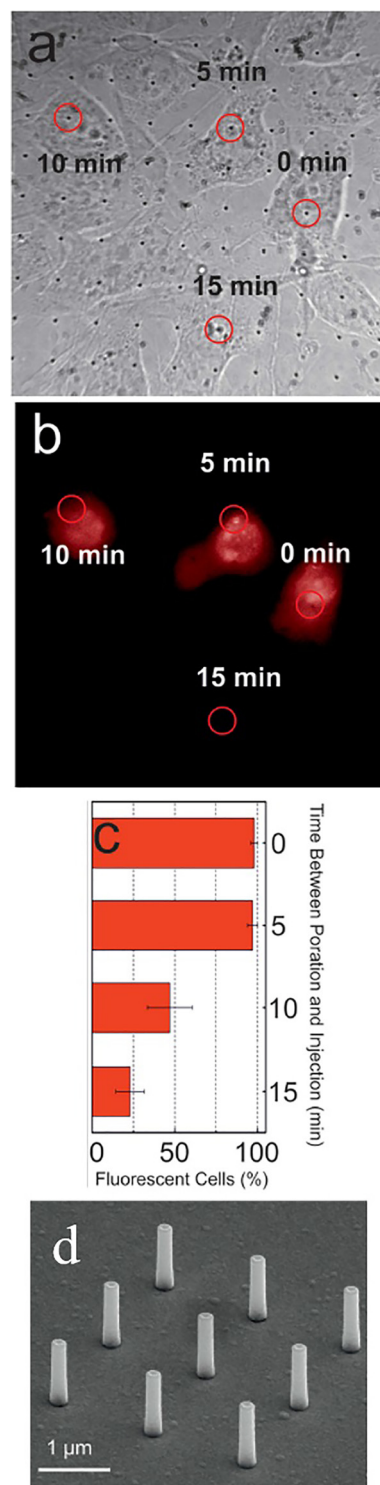


FIG. 11. Plasmonic gold nanotube array enhanced electroporation of NIH/3T3 cells: (a) NIH/3T3 cells cultured on the substrate, (b) fluorescence image indicating the intake of target substance into the cells, (c) time between injection and electroporation as a function of percentage of fluorescent cells, and (d) SEM image of the gold nanotube array as part of the substrate [Reproduced with permission from Messina *et al.*, Adv. Mater. **27**, 7145 (2015).⁴⁶ Copyright 2015 Author(s), licensed under a Creative Commons Attribution 4.0 License.].

systems. However, the results obtained so far are incomplete in two senses. First, they do not account for cell viscoelasticity, which eventually affects the Maxwell stress tensor calculation. Reproducing elastic moduli is an essential foundation

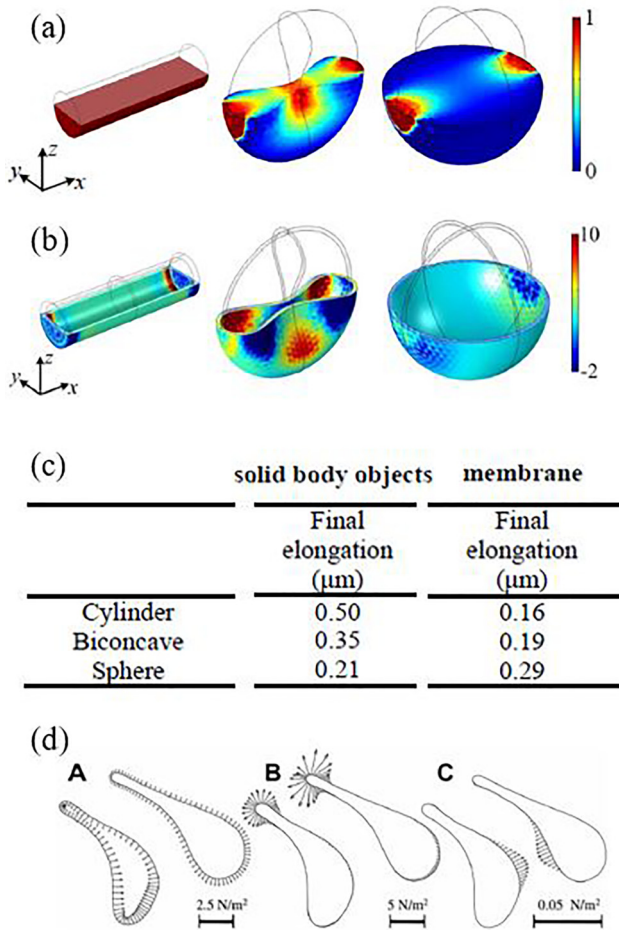


FIG. 12. Calculated stress distributions in cells: (a) bidirectional applied stress on the ends of cell is distributed in volume of the cell if elastic material is assumed to be filled inside, (b) bidirectional applied stress on the ends of cell is distributed on the membrane if elastic material is limited only to the membrane region while the inside is empty. Color bar: red indicates higher and blue indicates lower magnitude of stress (units of Pa). (c) The same amount of applied stress as considered in (a) and (b) produces different elongations of the cell, (d) stress defined and calculated only for the membrane boundary showing two nearby cells under an applied electric field due to coplanar electrodes and an applied Poiseuille fluid flow field; showing from left to right the DEP force, the viscous force due to fluid flow and the interaction force modelled with a formulation using a Morse potential between the cells [(a)–(c) and (d) are reproduced with permission from Yu and Sheng, *Opt. Express* **23**, 6020 (2015). Copyright 2015 Optical Society of America³¹ and Ye *et al.*, *Electrophoresis* **36**, 378 (2015). Copyright 2015 Wiley,³² respectively].

toward simulating mechanical properties of cells and cell assemblies. Second, while the well-established CS model [Fig. 2(b)] allows researchers to focus on solving, rather than defining, the problem is that it neglects the complex internal structure network of cell, i.e., cytoskeleton.

Simulations based on a 3D object-oriented approach to modelling individual and collective electromechanical cell behavior were also carried out. In the numerical study by Promayon and coworkers⁵² the effects of incorporating simplified cytoskeleton on the mechanical deformation of cells needs is worked out. These authors try to model cell aggregation by introducing a chemoattractant field for a cell population (36 cells) comprising of 2 types of cells which have different responses to the same field. Forces are calculated

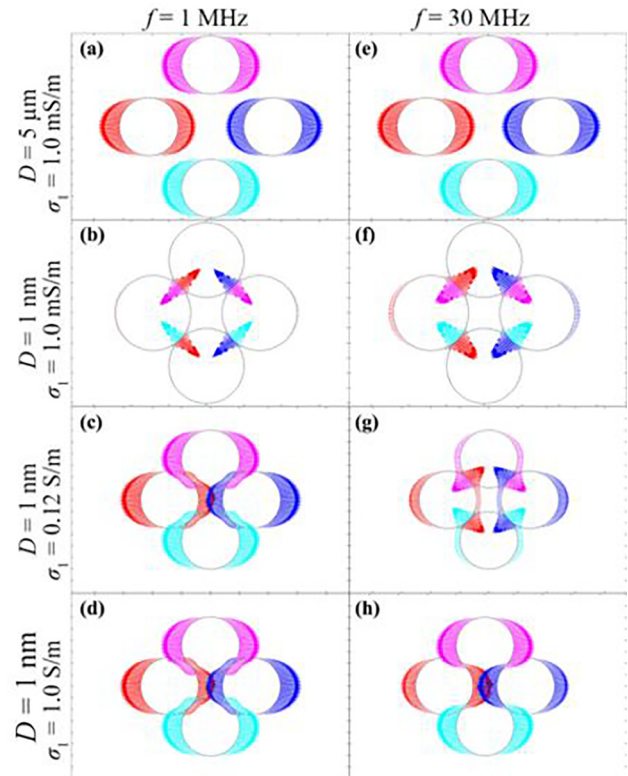


FIG. 13. The distribution of MST when 6 spherical cells positioned at the face-center of a cube shown in 2D (4 are visible), modelled with 3 distinct phases (each for cytoplasm, cell membrane, and the suspension media, see Ref. 2 for parameter values used) are close to each other, D being the distance between their centers and σ_1 being the conductivity of the suspension media; the colors are used to distinguish the stress distribution direction on each cell [Reproduced with permission from Murovec and Brosseau, *Phys. Rev. E* **92**, 042717 (2015).² Copyright 2015. American Physical Society].

over each cell surface and threshold rules are defined for formation of the aggregate. This approach can be considered as a simplification of a molecular dynamics (MD) type approach in which unique atoms have characteristic atomic potentials and bond energies. This object oriented approach allows for preserving multiple aspects associated with the cell but of course only few aspects can be stored due to limitation of computer memory.

A focused beam of light allows defining gradient forces due to the beam shape and scattering forces as the light transit through regions with different optical properties. Organelles in cells scatter the incident light and thereby alter the optical stress distribution. In Ref. 53 the authors show that the local distribution of optical stresses is affected by the relative size of nucleus and cell [Figs. 14(b) and 14(c)]. Optical stresses are explicitly calculated by making use of a dynamic ray tracing (DRT) algorithm which takes into account the vector nature of the electric field. Elastic stresses for the membrane are calculated from a strain energy density function using FE. These two forces are added to the incompressible Navier-Stokes equation which was then solved by the immersed boundary method. The deformation is quantified as the ratio of the difference to sum of the major and minor semi-axis deformed lengths [Fig. 14(a)]. It was shown that the deformations of the cell and the nuclear membranes can differ significantly.

Two additional simulations which illustrate the importance of multiscale modeling of intercellular forces in cell assemblies are worth describing in detail. In the first, we show simulation results to give an idea of how electric forces between cells can be controlled by changing the ac frequency of the applied electric field. In Fig. 15, we show two polarizable cells having same size (radius $10\ \mu\text{m}$) and properties separated by a small distance (500 nm) while the angular position of one of them is changed around the other. The ac electric field is applied along the vertical with an average magnitude of 1 kV/cm. Figure 15 illustrates another important feature arising from the interplay between the spatial distributions of cell surface charge and electric field which leads to specific patterns of total electric force on the second cell with respect to the first. Furthermore, the direction and magnitude of the force can differ significantly as the frequency is changed [Figs. 15(b) and 15(c)].

The second and very different example of interface influence occurs as an aggregate of two-size cells (with radii $10\ \mu\text{m}$ and $5\ \mu\text{m}$) is considered to study the mutual interaction between cells in the system [Fig. 16(a)]. We examine the local distribution of forces on the reference cell surface as the frequency of the applied field (adopting a coordinate system in which the field is oriented along the z vertical axis) is varied. The nearest neighbors around the central (reference) cell are separated by a distance of 50 nm. Figures 16(b) and 16(c) show the interplay between the distribution of cell surface charges and electric force (MST) for this specific cell configuration. Moreover, as the applied field magnitude is increased from 2 V/cm to 1 kV/cm, we observe several orders of magnitude increase in force (not shown). For frequency of 10^7 Hz, one can see several hot spots of high surface charge density which are spatially correlated with the positions of the nearest neighboring cells. When integrating the MST over one of these spots we obtain a value of the z -component of the force equal to 1.25 fN for an applied field of 2 V/cm and 312.64 pN when a 1 kV/cm field is applied. One can note the large difference in absolute values of the surface charge density for the situation found at lower frequencies for which large values of MST are close to the poles of the spherical reference cell and very weak at the equator as might be expected. This observation fits with the pearl chain effect, i.e., biological particles immersed in liquid media align themselves and form pearl chains under an applied electromagnetic field when the field strength is greater than a certain minimum value.⁵⁴ The presented calculations which provide a quantitative estimate for the level of the driving forces for cell deformation and polarization can be extended in a few directions. In real tissues there are more than two cell sizes and this brings to an interesting problem of cell topology and cell position upon the induced electric field (and subsequently the DEP forces) in a multiscale tissue model.⁵⁰ Furthermore, a conceptualization of the way the cells interact with one another is of paramount importance in these computer simulations. Finally, the flexibility of multiphysics modeling with FE methods will allow future models to incorporate greater sophistication, simulating also molecular transport across the membranes as well as the electromechanical properties of tissues.⁵⁵

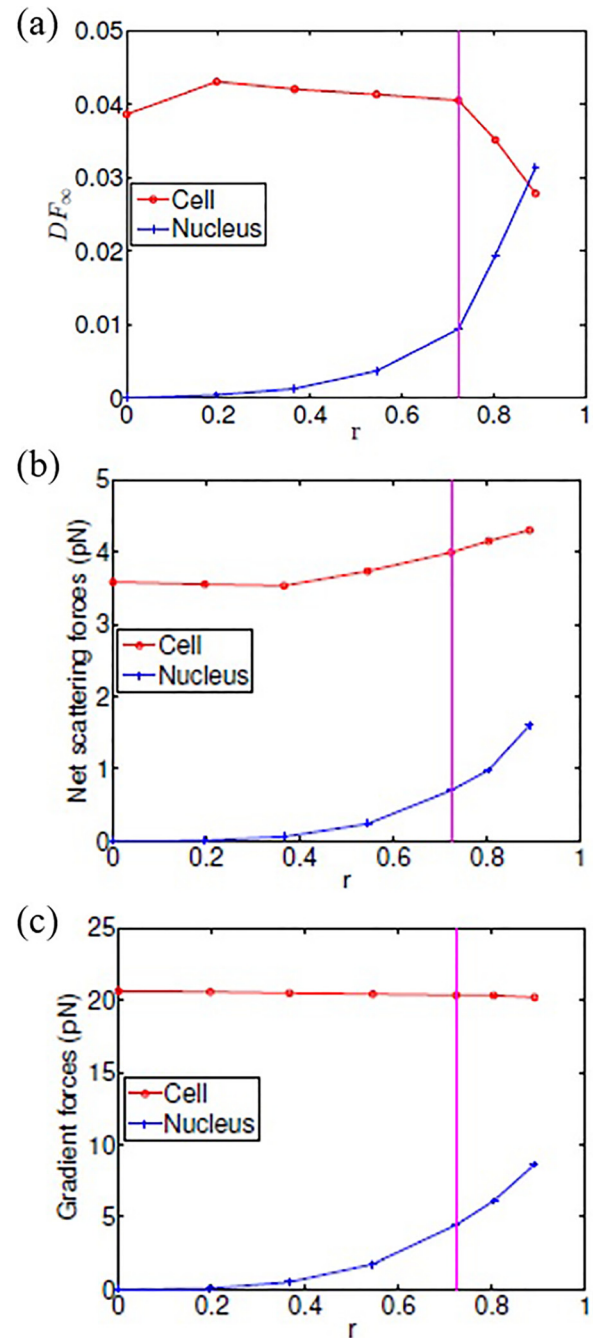


FIG. 14. Calculated deformations and forces in a nucleated CHO cell modelled as two spherical elastic membranes due to dynamically changing optical stresses where DF_∞ is the ratio of difference and sum of the deformed major and minor axes, r is the ratio of two membrane radii: (a) DF_∞ vs r , (b) net scattering forces vs r , (c) gradient forces vs r ; the vertical line denotes the nominal radius ratio $r = 0.72$ of CHO cell [Reproduced with permission from Srarj *et al.*, J. Opt. **17**, 075403 (2015). Copyright 2015. IOP Publishing Ltd.⁵³].

B. Modelling cell perforation

As mentioned previously, cell perforation models are usually based on ITV modelling above a threshold value. In Ref. 50, the authors describe a method for extracting realistic cell morphologies from fluorescence microscopy images to generate a piecewise mesh used to develop a finite element model in two dimensions. Both membranes are treated as a thin dielectric which acts as a parallel plate capacitor from which ITV is

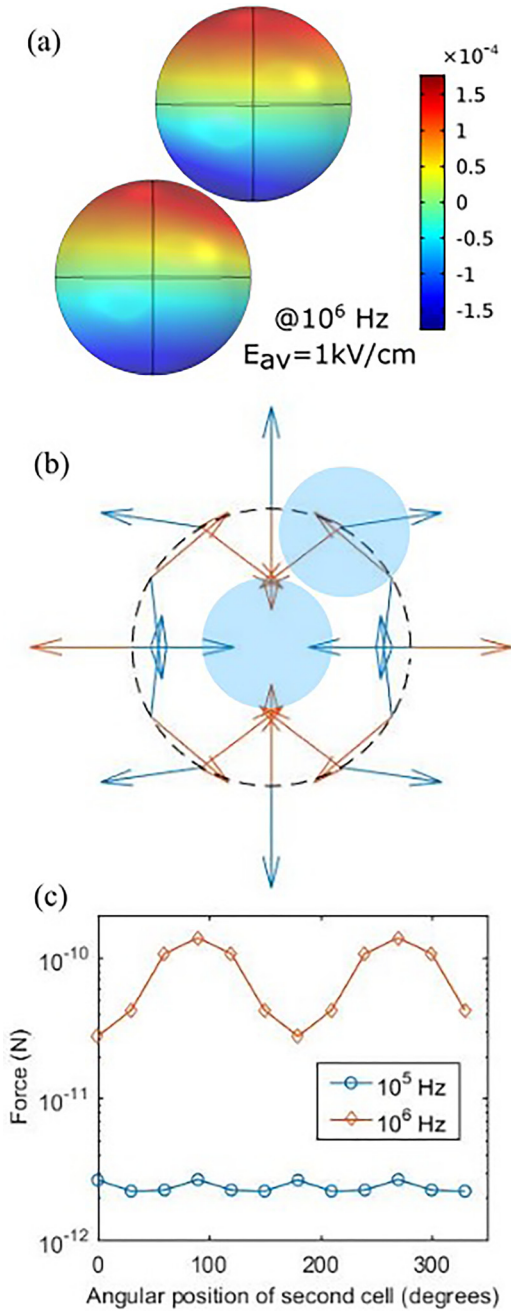


FIG. 15. Total electric forces between two cells under an applied ac field. (a) Surface charge distribution (in C/m^2) over two spherical cells of radii $10\ \mu\text{m}$ each, separated by a distance of $500\ \text{nm}$ when an average ac field magnitude of $1\ \text{kV/cm}$ with frequency of 10^6 Hz is applied vertically, (b) the direction of total electric force on the second cell at specific angular positions is depicted by arrows for frequency of 10^5 Hz (blue) and 10^6 Hz (brown), and (c) a comparison of force magnitudes for the two cases shown in (b).

calculated for two sets of pulse parameters inspired by clinical irreversible electroporation (IRE) treatments [Fig. 17(c)]. It is shown that high-frequency bipolar pulse trains are better able to raise the ITV of tightly packed cells to a simulated electroporation threshold than conventional IRE pulse trains, at the expense of larger applied potentials. Another strategy is suggested in Ref. 14 using multicellular models for studying the response of biological tissues exposed to electric fields. Simulations probing the conductivity changes of three-dimensional models of

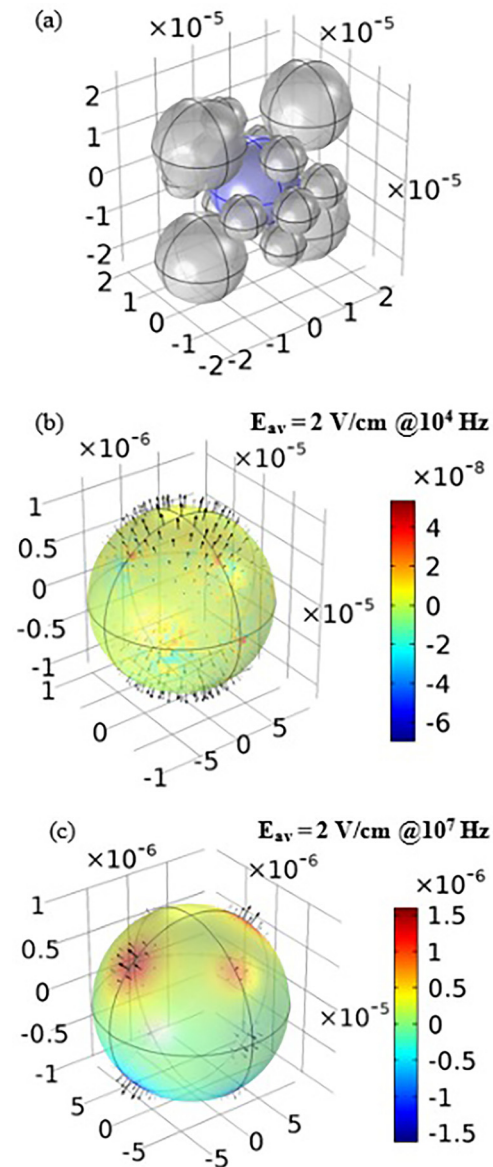


FIG. 16. Local electric forces on a cell surrounded by other cells under an applied ac field. (a) Model geometry consists of a random distribution of two-size spheres (radii 10 and $5\ \mu\text{m}$). The central (blue) sphere is chosen (as reference) for examining the local force distribution on its surface. MST is depicted by arrows and surface charge density (in C/m^2) is depicted by color for frequency of (b) 10^4 Hz and (c) 10^7 Hz.

biological tissues consisting of random ternary CS sphere packings with different spatial scales are described in Ref. 14. The algorithmic method consists of placing the CS particles in a random manner without any overlap between them. An example of such a geometric model is shown in Fig. 10(a). The asymptotic DeBruin-Krassowska (DBK) model of EP for a single cell based on the Smoluchowski equation is used and the FE method solves Laplace's equation in time domain to obtain the distribution of the electric potential in the model. The temporal evolution of the electric conductivity of these packings is investigated during application of an electric field with magnitude either below or above the value leading to cell membrane electroporation. The fraction of electroporated cells can be described by a hyperbolic tangent function of the electric field [Figs. 17(a) and 17(b)]. In Ref. 14, the authors demonstrated that the collective physical

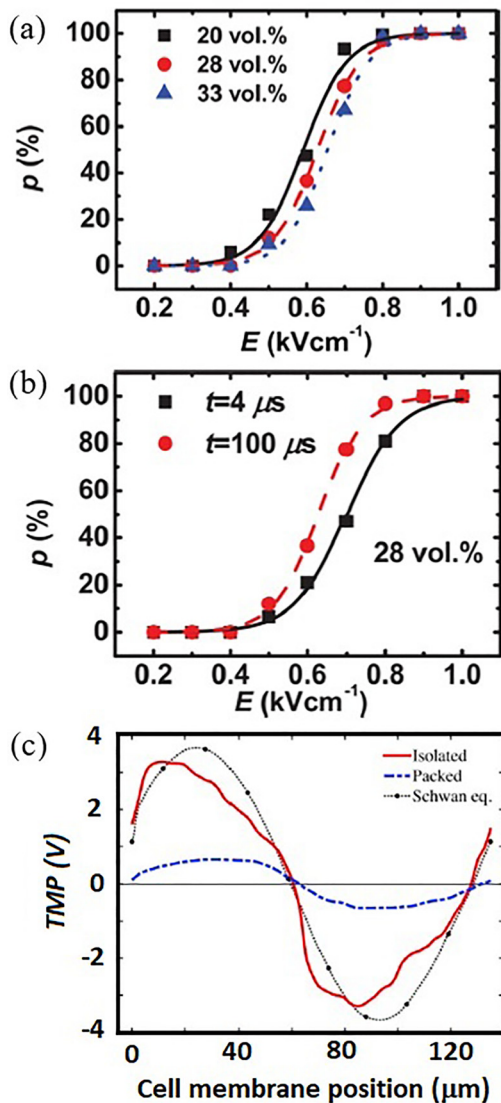


FIG. 17. Fraction of electroporated cells vs applied electric field for geometry shown in Fig. 10(a) for (a) several volume fractions in static analysis; (b) different pulse durations in dynamic analysis averaged for 5 realizations; the calculated data points were fitted to a hyperbolic tangent function. (c) Comparison of distribution of induced transmembrane potential over the membrane of individual isolated cell (solid line) or when it is part of the tissue (dashed line) for geometry shown in Fig. 10(b) when stimulated by electric pulse of $20\mu\text{s}$; the analytical Schwan equation is also plotted for comparison [(a) and (b) and (c) are reproduced from Appl. Phys. Lett. **100**, 143701 (2012). Copyright 2012 AIP Publishing¹⁴ and Murovec *et al.*, Biophys. J. **111**, 2286 (2016). Copyright 2016 Elsevier,⁵⁰ respectively).

processes causing the transient permeability of the cell membranes can be understood by analogy with the physics of a two-state system with an external field. Last but not least, it is worth noticing that Rems and coworkers⁵⁶ compared the theoretical predictions for an aqueous pore conductance by MD simulations.

V. LOOKING AHEAD IN ELECTROMECHANOBIOLOGY

The interfaces of applied physics and biology have both precedence and promise.⁵⁷ The quantitative study of living matter, trying to understand the living part of the world with the same precision as we understood the inorganic world is

eventually one of the most fascinating challenges of our time. We hope that this comprehensive report will serve to motivate newcomers who have never been exposed to the field of electromechanobiology.

In the present perspective, we focused on a few fundamental points emphasizing how the quantitative analysis of forces can be controlled by various stimulation parameters. A single multiscale theoretical model or experimental platform which would include subcellular, cellular and tissue details is still lacking. Such analysis can be envisioned through a hybrid continuum approach that takes into account coarse-grained biomolecular details as well as larger length scales up to hundreds of cells. While biochemical reactions were not considered in this report it should be noted that the physical responses are often coupled with specific biochemical reactions during regular biological processes that eventually impact physical models.

A. Theoretical perspectives

A physics perspective in this field will likely be to imagine numerical tools that lower the level of complexity of living BM by keeping only the relevant and most important structural features, and how to think about the collective mechanics of individual cells organized in a hierarchical structure which is stimulated with an electric field. Though simplifications must be made to any simulation, the trend of increasing computer power and performance enables many of these inhibitions to be overcome by simulations that achieve a greater predictive capacity and come ever closer to simulating precise experimental and clinical conditions. Immediate challenges are as follows: (i) develop a multiscale multiphysics analysis of BM.⁵⁸ What is needed is a way to gradually increase the BM complexity so that over complexity can be avoided but with the necessary physical features retained, for instance, linking the cell scale (continuum) electroporation model discussed earlier in Sec. VB and tissue model and then linking the biomolecular reactions database to it to test further responses.⁵⁹ To truly capture and explore physical phenomena in 3D systems requires accounting for more of the complexities of a biological cell, such as its irregular geometry and their inhomogeneous and anisotropic material properties, i.e., meaning that the material's mechanical properties do depend on the direction of the force; (ii) consider the behavior and self-assembly of cell collections. Out of thermodynamic equilibrium self-organization mechanisms can emerge and their understanding can open up paths to control emergent tissue patterns under external mechanical and electromagnetic fields; and (iii) analyze the role of ECM that surrounds and supports cells which is known to strongly affect cell/tissue organization; in particular the full exploitation of the interfacial properties will require an evaluation of the distance over which forces propagate by multiscale tissue modeling and to compare with experimental observations suggesting that long distance signals (typically, on the order of ten micrometers) are dependent on the inherent tension in the cytoskeleton.⁶⁰

B. Experimental perspectives

The ability to exert and experience force at various length and time scales is proving to be crucial for most cellular functions. For that specific purpose, experimental approaches are needed for the following: (i) devise a lab optofluidic platform for exploring cell signaling at single cell and multiple cell levels with control of the intracellular and intercellular force; (ii) investigate intercellular communication in the ECM through electric signals which offer the possibility to communicate on longer length scales and significant control as well for self-assembly; (iii) control in real time the electroporation which represents a way to implement customized treatments where the electric solicitation is inhibited once the desired degree of permeabilization is achieved. Eventually, this control system of the cell membrane permeabilization could be massively parallelized on a dedicated biochip for the electroporation of many cells, prior to cell fusion or integration of therapeutic vectors; measure experimentally forces and stresses *in situ* in electroporated living tissues; (iv) develop advanced bio-imaging techniques to analyze the cytoskeletal structures and stress propagation and distribution in living cells; (v) the growing interest in microfluidics has also raised questions about interfaces in BM.

C. Clinical perspectives

Understanding the role of physical forces in biology is not limited to fundamental research but can lead to applications to treat a wide variety of clinical conditions. In a not-so-distant future, the complexities related to 3D printing of biocompatible materials, cells and supporting components into complex 3D functional living tissues will be addressed by integrating technologies from the fields of imaging, biomaterials science, cell biology, physics and medicine. Combining electromechanobiology with 3D bioprinting would reveal the role of forces during tissue fabrication and organogenesis. It is anticipated that such developments will lead to innovative high-throughput 3D-bioprinted tissue models for research and drug discovery. Translating this research into the clinic can help create new paths for generation and transplantation of several tissues to repair damaged organs.

Electromechanobiology-based technology is likely to emerge as an innovative branch for developing precision diagnostics and therapeutics of diseases that are beyond the reach of existing toolboxes.

ACKNOWLEDGMENTS

D.S. acknowledges a doctoral grant from the Université de Brest. The Lab-STICC is Unité Mixte de Recherche CNRS 6285.

NOMENCLATURE

AC	Alternating current
AFM	Atomic force microscopy/mapping
BEP	Bulk electroporation
BM	Biological materials
CHO	Chinese hamster ovary

CM	Claussius-Mossotti
CS	Core-shell
DBK	DeBruin-Krassowska
DEP	Dielectrophoretic
DF	Deformation factor
DRT	Dynamic ray tracing
ECM	Extracellular medium
EF	Electrostatic forces
EFM	Electrostatic force microscopy/mapping
EHD	Electrohydrodynamic
EP	Electroporation
ET	Electrothermal
FE	Finite element
FRET	Fluorescence resonance energy transfer
HEK	Human embryonic kidney
IRE	Irreversible electroporation
ITV	Induced transmembrane voltage
MD	Molecular dynamics
MEP	Microelectroporation
MST	Maxwell stress tensor
NEP	Nanoelectroporation
NK	Natural killer
PC3	Prostate cancer
PZT	Lead zirconate titanate
RBC	Red blood cell
RNA	Ribonucleic acid
RTA	Repulsion to attraction
SEM	Scanning electron microscope

¹A. R. Dunn and A. Price, *Phys. Today* **68**(2), 27 (2015).

²T. Murovec and C. Brosseau, *Phys. Rev. E* **92**, 042717 (2015).

³K. Austen, P. Ringer, A. Mehlich, A. Chrostek-Grashoff, C. Kluger, C. Klingner, B. Sabass, R. Zent, M. Rief, and C. Grashoff, *Nat. Cell Biol.* **17**, 1597 (2015).

⁴M. R. Mofrad and R. D. Kamm, *Cytoskeletal Mechanics: Models and Measurements in Cell Mechanics* (Cambridge University Press, 2006).

⁵N. Wang, I. M. Tolić-Nørrelykke, J. Chen, S. M. Mijailovich, J. P. Butler, J. J. Fredberg, and D. Stamenović, *Am. J. Physiol. - Cell Physiol.* **282**, C606 (2002).

⁶D. Stamenovic, B. Suki, B. Fabry, N. Wang, and J. J. Fredberg, *J. Appl. Physiol.* **96**, 1600 (2004).

⁷M. L. Gardel, F. Nakamura, J. H. Hartwig, J. C. Crocker, T. P. Stossel, and D. A. Weitz, *Proc. Natl. Acad. Sci. U.S.A.* **103**, 1762 (2006).

⁸A. P. Ebrahimi, *J. Vasc. Interv. Neurol.* **2**, 155 (2009).

⁹R. Akhtar, M. J. Sherratt, J. K. Cruickshank, and B. Derby, *Mater. Today* **14**, 96 (2011).

¹⁰M. E. Mezeme and C. Brosseau, *J. Appl. Phys.* **107**, 014701 (2010).

¹¹M. E. Mezeme and C. Brosseau, *J. Appl. Phys.* **108**, 014701 (2010).

¹²M. E. Mezeme, S. Lasquellec, and C. Brosseau, *Phys. Rev. E* **81**, 057602 (2010).

¹³C. B. Arena, C. S. Szot, P. A. Garcia, M. N. Rylander, and R. V. Davalos, *Biophys. J.* **103**, 2033 (2012).

¹⁴M. E. Mezeme, G. Pucihar, M. Pavlin, C. Brosseau, and D. Miklavcic, *Appl. Phys. Lett.* **100**, 143701 (2012).

¹⁵M. E. Mezeme, M. Kranjc, F. Bajd, I. Sersa, C. Brosseau, and D. Miklavcic, *Appl. Phys. Lett.* **101**, 213702 (2012).

¹⁶L. D. Landau and L. P. Pitaevskii, *Electrodynamics of Continuous Media* (Pergamon Press, 1984).

¹⁷J. D. Jackson, *Classical Electrodynamics* (John Wiley & Sons, 2007).

¹⁸T. B. Jones, *Electromechanics of Particles* (Cambridge University Press, New York, 1995).

¹⁹X. Wang, X.-B. Wang, and P. R. Gascoyne, *J. Electrostat.* **39**, 277 (1997).

²⁰U. Zimmermann, *Biochim. Biophys. Acta* **694**, 227 (1982).

²¹T. Doerr and Y.-K. Yu, *Phys. Rev. E* **81**, 031925 (2010).

²²T. Doerr and Y.-K. Yu, *Phys. Rev. E* **73**, 061902 (2006).

- ²³T. Doerr and Y.-K. Yu, *Am. J. Phys.* **82**, 460 (2014).
- ²⁴W. Tian, J. Huang, and K. Yu, *J. Appl. Phys.* **105**, 102044 (2009).
- ²⁵J. Aragones, J. Steimel, and A. Alexander-Katz, *Nat. Commun.* **7**, 11325 (2016).
- ²⁶J. P. Steimel, J. L. Aragones, and A. Alexander-Katz, *Phys. Rev. Lett.* **113**, 178101 (2014).
- ²⁷A. Castellanos, A. Ramos, A. Gonzalez, N. G. Green, and H. Morgan, *J. Phys. D: Appl. Phys.* **36**, 2584 (2003).
- ²⁸N. S. K. Gunda, S. Bhattacharjee, and S. K. Mitra, *Biomicrofluidics* **6**, 034118 (2012).
- ²⁹H. P. Schwan, *Advances in Biological and Medical Physics* (Elsevier, 1957), pp. 147–209.
- ³⁰K. R. Foster and H. P. Schwan, *Handb. Biol. Eff. Electromagn. Fields* **2**, 25 (1995).
- ³¹T. Lewis, *IEEE Trans. Dielectr. Electr. Insul.* **11**, 739 (2004).
- ³²T. Ye, H. Li, and K. Lam, *Electrophoresis* **36**, 378 (2015).
- ³³T. Inoue and R. Krumlauf, *Nat. Neurol.* **4**, 1156 (2001).
- ³⁴D. Dimitrov, *Handb. Biol. Phys.* **1**, 851 (1995).
- ³⁵J. C. Weaver and Y. A. Chizmadzhev, *Bioelectrochem. Bioenergetics* **41**, 135 (1996).
- ³⁶G. Pucihar, D. Miklavcic, and T. Kotnik, *IEEE Trans. Biomed. Eng.* **56**, 1491 (2009).
- ³⁷L. Rems and D. Miklavcic, *J. Appl. Phys.* **119**, 201101 (2016).
- ³⁸T. D. Nguyen, N. Deshmukh, J. M. Nagarath, T. Kramer, P. K. Purohit, M. J. Berry, and M. C. McAlpine, *Nat. Nanotechnol.* **7**, 587 (2012).
- ³⁹C. Vaillier, T. Honegger, F. Kermarrec, X. Gidrol, and D. Peyrade, *PLoS One* **9**, e95231 (2014).
- ⁴⁰B. Cortese, I. E. Palamà, S. D'Amone, and G. Gigli, *Integr. Biol.* **6**, 817 (2014).
- ⁴¹K. Khoshmanesh, S. Nahavandi, S. Baratchi, A. Mitchell, and K. Kalantar-zadeh, *Biosens. Bioelectron.* **26**, 1800 (2011).
- ⁴²A. Pavesi, G. Adriani, M. Rasponi, I. K. Zervantonakis, G. B. Fiore, and R. D. Kamm, *Sci. Rep.* **5**, 11800 (2015).
- ⁴³K. Sugimura, P.-F. Lenne, and F. Graner, *Development* **143**, 186 (2016).
- ⁴⁴L.-H. Chau, W. Liang, F. W. K. Cheung, W. K. Liu, W. J. Li, S.-C. Chen, and G.-B. Lee, *PLoS One* **8**, e51577 (2013).
- ⁴⁵M. Gu, S. Kuriakose, and X. Gan, *Opt. Express* **15**, 1369 (2007).
- ⁴⁶G. C. Messina, M. Dipalo, R. La Rocca, P. Zilio, V. Caprettini, R. P. Zaccaria, A. Toma, F. Tantussi, L. Berdondini, and F. De Angelis, *Adv. Mater.* **27**, 7145 (2015).
- ⁴⁷L. Chang, L. Li, J. Shi, Y. Sheng, W. Lu, D. Gallego-Perez, and L. J. Lee, *Lab Chip* **16**, 4047 (2016).
- ⁴⁸B. S.-L. Lalonde, É. Boulais, J.-J. Lebrun, and M. Meunier, *Biomed. Opt. Express* **4**, 490 (2013).
- ⁴⁹C. Boutopoulos, E. Bergeron, and M. Meunier, *J. Biophot.* **9**, 26 (2016).
- ⁵⁰T. Murovec, D. C. Sweeney, E. Latouche, R. V. Davalos, and C. Brosseau, *Biophys. J.* **111**, 2286 (2016).
- ⁵¹L. Yu and Y. Sheng, *Opt. Express* **23**, 6020 (2015).
- ⁵²E. Promayon, J.-L. Martiel, and P. Tracqui, *Polymer and Cell Dynamics-Multiscale Modeling and Numerical Simulations* (Birkhauser, 2003), p. 125.
- ⁵³I. Sraj, J. Francois, D. W. Marr, and C. D. Eggleton, *J. Opt.* **17**, 075403 (2015).
- ⁵⁴S. Takashima and H.-P. Schwan, *Biophys. J.* **47**, 513 (1985).
- ⁵⁵H. Isambert, *Phys. Rev. Lett.* **80**, 3404 (1998).
- ⁵⁶L. Rems, M. Tarek, M. Casciola, and D. Miklavcic, *Bioelectrochemistry* **112**, 112 (2016).
- ⁵⁷C. Brosseau, *Ann. Mater. Sci. Eng.* **1**, 1 (2014).
- ⁵⁸Z. Qu, A. Garfinkel, J. N. Weiss, and M. Nivala, *Prog. Biophys. Mol. Biol.* **107**, 21 (2011).
- ⁵⁹*Multiscale Methods, Bridging the Scales in Science and Engineering*, edited by J. Fish (Oxford University Press, 2009).
- ⁶⁰S. Hu, L. Eberhard, J. Chen, J. C. Love, J. P. Butler, J. J. Fredberg, G. M. Whitesides, and N. Wang, *Am. J. Physiol. - Cell Physiol.* **287**, C1184 (2004).

2.3 A closer context on ED and EP

Having recalled several concepts and ideas in the publication Shamooun et al. (2018) [28] forming a broad perspective, several related studies on ED and/or EP that are closer to the goal of this work need to be discussed here separately.

A first interesting work is given by Riske & Dimova (2005) [21] on giant unilamellar vesicles (GUVs) which are very similar to biological cells but less complicated systems due to the lack of cytoskeleton and other organelles. GUVs also exhibit ED and EP that makes them an experimental model system to study their phenomena in a less complicated scenario. The vesicle radii are in the range 10-15 μm in this work that recorded the temporal dynamics (with a time resolution of 30 μs) of the GUV response on application of an electric pulse and its further mechanical relaxation over six decades of time. It is reported that macropores ($\sim 2 \mu\text{m}$ diameter) with pore lifetime of $\sim 10 \text{ ms}$ are formed. It is suggested that pore lifetime results from an interplay between pore edge tension and membrane viscosity. The conductivity ratio between inside to outside of the solution is ~ 1.3 ($6/4.5 \mu\text{S/cm}$). With this low conductivity solution, the charging time is larger than the pulse duration used and the GUVs deform to a prolate shape along the average field direction which is quantified by ratio a/b as shown in Fig.2.3, where a and b are semi-axes parallel and perpendicular to the field. This ratio should not be confused with ‘strain’ which is discussed for the next study in this section. Both quantify deformation, however, this ratio is more commonly used for quantifying stretching and compression simultaneously.

This study used several pulse strength-duration parameters (range: 1-3 kV/cm strength & 50-300 μs duration). The mechanical response corresponding to these parameters is shown in the same figure. As the pulse strength increases the maximum value of a/b increases, which also increases with increased pulse duration for a single pulse strength. The major result of this work is that ED is affected by EP. This can be particularly seen in Fig.2.3C by the additional

plateau as the vesicle relaxes. It is shown that the mechanical relaxation dynamics has three regimes – area relaxation due to stretching, pore closure and curvature relaxation.

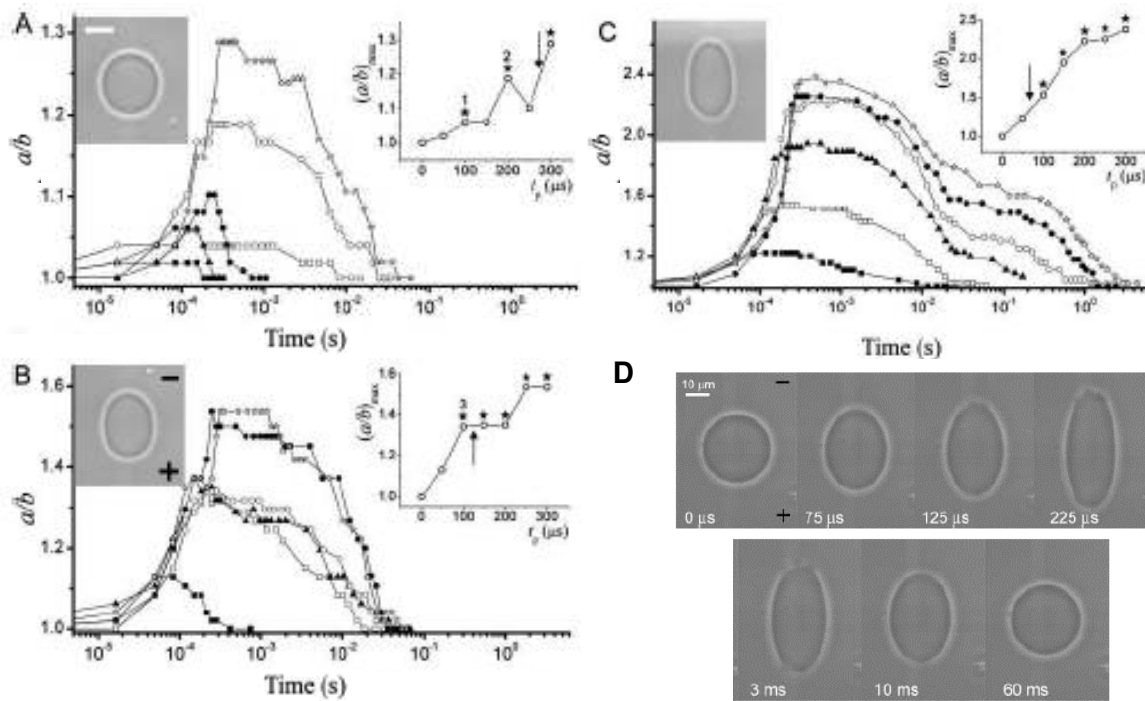


Fig.2.3: ED and EP of vesicles (Adapted from Fig.1 & 5 of [21]). Degree of deformation (a/b) induced on one vesicle when applying different square-wave pulses (A) 1 kV/cm, (B) 2 kV/cm, (C) 3 kV/cm. For each pulse strength, the pulse durations were 50-300 μ s in steps of 50 μ s denoted by symbols (\blacksquare , \square , \blacktriangle , \circ , \bullet , \star). Image acquisition rate is 30,000 fps. The pulse begins at $t=0$. The insets show maximum value of deformation $(a/b)_{\max}$ as a function of pulse duration, t_p . The scale bar in A-C is 15 μ m. (D) Timelapse of the vesicle deformation for pulse duration 200 μ s and applied field 2 kV/cm. (Porated in third frame onwards, pore lifetime is 10 ms). Scale bar is 10 μ m. See the reference for more details.

Another important study by MacQueen et al. (2010) [32] is used to characterize the ED of CHO cells and U937 promonocytes on a planar device. The device design is shown in Fig. 2.4 (a) and a pulsed AC field is applied. The frequency is set to 5×10^6 Hz and peak to peak voltage is varied between 2-10 V in the form of a square pulse. One cycle of this pulse is formed by letting the cell deform at 10 V up to its maximum deformation and letting it relax at 2 V (2V is used here as a ‘cell holding’ potential i.e. the applied stress is too weak to cause deformation). The strain data for one cycle of the pulse is shown in Fig.2.4 (b). CHO cells are found to be stiffer than U937 cells. There is 10 % strain observed in 70 s for CHO cells, while 23 % strain for U937 cells in 30 s which can be seen in Fig.2.4 (e). As the cycle continues, the strain cycle is also enhanced and thus subsequent deformation begins before a

full mechanical relaxation from the previous cycle. Up to 70 % strain is observed for U937 cells in the subsequent cycles while CHO cells reach up to 22 % strain.

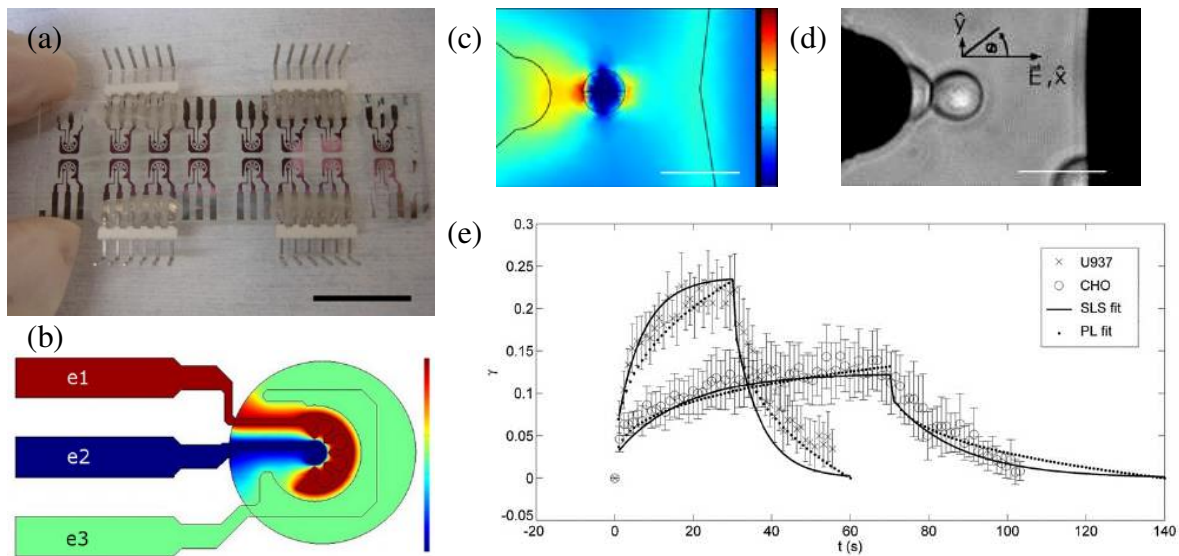


Fig.2.4: ED of biological cells (adapted from Fig.1b-c, Fig.2c-d and Fig.6 of [32]) Array of electrodes on a microscope glass slide, scale bar is 2 cm. A look at the electrodes geometry model, e1 is positive and e2 is negative. (c) A closer look at the electrode geometry model with a polarizable spherical object in between, scale bar is 25 μm (d) Optical microscopic image of a U937 cell between the electrodes, (e) Strain as a function of time during one cycle of the applied field.

The use of pulsed AC field in the previous study is limited to only two constant peak-peak voltages. In a very recent study, Qiang et al. (2018) [40] have employed pulsed AC fields by varying the peak-peak voltage in several ways using amplitude-modulated waveforms shown in Fig.2.5 (a), which smoothen the transition of exerted force over cell membrane and leads to unconventional strain profiles. The cell's major axis stretches to twice its original value while the minor axis is compressed to half its original value. Compare for example the deformation pattern shown in Fig.2.4 (e) with Fig.2.5 (b). It should be noted that the two studies quantify deformation slightly differently, the previous uses 'engineering strain' and the latter uses 'compression ratio'. The technique used in latter study essentially gives more control on the amount of ED of the cells than the usual techniques by virtue of smoothening the rise of force over time. Red Blood Cells (RBCs) are used in this study to measure nonlinear viscoelasticity of their membranes. This is accomplished by using Kelvin-

Voigt model of viscoelasticity which takes the shear stress calculation and deformation measurements as inputs and gives membrane shear modulus and viscous relaxation time as outputs.

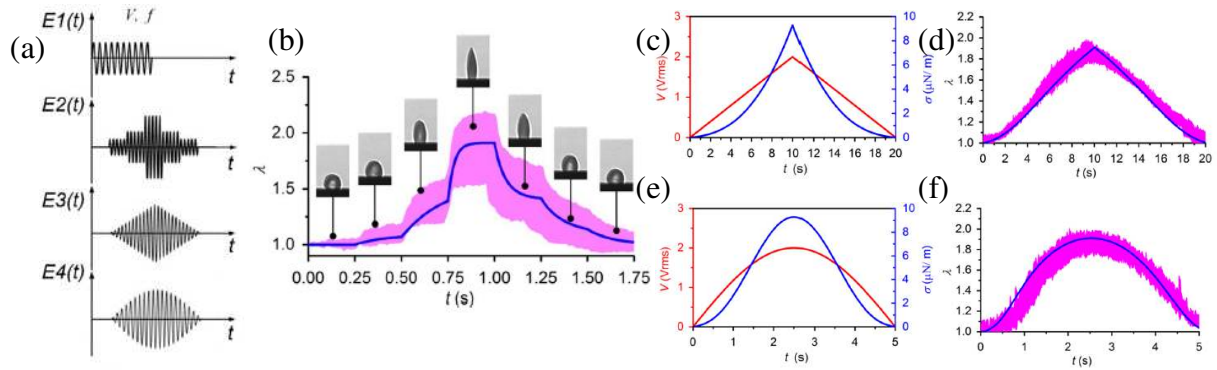


Fig.2.5: Unconventional strain profiles (Adapted from Fig. 1d, 5b, 6 of [40]) quantified by minor axis compression, $\lambda=b_0/b(t)$ (a) Amplitude modulated waveforms for excitation labelled E1(t)-E4(t), (b) λ for E2(t). Each step is 0.25 s. Insets show RBC deformations at specific times, (c) V_{rms} for E3(t) (red) and electrical stress (blue), (d) λ for E3(t), (e-f) As in (c-d) for E4(t).

All these reports covered a wide range of issues in context of ED and EP. The experimental studies considered either a single or few cells to obtain insights into the electromechanical response, however the realistic scenarios correspond to dense cell suspensions and complex cellular arrangements of a tissue for which simultaneous ED and EP have not been extensively studied yet either by numerical or experimental means. As the experimental precision and accuracy of force measurement and application at various scales of biological media improve, numerical models based on ED and EP of collective cell assemblies form a timely subject of research. The next chapter discusses how numerical methods can be useful in predicting measurable and observable quantities which can improve our understanding of the first-principles of the Multiphysics assemblies of the biological tissues.

3. Modelling cells and tissues

3.1 Introduction

Fundamental principles of physics (electrostatics and mechanics) can be used to construct mathematical models for the purpose of studying ED and EP phenomena. They rely on the resolution of partial differential equations (PDEs) in space and time. Analytical solutions of these PDEs can be obtained only for high-symmetry and simple geometries. Thus, for most of the realistic scenarios in biological media, which lack symmetry and have complex geometries, numerical methods are employed to approximate the solutions of involved PDEs. Solving them can be realized by many numerical methods such as Finite Element Methods (FEM) [41], Finite Difference Methods (FDM) [42], Boundary Element Methods (BEM) [43], etc. These methods differ in several aspects such as discretization of space, size scaling, etc. FDM differs from FEM and BEM in terms of representation of the derivative in PDEs as finite differences, whereas FEM and BEM use integration of the derivative in PDEs. Even though FDM has a simpler approach to solution (since numerical integration is more demanding than differentiation) and well established for analysis of a broad frequency range while using a short pulse in time, FDM is not suitable for modelling deforming object boundaries because it uses rectangular grids on which curved objects must be approximated whereas arbitrary or at least simply curved shape of cells is mandatory in this work. On the other hand, BEM cannot account for the electric potential and mechanical stress distribution in the volume regions away from the cell membrane because it is only implemented on the boundary, thus volume regions are not solved for. FEM is chosen here because firstly, the involved geometry may contain multiple arbitrary shaped cells with curved surfaces which are allowed to deform in time and FEM solves both on the boundaries as well as the volume in the space. Secondly, since several spatially and randomly distributed cells with deforming boundaries do not have any analytical

formulation for describing electrical and mechanical stress distribution in the volume regions. Lastly, since FEM is well suited for transient and nonlinear problems. All equations used in this work and the coupling of physics are discussed in this chapter. We first begin by giving a flavor of the FEM with an overview of the numerical procedures to generate a basic understanding for the reader.

3.2 Finite Element Method

Assuming that the solution of a PDE that is required to be solved is given by an unknown function f , defined on the x -axis (1D) (Fig.3.1). The function f can be approximated by a numerical method (FEM) as f_h by following a systematic procedure that has the advantage of modelling curved geometries and various material properties involving heterogeneity.

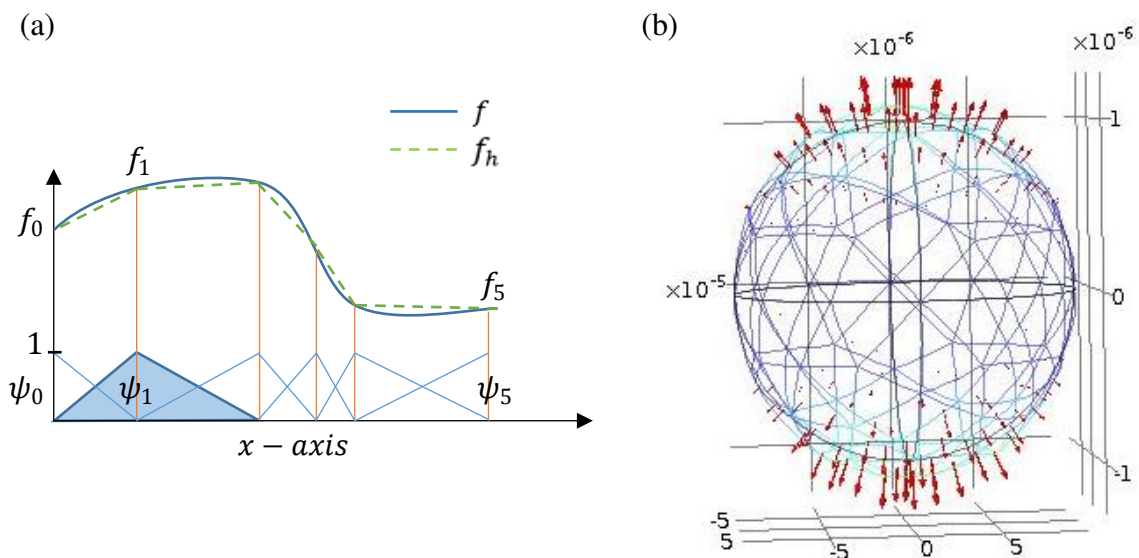


Fig. 3.1: (a) Illustration of an arbitrary 1D solution approximation by FEM. Blue solid curve represents the real solution, f . Green dashed curve is the approximated solution, f_h , [41], (b) 3D finite elements surface mesh of a spherical cell under an applied electric field (vertical direction), red arrows indicate electrical stress which is calculated from the approximated solution for the PDE – Poisson’s equation.

The first step considers the discretization of the domain of f on x -axis employing a larger number of elements, N_e . In 1D, the elements are line segments. For 2D, the elements take the shape of triangles or quadrilaterals while for 3D, they take the shape of prisms,

tetrahedrons or parallelepiped. Each element uses a set of n basis (or shape) functions ψ_i (polynomials) which can be linear, quadratic or cubic in order to make a ‘guess solution’. Each linear element uses 2 nodes, quadratic element uses 3 nodes and cubic element uses 4 nodes. Thus the choice of these basis functions further dictates the total number of nodes. There are $N_e + 1$ nodes for linear elements, $2N_e + 1$ nodes for quadratic elements and $3N_e + 1$ nodes for cubic elements.

The second step is to formulate element-level equations. For a single element, the guess solution is approximated using a linear combination of n basis functions and then it is plugged into the PDE to calculate a residual. The residual is then multiplied with a weight (or test) function w_j , which is also a polynomial, and integrated over the element length to obtain an algebraic equation. Since, n test functions are used therefore n algebraic equations per element are obtained forming a system matrix of size $n \times n$ per element. The basis functions, ψ_i are expressed as functions of the node position (x, y, z) defined on the local coordinate system between any two nodes on an interval $\mu: [-1, 1]$. They are shown in the image (Fig.3.1) as linear but they can be quadratic such as given below (Eq.3.1) or a higher order polynomial. The test functions can be chosen to be same as the basis functions (Galerkin method).

$$\psi_1 = \frac{1}{2}\mu(\mu - 1), \psi_2 = 1 - \mu^2, \psi_3 = \frac{1}{2}\mu(\mu + 1) \quad (\text{Eq.3.1})$$

The third step involves the assembly of the element-level equations (shown below) along with the boundary conditions imposed, thus forming a larger system of equation $K.U = F$ with a size of the system matrix K and the vectors U, F depending on the total number of nodes. The limits of the integral denote the nodal extents for the element in consideration. The system of equations is solved for the unknown coefficients listed in U thereby approximating the solution f over the complete domain, which equals f_h . The set of equations involved in the overall procedure are shown in Eq.3.2.

$$\begin{aligned}
f^1 &= \sum_i^n f_i^1 \psi_i^1 \dots f^{N_e} = \sum_i^n f_i^{N_e} \psi_i^{N_e} \\
\int_{h_{e-1}}^{h_e} w_1 PDE(f^1) d\Omega &= 0 \dots \int_{h_{e-1}}^{h_e} w_n PDE(f^1) d\Omega = 0 \\
&\vdots \\
\int_{h_{e-1}}^{h_e} w_1 PDE(f^{N_e}) d\Omega &= 0 \dots \int_{h_{e-1}}^{h_e} w_n PDE(f^{N_e}) d\Omega = 0
\end{aligned} \tag{Eq.3.2}$$

$$K.U = F$$

The three-step procedure shown above for equation formulation prepares the original PDE for numerical solvers which is now re-explained in different terms. The original PDE with all its boundary conditions specified is required to be solved in the entire domain at all material points. This is the so-called ‘strong form’ PDE. Solving a strong form PDE is numerically challenging. In the finite element formulation shown above, the strong form PDE is re-written in an integral form before plugging the element-level equations into it and using the method of weighted residuals (MWR, the integral statements above), a ‘weak form’ PDE is used in multiplication with the weight function. The weak form makes use of the Green’s Identity and reduces second order partial derivative to first order. MWR approach offers an alternative to the traditionally used energy minimization principles approach to equation formulation.

In order to solve for the coefficients of the system matrix, there are mainly two types of solvers - ‘Direct solvers’ and ‘Iterative solvers’ [44]. Direct solvers can be used for small and midrange-sized problems, while the iterative solvers can be used for larger linear systems or non-linear parts of the problem. The basic direct method in use is the ‘LU factorization’ method which is based on decomposing the system matrix into a product of two simpler matrices. Some commonly used direct solvers are MUMPS and PARDISO, they differ in computational efficiency which is better in the latter as it can use multiple cores of the CPU. Some commonly used iterative methods are CG, GMRES, BiCG-Stab etc. A number of iterative solvers with cutting-edge preconditioners, such as multigrid preconditioners are

available. These preconditioners provide robustness and speed in the iterative solution process. Iterative methods can be ‘Stationary’ and ‘Non-stationary’. In the stationary methods, the system matrix is re-written as a sum of a two to three matrices following preconditioning schemes defined by ‘Jacobi’ or ‘SOR’. In the non-stationary methods for linear systems, preconditioning schemes defined by ‘geometric or algebraic multigrid’ are used. The nonlinearity of models can be dealt with Newton-Raphson method which uses local derivative information to search for better solution candidates and linearize the non-linear problem. It then solves a sequence of linear equation systems, using the Jacobian matrix, in order to find the solution.

3.3 COMSOL Multiphysics and computational resources

COMSOL Multiphysics® software (v3.5a & v5.2) is used for performing simulations and post-processing along with its:

1. ‘AC/DC’ module that contains ‘Electrostatics’ and ‘Electric Currents’ interfaces,
2. ‘Structural Mechanics’ module that contains ‘Solid Mechanics’ and ‘Membrane’ interfaces and
3. ‘Mathematics’ module that contain ‘PDE Interfaces’.

Mathworks® MATLAB software (R14 and R2016a) is also used for further data analysis. All simulations and data analyses are performed on a computer equipped with INTEL® CORE™ i7-5500U CPU @ 2.4 GHz, 2 Cores, 4 Logical processors, 8 GB RAM and NVIDIA GeForce 920M graphics card. The time consumption for the simulations varies from a few seconds to one and a half hour depending upon the number of degrees of freedom which are determined by the type of analysis, geometric complexity, meshing and the involved PDEs. If one simulation is performed for each of the hundreds or thousands of statistical realizations (or configurations), then the computational time can go up to more than 24 hours.

3.4 Electric field fluctuations

Before dealing with the complexity of numerically modelling the multiphysics of biological structures in Section 3.5, this section presents our first results to compute the average effective permittivity (and its moments) for a single two-phase hetero-structure under an applied electric field. Our first idea in tackling the modelling of cell assemblies was to use tools from statistical physics which are appropriate for complex systems with a lot of interface boundaries. Checkerboard system was used to evaluate the roles of interface, corner and scaling to understand the electric field line distribution and polarization. The external electrical stimulus is applied by maintaining a potential difference across two electrodes at the top and bottom of the checkerboard. Fluctuations of the local electric field and its averages in a checkerboard can be used to approximate its effective dielectric response by considering hundreds to thousands of its statistical representations within ergodic assumption. In Shamooun et al. (2017) [45], we compare two averaging methods which are used to calculate the effective dielectric properties. The averaging methods are based either on using the local electric field values or its square which accounts for electrical energy, weighted with local material properties in the 2-phase media.

The 2D structures in the form of random checkerboards is formed by a distribution of two phases shown in black and white colors and scaled by the number of phases. In this study, the assigned relative permittivity is complex, having an imaginary part which signifies absorbing media. For example, Fig.3.2 shows all realizations for the smallest checkerboard of size 2x2. It is worth noting that only 6 realizations are possible for filling fraction set to 0.5. This number increases from 6 (size 2x2) to 12870 (size 4x4) to 9075135300 (size 6x6) to the order of 10^{18} (size 8x8). The total number of configurations including that for all area fractions is given by 2^{NxN} .

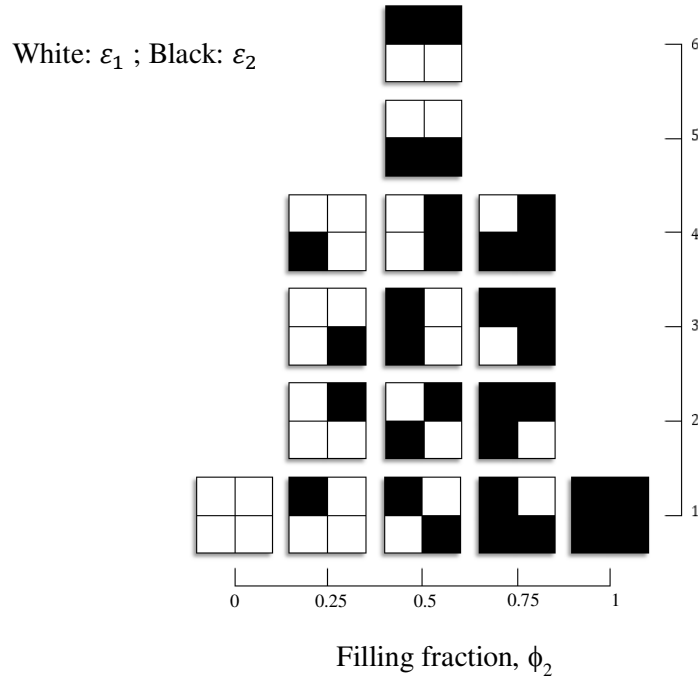


Fig.3.2: Smallest checkerboard of size 2x2 with all possible configurations with filling fraction of the second material (black) on the x-axis and number of configurations for the given filling fraction on the y-axis. Relative permittivity is denoted by ε .

The statistical realizations of the 2-phase media in the form of checkerboards of larger sizes (4x4 and beyond) are generated using an algorithm (Appendix A) based on Monte-Carlo method and the desired number of realizations is randomly sampled to solve Laplace equation. The checkerboard geometry inherently possesses interface boundaries of two phases at multiple corners. Sharp corners appearing on the material boundary interface are known to give rise to a high gradient of electric field. The mesh around each intersection point is made much finer than in regions away from it (Fig.3.3 (a)) to ensure a better accuracy of the solution. The generated checkerboards go through a steady-state analysis by applying an electric field going from bottom edge to the top. Once the solution is obtained, electric field line distribution can be plotted (Fig.3.3 (b)). The averaging procedures are then employed to estimate the effective dielectric properties.

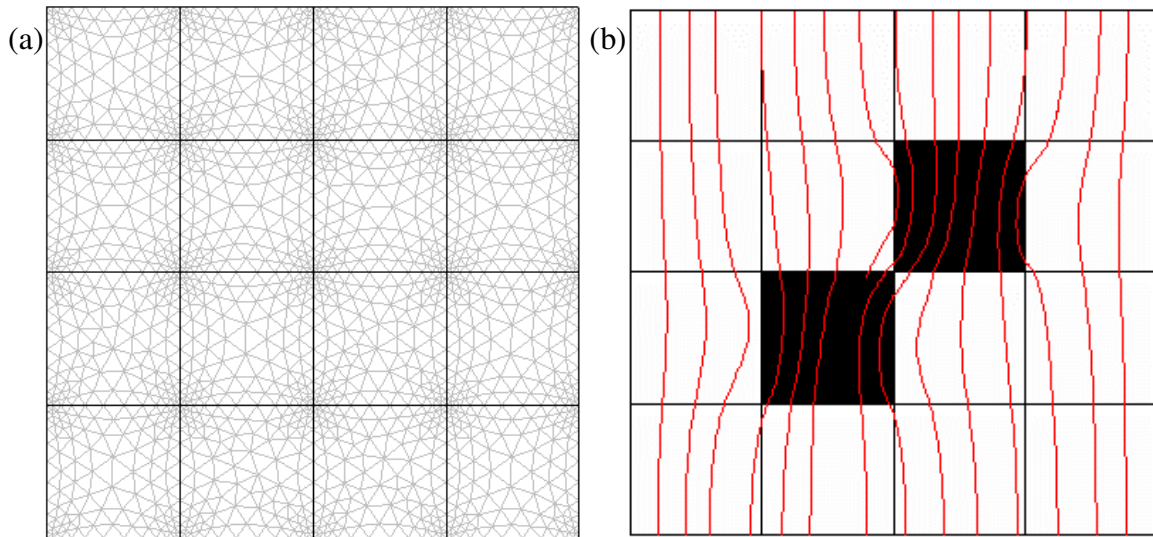


Fig.3.3: (a) Meshing in a 4x4 checkerboard. (b) Electric field streamlines for 4x4 checkerboard (a particular realization of filling fraction 1/8 with $\varepsilon_1 = 1, \varepsilon_2 = 5$) under an applied electric field from bottom to top edge.

It is worth noting that this individual simulation for electrical steady-state analysis takes only a few seconds but for a large number of realizations to be considered, it requires a computational time which can go over 24 hours.

Calculations of the effective dielectric properties of composite media have been extensively studied [46]. The current analysis of second order permittivity variations and comparison of accuracy among the different averaging methods stated above reveals that averaging local electric field is more accurate than averaging local electrical energy for obtaining effective permittivity of large black and white checkerboards. Additionally, the statistical approach allowed us to estimate the small number of realizations required to obtain a fixed accuracy. Even though the statistical approach employed for calculation of electric field fluctuations in heterogeneous media is interesting, it cannot be easily employed in the case of deforming and arbitrary shaped biological cell assembly mainly because the advanced selection methods for deforming boundary surfaces within COMSOL software environment are technically more demanding. Moreover, a thousand realizations of the N-cell assembly demand much larger amount of time for computation and post-simulation data analysis.

Shamoon et al. (2017)

Low-order statistics of effective permittivity and electric field fluctuations in two-phase heterostructures

D. Shamoon, S. Lasquellec and C. Brosseau

Journal of Applied Physics, 122 (4), (2017) 044106

DOI: 10.1063/1.4985799

Low-order statistics of effective permittivity and electric field fluctuations in two-phase heterostructures

D. Shamoon, S. Lasquellec, and C. Brosseau^{a)}

Université de Brest, Lab-STICC, CS 93837, 6 Avenue Le Gorgeu, 29238 Brest Cedex 3, France

(Received 30 May 2017; accepted 16 July 2017; published online 28 July 2017)

Understanding the collective, low-frequency dielectric properties of heterostructures is a major goal in condensed matter. In 1935, Bruggeman [Ann. Phys. Lpz. **24**, 636 (1935)] conceived the concept of an effective medium approximation (EMA) involving a decoupling between the low-order statistics of the electric field fluctuations and the characteristic length scales. We report on and characterize, via finite element studies, the low-order statistics effective permittivity of two-phase 2D and 3D random and deterministic heterostructures as geometry, phase permittivity contrast, and inclusion content are varied. Since EMA analytical expressions become cumbersome even for simple shapes and arrangements, numerical approaches are more suitable for studying heterostructures with complex shapes and topologies. Our numerical study verifies the EMA analytic predictions when the scales are well-separated. Our numerical study compares two approaches for calculating effective permittivity by explicit calculations of local average fields and energy as geometry, phase permittivity contrast, and inclusion content are varied. We study the conditions under which these approaches give a reliable estimate of permittivity by comparing with 2D/3D EMA analytical models and duality relation. By considering 2D checkerboards which consist of a multitude of contiguous $N \times N$ square cells, the influence of the internal length scale (i.e., N) on permittivity is discussed. *Published by AIP Publishing.*

[<http://dx.doi.org/10.1063/1.4985799>]

I. INTRODUCTION AND MOTIVATION

There is currently a significant push to explore the challenging problem of modelling the dielectric properties of disordered heterostructures for which the microscopic translational symmetry is broken. For recent progress in this direction, see Refs. 1–3. The effective medium approximation (EMA) at its heart is a statistical concept and is one of the overarching questions guiding the field of contemporary heterostructures physics.^{1–3} Generically, within the EMA, one can replace the heterogeneous system by a fictitious medium with uniform permittivity to understand the collective, low-frequency dielectric properties. Rooted in the pioneering work by Bruggeman⁴ in the 1930s, EMA is being tested ever more precisely by numerical simulation and experiments, even while conceptual questions remain, e.g., the interplay between disorder scale and interactions. In the case of multiphase heterostructures, the implementation of EMA requires that the typical size of heterogeneity is much smaller than the free space wavelength of the electromagnetic wave λ ($\ell \ll L \ll \lambda$, where ℓ and L are the transport mean free path and the thickness of the medium, respectively).

In many situations, it is desirable to have a precise and definite meaning for the “effective complex permittivity” $\varepsilon = \varepsilon_0(\varepsilon' + \varepsilon''i)$ of heterostructures, with ε_0 being the permittivity of vacuum. The imaginary part is often referred to as the dielectric loss factor. In discussing the dielectric properties of heterostructures, we note that there have essentially been two distinct approaches to define the effective

permittivity ε of a composite material.^{2,3,5} One approach is a field statistical one, and a variety of techniques have been devised in order to get ε as the average over the statistical variations of the material. On the other hand, an alternate approach to the problem is based on an energy viewpoint. The former is based on the first-order statistics of the electric field, while the latter is a second-order energy representation of the electric field. We have several motivations for considering this problem. First, the use of solely one of the two definitions given above does not guarantee an unambiguous determination of ε . Second, a few explicit studies investigated the equivalence between both definitions. Third, investigating ε and the local field concentration in multifunctional composite architectures is attracting considerable attention for many important technological implications owing to the drastic downscaling of devices.⁶

Ever-growing numerical simulations, e.g., finite element, have provided a comprehensive framework to describe ε .^{1–3,5,7,12} A recent example of such accurate effective models is how permittivity of randomised scalable checkerboard geometries varies with randomization of phases and scaling.⁷ In this paper, a comparison is made between the results of ε calculations of Ref. 7 dealing with real-valued phase permittivity and the current ones considering complex numbers describing lossy materials. However, attempts to reliably extract and understand the electric response of composite materials have been hindered by large systematic uncertainties of the phase permittivities and a detailed knowledge of their structures.¹³ Another source of difficulty is the limitation of many numerical techniques to relatively small systems. We improved our ε calculation algorithm by imposing

^{a)}Electronic mail: brosseau@univ-brest.fr

that each realization chosen out of the whole ensemble of all possible realizations is used only once in the statistics of ε . Consequently, the interpretation of their randomness and disorder signatures is often difficult and sometimes controversial. With these comments as motivation, we turn to assess if the EMA-based analysis of low-order statistics of permittivity and electric field gives the same quantitative results. Key questions at the intersection of computational physics and materials science are still to be resolved. How do the geometry and topology characteristics influence the two ways for evaluating ε ? What are the bounds of the electric field averages and how they depend on the symmetry of heterostructures? In order to tackle these essential issues, we consider simple possible (genuinely realizable) models of two-phase heterostructures, i.e., checkerboards, planar multilayers, and disk or sphere dispersions, which yet remain rich enough to exhibit a wide range of dielectric properties.^{2,3} Our numerical study verifies well the EMA analytic predictions for the effective permittivity and field statistics of these specific examples. Many models based on different approaches have been proposed to account for the evaluation of the field averages in heterostructures, e.g., Refs. 2, 8, and 14–16. The reader is encouraged to read these references to get a more complete understanding of this subject. Previous calculations of ε in two-phase heterostructures have reported different variations of ε as a function of volume fraction, inclusion shape, and arrangement. The main focus of this study is on the systematic comparison of ε obtained by different approaches, i.e., second-order ensemble average and first-order volume average using the finite element method. Precise knowledge of ε is important in understanding the relaxation processes, i.e., polarization and conduction, of heterostructures. The data are presented in tabular form, in hope that they can be useful to those interested in clarifying the use of low-order statistics equations for determining the effective complex permittivity of heterostructures.

We now proceed to outline the methodology required to characterize the statistics of permittivity and electric field. Before delving into the details, in Sec. II we briefly make some general remarks about the low-order statistics of ε which are relevant to our purpose. In Sec. III, we describe some basic features of the fluctuations of the electric field. Technical details on the calculation of ε are summarized in Sec. IV. In Sec. V, we discuss in detail, aided by illustrative simulations, a few different models demonstrating our claims. We conclude the paper in Sec. VI and discuss possible avenues for extension of this study.

II. LOW-ORDER STATISTICS OF THE EFFECTIVE PERMITTIVITY

Here, we recap previous work in statistical properties of heterostructures by introducing a formalism to calculate the effective permittivity and characterize its fluctuations. Within the usual mean-field approach^{2,3,14,15} defining the low-order statistics of the effective permittivity, we note that

$$\bar{\bar{\varepsilon}} \approx \bar{\varepsilon} - \text{var}(\varepsilon)/3\bar{\varepsilon}. \quad (1)$$

The first term of the right hand side of Eq. (1) is the average value of ε , while the second term is related to deviations of ε from its mean. The relative magnitudes of the terms can be assessed only if some specific assumptions are made regarding the statistics of ε . One observes that Eq. (1) does not involve shapes of particles and may be applied to a dispersion of any shaped and randomly oriented particles. As an example of the use of this formula and for later purpose, the interested reader might now ask, how the first- and second-order moments of ε can be calculated? We first consider the case of a “black-and-white” checkerboard^{2,3,7} composed of two isotropic phases for which $\varepsilon = \varepsilon_1$ with probability p and $\varepsilon = \varepsilon_2$ with probability $1-p$. In this case, $\bar{\varepsilon} = \varepsilon_1(p + (1-p)r)$ and $\text{var}(\varepsilon) = p(1-p)\varepsilon_1^2(1-r)^2$, where $r = \varepsilon_2/\varepsilon_1$. Under the assumption of ergodicity, i.e., $p = \phi_2$ in the limit of infinitely large volume, the effective permittivity can be expressed as

$$\bar{\bar{\varepsilon}} = (\phi_2 + (1 - \phi_2)r) - \frac{\phi_2(1 - \phi_2)(1 - r)^2}{3(\phi_2 + (1 - \phi_2)r)}, \quad (2)$$

where the order parameter which characterizes the coplanar ordering is the surface fraction ϕ_2 of phase 2. Certain limiting forms for the effective permittivity can be found when the constituent fluctuations of the checkerboard have a large variance, e.g., when r is large. These limiting forms can provide useful approximations when the conditions for their validity are met. Another simple example deals with the series law.^{2,3} In that case, $\bar{\varepsilon} = \varepsilon_1\phi_1 + \varepsilon_2\phi_2 = \varepsilon_1 + (\varepsilon_2 - \varepsilon_1)\phi_2$ and the variance is $\text{var}(\varepsilon) = (\varepsilon_2 - \varepsilon_1)^2\phi_2(1 - \phi_2)$, so that according to Eq. (1) the effective permittivity is

$$\bar{\bar{\varepsilon}} = \varepsilon_1 - \frac{(r - 1)^2\phi_2(1 - \phi_2)}{3(1 + (r - 1)\phi_2)^2}. \quad (3)$$

The fact that average permittivities of composite particulate materials may be accompanied by appreciable standard deviations has been recognized by many authors,^{7–11} to which the reader is referred for detailed discussion of this question. To be specific, these authors calculated the average and standard deviation of the permittivity of an ensemble of many realizations corresponding to planar multilayers⁹ and 2D two-color checkerboards^{2,3,7} for which a rigorous theory exists.

III. FIELD STATISTICAL ANALYSIS

As described in much detail in Refs. 1–5, the idea of effective medium for describing the dielectric properties of heterostructures was put on a firm mathematical foundation by Bruggeman. This work has inspired a large amount of studies about implications and predictions.¹ One result from these early papers is that ε satisfies

$$\langle \varepsilon(\mathbf{R})\mathbf{E}_n(\mathbf{R}) \rangle = \varepsilon_n \langle \mathbf{E}_n(\mathbf{R}) \rangle, \quad (4)$$

which relates the spatial average of the electric displacement field $\langle \mathbf{D} \rangle$ to the spatial average of the electric field $\langle \mathbf{E} \rangle$, with \mathbf{R} being the notation for a given point in space and \mathbf{n} being a unit vector parallel to the direction of the applied electric field. In the ensuing discussion, we will omit the running

projection subscript n on fields. This decoupling has another important feature: it does not depend on the internal length scales, i.e., we can replace the heterostructure that has rapid oscillations in its permittivity by an effective material with a slowly varying effective permittivity without changing the local averages of the electric fields.

Two generic implications are that (i) the composite contains subwavelength components but with a sufficiently large scale so that in each component the behavior of the material is controlled by macroscopic constitutive equations and (ii) the random composite material is assumed to be statistically homogeneous. Further simplification can be accomplished by adopting an ergodic assumption, i.e., the ensemble averages can be

replaced with the spacial averages. Unfortunately, this straightforward definition often leads to complications because Eq. (4) does not lead to an efficient way to find ϵ because the problem of determining global physical quantities of interest consistent with the local data is known to be computationally hard. An examination of Eq. (4) shows that it requires that we know the microgeometry of the composite, a task not easy to carry out. Another drawback with this approach is that ϵ depends not only on the microstructure but also on the permittivity contrast $r = \epsilon_2/\epsilon_1$. If r is changed, all calculations need to be repeated.

Consider again the two-(isotropic) phase composite materials shown in Figs. 1 and 2. The spatial average fields in each phase are $\langle E \rangle_1 = V_1^{-1} \int_{V_1} E(\mathbf{R}) d\tau$ and $\langle E \rangle_2 = V_2^{-1}$

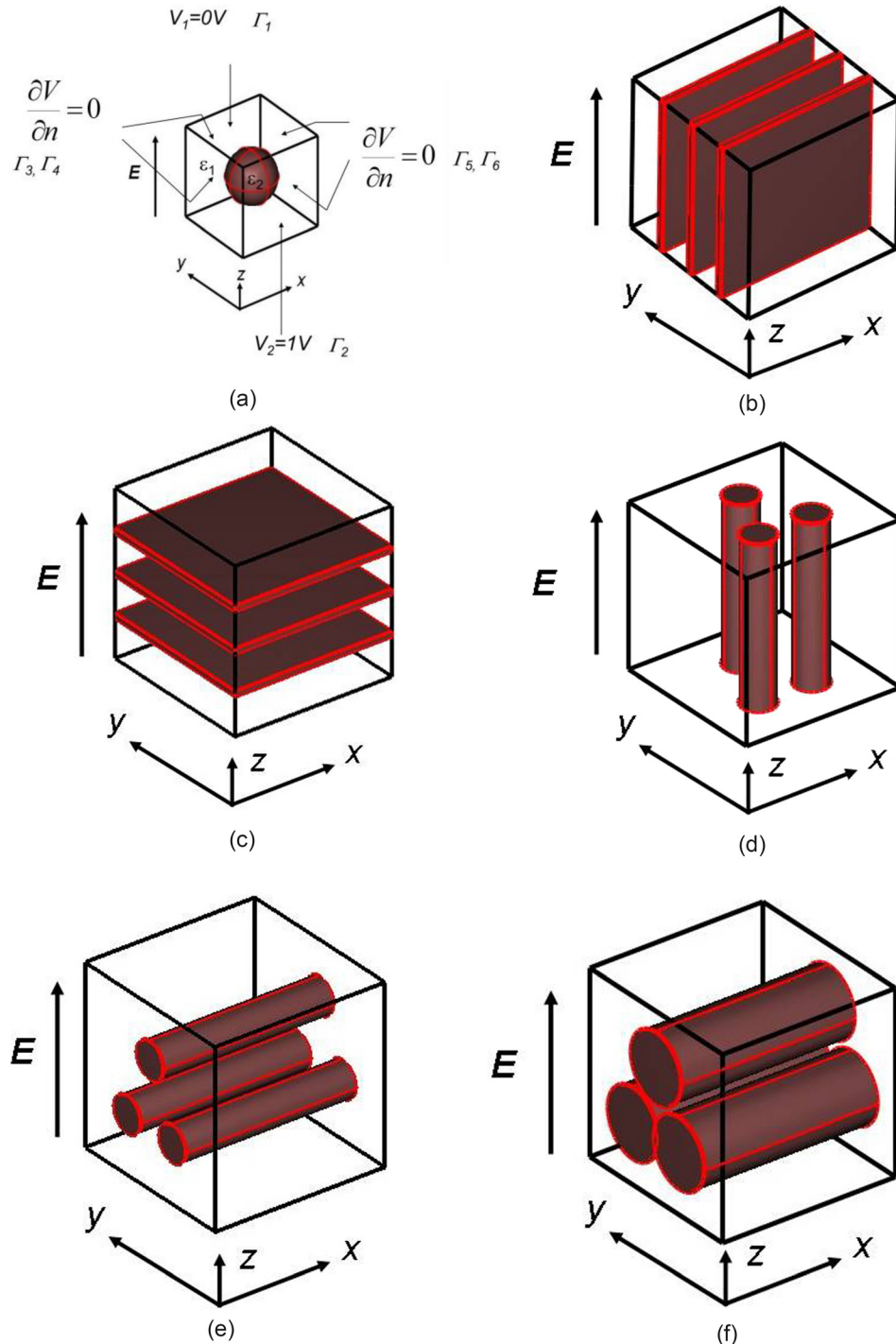
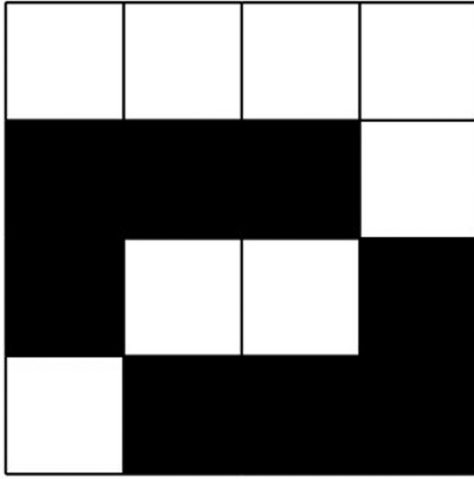
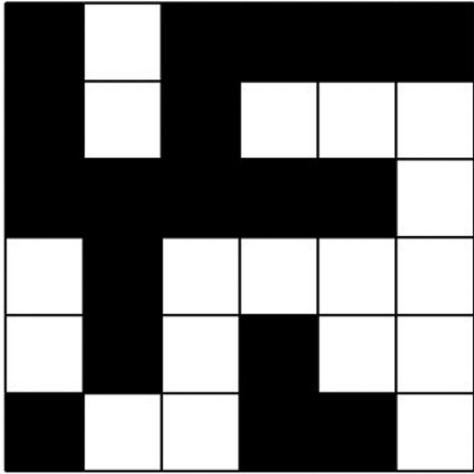


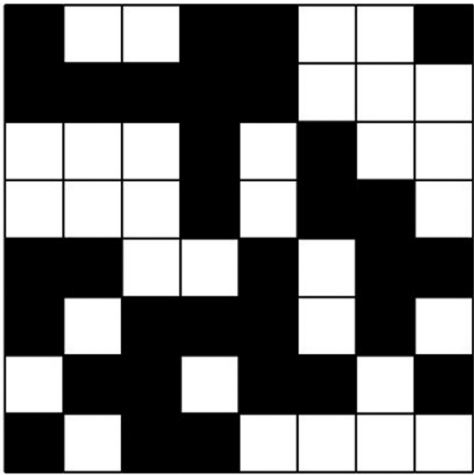
FIG. 1. Deterministic two-phase heterostructures considered in this study: (a) single sphere (i.e., isotropic phase 1: scalar permittivity ϵ_1 , red area) embedded in the other (i.e., isotropic phase 2: scalar permittivity ϵ_2 , white area); (b) laminate material; Let us consider a semi-infinite medium composed of infinite slabs (along the y direction) with randomly chosen thicknesses. We assume that the composite medium is fabricated by alternately placing one type slab (i.e., isotropic phase 1: scalar permittivity ϵ_1 , red area) upon the other (i.e., isotropic phase 2: scalar permittivity ϵ_2 , white area); (c) differs by the orientation of the stratification axis with respect to the applied electric field. One immediately sees that the two cases correspond to condensers in series and parallel; (d) three cylinders with axis oriented in the direction of the applied electric field; (e) (e) differs from (d) by the orientation of the cylinder axis with respect to the applied electric field; (f) as in (e) but filling fraction is increased by increasing the radius such that two of the cylinders overlap.



(a)



(b)



(c)

FIG. 2. (a) 2D representation of a two-color 2D checkerboard ($N=4$) with phase 1 (host matrix) in white color and phase 2 (inclusion) in black color. Our algorithm allows us to create M realizations for each structure. To generate randomized colored checkerboards, a program was written in MATLAB[®], (b) as in (a) for $N=6$, (c) as in (a) for $N=8$.

$\int_{V_2} \mathbf{E}(\mathbf{R}) d\tau$, respectively. From the linearity of expectation, $\langle \mathbf{E} \rangle$ is given exactly by $\langle \mathbf{E} \rangle = (1 - \phi_2) \langle \mathbf{E} \rangle_1 + \phi_2 \langle \mathbf{E} \rangle_2$ and Eq. (4) reads

$$\varepsilon \langle \mathbf{E} \rangle = (1 - \phi_2) \varepsilon_1 \langle \mathbf{E} \rangle_1 + \phi_2 \varepsilon_2 \langle \mathbf{E} \rangle_2. \quad (5)$$

Using these expressions, we find $\frac{\langle \mathbf{E} \rangle_2}{\langle \mathbf{E} \rangle} = \frac{1}{\phi_2} \left(\frac{\varepsilon/\varepsilon_1 - 1}{r-1} \right)$. Perhaps the most straightforward examples of two-phase composite materials are the stratified mixtures [Figs. 1(b) and 1(c)]. When the field is perpendicular to all interfaces of the composite, $\langle \mathbf{E} \rangle = r \left(\frac{1-\phi_2}{\phi_2} \right) \langle \mathbf{E} \rangle_2$, and when it is perpendicular to none, we get $\langle \mathbf{E} \rangle = \langle \mathbf{E} \rangle_2$.

A handful of papers have proposed ε definition via the energy stored in the dielectric of a parallel plate capacitor, e.g., Ref. 16. This energy representation approach purportedly allows ε to be determined as

$$\langle \varepsilon(\mathbf{R}) |\mathbf{E}(\mathbf{R})|^2 \rangle = \varepsilon \langle |\mathbf{E}(\mathbf{R})|^2 \rangle. \quad (6)$$

From Eq. (6), we see that ε is obtained regardless of the electric vector field direction. The question of whether Eq. (6) is determining the same value of ε as that calculated from Eq. (4) is of great practical importance.

For a two-phase system, Eq. (6) takes the form

$$\varepsilon \langle |\mathbf{E}|^2 \rangle = \phi_2 \varepsilon_2 \langle |\mathbf{E}|^2 \rangle_2 + (1 - \phi_2) \varepsilon_1 \langle |\mathbf{E}|^2 \rangle_1. \quad (7)$$

Using general arguments, a recent study¹⁷ has suggested that $|\langle \mathbf{E} \rangle_2|^2 / \langle |\mathbf{E}|^2 \rangle_2 \leq 1$ by making use of Schwarz's inequality. Additionally, these authors found that the spatially averaged electric field should satisfy

$$\alpha_p = |\langle \mathbf{E} \rangle_2|^2 / \langle |\mathbf{E}|^2 \rangle_2, \quad (8a)$$

or, analytically

$$\alpha_p = \frac{1}{\phi_2} \left| \frac{\frac{\varepsilon}{\varepsilon_1} - 1}{\frac{\varepsilon_2}{\varepsilon_1} - 1} \right|^2 \left(\frac{\varepsilon_2'' - \frac{\varepsilon_1'' \varepsilon_2'}{\varepsilon_1'}}{\varepsilon_1'' - \frac{\varepsilon_1'' \varepsilon_2'}{\varepsilon_1'}} \right). \quad (8b)$$

We now have some ammunition to tackle the questions we raised in Sec. I. We will restrict our attention to the EMA of the dielectric response, i.e., the electric field being curl-free, it must satisfy $\nabla \cdot [\varepsilon(\mathbf{R}) \mathbf{E}] = 0$.

IV. TECHNICAL DETAILS

Here, we review a few basic technical details about the simulations. The assumptions behind the results we present here are that (i) two isotropic phases are present and (ii) perfect contact between the two phases is assumed so the electric potential and normal component of the displacement vector are continuous across the two-phase interface. The present day workhorse for *ab initio* modelling and prediction of dielectric heterostructures, finite element method, is particularly efficient and computationally inexpensive.³ Here, electrical modeling is carried out using the commercially available 2D and 3D finite element modeling software COMSOL[®] 3.4 Multiphysics package (COMSOL, Inc.).¹⁹ Our procedure for calculating ε is the following when a constant, static, external electric field is applied. The effective permittivity along the direction corresponding to the applied field [e.g., z direction in Fig. 1(a), 3D case] is found by integration via either

$$\varepsilon_z = \frac{\iiint_V \varepsilon_k(x, y, z) \partial_z V dx dy dz}{\iiint_V \partial_z V dx dy dz}, \quad (9)$$

or

$$\varepsilon = \frac{\iiint_V \varepsilon_k(x, y, z) [(\partial_x V)^2 + (\partial_y V)^2 + (\partial_z V)^2] dx dy dz}{\iiint_V [(\partial_x V)^2 + (\partial_y V)^2 + (\partial_z V)^2] dx dy dz}, \quad (10)$$

where $k = 1, 2$, and V is the electric potential. The effective permittivity ε was calculated by considering as a model system a cubic cell of size L [Fig. 1(a)] with boundary conditions by imposing $V = V_2 = 1V$ on Γ_2 , $V = V_1 = 0V$ on Γ_1 , and $\partial_n V = 0$ on $\Gamma_3, \Gamma_4, \Gamma_5$, and Γ_6 . Corresponding equations for the 2D case are obtained by changing V in S which is the surface of the unit cell perpendicular to the applied field. The finite element method is employed for the discretization of the aforementioned equation and was carried out in static condition with the DC module of COMSOL using a personal computer with a Pentium IV processor (3 GHz).

Triangular meshes were used. We triple-checked our calculations by making use of different mesh densities [standard (type1), finer (type2), and dense (type3) at corner points]. Each tile was submeshed. For example, the 4×4 checkerboard has a total of 722 triangular elements for type1 (44 per tile), 2888 for type2, and 3136 for type3. For 12×12 checkerboards, the numbers are 2016 for type1 (14 per tile), 8064 for type2, and 11232 for type3. Type3 is a variable mesh as it gets dense at the corners. Typical min and max element edge lengths can be estimated from the numbers given above. We did not differentiate in meshing the background and inclusions separately. Even for the higher permittivities tested, the cross check with the three types of meshes used gave small differences in the results affecting only the third or fourth decimal places.

V. COMPUTATIONAL RESULTS

With this in mind, we are now ready to analyze (experimentally realizable) 2D and 3D two-phase heterostructures. In our study, we consider the various static systems shown in Figs. 1 and 2. We start by addressing the question of permittivity statistics in two-color checkerboards which provide an intuitive picture for much of the fascinating physics that occurs in random heterostructures.

A. Random heterostructures

A specific example is the two-color 2D checkerboard structure illustrated in Fig. 2 which consists of a multitude of contiguous $N \times N$ square cells, with randomly and independently chosen intrinsic permittivity for each cell. Our algorithm uses a specific test to ensure that his permittivity assignment is not repeated in subsequent realizations. Each realization of the checkerboard structure may be regarded as

being infinite in extent, but to ensure a model that is at least wide-sense stationary over space, the location of each phase is taken to be random, with a uniform distribution of probability over an $N \times N$ square. We attribute to each elementary square cell either the white (phase 1, host matrix) or the black color (phase 2, inclusion). For given ϕ_2 , there is a set of combinatorial structures ($\Xi = 2^{N^2}$) corresponding to the allowable realizations for this 2-color encoding. For $\phi_2 = 0.5$, the grid can be tiled $\binom{N^2}{N^2/2} = \Omega$ ways. Exploring the statistical behavior of checkerboards for $N \geq 4$ is hindered by the large computational cost. As such, our procedure only tests a conspicuously small subset of the prodigious number of possible realizations of square $N \times N$ random checkerboards. Using an iterative algorithm,⁷ previous simulations have suggested that an accurate approximate EMA representation of ε can be obtained by considering M realizations of disorder at different permittivity ratios r . We first point out an important general observation with regard to the convergence of our results. For all surface fractions and N considered, M can be as low as 10 for low permittivity contrast but it can be of the order of 1000 for high permittivity contrast to get a very good approximation of ε , consistent with previous work.⁷ The subset selectivity is made randomly and we check carefully that the results of our numerical simulations are independent of this choice. Thus, our algorithm requires only modest computing resources. No algorithm has so far managed to probe the statistical properties of random checkerboards, due to the impossibility of dealing with the tremendous number of possible realizations when N is large and ϕ_2 takes an arbitrary value.¹⁸ One important aspect of the ongoing simulations is that $\phi_2 = 0.50$ corresponding to the half-filling statistically isotropic case. In that case, ε is invariant under rotation and Keller-Dykhne duality relation states that the effective permittivity of the checkerboard array of squares is equal to the geometric mean of those of the two phases, i.e., $\varepsilon = \sqrt{\varepsilon_1 \varepsilon_2}$. Differently from Ref. 7, we consider inclusion permittivity characterized by complex numbers.

A summary of the calculated ε and α_p values is provided in Tables I–VII. In practice, the performance of our numerical scheme is good as shown by exact numerical simulations. A consistency check is making sure that for $\phi_2 = 0.5$, the ensemble average over M random realizations $\bar{\varepsilon} = M^{-1} \sum_{i=1}^M \varepsilon_i$ gives the exact value. This result follows from the fact that in the EMA, a disordered but on average isotropic structure has its effective permittivity satisfying the duality transformation. References 2, 3, and 7 provide support for this conclusion. Therefore, robust ε values can be obtained by our method. For $\varepsilon_1 = 1$ and $\varepsilon_2 = 3 + i$ ($N = 4$, Table I), ($N = 6$, Table IV), and [$N = 8$, Table VII(a)], there is good agreement between the numerical estimate of ε obtained from Eq. (9) and its analytical exact value. We find that calculations of ε obtained from Eq. (6) are significantly different from their exact value (up to $\pm 15\%$) as shown in Fig. 3 and thus are not shown in the tables. We believe that this error arises because of an error of $2\% - 4\%$ in calculation of electric field norm due to the boundary conditions on the transverse sides which force the x components of the electric field to zero. For a high permittivity contrast

TABLE I. First principles effective permittivity calculations for the two-color 2D checkerboard ($N=4$) with $\varepsilon_1=1$ [white (phase 1, host matrix)] and $\varepsilon_2=3+i$ [black color (phase 2, inclusion)]. Calculation of ε is performed by using Eq. (8a). The content (surface fraction) of the black phase is $\phi_2=0.5$. The exact value predicted from the Keller-Dykhne duality relation is $\varepsilon = \sqrt{3+i}=1.7553+0.2848i$. M is the number of random realizations considered for the statistical average $\bar{\varepsilon} = M^{-1} \sum_{i=1}^M \varepsilon_i$ and variance $\text{var}(\varepsilon) = M^{-1} \sum_{i=1}^M (\varepsilon_i - \bar{\varepsilon})^2$. The coefficient $\bar{\alpha}_p$ is computed via statistical average over the number M of realizations and is compared to the value defined by Eq. (9). Note that $\bar{\alpha}_p = M^{-1} \sum_{i=1}^M \alpha_{pi}$ and $\bar{\alpha}_p \cong 0.9151$ are obtained from Eq. (8b).

M	$\bar{\varepsilon}$	$\bar{\bar{\varepsilon}}$	$\bar{\alpha}_p$
10	1.7670 + 0.2948i	1.7655 + 0.2876i	0.9354
50	1.7552 + 0.2882i	1.7542 + 0.2832i	0.9250
100	1.7519 + 0.2831i	1.7513 + 0.2797i	0.9271
1000	1.7553 + 0.2873i	1.7545 + 0.2834i	0.9247
12870	1.7565 + 0.2883i	1.7557 + 0.2844i	0.9249

structure, this error is expected. But since the displacement field method uses only the y-components, this error is avoided. Significant errors may arise due to the topological defects imposed by heterogeneous boundary conditions, i.e., corner points, affecting the effective properties depending on the permittivity ratio between the phases.⁷ In the following, we will restrict our ε data comparison between the ensemble averages for Eq. (4) and the results of Eq. (1) using average using the finite element method.

Tables II, III, V, VI, and VII illustrate the situation considered for cases different than the special half filling case. The most conspicuous feature of these tables is the close similarity between the values of ε and α_p obtained by the two approaches. We also performed a series of phase exchange (duality) simulations since if the material is macroscopically isotropic, then the Keller-Dykhne duality relation takes the

TABLE II. (a) As in Table I for $\varepsilon_1=1$ and $\varepsilon_2=3+i$, with $\phi_2=3/16=0.1875$; (b) As in (a) for $\phi_2=13/16=0.8125$; (c) Compare with the value $\varepsilon(\varepsilon_1, \varepsilon_2)\varepsilon(\varepsilon_2, \varepsilon_1)$ obtained from the Keller-Dykhne duality relation of $\varepsilon(\varepsilon_1, \varepsilon_2)\varepsilon(\varepsilon_2, \varepsilon_1) = \varepsilon_1\varepsilon_2 = 3+i$. Note that $\bar{\alpha}_p = M^{-1} \sum_{i=1}^M \alpha_{pi}$ and $\bar{\alpha}_p$ are obtained from Eq. (8b).

(a)				
M	$\bar{\varepsilon}$	$\bar{\bar{\varepsilon}}$	$\bar{\alpha}_p$	$\bar{\bar{\alpha}}_p$
10	1.2211 + 0.0598i	1.2209 + 0.0588i	0.9510	0.9508
50	1.2319 + 0.0661i	1.2317 + 0.0648i	0.9579	0.9578
560	1.2300 + 0.0650i	1.2298 + 0.0636i	0.9582	0.9581
(b)				
M	$\bar{\varepsilon}$	$\bar{\bar{\varepsilon}}$	$\bar{\alpha}_p$	$\bar{\bar{\alpha}}_p$
10	2.4692 + 0.6789i	2.4689 + 0.6779i	0.9521	0.9521
50	2.4746 + 0.6835i	2.4742 + 0.6823i	0.9546	0.9545
560	2.4763 + 0.6855i	2.4760 + 0.6845i	0.9541	0.9541
(c)				
M	$\bar{\varepsilon}_{(a)}\bar{\varepsilon}_{(b)}$			
10	2.9745 + 0.9767i			
50	3.0033 + 1.0058i			
560	3.0013 + 1.0040i			

TABLE III. (a) As in Table II (a) for $\varepsilon_1=1$ and $\varepsilon_2=30+i$ with $\phi_2=3/16=0.1875$; (b) As in (a) for $\phi_2=13/16=0.8125$; (c) As in Table II (c): in this case $\varepsilon(\varepsilon_1, \varepsilon_2)\varepsilon(\varepsilon_2, \varepsilon_1) = \varepsilon_1\varepsilon_2 = 30+i$.

(a)				
M	$\bar{\varepsilon}$	$\bar{\bar{\varepsilon}}$	$\bar{\alpha}_p$	$\bar{\bar{\alpha}}_p$
10	1.5335 + 0.0030i	1.5276 + 0.0022i	0.7807	0.7693
50	1.5967 + 0.0035i	1.5888 + 0.0028i	0.7905	0.7803
560	1.5896 + 0.0036i	1.5805 + 0.0026i	0.7905	0.7797
(b)				
M	$\bar{\varepsilon}$	$\bar{\bar{\varepsilon}}$	$\bar{\alpha}_p$	$\bar{\bar{\alpha}}_p$
10	19.3114 + 0.6148i	19.2523 + 0.6121i	0.8050	0.8031
50	19.4828 + 0.6211i	19.3979 + 0.6171i	0.8133	0.8108
560	19.5715 + 0.6245i	19.5060 + 0.6214i	0.8154	0.8133
(c)				
M	$\bar{\varepsilon}_{(a)}\bar{\varepsilon}_{(b)}$			
10	29.6124 + 0.9999i			
50	31.1065 + 1.0607i			
560	31.1086 + 1.0632i			

TABLE IV. As in Table I for the case $N=6$ with $\varepsilon_1=1$ and $\varepsilon_2=3+i$, $\phi_2=0.5$. The exact value predicted by the Keller-Dykhne duality relation is again $\varepsilon = \sqrt{3+i}=1.7553+0.2848i$. Note that $\bar{\alpha}_p = M^{-1} \sum_{i=1}^M \alpha_{pi}$ and $\bar{\alpha}_p \cong 0.9151$ are obtained from Eq. (8b).

M	$\bar{\varepsilon}$	$\bar{\bar{\varepsilon}}$	$\bar{\alpha}_p$
10	1.7414 + 0.2784i	1.7411 + 0.2773i	0.9056
50	1.7533 + 0.2857i	1.7529 + 0.2839i	0.9164
1000	1.7576 + 0.2887i	1.7573 + 0.2873i	0.9198
10000	1.7572 + 0.2882i	1.7569 + 0.2867i	0.9173

TABLE V. (a) As in Table IV (a) for $\varepsilon_1=1$ and $\varepsilon_2=3+i$ with $\phi_2=7/36=0.1944$; (b) As in (a) for $\phi_2=29/36=0.8056$; (c) As in Table II (c): in this case $\varepsilon(\varepsilon_1, \varepsilon_2)\varepsilon(\varepsilon_2, \varepsilon_1) = \varepsilon_1\varepsilon_2 = 3+i$. Note that $\bar{\alpha}_p = M^{-1} \sum_{i=1}^M \alpha_{pi}$ and $\bar{\alpha}_p$ are obtained from Eq. (8b).

(a)				
M	$\bar{\varepsilon}$	$\bar{\bar{\varepsilon}}$	$\bar{\alpha}_p$	$\bar{\bar{\alpha}}_p$
10	1.2357 + 0.0661i	1.2356 + 0.0658i	0.9379	0.9378
50	1.2441 + 0.0791i	1.2440 + 0.0713i	0.9347	0.9346
1000	1.2418 + 0.0701i	1.2417 + 0.0694i	0.9398	0.9397
(b)				
M	$\bar{\varepsilon}$	$\bar{\bar{\varepsilon}}$	$\bar{\alpha}_p$	$\bar{\bar{\alpha}}_p$
10	2.4618 + 0.6771i	2.4616 + 0.6765i	0.9532	0.9532
50	2.4485 + 0.6650i	2.4483 + 0.6646i	0.9498	0.9498
1000	2.4573 + 0.6726i	2.4571 + 0.6722i	0.9523	0.9523
(c)				
M	$\bar{\varepsilon}_{(a)}\bar{\varepsilon}_{(b)}$			
10	2.9972 + 0.9995i			
50	2.9984 + 1.0032i			
1000	3.0043 + 1.0076i			

TABLE VI. (a) As in Table V (a) for $\varepsilon_1 = 1$ and $\varepsilon_2 = 30 + i$ with $\phi_2 = 7/36 = 0.1944$; (b) As in (a) for $\phi_2 = 29/36 = 0.8056$; (c) As in Table II (c): in this case $\varepsilon(\varepsilon_1, \varepsilon_2)\varepsilon(\varepsilon_2, \varepsilon_1) = \varepsilon_1\varepsilon_2 = 30 + i$. Note that $\bar{\alpha}_p = M^{-1} \sum_{i=1}^M \alpha_{pi}$ and $\bar{\bar{\alpha}}_p$ are obtained from Eq. (8b).

(a)				
M	$\bar{\varepsilon}$	$\bar{\bar{\varepsilon}}$	$\bar{\alpha}_p$	$\bar{\bar{\alpha}}_p$
10	1.6174 + 0.0041i	1.6155 + 0.0039i	0.6282	0.6174
50	1.7047 + 0.0057i	1.6991 + 0.0050i	0.6300	0.6198
1000	1.6744 + 0.0052i	1.6659 + 0.0035i	0.6714	0.6612
(b)				
M	$\bar{\varepsilon}$	$\bar{\bar{\varepsilon}}$	$\bar{\alpha}_p$	$\bar{\bar{\alpha}}_p$
10	19.1705 + 0.6082i	19.1150 + 0.6052i	0.8060	0.8044
50	18.6817 + 0.5898i	18.6432 + 0.5878i	0.7864	0.7853
1000	18.9709 + 0.6006i	18.9305 + 0.5986i	0.7982	0.7970
(c)				
M	$\bar{\varepsilon}_{(a)}\bar{\varepsilon}_{(b)}$			
10	31.0037 + 1.0629i			
50	31.8435 + 1.1115i			
1000	31.7618 + 1.1041i			

form $\bar{\varepsilon}(\varepsilon_1, \varepsilon_2)\bar{\varepsilon}(\varepsilon_2, \varepsilon_1) = \varepsilon_1\varepsilon_2$. It is widely believed that this result is independent of the details of the morphology of the material.^{2,3,5} From Tables II, III, V, VI, and VII, we find that, in all cases ($N=4$, $\varepsilon_1 = 1$ and $\varepsilon_2 = 3 + i$; $N=4$, $\varepsilon_1 = 1$ and $\varepsilon_2 = 30 + i$; $N=6$, $\varepsilon_1 = 1$ and $\varepsilon_2 = 3 + i$; $N=6$, $\varepsilon_1 = 1$ and $\varepsilon_2 = 30 + i$; $N=8$, $\varepsilon_1 = 1$ and $\varepsilon_2 = 3 + i$), the ε dependence in the phase inversion follows the Keller-Dykhne duality relation. From these tables, we find that, in all cases, this result is obtained for both calculation approaches.

For isotropic two-phase mixtures, the field averages and the effective permittivity are related by $\langle E^2 \rangle_j / \langle E \rangle^2 = \phi_j^{-1} \partial_j \varepsilon$, where $\partial_j = \partial / \partial \varepsilon_j$. Hence, for the half filling case,⁷ we have

$$\langle E^2 \rangle_2 / \langle E \rangle^2 = r^{-1/2}. \quad (11)$$

This result provides us with an exact expression for the field averages. We emphasize that this prediction valid for arbitrary $N \times N$ random checkerboard is free from the rescaling procedure. Another quantity of interest to us is α_p which is defined in terms of field averages according Eq. (8a). Importantly, α_p and $\bar{\alpha}_p$ have a maximum value of 1 (within the numerical uncertainty). The calculated values for a wide range of cases (Tables I and IV) show that the results of our numerical simulations are close to the exact value, even for small values of M .

Further scrutiny of Tables I to VI leads to two additional observations. For cases different than the special half filling case, one can see that $\alpha_p \leq 1$ even when the ratio of the real part of the phase permittivity is large. Remarkably, we see that α_p is significantly reduced when phase inversion is case of a large contrast between real part of permittivity of the phases (Tables III and VI). Second, in Fig. 4 we show the evolution of the real and imaginary parts of ε with increasing N , i.e., decreasing the internal length scale of the stochastic inhomogeneities characterizing disorder and connectedness.

TABLE VII. (a) As in Table I for the case $N=8$ with $\varepsilon_1 = 1$ and $\varepsilon_2 = 3 + i$, $\phi_2 = 0.5$. The exact value predicted by the Keller-Dykhne duality relation is again $\varepsilon = \sqrt{3+i} = 1.7553 + 0.2848i$; (b) As in (a) for $\phi_2 = 13/64 = 0.2031$; (c) As in (a) for $\phi_2 = 51/64 = 0.7969$; As in Table II(c): in this case $\varepsilon(\varepsilon_1, \varepsilon_2)\varepsilon(\varepsilon_2, \varepsilon_1) = \varepsilon_1\varepsilon_2 = 3 + i$. Note that $\bar{\alpha}_p = M^{-1} \sum_{i=1}^M \alpha_{pi}$ and $\bar{\bar{\alpha}}_p \cong 0.9151$ are obtained from Eq. (8b).

(a)			
M	$\bar{\varepsilon}$	$\bar{\bar{\varepsilon}}$	$\bar{\alpha}_p$
10	1.7544 + 0.2849i	1.7542 + 0.2837i	0.9173
50	1.7559 + 0.2869i	1.7558 + 0.2861i	0.9151
1000	1.7575 + 0.2887i	1.7574 + 0.2880i	0.9138
10 000	1.7583 + 0.2895i	1.7581 + 0.2887i	0.9136
(b)			
M	$\bar{\varepsilon}$	$\bar{\bar{\varepsilon}}$	$\bar{\alpha}_p$
10	1.2552 + 0.0758i	1.2552 + 0.0753i	0.9263
50	1.2546 + 0.0747i	1.2545 + 0.0743i	0.9335
1000	1.2550 + 0.0751i	1.2549 + 0.0747i	0.9318
(c)			
M	$\bar{\varepsilon}$	$\bar{\bar{\varepsilon}}$	$\bar{\alpha}_p$
10	2.4289 + 0.6532i	2.4289 + 0.6529i	0.9494
50	2.4365 + 0.6607i	2.4364 + 0.6603i	0.9508
1000	2.4348 + 0.6593i	2.4347 + 0.6590i	0.9501
(d)			
M	$\bar{\varepsilon}_{(a)}\bar{\varepsilon}_{(b)}$		
10	2.9994 + 1.0040i		
50	3.0074 + 1.0109i		
1000	3.0061 + 1.0103i		

Furthermore, it is observed that the standard deviation for both ε' and ε'' leads also to a power law dependence, $\sigma \propto N^{-\beta}$ with $\beta \approx 1.1 \pm 0.1$. This indicates that the smaller the value of N , the higher the role of fluctuations that can be achieved in evaluating ε . Figure 3 shows the average value and variance of the real and imaginary parts of ε obtained from either Eq. (4) or Eq. (6) as a function of the number M of realization used to determine the moments. In accordance with our previous remark, 10^3 realizations seem to be a sufficient value to get reproducible and convergent permittivity data.

Another important feature is the electric field spatial distribution [Fig. 5(a)]. The field within each phase is controlled by the applied voltage gradient and by the polarization charges on the interfaces between the two phases. In Ref. 17, it was considered that $\alpha_p = 1$ holds only if the electric field in phase 2 does not vary spatially. We observe that this field spatial distribution and the nominal value obtained from Eq. (8b), i.e., $\bar{\bar{\alpha}}_p \cong 0.9151$, are consistent with this statement.

B. Further analysis: Deterministic heterostructures

We now proceed with a detailed analysis of the deterministic systems with different symmetries illustrated in Fig. 1. This time, our calculation method only requires one sweep over scale, and it is therefore computationally very efficient. The results from our 3D numerical simulations are shown in Tables VIII to X.

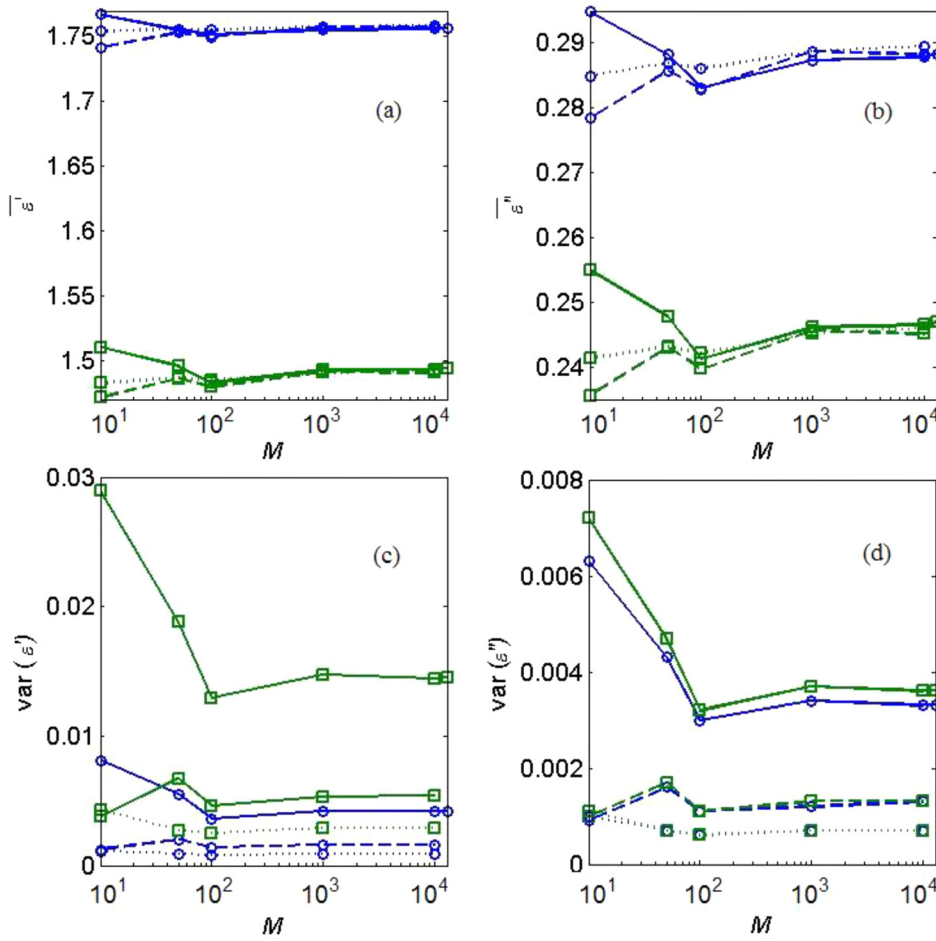


FIG. 3. (a) Comparison of the ensemble average of the real part of ϵ obtained from Eqs. (4) and (6) for checkerboards of size $N=4, 6$, and 8 . $\epsilon_1=1$ [white (phase 1, host matrix)] and $\epsilon_2=3+i$ [black color (phase 2, inclusion)], $\phi_2=0.5$. Symbols are for data obtained from Eq. (4) open blue circles and solid line ($N=4$), open blue circles and dashed line ($N=6$), and open blue circles and dotted line ($N=8$). For data obtained from Eq. (6), the blue circles are changed to green squares; (b) As in (a) for the imaginary part of ϵ ; (c) As in (a) for the variance of the real part of ϵ ; (d) As in (b) for the variance for the imaginary part of ϵ .

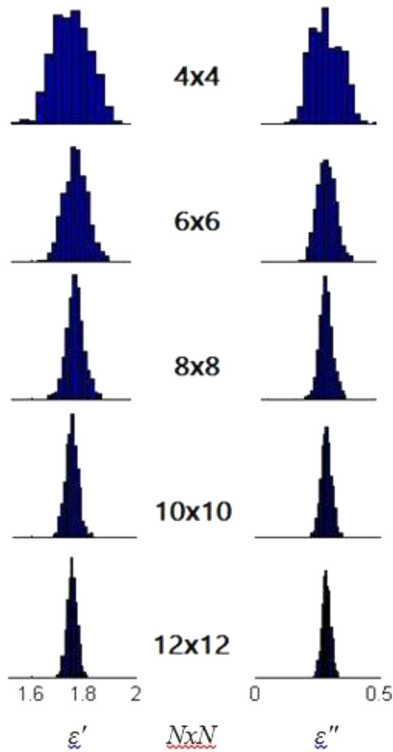


FIG. 4. (a) Histograms showing distributions of the real part of ϵ for 1000 randomly chosen realizations from a set of over 10000 trials with $\epsilon_1=1$ [white (phase 1, host matrix)] and $\epsilon_2=3+i$ [black color (phase 2, inclusion)], $\phi_2=0.5$ as a function of N ; (b) as in (a) for the imaginary part of ϵ .

Consider, first, the case of a single inclusion inside the matrix [Fig. 1(a)]. In that case, we can use the virial equation to evaluate ϵ . The calculations in this study have mostly $\phi_2=0.1$. Thus, to first order^{2,3,5,12}

$$\frac{\epsilon}{\epsilon_1} = 1 + 3\phi_2 \frac{r-1}{r+2} + O(\phi_2^2), \quad (12)$$

allows calculation of ϵ as a function of ϕ_2 and r . Simulation data collected in Tables VIII–X show no observable

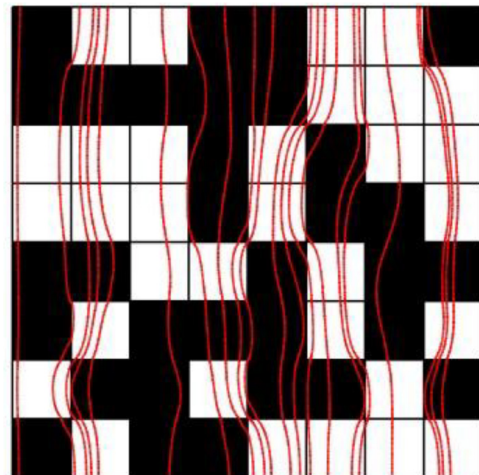


FIG. 5. Electric field line distribution in the realization of the 8×8 checkerboard shown in Fig. 2(c) with ϵ and α_p data corresponding to Table VII(a). $\epsilon_1=1$ and $\epsilon_2=3+i$.

TABLE VIII. First principles effective permittivity calculations for the 3D configurations shown in Fig. 1 with $\varepsilon_1 = 1$ [white (phase 1, host matrix)] and $\varepsilon_2 = 3 + i$ [red color (phase 2, inclusion)]. Two ways are considered for the calculation of ε , either by using Eqs. (4) and (8a). The content (volume fraction) of phase 2 is ϕ_2 .

Configuration ϕ_2	$\bar{\varepsilon}$	ε exact value	$\bar{\alpha}_p$ [Eq. (8a)]	α_p [Eq. (8b)]
Fig. 1(a) $\phi_2 = 0.1$	1.1320 + 0.0377i	Eq. (10) = 1.1320 + 0.0377i	0.9999	1
Fig. 1(b) $\phi_2 = 0.1$	1.1980 + 0.0990i	Eq. (11) = 1.2 + 0.1i	1	1
Fig. 1(c) $\phi_2 = 0.1$	1.0743 + 0.0114i	Eq. (12) = 1.0751 + 0.0116i	1	1
Fig. 1(d) $\phi_2 = 0.1$	1.2000 + 0.1000i	Eq. (11) = 1.2 + 0.1i	1	1
Fig. 1(e) $\phi_2 = 0.1$	1.1120 + 0.0266i		0.9954	
Fig. 1(f) $\phi_2 = 0.337$	1.4438 + 0.1299i		0.9778	

TABLE IX. As in Table VIII for $\varepsilon_1 = 1$ and $\varepsilon_2 = 30 + i$.

Configuration ϕ_2	$\bar{\varepsilon}$	ε exact value	α_p [Eq. (8a)]	α_p [Eq. (8b)]
Fig. 1(a) $\phi_2 = 0.1$	1.2991 + 0.0011i	Eq. (10) = 1.2987 + 0.0011i	0.9970	0.9645
Fig. 1(b) $\phi_2 = 0.1$	3.8710 + 0.0990i	Eq. (11) = 3.9 + 0.1i	1	1
Fig. 1(c) $\phi_2 = 0.1$	1.1058 + 0.0001i	Eq. (12) = 1.1069 + 0.0262i	0.9999	
Fig. 1(d) $\phi_2 = 0.1$	3.8994 + 0.1000i	Eq. (11) = 3.9 + 0.1i	1	1
Fig. 1(e) $\phi_2 = 0.1$	1.2099 + 0.0005i		0.9860	
Fig. 1(f) $\phi_2 = 0.337$	2.0618 + 0.0043i		0.9312	

differences between the values obtained from both equations. As seen from the first line of these tables, we match exactly the permittivity data and this is consistent with earlier computational studies.^{3,7,13} We have also obtained $\alpha_p \approx 1$ and close to the calculated value obtained from Eq. (8).

We now turn to the case of stratified mixtures composed of 3 slabs (along the z direction) of phase 2. The two diagrams differ by the orientation of the stratification axis with respect to the applied electric field, i.e., parallel (resp. perpendicular) to \mathbf{E} shown in Fig. 1(b) [resp. Fig. 1(c)]. If \mathbf{E} is parallel to all the dielectric interfaces of the composite [Fig. 1(b)], similar considerations lead to the conclusion that ε_{\parallel} is equal to the weighted average of the permittivity of the constituents

$$\frac{\varepsilon_{\parallel}}{\varepsilon_1} = 1 + \phi_2(r - 1). \quad (13)$$

It is simple to check explicitly that the permittivity ε_{\perp} of the composite material with the electric field along the z axis, i.e., perpendicular to the dielectric interfaces [Fig. 1(c)], takes the form

$$\frac{\varepsilon_{\perp}}{\varepsilon_1} = \frac{r}{\phi_2 + r(1 - \phi_2)}. \quad (14)$$

In this case, the field in each phase will be uniform but different. In Table IX, we give both the ε and α_p of each of the

case illustrated in Figs. 1(b) and 1(c). Most notable from Table IX is the good approximation obtained from Eq. (4) using finite element calculations. This is consistent with Ref. 17. Next, we examine to what extent symmetry and dimensionality can affect these results. Additionally, Table X illustrates good agreement between the results obtained for the 2D counterparts of 3D geometries shown in Fig. 1 with the corresponding analytical results.

VI. CONCLUSION AND POTENTIAL FUTURE DIRECTIONS

In conclusion, while the determination of the effective permittivity and electric field fluctuations in composite structures is an extensively studied subject, the present study reveals how nontrivial is the computation of the low-order statistics of electric fields of 2D and 3D two-phase random and deterministic structures in the absence of translational invariance. Although wave propagation in such materials is still experimentally and theoretically challenging, recent numerical advances make it more accessible. As stringent tests of our approach, we compare the theoretically predicted effective permittivity and field average with their numerically simulated counterparts for different 2D and 3D geometries, inclusion contents, and symmetries. Comprehensive evidence shows that Eq. (4) provides an efficient numerical

TABLE X. As in TABLE VIII for 2D configurations. $\varepsilon_1 = 1$ and $\varepsilon_2 = 3 + i$. In that case, the analytical exact value of ε is performed by using $\frac{\varepsilon}{\varepsilon_1} = 1 + 2\phi_2 \frac{r-1}{r+1-\phi_2(r-1)} + O(\phi_2^2)$.^{2,3,12,15}

Configuration ϕ_2	$\bar{\varepsilon}$	ε exact value	α_p [Eq. (8a)]	α_p [Eq. (8b)]
Fig. 1(a) $\phi_2 = 0.1$	1.1115 + 0.0262i	1.1114 + 0.0262i	1	1
Fig. 1(b) $\phi_2 = 0.1$	1.2000 + 0.1000i	Eq. (11) = 1.2 + 0.1i	1	1
Fig. 1(c) $\phi_2 = 0.1$	1.0752 + 0.0114i	Eq. (12) = 1.0751 + 0.0116i	1	1
Fig. 1(e) $\phi_2 = 0.1$	1.1119 + 0.0266i		0.9954	
Fig. 1(f) $\phi_2 = 0.337$	1.4437 + 0.1297i		0.979	

way to estimate ε over an extended range of material parameters.

What we can learn from the field of heterostructures can have far-reaching implications in many fields of science. There is a wide variety of directions for further research. Going one step further, it would be interesting to push our analysis further by considering multifunctional composite architectures, e.g., additional unique properties can emerge (such as magnetoelectricity) that are absent in intrinsic phases,⁶ and hierarchical composites with dielectric properties that are superior to those of the constituent materials, e.g., biocomposites.²⁰ Another natural next step is to investigate the dynamics of polarization in an electric field when the phase permittivities are frequency dependent in the gigahertz and terahertz ranges of frequency for which most applications of interest lie. We hope to return to some of these issues in the near future.

¹C. Brosseau, *J. Phys. D: Appl. Phys.* **39**, 1277 (2006).

²G. W. Milton, *The Theory of Composites* (Cambridge University Press, Cambridge, 2002).

³J.-Y. Li, C. Huang, and Q. Zhang, *Appl. Phys. Lett.* **84**, 3124 (2004); A. H. Sihvola, *Electromagnetic Mixing Formulas and Applications* (IEE Publishing, London, 1999); A. H. Sihvola, *IEEE Trans. Geosci. Remote Sens.* **27**, 403 (1989); A. H. Sihvola and I. V. Lindell, *J. Electromagn. Waves Appl.* **3**, 37 (1989); L. Jylhä and A. Sihvola, *IEEE Trans. Dielectr. Electr. Insul.* **13**, 760 (2006); M. Y. Koledintseva, S. K. Patil, R. W. Schwartz, W. Huebner, K. N. Rozanov, J. Shen, and J. Chen, *ibid.* **16**, 793 (2009); A. N. Lagarkov, S. M. Matytsin, K. N. Rozanov, and A. K. Sarychev, *J. Appl. Phys.* **84**, 3806 (1998); D. J. Bergman and D. Stroud, in *Solid State Physics, Advances in Research and Applications*, edited by H. Ehrenreich and D. Turnbull (Academic Press, New York, 1992), Vol. 46; D. Stroud and D. Bergman, *Phys. Rev. B* **25**, 2061 (1982).

⁴D. G. A. Bruggeman, *Ann. Phys. Lpz.* **24**, 636 (1935).

⁵M. Sahimi, *Heterogeneous Materials I: Linear Transport and Optical Properties* (Springer, New York, 2003).

⁶V. Castel and C. Brosseau, *Appl. Phys. Lett.* **92**, 233110 (2008).

⁷C. S. Olariu, S. Lasquellec, and C. Brosseau, *J. Appl. Phys.* **114**, 074104 (2013).

⁸V. Myroshnychenko and C. Brosseau, *Phys. Rev. E* **71**, 016701 (2005); V. Myroshnychenko and C. Brosseau, *J. Appl. Phys.* **97**, 044101 (2005); V. Myroshnychenko and C. Brosseau, *J. Phys. D: Appl. Phys.* **41**, 095401 (2008); V. Myroshnychenko and C. Brosseau, *J. Appl. Phys.* **103**, 084112 (2008); V. Myroshnychenko and C. Brosseau, *IEEE Trans. Dielectr.* **16**, 1209 (2009); V. Myroshnychenko and C. Brosseau, *Physica B* **405**, 3046 (2010).

⁹A. Mejdoubi and C. Brosseau, *Phys. Rev. E* **73**, 031405 (2006); **74**, 031405 (2006); *Phys. Rev. B* **74**, 165424 (2006); *J. Appl. Phys.* **99**, 063502 (2006); **100**, 094103 (2006); **101**, 084109 (2007).

¹⁰M. E. Mezeme, S. Lasquellec, and C. Brosseau, *Phys. Rev. E* **81**, 057602 (2010); **84**, 026612 (2011); M. E. Mezeme and C. Brosseau, *J. Appl. Phys.* **108**, 014701 (2010); M. E. Mezeme, S. Lasquellec, and C. Brosseau, *ibid.* **109**, 014302 (2011).

¹¹C. F. Bohren, X. Xiao, and A. Lakhtakia, *J. Mod. Opt.* **59**, 1312 (2012).

¹²S. Torquato, *Random Heterogeneous Materials* (Springer, New York, 2002).

¹³M. E. Mezeme, S. El Bouazzaoui, M. E. Achour, and C. Brosseau, *J. Appl. Phys.* **109**, 074107 (2011).

¹⁴L. Landau, I. M. Lifshitz, and L. P. Pitaevskii, *Electrodynamics of Continuous Media* (Elsevier, New York, 1984).

¹⁵M. J. Beran, *Statistical Continuum Theories* (Wiley, New York, 1968).

¹⁶D. J. Bergman and D. Stroud, in *Solid State Physics, Advances in Research and Applications*, edited by H. Ehrenreich and D. Turnbull (Academic Press, New York, 1992), Vol. 46.

¹⁷R. Pelster, B. Hallouet, and C. Volz, *J. Phys. D: Appl. Phys.* **48**, 145306 (2015).

¹⁸J. Helsing, *Phys. Rev. B* **44**, 11677 (1991); J. Helsing, *Commun. Numer. Methods Eng.* **16**, 37 (2000); J. Helsing, *J. Comput. Phys.* **230**, 7533 (2011).

¹⁹COMSOL[®] Multiphysics 3.4 (2013).

²⁰U. G. K. Wegst, H. Bai, E. Saiz, A. P. Tomsia, and R. O. Ritchie, *Nat. Mater.* **14**, 23 (2015).

3.5 Numerical protocol

The Multiphysics modelling protocol for 3D biological cells is now introduced. It begins by describing the geometry, setting up the material properties and parameters to be used in the model. The geometry is then discretized by meshing prior to solving. Adjusting the mesh parameters can result in a coarser or finer mesh. As an illustration, the geometry and meshing for a single cell is shown in Fig.3.4. The geometry of the model contains several boundaries (3D surfaces) which are handled with appropriate constraints or boundary conditions. The initial values, parameters and material properties are in fact required by the accompanying differential equations or boundary conditions which are implemented as part of the sub-models – Electrical, Structural and Pore models. The output solution of one sub-model is coupled to the input of the other, wherever needed. Then, the model is solved for a steady-state analysis, frequency analysis or a time-dependent (transient) analysis. The obtained results are further post-processed for better visualizations and a statistical analysis thereafter in case of multiple configurations. This completes the numerical protocol. It must be noted that all the mentioned sub-models are coupled in this work for the time-dependent analysis in contrast to the results shown in sections 3.4 and 4.2 where only electrical sub-model is used in context of static and frequency analysis.

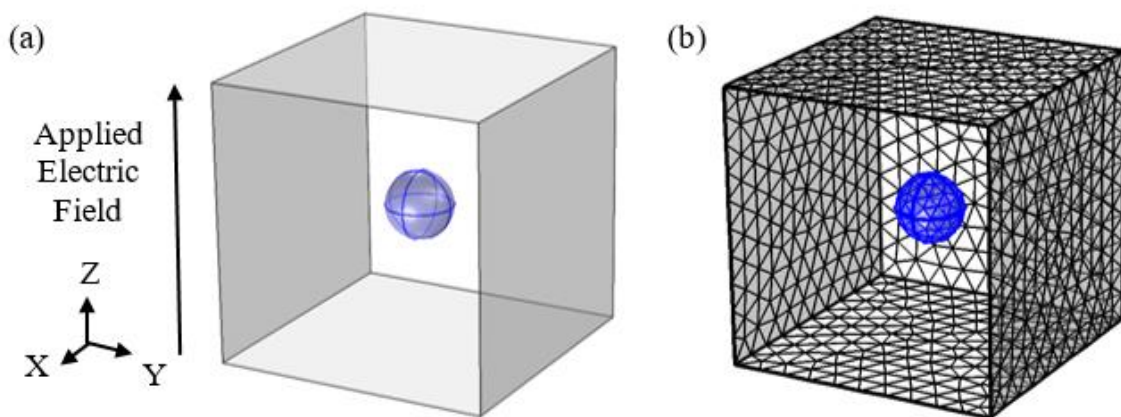


Fig.3.4. Single cell (a) model geometry and (b) meshing (shown for surfaces only).

The aspects of geometry, meshing and modelling coupled physics are discussed in more detail in the next two sections.

3.6 Geometry and meshing

The geometry for the model is described in a 3D computational cube in which initially spherical cells are placed. Radii in the range from $4\ \mu\text{m}$ to $12\ \mu\text{m}$ have been used in this work. The positioning of spherical cells divides the computational cube in two distinct domains – one that refers to the cell interior and the other that refers to the cell exterior. As shown in Fig.3.5, multiple cells can be positioned in the cube. The space occupied by the cells in the cube defines the filling fraction.

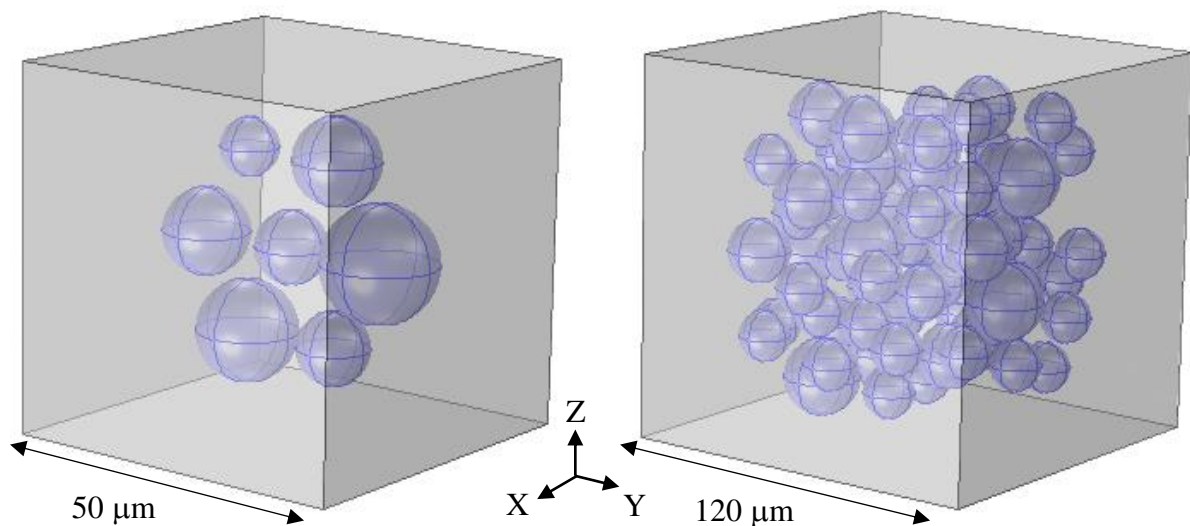


Fig.3.5. Positioning the spherical cells in the computational cube of sides $50\ \mu\text{m}$ by direct placement (left, filling fraction = 0.0536) and $120\ \mu\text{m}$ by the algorithm-assisted placement (right, filling fraction = 0.1337)

When the number of cells is small, only a few (e.g. less than ten) realizations are required and they can be positioned by manually specifying their locations ensuring desired proximity distances among the neighbors' non-overlapping boundaries. But, when the number of cells is large enough or many realizations are required, it becomes necessary to use a computer algorithm which takes care of the non-overlapping constraint between cells and

iterative generation of new realizations (see Appendix A). The two methods are referred to in this text as ‘Direct’ placement and ‘Algorithm assisted’ placement. The latter is more relevant for having closer resemblance to high density multicellular cell suspensions and tissue.

All distinct domains or volume regions are meshed with tetrahedral elements and thus all boundary surfaces with triangular elements and all lines with edge elements. The mesh is automatically refined in regions wherever two boundary surfaces occur in close proximity or a boundary becomes too curvy. Further refinement is always possible to control the mesh density by adjusting the mesh parameters. 2D cross section is shown in Fig.3.6. Since the cell membranes are very thin ($\sim 5\text{-}10\text{ nm}$) in comparison to the overall size of the cell ($\sim 5\text{-}10\text{ }\mu\text{m}$), modelling them with distinct computational volume leads to a much denser mesh around it (Fig.3.6 (a)). Thus, cell membrane is rather modelled only as a meshed surface over which ‘contact impedance’ boundary conditions are applied (shown in Eq.3.4, later) taking into account the voltage drop across it due to relevant factors i.e. the membrane thickness and its electrical and structural material properties. It is worth mentioning that both ways of modelling the cell membrane represent a Core-Shell structure.

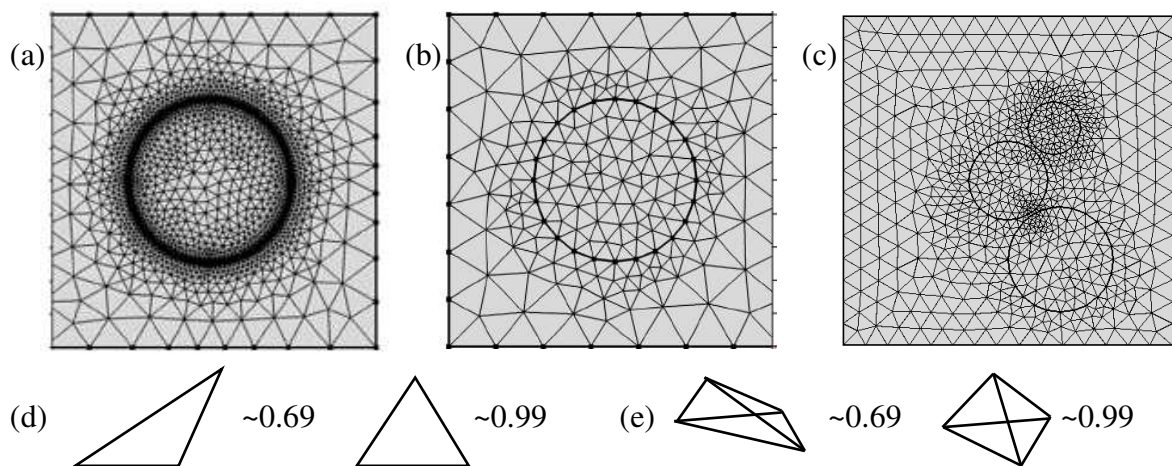


Fig. 3.6. 2D illustrations of the meshing of (a) single cell with its cell membrane modelled as a distinct region leading to a very dense mesh, (b) single cell with its cell membrane modelled not as a distinct region but via a ‘Contact Impedance’ boundary condition that couples the electric potential on either side of the membrane to its width and material properties, leading to a coarse mesh, (c) three cells in close proximity with same conditions as in (b) leading to a mesh density that is somewhere between (a) and (b). (d-e) Mesh quality illustrations for typical triangular and tetrahedral elements indicating a lower quality (~ 0.5) for skewed shapes and higher quality (~ 0.5 -1) for regular shapes.

To compare the number of mesh elements generated when using different number of cells, consider a 50 μm cube containing a single cell of radius 6 μm in 3D, modelled with a distinct thickness for the membrane (20 times the usual 5 nm, i.e. 100 nm). It leads to 44390 tetrahedral elements and 5259 triangular elements. Now, compare these numbers in Table 3.1 with cases for a 19 cells configuration (put in a 55 μm cube with cell radii as 5 and 10 μm) and 76 cells configuration (put in a 120 μm cube with cell radii as 8, 10 and 12 μm) which are shown in Fig.3.7, where the cell membrane is modelled as a meshed surface employing the ‘contact impedance’ boundary condition. The table also shows the average mesh quality estimate for both element types. The range of quality is 0 to 1, the latter indicating the best possible element. One can notice from the table and Fig.3.7 (a) that the number of elements increases further when cells are in close proximity to each other or when the number of cells is high. Larger volume of the cube also accommodates more number of tetrahedral elements.

Element Type	1 Cell*	1 Cell	19 Cells	76 Cells
Tetrahedral	44390	15833	46510	85934
Quality (Avg.)	0.6568	0.7637	0.6833	0.6859
Triangular	5259	1688	7144	13348
Quality (Avg.)	0.9217	0.9703	0.9309	0.9282

Table.3.1: Number of finite elements used for meshing computational domain. * denotes that ‘contact impedance’ boundary condition is not used but a distinct volume for membrane is meshed.

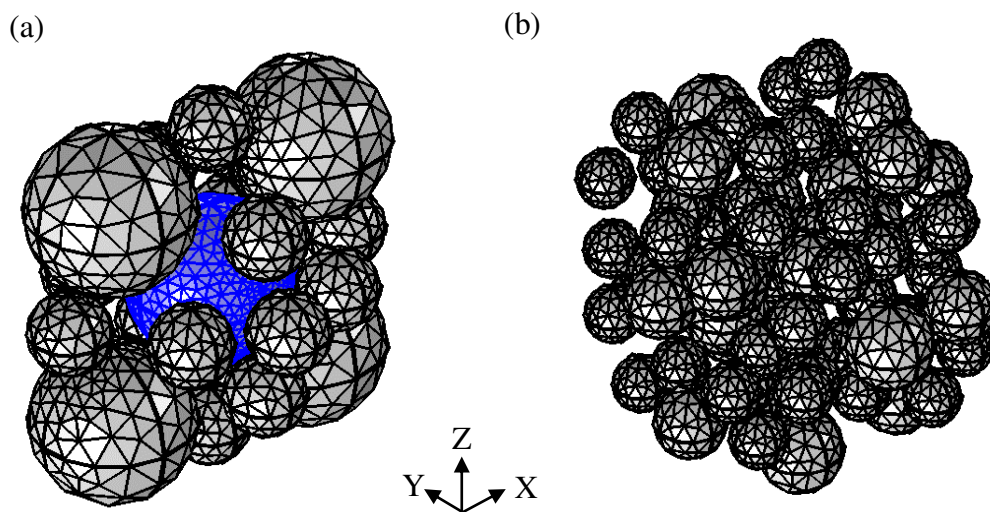


Fig.3.7: Surface meshing for 3D multicellular configurations consisting of (a) 19 cells put in a 55 μm cube with cell radii as 5 and 10 μm , and (b) 76 cells put in a 120 μm cube with cell radii as 8, 10 and 12 μm . Cubes not shown.

3.7 Modelling coupled physics

Three differential equations having three dependent variables, corresponding to the three distinct sub-models – electrical, structural and pore models will be considered. All distinct materials are modelled within continuum theory. Molecular description is ignored. All material parameters with the exception of membrane conductivity are time-independent. Initial conditions are assigned and the model solves for next time-steps chosen adaptively. The time-steps become smaller when the intermediate solutions change rapidly and become larger when the change is slower. Fig.3.8 (a) depicts the coupling of the solution from electrical model to structural and pore models as inputs, in one time step.

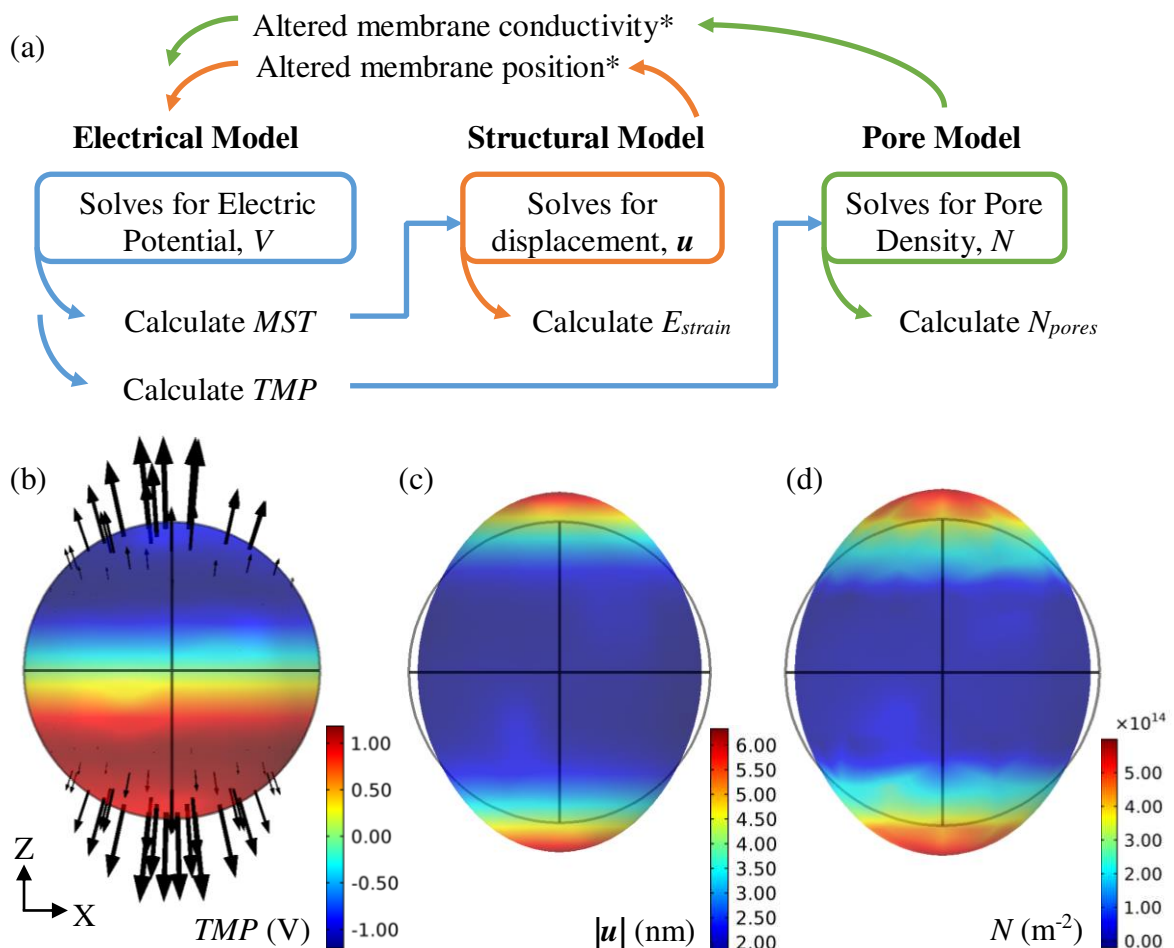


Fig.3.8. Modelling an isolated spherical cell under an applied electric field. (a) Coupled physics with submodels, (b) Transmembrane potential, TMP in color and normal components of Maxwell Stress Tensor, MST by arrows (arrow length is proportional to the magnitude of stress), (c) Magnitude of membrane displacement, $|\mathbf{u}|$ and (d) Pore density, N . *Altered values are used in the next time step; E_{strain} is strain energy; N_{pores} is total number of pores.

The structural model and pore model alter one or several quantities which are fed back into the electrical model in the next time-step. This cycle repeats every time-step until the last pre-assigned value of time. When multiple cells are considered, the deforming membranes may come close to each other but their overlapping as well as any adhesive forces are not accounted and we ensure that the calculated deformation is small enough to prevent any overlapping.

3.7.1 Electrical model

Cells can simply be considered as effective spheres composed of a conducting core representing cytoplasm and thin insulating shell representing cell membrane, which is also known as a Core-Shell (CS) structure. CS description has been extensively employed to derive analytical expressions for dielectric response or total force acting on the cell.

Under an applied electric field, the spherical cell gets polarized. The field can be applied by specifying the voltage, $V_{\text{applied}}(t)$ on a face of the cube along with boundary conditions as shown in Fig.3.9. Assuming charge conservation, the continuity equation for the electric current density, \mathbf{J} , can be written as $\nabla \cdot \mathbf{J} = -\partial_t \rho_{\text{chg}}$ where ρ_{chg} is the charge density and ∂_t denotes the time derivative. The Poisson equation, $\nabla^2 V = -\frac{\rho_{\text{chg}}}{\epsilon_r \epsilon_0}$, along with the continuity of current density and Ohm's law ($\mathbf{J} = \sigma \mathbf{E}$) leads to (Eq.3.3) which solves for electric potential

$$-\nabla \cdot ((\sigma + \epsilon_r \epsilon_0 \partial_t) \nabla V) = 0 \quad (\text{Eq.3.3})$$

where σ and ϵ_r are the conductivity and relative permittivity of the subdomain regions i.e. interior and exterior of the cell. The electric potentials on either side of the cell membrane are coupled through a specific 'contact impedance' boundary condition (Eq.3.4) as given by

$$\mathbf{n} \cdot \mathbf{J}_2 - \mathbf{n} \cdot \mathbf{J}_1 = \frac{1}{d_m} (\sigma_m + \epsilon_m \epsilon_0 \partial_t) (V_2 - V_1) \quad (\text{Eq.3.4})$$

where \mathbf{n} is the unit vector normal to the boundary surface on either sides, σ_m is the membrane conductivity, ϵ_m is the membrane relative permittivity, d_m is the membrane thickness, and '1'

and '2' denote the exterior and the interior of cell, respectively. This step essentially gives the *TMP* (Eq.3.5). Initially, at $t = 0$, $V_1 = V_{rest}$ and $V_2 = 0$. At any arbitrary time it is given as

$$TMP = V_1 - V_2 \quad (\text{Eq.3.5})$$

We implement the outer boundary conditions on the cube faces. Dirichlet boundary condition specifies the value of potential. The external potential can be applied to any of the cube faces (the bottom face is used here). The potential at the face opposite to it is set to zero. Neumann boundary condition, which is applied at the side faces, ensures that the normal component of electric field is set to zero i.e. the electric field at those faces remains parallel.

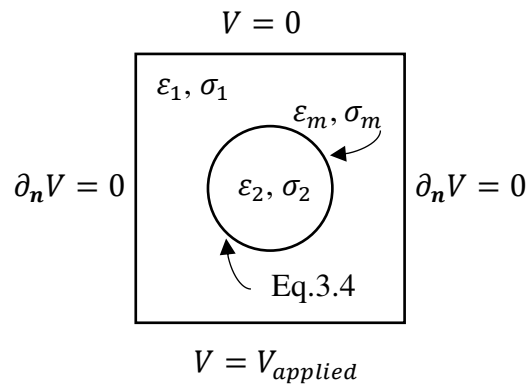


Fig.3.9: Material properties and boundary conditions in electrical model.

If the external potential is assumed sinusoidal with angular frequency ω , then the frequency dependence (dispersion) is incorporated into the complex relative permittivity of the all regions of the cell. In particular, we use the following relation (Eq.3.6):

$$\epsilon_{complex} = \epsilon_{static} - i\left(\frac{\sigma}{\epsilon_0 \omega}\right) \quad (\text{Eq.3.6})$$

where ϵ_{static} represents the relative permittivity at low frequencies (static limit). Once the electric potential distribution and thus the electric field distribution has been calculated, then Maxwell Stress Tensor (*MST*) that signifies the electrical stress can be calculated as (Eq.3.7):

$$MST_{ij} = \varepsilon_r \varepsilon_0 \begin{pmatrix} E_x^2/2 & E_x E_y & E_x E_z \\ E_y E_x & E_y^2/2 & E_y E_z \\ E_z E_x & E_z E_y & E_z^2/2 \end{pmatrix} \quad (\text{Eq.3.7})$$

where i, j can be x, y and z , and E is the electric field component. The diagonal components signify normal stress while the off-diagonal components signify shear stress. A surface integral of MST will give total force over that surface. Hence, one can calculate total force on a full or a partial membrane surface of the cell.

3.7.2 Structural model

In three dimensions, the mechanical stress \mathbf{S} at any arbitrary point in the material can be written in the form of a tensor as follows (Eq.3.8):

$$\mathbf{S} = \begin{pmatrix} S_{xx} & S_{xy} & S_{xz} \\ S_{yx} & S_{yy} & S_{yz} \\ S_{zx} & S_{zy} & S_{zz} \end{pmatrix} \quad (\text{Eq.3.8})$$

The law of momentum conservation (Newtonian mechanics) can be written as $\nabla \mathbf{S} + \mathbf{f} = \rho \partial^2_{t^2} \mathbf{u}$ where ρ denotes the initial mass density, $\mathbf{u}: (u_x, u_y, u_z)$ denotes the displacement field and \mathbf{f} denotes the external volume distribution force field. Since the electrical stress is distributed variably over the cell surface only and not in the volume regions of the remaining media, \mathbf{f} is set to zero and MST is added to \mathbf{S} at the boundaries. Effectively, we solve for the deformation distribution as follows (Eq.3.9):

$$\begin{pmatrix} \partial_x S_{xx} & \partial_y S_{xy} & \partial_z S_{xz} \\ \partial_x S_{yx} & \partial_y S_{yy} & \partial_z S_{yz} \\ \partial_x S_{zx} & \partial_y S_{zy} & \partial_z S_{zz} \end{pmatrix} = \rho \begin{pmatrix} \partial^2_{t^2} u_x \\ \partial^2_{t^2} u_y \\ \partial^2_{t^2} u_z \end{pmatrix} \quad (\text{Eq.3.9})$$

The mechanical stress distribution includes the electric stress distribution (as given in previous sub-section) and the generated responsive stress distribution that essentially depends on the constitutive relation used. The equation is valid for all regions and particularly

significant for the cell membrane. All boundaries of the computational domain are allowed to displace as per the calculation of displacement i.e. they are free to move/deform.

The time-dependent strain at the cell membrane can be defined in terms of its reference position, say R_0 and its current deformed position at a given instant, say $R(t)$ as (Eq.3.10):

$$\gamma(t) = \frac{R(t) - R_0}{R_0} \quad (\text{Eq.3.10})$$

The general strain tensor for any region can be written as (Eq.3.11):

$$\gamma = \begin{pmatrix} \gamma_{xx} & \gamma_{xy} & \gamma_{xz} \\ \gamma_{yx} & \gamma_{yy} & \gamma_{yz} \\ \gamma_{zx} & \gamma_{zy} & \gamma_{zz} \end{pmatrix} \quad (\text{Eq.3.11})$$

Under the assumption of small displacements and rotations, the normal and shear strain components are given as (Eq.3.12):

$$\begin{aligned} \gamma_{xx} &= \partial_x u_x & \gamma_{xy} &= \gamma_{yx} = (\partial_y u_x + \partial_x u_y)/2 \\ \gamma_{yy} &= \partial_y u_y & \gamma_{yz} &= \gamma_{zy} = (\partial_z u_y + \partial_y u_z)/2 \\ \gamma_{zz} &= \partial_z u_z & \gamma_{xz} &= \gamma_{zx} = (\partial_z u_x + \partial_x u_z)/2 \end{aligned} \quad (\text{Eq.3.12})$$

By taking the ratio of compression to elongation, one obtains the so called Poisson's ratio given by (Eq.3.13)

$$\nu = -\frac{\gamma_{compression}}{\gamma_{elongation}} \quad (\text{Eq.3.13})$$

The normal and shear components (six in total) of stress and strain can also be represented as vectors. The simplest constitutive relation that relates the stress to strain is an equivalent of Hooke's Law i.e. containing a single elastic constant, the Young's modulus, Y (used here in Shamooun et al, (2019-a) [47]). For a linear isotropic Hookean material, the stress is proportional to the strain and this constitutive relation can be written as (Eq.3.14) below:

$$\begin{pmatrix} S_{xx} \\ S_{yy} \\ S_{zz} \\ S_{yz} \\ S_{zx} \\ S_{xy} \end{pmatrix} = \frac{Y}{(1+\nu)(1-2\nu)} \begin{pmatrix} 1-\nu & \nu & \nu & 0 & 0 & 0 \\ \nu & 1-\nu & \nu & 0 & 0 & 0 \\ \nu & \nu & 1-\nu & 0 & 0 & 0 \\ 0 & 0 & 0 & 1-2\nu & 0 & 0 \\ 0 & 0 & 0 & 0 & 1-2\nu & 0 \\ 0 & 0 & 0 & 0 & 0 & 1-2\nu \end{pmatrix} \begin{pmatrix} \gamma_{xx} \\ \gamma_{yy} \\ \gamma_{zz} \\ \gamma_{yz} \\ \gamma_{zx} \\ \gamma_{xy} \end{pmatrix}$$

In the above relation, some literature may also contain a factor of $\frac{1}{2}$ in the bottom three diagonal components of the stiffness matrix as per the difference in defining the shear strain. The strain predicted by a Hookean material can thus be written as (Eq.3.15):

$$\gamma(t) = \frac{1 + \nu}{Y} (\mathbf{S} \cdot \mathbf{n}) - \frac{\nu}{Y} \text{tr}(\mathbf{S} \cdot \mathbf{n}) \mathbf{I} \quad (\text{Eq.3.15})$$

where $\mathbf{S} \cdot \mathbf{n}$ denotes the diagonal stress components at any arbitrary cross-sectional area in the computational domain with a unit normal \mathbf{n}

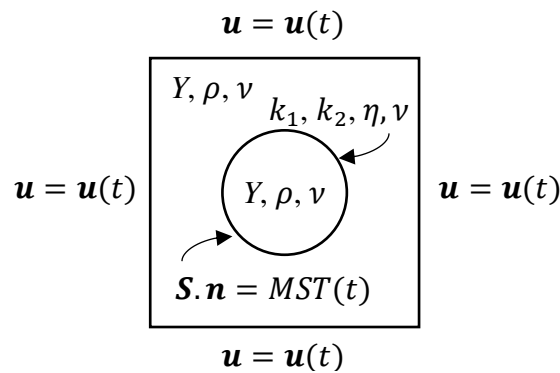


Fig.3.10: Material properties and boundary conditions in structural model.

The simplest viscoelastic model that can be used for describing cell membrane deformability is Standard Linear Solid (SLS) model. The SLS model has three parameters (used here in Shamooun et al, (2019-b) [49]) – two elastic constants, k_1, k_2 and one viscous constant, η (See Fig.3.11).

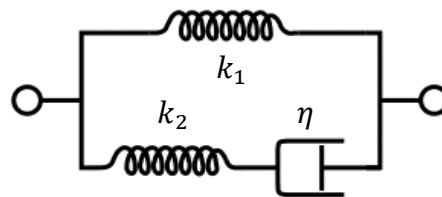


Fig.3.11: Maxwell representation of a simple viscoelastic model called Standard Linear Solid (SLS) model. The springs with elastic constants k_1 and k_2 represent the elastic component of the model's response and the dashpot with viscous constant η represents the viscous component of the model's response.

The SLS model predicts the membrane strain as follows (Eq.3.16):

$$\frac{d\gamma(t)}{dt} = \frac{k_2 \left(\frac{\eta}{k_2} \frac{d(MST(t))}{dt} + MST(t) - k_1 \gamma(t) \right)}{k_1 + k_2} \quad (\text{Eq.3.16})$$

The strain energy density function for linear isotropic materials within the small strain assumption can be written as follows (Eq.3.17):

$$W = \frac{1}{2} \sum_{i=1}^3 \sum_{j=1}^3 \sigma_{ij} \gamma_{ij} = \frac{1}{2} (\sigma_{xx} \gamma_{xx} + \sigma_{yy} \gamma_{yy} + \sigma_{zz} \gamma_{zz} + 2\sigma_{xy} \gamma_{xy} + 2\sigma_{yz} \gamma_{yz} + 2\sigma_{xz} \gamma_{xz})$$

The formulae presented in this section were adapted from [47-a] with some changes in symbols. The structural input parameters used in the model are based on experimental estimation of material properties obtained from the archival literature. Elasticity and viscoelasticity has been implemented in multiple ways in this work which are not always the same (see Table 4.1). The material property values pertaining to electrical and pore models are discussed in various references and noted here in Chapter 2, Table 2.2.

3.7.3 Pore model

Thermal fluctuations on the membrane lead to stochastic events of formation and destruction of nanopores. It is assumed that an equilibrium pore density exists even before the application of the electrical stimulus. When the local electric field near the membrane becomes high enough due to an external stimulus, it causes an increased formation of nanopores on the cell. Modelling of this phenomenon began since the seminal work of DeBruin and Krassowska (1999) [48] using an asymptotic form of the Smoluchowski equation. In particular, we calculate the pore density, N , over the membrane based on its highly non-linear dependence on TMP . For simplicity, we assume a fixed pore radius (0.75 nm) for all the pores. The following equation (Eq.3.18) gives the rate of formation (and destruction) of pore density.

$$\partial_t N(t) = \alpha \exp \left(\left(\frac{TMP}{V_{ep}} \right)^2 \right) \left[1 - \left(\frac{N(t)}{N_0} \right) \exp \left(-q \left(\frac{TMP}{V_{ep}} \right)^2 \right) \right] \quad (\text{Eq.3.18})$$

In this equation, TMP is sourced from the solution of electrical model. If the TMP evolves in time due to any external factor then it directly affects the pore density through the equation shown above. Here, N_0 is the pore density in the non-electroporated membrane, V_{ep} is the electroporation threshold, α and q are two parameters describing the EP process. This equation is solved only on the cell membrane surfaces.

The membrane conductivity is linked to the pore density by the following equation (Eq.3.19)

$$\sigma(t) = N(t) \left(\frac{2\pi r_p^2 \sigma_p d_m}{\pi r_p + 2d_m} \right) \quad (\text{Eq.3.19})$$

where r_p is the fixed pore radius, σ_p is the single pore conductivity, d_m is the membrane thickness. It should be noted that the relation above is in addition to the existing conductivity of the membrane.

Commenting on the limitations of EP model used. The pore radius is set to 0.75 nm, however, this assumption is relaxed in several more advanced pore models to study the dynamics of each pore size that can evolve based on a collective contribution to pore energy landscape which further adds to the cell membrane free energy. Another limitation is regarding the shape of the pore considered. A pore can be considered as cylindrical, trapezoidal and toroidal. Cylindrical pores have been considered in this work. These considerations affect the quantities like conductance and the energy of individual pores that contributes to the free energy of the membrane.

3.8 Problem size and solver techniques

The meshing and coupled physics influence the number of degrees of freedom for the whole model. All involved equations are solved for each node. The number of degrees of freedom is given by the product of the number of all mesh nodes and equations. Listed below are the number of degrees of freedom for 1 cell and 76 cell configurations.

Degrees of Freedom	1 Cell	76 Cells
Electrical Model	24027	140213
Structural Model	71163	129795
Pore Model	306	23768
Total	95496	293776

Table 3.2: The number of degrees of freedom in the COMSOL models used.

The degrees of freedom mentioned in Table 3.2 are for the cases where visco-elastic membrane is not considered. The case where it is considered, is for the seven cell configurations (Publication by Shamoon et al (2019-b) [49]). There, the total number goes to 170764.

The direct method PARDISO (Parallel direct sparse solver interface) is used as general time-dependent solver which utilizes multiple cores of the CPU and BDF (backward differentiation formula) for time-stepping. The steady-state and frequency domain solutions are obtained by an iterative solver called BiCG-STAB (Biconjugate gradient stabilized method). Technical details of the model have been sufficiently introduced and now, we are in good position to numerically study the ED and EP of cell-assemblies.

4. Results and discussion: ED and EP of cell assemblies

In this chapter, the major results and analyses of this work are presented by simulating time-dependent ED and EP for N-cell assemblies under an applied electric pulse. N-cell assemblies considered here have $N = \{1, 3, 7, 76\}$. Results for electrical force modulation by frequency analysis among neighboring cells are shown later for $N = \{2, 15, 19, 23, 27, 35, 43\}$.

4.1 Time-dependent analyses

The results of the time-dependent analysis are organized in two sub-sections – the first one deals with a small number of cells, the second one considers a large number of cells. The summary of the similarities and differences among different studies is shown in Table 4.1.

Aspects	Shamoon et al. (2019-a)	Shamoon et al. (2019-b)	Unpublished, Large value of N
N-spherical-cells	1 and 3	7	76
Electrical pulse durations	100 μs +	100 μs +, 100 μs +: 25 μs -, 100 μs +: 50 μs -	1 μs +: 1 μs 0: 1 μs -
Simulated time	200 μs	200 μs	6 μs
Electrical materials	Defined by Permittivity, Conductivity		
Structural materials	Elastic (Cells & ECM)	Elastic (Cells & ECM); Viscoelastic (membrane)	Elastic (Cells)
Pore model features	Pore density with fixed pore radius		

Table 4.1: Main similarities and differences in the time-dependent analyses of N-cell configurations.

Firstly, the common assumptions and calculation steps in the three studies are stated. The electrical properties are defined by the relative permittivity and conductivity of the distinct homogeneous and isotropic phases describing the cell interior, exterior and membrane. The time-varying electric pulse is applied on one face of the cube while the opposite face is grounded. Poisson's equation is solved for electric potential distribution. The calculation of the transmembrane potential and electrical forces, which appear on the location of the deforming boundaries of the cells, is done in the same way in all studies. In terms of output, the structural

model gives the membrane displacement and the pore model gives the pore density which is analyzed locally on the membrane surface. Strain energy for the elastic and viscoelastic media is calculated. The membrane conductivity, which is a measurable quantity in experiments is increased in proportion to the calculated pore density. Pore number or area occupied by the pores on the membrane is also calculated which serves as an indirect measure of membrane perforation. See the previous chapter for involved equations. It must be noted that since the simulation time is limited to a maximum of 200 μs , the pore density remains constant in this duration. The time constant for the decay of pores is ~ 1.5 s which is much larger than the simulation time. Most of the material properties except for the membrane conductivity and mass density, are assumed to be constant during the time dependent analysis unless otherwise stated. Membrane conductivity varies with the calculated pore density while the mass density varies as the deformations cause a small change in volume.

4.1.1 Small number of deforming cells

For the two publications Shamooun et al. (2019-a) [47] and Shamooun et al. (2019-b) [49], Fig. 4.1 shows the time-varying electrical stimuli and Fig. 4.2 shows the model geometries used in each simulation which is performed for 200 μs .

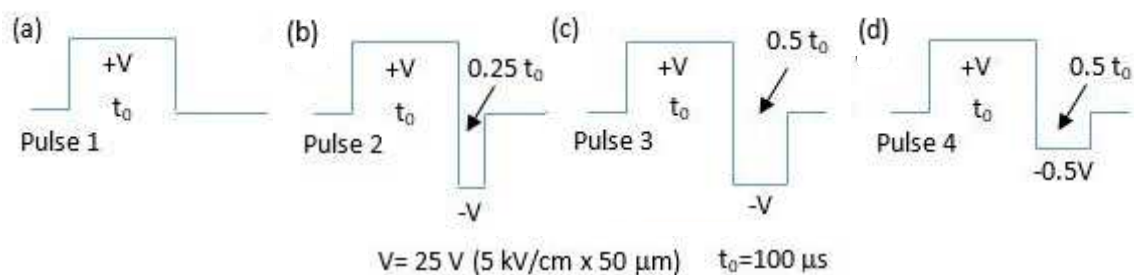


Fig.4.1: Electrical voltage pulses used to stimulate the N-cell assemblies in Shamooun et al. (2019-a) [47] (Pulse 1 only) and in Shamooun et al. (2019-b) [49] (Pulses 1-4).

All cells are placed in a cube of sides $50\ \mu\text{m}$ (Fig.4.2). The one and three cell configurations in Shamoon et al. (2019-a) [47] are analyzed by means of a single configuration. However, in the analysis of the seven-cell configurations in Shamoon et al. (2019-b) [49], we consider eight configurations with size and position which can be varied in orderly and symmetric arrangement or in a disordered and non-symmetric fashion in terms of size and intercellular boundary-boundary distances along the centers of respective cell-pairs.

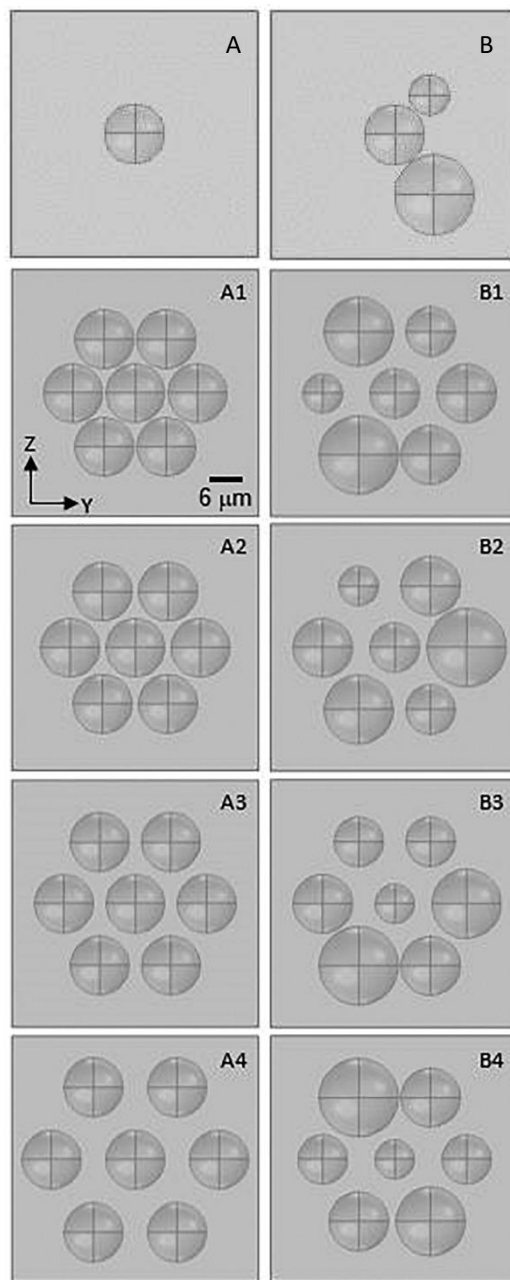


Fig.4.2: Model geometries A and B used in Shamoon et al. (2019-a) [47] while A1-A4, B1-B4 used in Shamoon et al. (2019-b) [49]. The cube has side length $50\ \mu\text{m}$. The radii fall in the range of $4\text{-}8\ \mu\text{m}$.

In the first paper i.e. Shamooun et al. (2019-a) [47], the mechanical properties of the interior and exterior of the cells are modelled with a single homogeneous and isotropic elastic material (Young's modulus = 1000 Pa). The electrical stress appears on the cell membrane under an applied field of 5 kV/cm while the pulse is on for 100 μ s and simultaneously affects the rest of the media generating the mechanical stress. As the pulse falls, the electrical stress quickly vanishes while the deformed configuration begins to relax mechanically. A small assembly of three neighboring spherical cells of different sizes is compared to that of a single, isolated spherical cell under an applied electric pulse in the context of its time evolving electromechanical response. In this respect, the local behavior of various important quantities over the cell membrane is analyzed. On the one hand, this approach allows us to compare single cell simulations with existing literature for which several studies have been undertaken previously. On the other hand, it gives evidence that the presence of even a few neighbors in proximity alters the usual single cell response, either the electrical or the mechanical response. For instance, Fig.3 and Fig.4 in the publication Shamooun et al. (2019-a) [47] show how surface charge, MST and thereby the membrane displacement and pore density over the cell membrane of isolated and non-isolated cell differ from each other. The same figures show that ED and EP are enhanced by several times over the proximity regions in comparison to an isolated cell. This leads to the conclusion that the collective response of multi-cellular configurations is composed of contributions from several individual cells that also affect each other when cells are in proximity. Thus, the N-cell arrangement i.e. the way the cell assembly is realized is also an important ingredient of the analyses for designing simple models of biological tissue.

In the second paper i.e. Shamooun et al. (2019-b) [49], the consideration of elasticity is one step more complex than the previous one considered. It considers a homogeneous and isotropic viscoelastic membrane (Young's modulus = 500 Pa, Shear modulus = 1500 Pa, viscous relaxation time = 0.1 s) modelled apart from the same elastic media for interior and

exterior of the cells as mentioned before. The appearance of stress is also as before, i.e. initially the electrical stress appears on the membrane which is then transferred to other regions. Seven-cell assemblies in two sets of configurations characterized by order and weak disorder are considered. The variations in the time evolving response are examined with different pulse parameters. The major results include the strong variations in enhanced electric field and membrane strain energy in relation to diverse characteristics of pulse. These two quantities are very sensitive to minor variations of the cellular spatial arrangements.

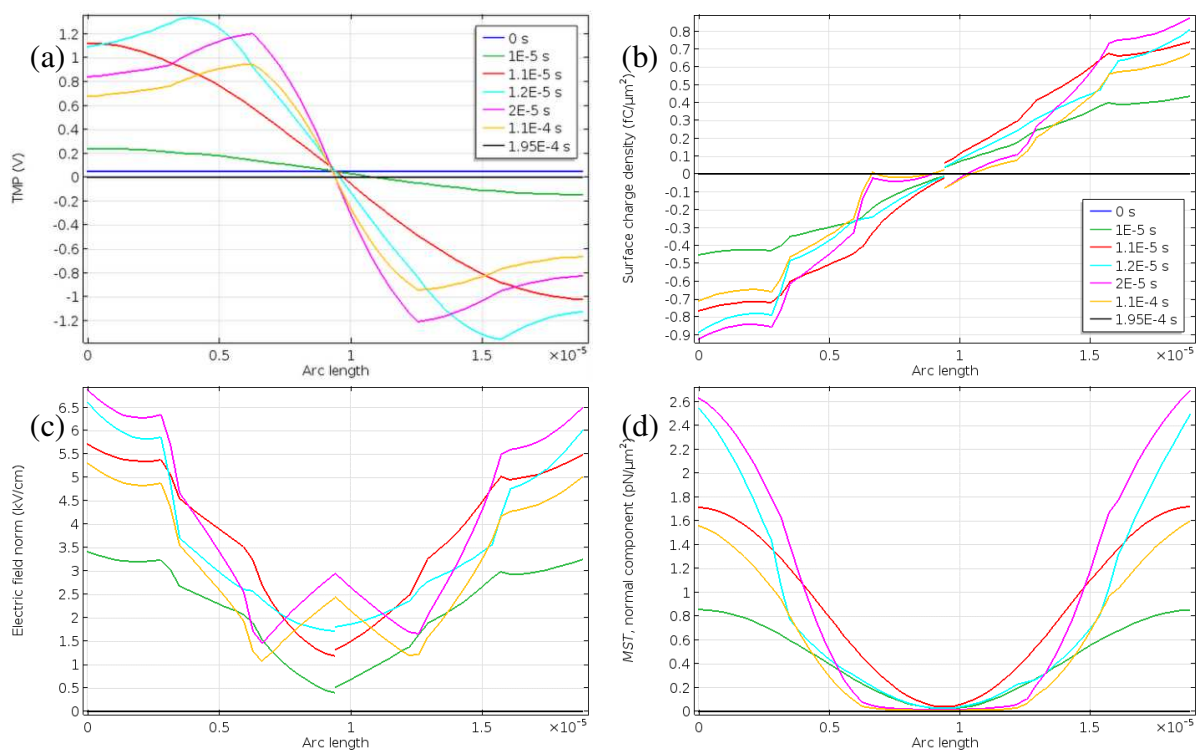


Fig.4.3: Spatio-temporal variations of electrical quantities for the case of single cell under an applied field of 5 kV/cm. The pulse duration is 100 μ s which begins at 10 μ s and ends at 110 μ s (see Pulse 1, Fig.4.1). The x-axis represents the arc length from $-z$ to $+z$ direction over the cell membrane. The y-axis represents (a) TMP , (b) surface charge density, (c) norm of the surface electric field and (d) MST . The time instants are marked in the legends.

Results for the case of a deformable single cell are presented in Fig.4.3. The temporal variations of TMP around the cell Fig.4.3 (a) agree with previous results found in the archival literature [48]. At $t = 0$ s, the resting potential set to -50 mV leads to a TMP of 50 mV (shown in blue). As the pulse begins to rise at $t = 10 \mu$ s, TMP also begins to rise as a cosine around the

membrane revealing the depolarized and hyperpolarized poles (shown in green). It takes only $1 \mu\text{s}$ for the *TMP*, after the beginning of the pulse, to rise to 1 V over the poles. A small asymmetry in the values confirms our results, 1.1 V and -1 V for the depolarized and hyperpolarized poles with the existing trends shown in [48]. As time evolves, the cosine behavior is altered as the extrema of the *TMP* shift from the poles to regions between the poles and equator. Finally, as the pulse begins to fall, *TMP* falls to zero. In the other panels of Fig.4.3, surface charge density, surface electric field norm and *MST* are plotted which reveal the non-uniform distributions of these quantities over the cell membrane. The surface charge density ranges from -0.9 to 0.9 fC/ μm^2 . The local electric field norm at the poles reaches over 6.5 kV/cm beyond the average value i.e. 5 kV/cm for the whole media. *MST* at the poles reaches over 2.6 pN/ μm^2 . Next, Fig.4.4 shows identical trends of the pore density N (calculated from Eq.3.18) and the membrane conductivity (given by Eq.3.19). The pore density rises typically from 10^9 to 10^{14} per m^2 while the membrane conductivity is increased from 10^{-6} to 10^{-4} S/m. The temporal trends are shown for the three points situated at the poles and equator of the cell.

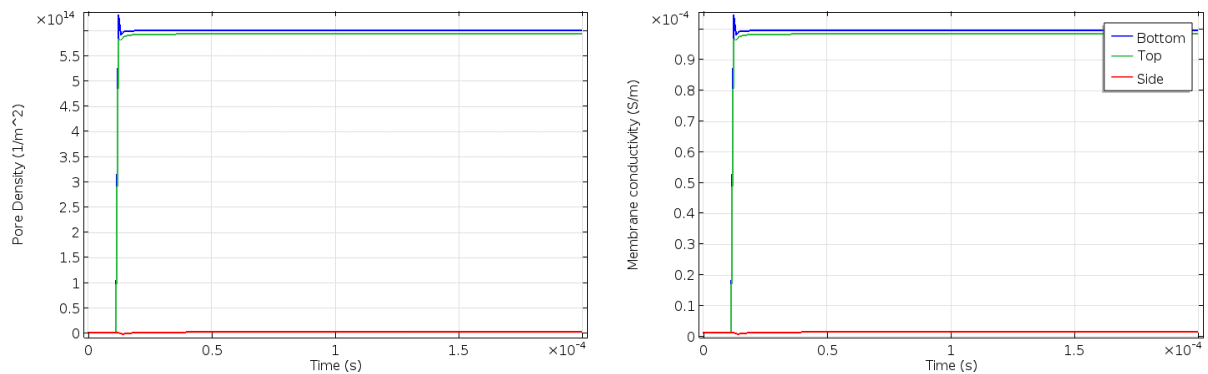


Fig.4.4: Time evolution of the pore density and membrane conductivity at polar and equatorial points of the single cell under an applied electric field.

The time-dependent force averaged on polar halves of the cell can be calculated from the *MST* and is shown in Fig.4.5 (a) for the upper half of the cell. The force shows a spike at the start of the pulse but quickly stabilizes slightly above 0.11 nN. Given the elastic properties for the media, under the application of this electric field induced force, the cell membrane

begins to deform which also pushes the regions around it resulting in deformation of the cube boundaries as well. The deformation of the whole media can be globally quantified by strain energy shown in Fig.4.5 (c). The contribution of the deforming boundaries of the cell and cube to the strain energy can be inferred from the maximum values of boundary displacements of the cell membrane and cube shown in Fig.4.5 (d). It can be seen that the deforming cell membrane contributes more to the strain energy than the deforming cube boundary. This is because the cell membrane is far enough from the cube boundary in the case of single cell. It will be seen shortly, in the case of denser packing of cells, when the cell membrane is close to the cube boundary, then the cube boundary is also deformed significantly and contributes much more to the strain energy.

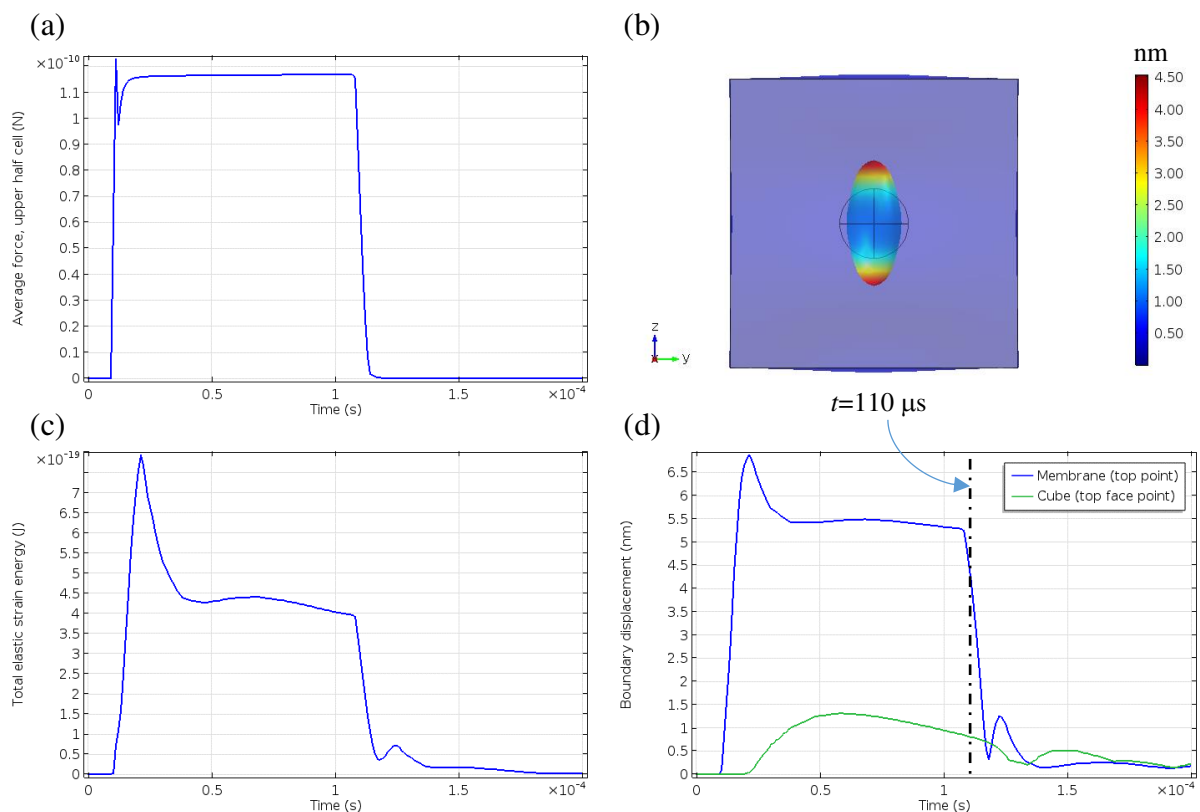


Fig.4.5: (a) Time dependence of the force averaged on the upper half of the cell, (b) Deformed configuration (not to scale) at the end of the pulse at $t=110 \mu\text{s}$ (see Pulse 1 in Fig.4.1), (c) Strain energy in J for the deforming media, (d) Boundary displacements in nm of the membrane and cube.

The deformation of a single cell or single vesicle is often quantified by an aspect ratio defined as ‘ $D=b/a$ ’ where the stretched radius ‘ b ’ is along the applied field direction and the compressed radius ‘ a ’ is orthogonal to it. This aspect ratio along with the changing radii is plotted in Fig.4.6(a) for different conductivity values of those used for the results shown in Fig.4.5 and Shamooun et al. (2019-a) [47]: 0.20 S/m for the extracellular region and 0.15 S/m for the cytoplasm. Additionally, the Young’s modulus is changed from 1000 Pa to 800 Pa, so that the media is more elastic. All other parameters are identical. It is clear that a more elastic cell leads to a larger deformation (up to 9.7 μm as opposed to 6.9 μm in the previous case while the original radius was 6 μm).

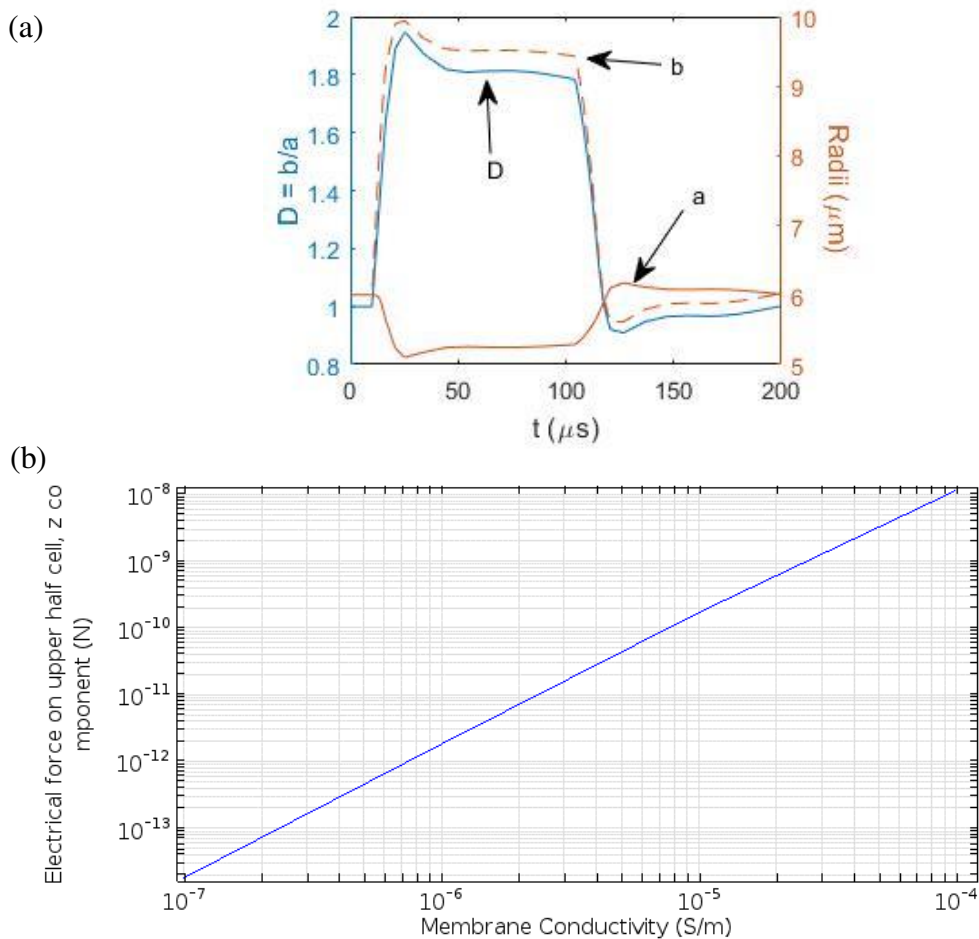


Fig.4.6: (a) The aspect ratio (y-axis, left) and radii (y-axis, right) of a single cell under an applied electric field (see Pulse 1 in Fig.4.1), (b) Steady state calculation of the electrical force on upper half of a single cell under an applied field of 5 kV/cm.

Electrical force can also vary as the conductivities of the media change. This is depicted in Fig.4.6 (b) with the calculation of steady state electrical force on the upper half of a single cell. The conductivity of membrane is varied as a parameter while keeping the conductivities of the inner and outer regions unchanged. The log of the average force varies linearly with the log of the membrane conductivity. A variation of six orders of magnitude of force (10^{-14} to 10^{-8} N) is computed from a variation of four orders of magnitude of membrane conductivity (10^{-7} to 10^{-4} S/m).

Having considered the deformable single cell case in detail, we discuss now a simple case of asymmetric configuration with three neighboring cells of different radii. Cells 1-3 have radii 6, 4 and 8 μm as depicted in Fig.4.7 (a). The results are depicted in Fig.4.7.

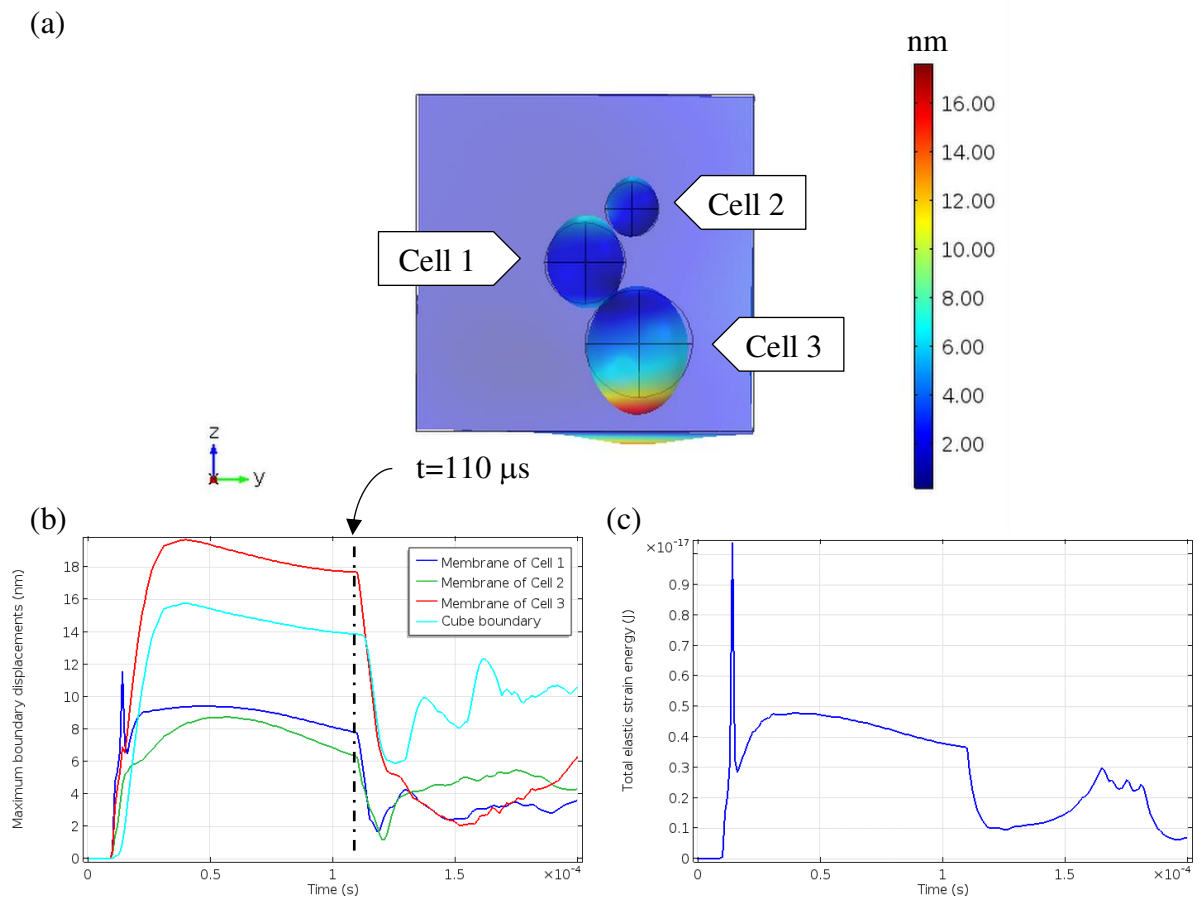


Fig.4.7: (a) Deformation of three-cell configuration at $t=110 \mu\text{s}$ under an applied field (see Pulse 1 in Fig.4.1). (b) Maximum value of the calculated displacements on the boundary of each cell and the cube. (c) Strain energy in J for the deforming media.

As the number of cells increase in the cell assembly, the number of deforming boundaries increase which essentially results into a more complex contribution to the strain energy. The individual membrane deformation analysis, as done for single cell before (Fig.4.5 (d)) and for the three-cell case now (Fig.4.7 (b)), becomes more cumbersome when the number of cells is increased. Hence it is more practical to assess deformation directly from the strain energy. A comparison of the membrane deformation for the two cases shows that Cell 1 (shown in Fig.4.7 (a)) experiences more deformation (~ 9.5 nm) than that when it is isolated (~ 5.5 nm). Among the three cells, the membrane displacement is minimum for the smallest cell and maximum for the largest cell. The large cell is near the cube boundary which essentially increases its displacement as well making it more significant than those for cells 1 and 2.

Shamoon et al. (2019-a)

Assessing the electro-deformation and electro-poration of biological cells using a three-dimensional finite element model

D. Shamoon, J. Dermol-Černe, L. Rems, M. Reberšek, T. Kotnik, S. Lasquellec, C. Brosseau, and D. Miklavčič

Applied Physics Letters, 114 (6), (2019) 063701

DOI: 10.1063/1.5079292

Assessing the electro-deformation and electro-poration of biological cells using a three-dimensional finite element model

Cite as: Appl. Phys. Lett. **114**, 063701 (2019); doi: [10.1063/1.5079292](https://doi.org/10.1063/1.5079292)

Submitted: 30 October 2018 · Accepted: 18 January 2019 ·

Published Online: 11 February 2019



View Online



Export Citation



CrossMark

D. Shamoon,¹ J. Dermol-Černe,² L. Rems,² M. Reberšek,² T. Kotnik,² S. Lasquelles,^{1,a)} C. Brosseau,^{1,a)} and D. Miklavčič²

AFFILIATIONS

¹Univ Brest, CNRS, Lab-STICC, CS 93837, 6 Avenue Le Gorgeu, 29238 Brest Cedex 3, France

²University of Ljubljana, Faculty of Electrical Engineering, Tržaška 25, 1000 Ljubljana, Slovenia

^{a)}brosseau@univ-brest.fr

ABSTRACT

In this Letter, we explore how cell electro-deformation and electro-poration are connected. We build a time-domain model of layered concentric shells (a model of biological cells) including their dielectric and elastic properties. We simulate delivery of one trapezoidal voltage pulse to either a single spherical cell or an assembly of three neighboring cells in a specific configuration and calculate cell deformation and pore formation. We describe the qualitative features of the electric field, surface charge density, transmembrane voltage, cell elongation, and pore density distribution at specific times i.e., before, during and after the application of the electric pulse and explore the correlations between them. Our results show that (1) the polarization charge redistribution plays a significant role in the spatial distribution of electrical stresses at μs time scales and (2) the cell deformation and pore density can be correlated with regions of high surface charge density. In future work, our model could be used for understanding basic mechanisms of electro-deformation and electro-poration with high-frequency short bipolar pulses of biological cells in suspension or tissues.

Published under license by AIP Publishing. <https://doi.org/10.1063/1.5079292>

The pursuit of understanding the mechanisms of electro-deformation and electro-poration (EP) of biological cells in suspension or tissue began decades ago^{1,2} and the search continues with renewed enthusiasm.^{3,4} Understanding the connection between cell electro-deformation and EP is still a relatively unexplored area of research. One of the significant challenges in EP is high molecular weight molecules delivery such as DNA into the living cells. However, most of the existing numerical and analytical studies have tackled the modelling of this phenomenon based on various assumptions and constraints to predict and evaluate cell and tissue EP.¹⁻¹⁴ Typically, EP takes place when the transmembrane potential (TMP) exceeds a threshold V_{ep} above which electrically conductive pores start forming in the membrane.¹⁻³ Experimental estimates for V_{ep} fall in the range of 0.5–1.2 V but theoretical estimates point to $V_{ep} = 0.258$ V.¹⁵ Most of the existing studies have so far assumed that cell membranes are rigid. This is valid assuming the electro-deformation is much slower in time as compared to the formation of pores. Cells change shape during

the application of μs duration pulses and relax to their original shape when the external stimuli stop.^{16,17} Yet, these volumetric deformations which are ubiquitous in the context of experimental EP, have not gained much attention in numerical models. Figure 1 shows optical microscopy images of two Chinese Hamster Ovary (CHO) cells from a time-lapse imaging (Multimedia view) of five cells. The applied electric field direction is shown in the middle snapshot. A CHO cell is observed to elongate up to 55% of its initial radius in the direction of the neighboring cell during application of a 100 μs long trapezoidal pulse. After the end of the pulse, the cell returns gradually to its initial shape. Elongation decreases from 55% to 28% in the next 100 μs after the pulse, to 8% after 1 ms and to 5% after 2 ms. It is noteworthy that in physiological experimental conditions, the electro-deformation is much smaller than the present case which may not be captured unless more advanced ultrafast imaging is used.

In this Letter, 3-D finite-element method is used to simulate the time-dependent electro-deformation and EP of a

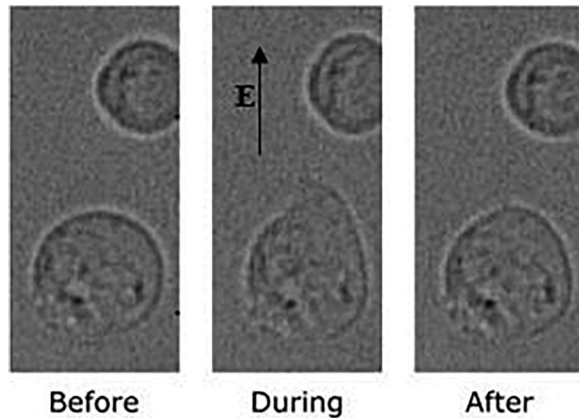


FIG. 1. Snapshots from the time-lapse of CHO cells treated with a $100\ \mu\text{s}$ long pulse (for details on the experimental setup, see [supplementary material](#)). Multimedia view: <https://doi.org/10.1063/1.5079292.1>

single-cell and an assembly of three cells in a specific configuration when one trapezoidal pulse is delivered. Specifically, we borrow from the existing research (see, e.g., Refs. 3, 7, 18, and 19) on the DeBruin and Krassowska asymptotic model of EP for a single cell based on the Smoluchowski equation which is solved on the cell surface to give pore density. The surface patterns of various important quantities like the electric field and surface charge density, Maxwell stress tensor (MST), TMP and pore density are examined at specific times, i.e., at the beginning, during and the end of the pulse. The main innovation of this Letter is to evaluate the correlation between the electric field, TMP, surface charge, and pore density distributions at the cell surface. This modelling is motivated in part by the recently proposed irreversible EP with high-frequency short bipolar pulses^{11,12} that reduces the occurrence of muscle contractions during clinical therapy showing that it is of utmost importance to consider the physical forces that govern cell deformation in order to optimize the EP efficiency.⁴ We also note that other authors have proposed interesting 3D models of simple or realistically shaped cells in densely packed tissues.^{11–14,19,20}

We use a model characterized by a principle of minimality in many respects. As in Refs. 21–23, the electrical properties are deduced from a core-shell modelling. In the case which is considered here, the elastic properties of cells are assumed to be spatially uniform, i.e., both cell and suspension medium have the same properties. Two reasons that spatially uniform properties are used here are that we already know that the mechanical properties of cells remain poorly understood fundamentally^{16,17} and the cell cytoplasm contains an elastic cytoskeleton while the cell exterior may contain an elastic matrix in the case of tissue or less of this in case of suspension media, all of which are too complex to be a part of this model. The purpose of our model remains to highlight some specific features in the results irrespective of the complexity of either the mechanical model or poration model used. Several factors can influence the distribution of electrical stress over the membrane such as the membrane compositional heterogeneity or different conductivity

ratio across the membrane. In this work, we are focused in a particular scenario but such a model raises the question of how the electrical stress induced deformation of the cell would affect the final relaxation state when the electrical pulse delivery is finished. Furthermore, we expect the EP behavior is similar to that observed in previous studies so we can approximate the membrane conductivity by $\sigma(t) = N(t) \left(2\pi r_p^2 \sigma_p d_m / (\pi r_p + 2d_m) \right)$, where we denote the pore density in the cell membrane, the radius and the internal electrical conductivity of a single pore, and the membrane thickness by N , r_p and σ_p , and d_m , respectively.¹⁸ In Refs. 15 and 18 (see also references therein), it was shown that one can extract information about pores by solving a differential equation that governs the dynamics of the pore density as a function of time t , $\dot{N}(t) = \alpha \exp\left(\frac{\text{TMP}}{V_{ep}}\right) \left[1 - \frac{N(t)}{N_0} \exp\left(-q\left(\frac{\text{TMP}}{V_{ep}}\right)^2\right) \right]$, where N_0 is the pore density in the non-electroporated membrane, while α and q are two parameters describing the EP process.

Our starting point is to consider a single spherical cell (at rest) and an assembly of three cells in a specific configuration (Fig. 2) that are exposed to a positive polarity trapezoidal voltage pulse (applied in the z -direction) which delivers an average electric field of strength $E_0 = 5\ \text{kV/cm}$. Of course, one could also consider the case of a multicellular environment modelling tissue,⁹ an interesting generalization that we will discuss later. The electric and elastic properties are given as input parameter values for our simulations (see [supplementary material](#)). First, the Laplace equation is solved for electric potential, and then MST is calculated at the cell membrane as $MST_{ij} = \epsilon \left(E_i E_j - \frac{1}{2} \delta_{ij} E^2 \right)$ where i, j can be x, y , and z , E is the electric field, and ϵ is the membrane permittivity. In this, the surface electric field is obtained from the solution of electric potentials that are coupled at the cell membrane through a boundary condition $\mathbf{n} \cdot \mathbf{J} = \frac{1}{d_m} \left(\sigma - \epsilon \frac{\partial}{\partial t} \right) (V_{int} - V_{ext})$ where \mathbf{J} is the current density \mathbf{n} the outward normal from the cell, d_m is the membrane thickness, σ is the membrane conductivity, and “int” and “ext” denote the cell interior and exterior, respectively. The average electric stretching force experienced by upper or the lower half of the reference cell is within the range of 0.1–0.3 nN. The MST distribution over the cell surface is an input parameter of the elastic model, which solves the time evolution of cell shape. The polarization charge redistribution induces stresses and changes the initially spherical surface of the cell into a prolate shaped surface. For a $6\ \mu\text{m}$ cell radius (R), the electro-deformation $\Delta R/R$, gradually increases the dimension along the z -axis. In our example model, the pulse delivery begins at $t = 10\ \mu\text{s}$ and is finished at $110\ \mu\text{s}$ to achieve good electrostatics. The total simulation runtime is 200 μs .

Simulations are performed using COMSOL Multiphysics® v5.2.²⁴ The simulations use a $50 \times 50 \times 50\ \mu\text{m}^3$ computational domain with electrically insulated boundary conditions for the y - z and x - z planes (conservation of the electric current density), adopting previously published techniques.^{4,8,9,23} Tetrahedral meshes are used in our calculations. The number of tetrahedral elements varies between 16 570 (single-cell) and 19 320 (3-cell configuration). The membrane is replaced by a thin surface to which a boundary condition is assigned between the cytoplasm

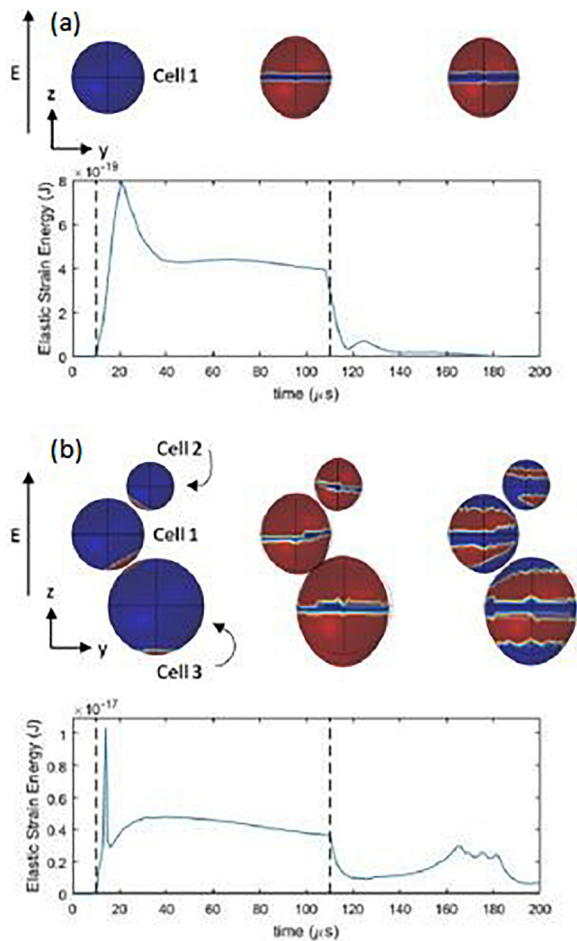


FIG. 2. Simulation results highlighting the trends of the total elastic strain energy in (a) single and (b) 3-cell configurations versus time. The pulse begins at $10 \mu\text{s}$ and ends at $110 \mu\text{s}$ —the limits of the pulse are marked with vertical dashed lines. The 3-dimensional plots represent the areas corresponding to $\text{TMP} \geq V_{\text{ep}} = 0.258 \text{ V}$ (shown in red, otherwise blue) at $t = 10 \mu\text{s}$ (left), $t = 109 \mu\text{s}$ (middle), and $t = 112 \mu\text{s}$ (right). The radii for cells 1–3 are $6, 4,$ and $8 \mu\text{m}$, respectively. Multimedia views: <https://doi.org/10.1063/1.5079292.2>; <https://doi.org/10.1063/1.5079292.3>

and the extracellular medium.^{4,9} The average computational time of a typical simulation is about 13 min for a single cell and 38 min for three cells on Intel® Core™ i7-5500U CPU.

Figure 2 (Multimedia views) shows the area corresponding to $\text{TMP} \geq V_{\text{ep}}$ in red color, starting from the poles, then spreading with time to other regions of the cell surface except near the equator ($\theta = \pi/2$), and then shrinking once the pulse is finished. Charge distribution induces asymmetry along the z -direction, and the appearance of the characteristic prolate-shaped cells is observed as those shown experimentally in Fig. 1. These plots are interesting because a possible indirect detection of EP is that a large rise in the surface charge density is seen once the TMP exceeds V_{ep} corresponding to the induced buildup of charges across the cell membrane. We now describe the temporal dynamics of the elastic strain energy which is equivalent to

the potential energy stored in the material when it is stretched with a force. Within this elastic model, the strain energy follows the voltage excitation up to a maximum, then shows a relaxation followed by a plateau, and has a complex behavior when the pulse is finished depending on the induced buildup of charges across the cell membrane. This is reasonable because we expect that the charge relaxation process for longer times ($>100 \mu\text{s}$) is describable by reversible physics. There is another noticeable point, i.e., the strain energy is two orders of magnitude weaker for the single cell configuration compared to the multiple cell one. Since strain energy represents the energy absorbed in the structure when strained, the larger number of cells the larger energy strain.

Besides determining the dependence of the cell elongation perpendicular to the high electric field regions over the membrane, such calculations can also serve to direct access into the symmetries of the surface charge and pore density and to achieve a correlation between them. The TMP is most naturally described in terms of the Maxwell-Wagner-Sillars interfacial polarization of the membrane. The TMP caused by the delivery of external electric field scales with time as $\propto E_0 R \cos(\theta)[1 - \exp(-t/\tau)]$, where $\tau \propto \sigma^{-1}$ is the time constant of membrane charging. For a single cell configuration (Fig. 3, left column), θ is a polar angle

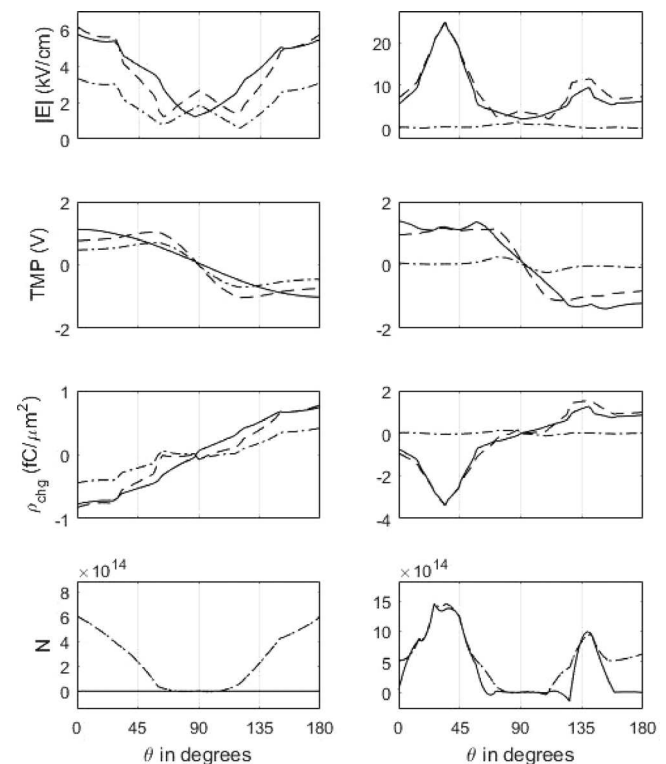


FIG. 3. Comparison of the $(y-z)$ plane distribution of the electric field norm, TMP, surface charge, and pore density of the single (left) and three-cell (right) in suspension at specific times of the electric pulse: $t = 11 \mu\text{s}$ (solid line), $t = 109 \mu\text{s}$ (dashed line), and $t = 112 \mu\text{s}$ (dash-dotted line). θ is a polar angle measured from the center of the cell 1 (of radius $6 \mu\text{m}$) going counterclockwise from the $-z$ to the $+z$ direction.

measured from the center of the cell 1 (of radius $6\mu\text{m}$) going counterclockwise from the $-z$ to the $+z$ direction. To further explore how redistribution of polarization charges can be contrasted with the single cell case, we now consider a 3-cell configuration. For the 3-cell configuration (Fig. 3, right column), θ is defined with respect to cell 1 as before. Cell 2 has a radius of $4\mu\text{m}$ and cell 3 has a radius of $8\mu\text{m}$. The initial gap distances between the closest points of cell 2 and cell 3 surfaces with respect to cell 1 are 630 nm and 420 nm , respectively. The results in Fig. 3 show the asymmetry of the electric field norm, TMP, surface charge density, and pore density.

We first consider a single spherical cell in suspension (Fig. 3, left column) and make some consistency checks, i.e., at $11\mu\text{s}$, one finds a cosine law dependence of the electric field. A closer look at the pore density shows that once pores are created the highest density remains localized at the polarized poles. In our calculations for the 3-cell configuration, the electric field norm shows two peaks. The results show that the angle for the higher peak corresponds to the larger cell and the other peak corresponds to the smaller cell. It is also useful to look at the surface charge density: in the isolated cell case, it correlates well with TMP, but for the 3-cell configuration it correlates with high electric field areas. From the right column of Fig. 3, we also note that there is a coincidence of the extrema of the electric field, TMP, and pore density. Such behavior has been corroborated experimentally in red blood cells as well as in supramolecular giant unilamellar lipid vesicles.⁴ Additionally, the remarkable aspect of this geometry is that it can give rise to the Coulomb repulsion-to-attraction transition when very closely approaching a pair of static bodies having dissimilar surface potentials, a phenomenon associated with an asymmetric electrostatic screening at very small separation between cells.²⁵ From the perspective of generating a cell hierarchy for tissue modelling, the important aspect of this geometry is that it allows simultaneously analyzing proximity, crowding, and correlation effects between cells.

To further challenge our simulation data, in Fig. 4, we plot the MST distribution and elongation δy and δz in the y - and z -directions, respectively.

Firstly, proximity effects lead to distortions of the spatial distributions of δy and δz . Especially instructive is the clearly established correlation between the MST distribution and elongation in the y and z directions as presented in the right column of Fig. 4. The fact that simulations see a much better alignment of these quantities in the direction of the maximum electric field is reflective of the interplay between the surface charge distribution and the mechanical restoring forces of the cell in our model. When the number of cells in proximity is large, it is expected to have the following behavior: the larger local electric field, the more pronounced pore formation.

In summary, this study reveals some of the subtleties of cell electrostatics and mechanics, either for a spherical cell or an assembly of 3-cells in a specific configuration, that involve a complex interplay of the effects of the electric field, cell surface charge, TMP, pore density, and characteristics of the delivered pulse. Together, these observations suggest that the spatial organization of the polarization charges can play an important

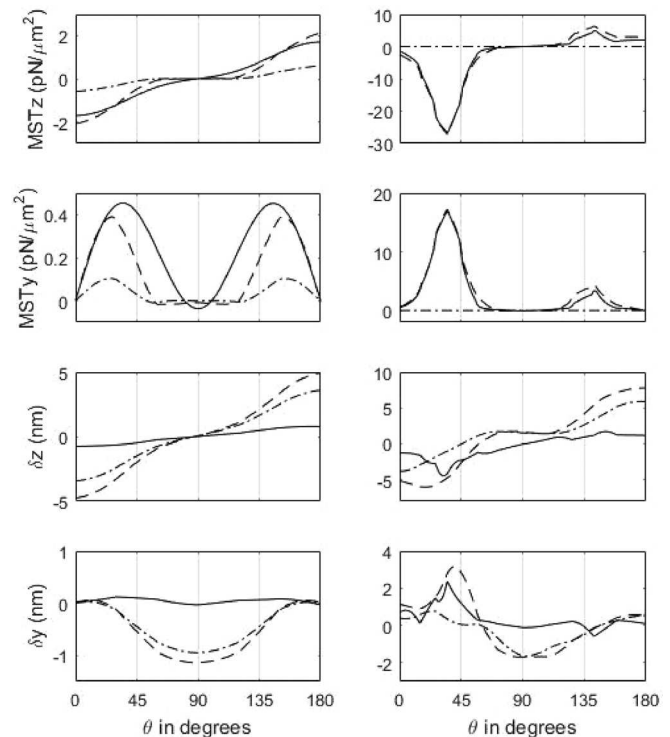


FIG. 4. As in Fig. 3 for the MST distribution and elongation in the y - and z -directions, respectively.

role in electro-deformation and EP of biological cells and that this organization can be controlled to facilitate EP. Our model can also be extended in directions such as linking to various device configurations with microfluidics and transport of dilute species from the cell exterior to its interior or vice-versa. This will render the extended models more appropriate for experimental validations with existing studies.²⁶ A two-dimensional model describing several irregularly shaped cells in proximity has recently been studied by Mescia and co-workers.²⁷

From a physical perspective, it is important to note that some EP models incorporate the change in the membrane tension due to the presence of pores which might also affect membrane elasticity. A more refined elastic model of the cell treating the contributions of the actomyosin cytoskeleton to the cell size and shape variations under external electric perturbation is required for a broader perspective. In particular, we plan to include the effect of cytoskeletal structures since the tensegrity architecture is a fundamental principle that governs how real cells are structured to respond biomechanically to mechanical forces. It is also worth mentioning that electric pulses leading to EP have an effect on the integrity of the cytoskeleton.²⁸ From a biophysics perspective, our study sets the stage to explore more complicated coarse-grained models that generate dense heterogeneous and anisotropic tissues such as in Ref. 8. Also, different kinds of voltage excitation, e.g., high-frequency short bipolar pulses need special attention. Such features will be considered in future work.

See [supplementary material](#) contains the details of the experimental setup and the list of parameters used in our model.

This work was partially supported by the Université de Brest through its mobility program. The Lab-STICC is the Unité Mixte de Recherche CNRS 6285. This work is also partially supported by the Slovenian Research Agency (research core Funding Nos. P2-0249 and IP-0510). The research is conducted within the scope of the electroporation in the Biology and Medicine (EBAM) European Associated Laboratory (LEA). The Vision Research Phantom v2010 camera was kindly provided by Vision Research Europe.

REFERENCES

- ¹D. S. Dimitrov, "Electroporation and electrofusion of membranes," in *Handbook of Biological Physics*, edited by R. Lipowsky and E. Sackmann (Elsevier, Amsterdam, 1995), Vol. 1B, pp. 851–901.
- ²J. C. Weaver and Y. A. Chizmadzhev, "Theory of electroporation: A review," *Bioelectrochem. Bioenergy* **41**, 135–160 (1996).
- ³L. Rems and D. Miklavčič, "Electroporation of cells in complex materials and tissue," *J. Appl. Phys.* **119**, 201101 (2016).
- ⁴E. Goldberg, C. Suárez, M. Alfonso, J. Marchese, A. Soba, and G. Marshall, "Cell membrane electroporation modeling: A multiphysics approach," *Bioelectrochemistry* **124**, 28–39 (2018).
- ⁵M. Bier, W. Chen, T. R. Gowrishankar, R. D. Astumian, and R. C. Lee, "Resealing dynamics of a cell membrane after electroporation," *Phys. Rev. E* **66**, 062905 (2002).
- ⁶C. Chen, S. W. Smye, and M. P. Robinson, "Membrane electroporation theories: A review," *Med. Biol. Eng. Comput.* **44**, 5–14 (2006).
- ⁷G. Pucihar, D. Miklavčič, and T. Kotnik, "A time-dependent numerical model of transmembrane voltage inducement and electroporation of irregularly shaped cells," *IEEE Trans. Biomed. Eng.* **56**, 1491–1501 (2009).
- ⁸T. Murovec, D. C. Sweeney, E. Latouche, R. V. Davalos, and C. Brosseau, "Modeling of transmembrane potential in realistic multicellular structures before electroporation," *Biophys. J.* **111**, 2286–2295 (2016).
- ⁹M. Essone Mezeme, G. Pucihar, M. Pavlin, C. Brosseau, and D. Miklavčič, "A numerical analysis of multicellular environment for modeling tissue electroporation," *Appl. Phys. Lett.* **100**, 143701 (2012); See also M. Essone Mezeme, M. Kranjc, F. Bajd, I. Sersa, C. Brosseau, and D. Miklavčič, "Assessing how electroporation affects the effective conductivity tensor of biological tissues," *Appl. Phys. Lett.* **101**, 213702 (2012).
- ¹⁰H. Isambert, "Understanding the electroporation of cells and artificial bilayer membranes," *Phys. Rev. Lett.* **80**, 3404 (1998).
- ¹¹H. Li, A. Denzi, X. Ma, X. Du, Y. Ning, X. Cheng, F. Apollonio, M. Liberti, and J. C. M. Hwang, "Distributed effect in high-frequency electroporation of biological cells," *IEEE Trans. Microwave Theory Tech.* **65**, 3503–3511 (2017); S. Dong, H. Wang, Y. Zhao, Y. Sun, and C. Yao, "First human trial of high-frequency irreversible electroporation therapy for prostate cancer," *Technol. Cancer Res. Treat.* **17**, 1–9 (2018); B. Valič, M. Golzio, M. Pavlin, A. Schatz, C. Faurie, B. Gabriel, J. Teissié, M. Rols, and D. Miklavčič, "Effect of electric field induced transmembrane potential on spheroidal cells: Theory and experiment," *Eur. Biophys. J.* **6**, 519–528 (2003).
- ¹²C. B. Arena, M. B. Sano, M. N. Rylander, and R. V. Davalos, "High-frequency irreversible electroporation (H-FIRE) for non-thermal ablation without muscle contraction," *IEEE Trans. Biomed. Eng.* **58**, 1474–1481 (2011); D. C. Sweeney, M. Reberšek, J. Dermol, L. Rems, D. Miklavčič, and R. V. Davalos, "Quantification of cell membrane permeability induced by monopolar and high-frequency bipolar bursts of electrical pulses," *Biochim. Biophys. Acta (BBA)-Biomembr.* **11**, 2689–2698 (2016); L. Mescia, M. A. Chiapperino, P. Bia, J. Gielis, and D. Caratelli, "Modeling of electroporation induced by pulsed electric fields in irregularly shaped cells," *IEEE Trans. Biomed. Eng.* **65**, 414–423 (2018).
- ¹³E. C. Gianulis, M. Casciola, S. Xiao, O. N. Pakhomova, and A. G. Pakhomov, "Electropermeabilization by uni- or bipolar nanosecond electric pulses: The impact of extracellular conductivity," *Bioelectrochemistry* **119**, 10–19 (2018).
- ¹⁴V. Novickij, P. Ruzgys, A. Grainys, and S. Šatkauskas, "High frequency electroporation efficiency is under control of membrane capacitive charging and voltage potential relaxation," *Bioelectrochemistry* **119**, 92–97 (2018); J. Dermol and D. Miklavčič, "From cell to tissue properties—modeling skin electroporation with pore and local transport region formation," *IEEE Trans. Biomed. Eng.* **65**, 458–468 (2018).
- ¹⁵K. A. DeBruin and W. Krassowska, "Modeling electroporation in a single cell. I. Effects of field strength and rest potential," *Biophys. J.* **77**, 1213–1224 (1999); "Modeling electroporation in a single cell. II. Effects of ionic concentrations," **77**, 1225–1233 (1999); J. C. Neu and W. Krassowska, "Asymptotic model of electroporation," *Phys. Rev. E* **59**, 3471–3482 (1999).
- ¹⁶B. Varga, C. Fazakas, I. Wilhelm, I. A. Krizbai, Z. Szegetes, G. Váró, and A. G. Véghe, "Elasto-mechanical properties of living cells," *Biochem. Biophys. Rep.* **7**, 303–308 (2016).
- ¹⁷M.-A. Meyers, P.-Y. Chen, A. Y.-M. Lin, and Y. Seki, "Biological materials: Structure and mechanical properties," *Prog. Mater. Sci.* **53**, 1–206 (2008).
- ¹⁸L. Rems, "Cell electrofusion using nanosecond electric pulses," *Sci. Rep.* **3**, 3382 (2013); J. Li and H. Lin, "Numerical simulation of molecular uptake via electroporation," *Bioelectrochemistry* **82**, 10–21 (2011).
- ¹⁹D. Voyer, A. Silve, L. M. Mir, R. Scorretti, and C. Poignard, "Dynamical modeling of tissue electroporation," *Bioelectrochemistry* **119**, 98–110 (2018); G. Pucihar, T. Kotnik, B. Valič, and D. Miklavčič, "Numerical determination of transmembrane voltage induced on irregularly shaped cells," *Ann. Biomed. Eng.* **34**, 642 (2006).
- ²⁰D. Shamoony, S. Lasquelles, and C. Brosseau, "Perspective: Towards understanding the multiscale description of cells and tissue by electro-mechanobiology," *J. Appl. Phys.* **123**, 240902 (2018).
- ²¹R. Pethig, *Dielectric and Electronic Properties of Biological Materials* (Wiley, New York, 1979).
- ²²M. R. Willis, "Dielectric and Electronic Properties of Biological Materials" by R. Pethig, pp 376. John Wiley & Sons, Chichester and New York. 1979. £15, [book review], *Biochem. Educ.* **8**(1), 31 (1980).
- ²³M. Essone Mezeme and C. Brosseau, "Simulation of a toy model of cylindrical cells submitted to nonionizing electromagnetic field: Effect of membrane cell disruption," *J. Appl. Phys.* **107**, 014701 (2010).
- ²⁴COMSOL Multiphysics version 5.2.
- ²⁵T. Murovec and C. Brosseau, "Anisotropy of the crossover between electrostatic attraction and repulsion of biological cells," *Appl. Phys. Lett.* **103**, 193702 (2013).
- ²⁶Y. Zhan, C. Sun, Z. Cao, N. Bao, J. Xing, and C. Lu, "Release of intracellular proteins by electroporation with preserved cell viability," *Anal. Chem.* **84**, 8102 (2012); B. del Rosal, C. Sun, D. N. Loufakis, C. Lu, and D. Jaque, "Thermal loading in flow-through electroporation microfluidic devices," *Lab Chip* **13**, 3119 (2013); T. Geng and C. Lu, "Microfluidic electroporation for cellular analysis and delivery," *Lab Chip* **13**, 3803 (2013).
- ²⁷L. Mescia, M. A. Chiapperino, P. Bia, C. M. Lamacchia, J. Gielis, and D. Caratelli, "Design of electroporation process in irregularly shaped multicellular systems," *Electronics* **8**, 37 (2019).
- ²⁸T. Kotnik, L. Rems L, M. Tarek, and D. Miklavčič, "Membrane electroporation and electropermeabilization: Mechanisms and models," *Annu. Rev. Biophys.* (in press).

Supplemental Material for 'Assessing the electro-deformation and electro-poration of biological cells using a three-dimensional finite element model'

D. Shamoon,¹ J. Dermol-Černe,² L. Rems,² M. Reberšek,² T. Kotnik,² S. Lasquelles,¹ C. Brosseau,^{1,*} and D. Miklavčič²

¹Univ Brest, CNRS, Lab-STICC, CS 93837, 6 avenue Le Gorgeu, 29238 Brest Cedex 3, France

²University of Ljubljana, Faculty of Electrical Engineering, Tržaška 25, 1000 Ljubljana, Slovenia

1. Experimental details

Cell culture

CHO-K1 cells were grown in 25 cm² flasks in HAM's F12 culture medium, supplemented with 10% fetal bovine serum, L-glutamine and antibiotics at 37°C in a humidified 5% CO₂ until 60–80% confluence.

Cell preparation

On the day of experiments, the cell suspension was prepared. After counting the cells, aliquots of 2x10⁵ cells were placed into 1.5 ml centrifuge tubes and centrifuged (270g, 4°C, 5 min). The centrifuged tubes were kept at 4°C up to two hours. Right before the experiments, the cells in the centrifuge tube were first washed with 1 ml of the hypoosmolar medium (0.5 mM Mg²⁺ acetate, 0.1 mM Ca²⁺ acetate, 1 mg/ml bovine serum albumin, and 90 mM glucose (all from Sigma-Aldrich), 12 mS/m). Then, they were centrifuged again in a Labnet C1301 centrifuge for 20 s. Finally, they were resuspended in 200 µl of the hypoosmolar medium. 20 µl of the final cell suspension was transferred to the Eppendorf microfusion chamber (parallel wire electrodes with electrode distance of 200 µm), which was placed on the microscope stage. The fusion chamber was covered with cover glass to prevent medium evaporation.

Pulse delivery

After the transfer to the fusion chamber, cells were left for five minutes to sediment onto the bottom of the chamber. Then, three rectangular pulses of 100 µs and 100 V with a repetition period of 3 ms were delivered with the pulse generator βtech (Electro cell B10, BetaTech, France). The delivered pulses were monitored on LeCroy WavePro 7300A oscilloscope using probe LeCroy PP005A.

Image capture

Cells were monitored under inverted microscope Zeiss Axiovert 200 with ×40 objective magnification. Images were captured with the high-speed camera Phantom v2010 (Vision Research) in PCC 2.5 software (Vision Research). The camera was triggered by the rising edge of the first applied pulse. The delay between the onset of the pulse and the onset of the trigger signal was about 100 ns. We acquired images before, during and after pulse delivery at a frame rate 50000 per second (each image corresponds to 20 µs) with an exposure time of 10 µs. The image resolution was 256×128 pixels, 12 bits per pixel.

2. List of model parameters

Electric pulse parameters	
Pulse duration	100 μ s
Transition time	1 ns
Pulse start time	10 μ s
Pulse end time	110 μ s
Applied voltage	5 kV/cm x 50 μ m = 25 V
Total simulation time	200 μ s
Electrical properties of media	
Relative permittivity of cytoplasm	60
Conductivity of cytoplasm	0.42 S/m
Relative permittivity of suspension	80
Conductivity of suspension	0.012 S/m
Relative permittivity of membrane	8.85
Conductivity of membrane	10^{-6} S/m
Resting membrane potential	-50 mV
Mechanical properties of media	
Density	1050 kg/m ³
Young's modulus	1000 Pa
Poisson ratio	0.4
Pore density model parameters	
Electroporation threshold, V_{ep}	258 mV
Initial pore density, N_0	1.5×10^9 1/m ²
Pore radius, r_p	0.75 nm
α	10^9 1/(m ² s)
q	2.46

Having discussed the deformable single cell and three cell configurations, seven cell configurations are hereby. This case particularly differs from the last two cases as it considers the membrane viscoelasticity additionally. The strain energy of the membrane is analyzed for many realizations and different pulse shapes as well (see Fig.4.1 for pulse shapes).

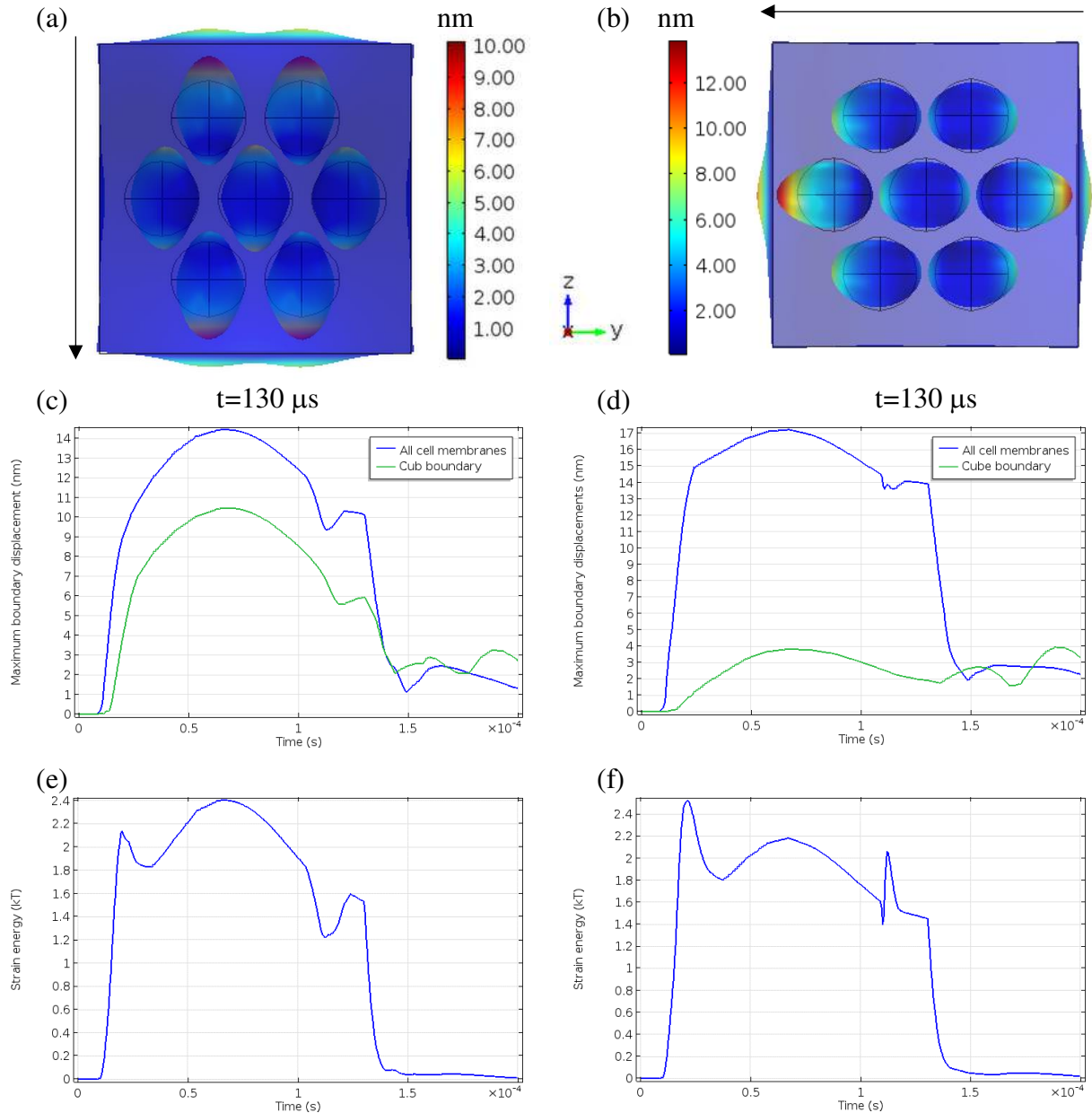


Fig.4.8: (a) Deformation of seven cell configuration A3* (see Fig.4.2 for geometry) stimulated with Pulse 2 (see Fig.4.1 for pulse shape) near the end of the pulse at $t=130 \mu\text{s}$, excited along z axis. (b) Same as in (a) but with excitation along y axis (c) Maximum value of the deforming boundaries of all cells and cube. (d) Same as in (c) but for excitation along y axis. (e) Strain energy in kT with $T=310 \text{ K}$. (f) Same as in (e) but for excitation along y axis.

The case of two configurations (A3* and B2, see Fig.4.2) stimulated separately along orthogonal directions is discussed here while more cases can be found in the publication overleaf. The results are shown in Fig.4.8 and 4.9. ‘*’ signifies a difference that the intercellular distances are more than those in A3 and less than those in A4.

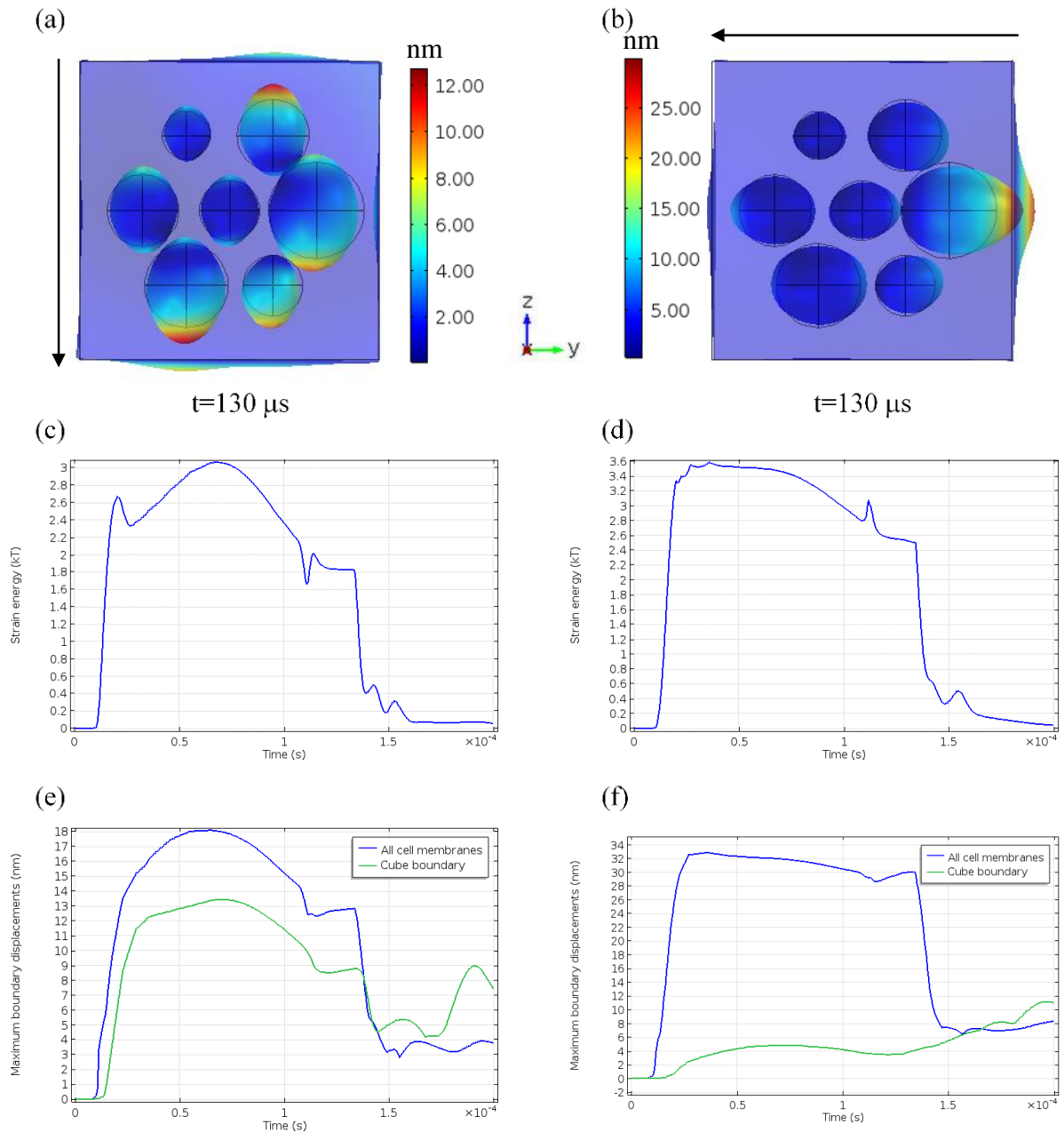


Fig.4.9: (a) Deformation of seven cell configuration B2 (see Fig.4.2 for geometry) stimulated with Pulse 2 (see Fig.4.1 for pulse shape) near the end of the pulse at $t=130 \mu\text{s}$, excited along z axis. (b) Same as in (a) but with excitation along y axis (c) Maximum value of the deforming boundaries of all cells and cube. (d) Same as in (c) but for excitation along y axis. (e) Strain energy in kT with $T=310 \text{ K}$. (f) Same as in (e) but for excitation along y axis.

Shamoon et al. (2019-b)

A multiphysics analysis of the strain energy in multicellular environments

D. Shamoon, S. Lasquelles and C. Brosseau

Applied Physics Letters, 115 (4), (2019) 043701

DOI: 10.1063/1.5109533

A multiphysics analysis of the strain energy in multicellular environments

Cite as: Appl. Phys. Lett. **115**, 043701 (2019); doi: [10.1063/1.5109533](https://doi.org/10.1063/1.5109533)

Submitted: 9 May 2019 · Accepted: 7 July 2019 ·

Published Online: 22 July 2019



View Online



Export Citation



CrossMark

D. Shamoon,  S. Lasquellec, and C. Brosseau^{a)} 

AFFILIATIONS

Univ. Brest, CNRS, Lab-STICC, CS 93837, 6 avenue Le Gorgeu, 29238 Brest Cedex 3, France

^{a)} Author to whom correspondence should be addressed: brosseau@univ-brest.fr

ABSTRACT

This letter considers the strain energy distribution in cell assemblies. Our scalable model consists of N -core-shell spherical structures modeling biological cells with assumptions based on two fundamental premises. First, we use a finite element in the framework of time-domain to solve for the electrodeformation and cell electroporation when a well-defined electrical stimulus is delivered to a multicellular environment. Second, the strain-stress response of the cell assemblies is characterized by a relaxation time which is much larger than the time constant of the membrane charging. A “switch off” (corresponding to times after electrical pulsing) phenomenon observed in the strain energy signal might provide an interesting discriminant test capable of providing different information on the proximity (coupling) effect between cell and assembly anisotropy depending on the type of electrical stimulus employed. In the explicit examples we study, we learn up to date facts about how the local enhancement of the electric field, deformation of the cell, strain energy, and relative area occupied by the pores are modified by varying the intercellular distance distribution.

Published under license by AIP Publishing. <https://doi.org/10.1063/1.5109533>

In this letter, we examine in detail the physics ideas which may be used to obtain a multiphysics model of the strain energy distribution in cell assemblies. The ability of controlling tensegrity in biological materials is still an open question in tissue engineering and has generated widely debated mechanisms on the mechanical forces between cells in tissue based on energetic, time scale, and cell number considerations.^{1–13} From the vantage point of what is seen in experiments, this is an important question since it has been difficult to quantify stress in cells due to their complex shapes and internal structures. Tissue and cell level architecture prevent disruptions from occurring, either by shielding cells from damaging levels of force or, when this is not possible, by promoting safe force transmission through the plasma membrane via protein-based cables and linkages. On the other hand, the issue of electroporating a single cell when an electric excitation is applied is technically challenging.^{1–4}

Throughout this letter, we consider 7-cell groups embedded in an extracellular medium. The motivation for studying these assemblies lies in their potential to help answer current theoretical and experimental questions regarding the collective electromechanical response of deformable spherical cells in proximity to each other, to assess how the intracellular distance and cell compactness can affect the strain energy distribution, and to provide clues for where to search for simple tissue models which are efficient to provide theoretical predictions for classic biological research such as electroporation scenarios. Each cell is assumed to be heterogeneous (core-shell

spherical structures modeling biological cells), with a viscoelastic membrane. This important additional feature in our model is largely based on reports showing evidence that most living cells show a viscoelastic deformation under mechanical forces.¹⁴ In our work, the DeBruin and Krassowska self-consistent model (to give pore density) can be solved locally on the cell surface area for which the local values of the transmembrane potential (TMP) become the input variable.⁴ In our simulations, the surface patterns of the electric field, surface charge density, Maxwell stress tensor (MST), TMP, and pore density can be obtained at specific times, i.e., at the beginning, during, and the end of the electrical stimulus. In order to be concrete, and for illustration purposes, we first consider an assembly of seven cells in specific configurations (Fig. 1) that are exposed to a positive polarity trapezoidal voltage pulse which delivers an average electric field of strength $E_0 = 5$ kV/cm.

First, the electromagnetic equations are solved for electric potential, and then, MST is calculated at the cell membrane. The MST distribution over the cell surface is an input parameter of the viscoelastic model, which solves the time evolution of cell shape. The polarization charge redistribution induces stresses and changes the initially spherical surface of the cell into a prolatelike shaped surface. Typically, electroporation takes place when TMP exceeds a threshold V_{ep} above which electrically conductive pores start forming in the membrane.^{1,3,4} Experimental estimates for V_{ep} fall in the range of 0.5–1.2 V, but in modeling studies, it is usually set to $V_{ep} = 0.258$ V.¹

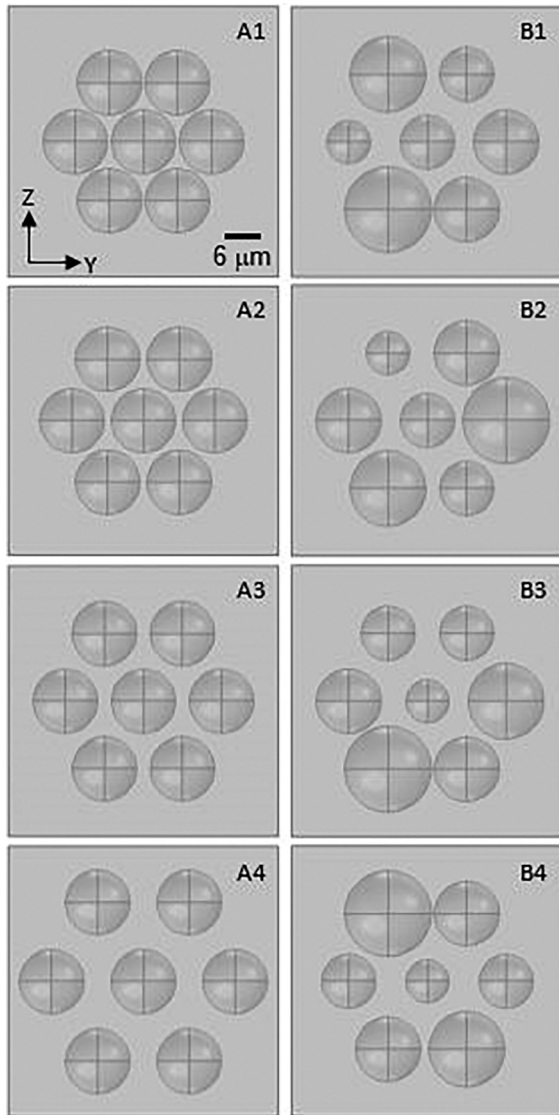


FIG. 1. Schematic of the eight canonical examples of 7-core-shell arbitrarily fixed in space cell configurations and subjected to an electric field pulse. In the A1–A4 configurations, all cells have the same radius set to $6\ \mu\text{m}$, and the intercellular boundary-boundary distance, d_{b-b} , with respect to the central cell is varied from $0.625\ \mu\text{m}$ (A1), $1.25\ \mu\text{m}$ (A2), $2.5\ \mu\text{m}$ (A3) to $5\ \mu\text{m}$ (A4). In the B1–B4 configurations, cells have a radius distribution, leading to a broader d_{b-b} distribution with a minimum set to $0.5\ \mu\text{m}$ with respect to the nearest neighbor. The side of the computational cube domain is $50\ \mu\text{m}$. The cell-size and distance distribution information are given in the [supplementary material](#).

The continuum multiphysics model for calculating the strain energy in multicellular assemblies is performed in three steps. First, under the assumption that cells can be described by (conducting)core-(dielectric)shell structures, the spatial distribution of the electric potential in a subdomain of the cell is solved by making use of Poisson’s equation $-\nabla \times ((\sigma + \epsilon \partial_t) \nabla V) = 0$, where ∂_t denotes the time derivative and σ and ϵ are the conductivity and permittivity of the

subdomain, respectively. The generated fields polarize the cells, leading to emergence of surface charge distributions that locally correlate with enhanced electric field regions, and thus, electrical forces are exerted on the cell membrane that are calculated using MST. Undergraduate textbooks and pioneering papers¹⁹ show that the MST is given by $MST_{ij} = \epsilon(E_i E_j - \frac{1}{2} \delta_{ij} E^2)$, where i, j can be x, y , and z and E is the electric field. The surface electric field is obtained from the solution of electric potentials that are coupled at the cell membrane through the specific boundary condition given by

$$\mathbf{n} \times \mathbf{J} = \frac{1}{d_m} (\sigma_m + \epsilon_m \partial_t) (V_{int} - V_{ext}),$$

where \mathbf{n} is the unit vector normal to the boundary surface, \mathbf{J} is the electric current density, σ_m is the membrane conductivity, d_m is the membrane thickness, and “int” and “ext” denote the cell interior and exterior sides, respectively. A resting potential of $-50\ \text{mV}$ is set. To be specific, we will assume that the conductivity and permittivity values for the interior and exterior sides of the cell and for the membrane are listed in Table S1 of the [supplementary material](#). The second stage in the procedure is to model the cell deformation. From this prospective, the resulting stress distribution is coupled to the structural model for calculation of membrane displacement u . In the case at hand, the strain energy was calculated by solving first $\rho \partial_t^2 \mathbf{u} = \nabla \times \mathbf{S}$, where it should be borne in mind that ρ denotes the mass density and \mathbf{S} denotes the stress.^{21,22} The membrane is modeled with a viscoelastic material, while the inner and outer regions of the cell are modeled with an elastic material. The stress leads to deformation in all media (elastic and viscoelastic). The strain energy of the cell membrane can be calculated for both deformable materials as $E_{mem/med} = \int \int \int \mathbf{S} \times \gamma \, d\Omega / 2$, where γ is the strain and $d\Omega$ is the volume or surface element. The final stage is to focus on the pore dynamics during pulsing. For simplicity, we assume a fixed pore radius ($0.75\ \text{nm}$).²¹ We calculate the pore density in the membrane, N , based on the highly nonlinear dependence on TMP, i.e., $\partial_t N = \alpha \exp((TMP/V_{ep})^2) [1 - (N(t)/N_0) \exp(-q(TMP/V_{ep})^2)]$, which alters the initial cell membrane conductivity by adding the following term:

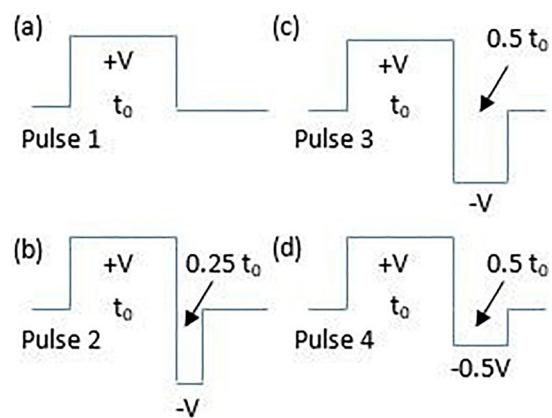


FIG. 2. Different electric pulse stimuli used in this study: (a) unipolar pulse, (b) bipolar pulse, (c) the same as (b) but differing in the width and depth of the second pulse, (d) the same as (b) but differing in the width and depth of the second pulse. Here, $V = 25\ \text{V}$ applied over the distance $50\ \mu\text{m}$, leading to an average field of $5\ \text{kV/cm}$ during the time interval $t_0 = 100\ \mu\text{s}$.

$$\sigma_{ep}(t) = N(t) \left(\frac{2\pi r_p^2 \sigma_p d_m}{(\pi r_p + 2d_m)} \right).$$

Here, we denote the pore density in the cell membrane, the radius and the electrical conductivity of a single pore, and the membrane thickness by N , r_p and σ_p , and d_m , respectively; N_0 is the pore density in the nonelectroporated membrane; α and q are two parameters describing the EP process.⁴ With this result in hand, the number of pores involves surface integration of pore density over the total cell membrane surface area, and so we obtain $N_{pores} = \int \int N dA$. Likewise, the total membrane surface area for the configuration is $3.16 \times 10^{-9} \text{ m}^2$.

It is useful for us to first focus on the trapezoidal voltage pulse excitation [Fig. 2(a)] of 100 μs duration. As a matter of practice, the

total simulation runtime is 200 μs . Simulations are performed using COMSOL Multiphysics®.¹⁵ Unless specifically noted, the electric field is oriented along the z-axis. Other types of well-defined electric stimuli, depicted in Figs. 2(b)–2(d), will be considered later.

As an example, Fig. 3 (Multimedia view) shows the evolution of TMP exceeding the electroporation threshold voltage V_{ep} which is shown by regions colored in red for three fixed times during the application of the voltage pulse. In the “switch on” state, as time goes by, the red region in proportion to the total area increases from the poles and subsequently decreases because the TMP decreases. It is worth observing that these 3D plots are consistent with the anisotropic dependence of the TMP, i.e., the induced TMP varies locally with the position on the membrane with the highest established $|TMP|$ at the poles of the cell and minimal $|TMP|$ established around the equator, and so only the poles are electroporated. It appears that pore density persists in all areas where TMP is above threshold, but as the pulse falls, TMP quickly decreases from the poles (Fig. 3), while pore density decreases more slowly outside the simulation temporal window.

With this understanding, we proceed to estimate the temporal dynamics of the maximum value of the electric field norm on the cell membrane [Fig. 4(a)], the total number of pores [Fig. 4(b)] assuming a fixed pore radius set to 0.75 nm, and the relative pore area [Fig. 4(c)]. It turns out that the observed behavior of the electric field norm of the Ai configurations is qualitatively similar to those of the Bi configurations, but the larger amplitude of the electric field evidenced for configurations B2 and B3 is attributed to the proximity (coupling) effect. In

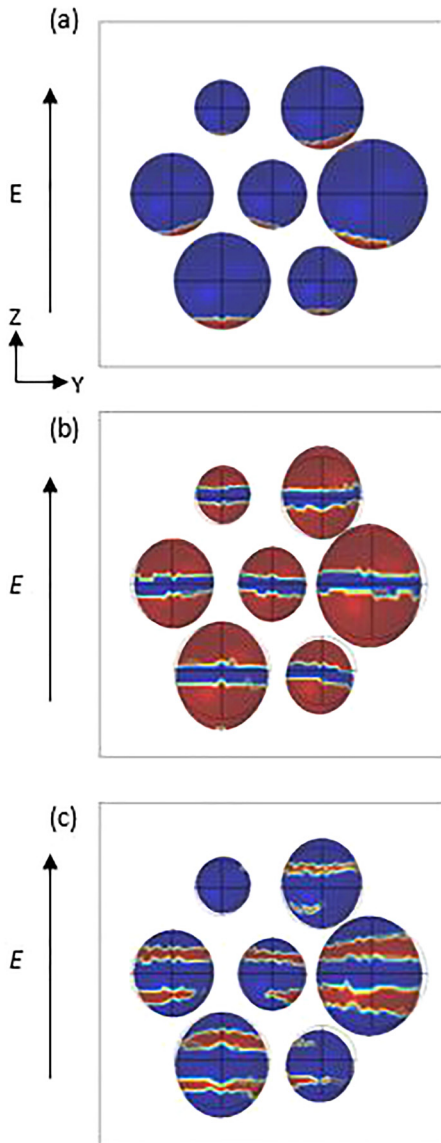


FIG. 3. The 3D plots represent the regions for configuration B2 corresponding to $TMP \geq V_{ep} = 0.258 \text{ V}$ (shown in red, otherwise blue) when pulse 1: (a) rises, (b) is maintained on, and (c) falls. Multimedia view: <https://doi.org/10.1063/1.5109533.1>

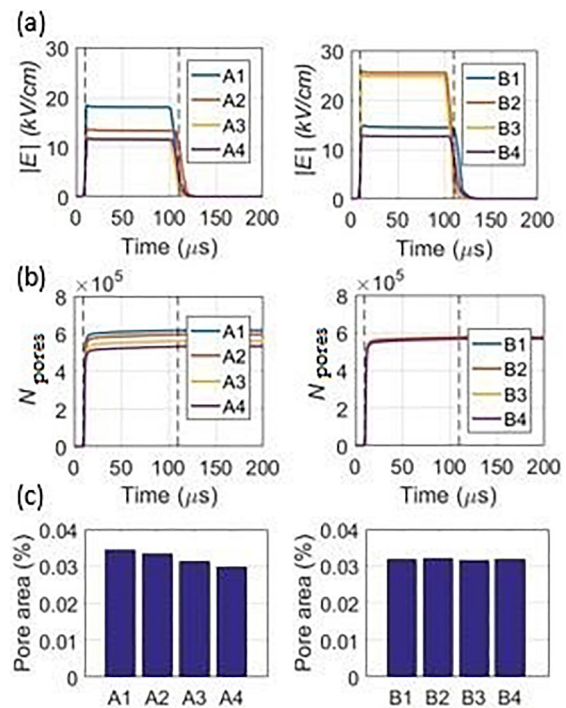


FIG. 4. (a) The maximum value of the electric field norm on membranes, (b) the total number of pores, and (c) the fractional pore area occupied on the cell membrane for the different configurations studied excited with pulse 1. The dashed lines indicate the beginning and end of the pulse.

point of fact, the smallest d_{b-b} value in these configurations occurs at a specific angle of the electric field orientation leading to large local field enhancement. The number of pores exhibits a transition that is abrupt as the voltage pulse is switched on [Fig. 4(b)]. The plateau in the number of pores dynamics can be accounted for by the much slower rate of pore destruction than the rate of pore creation.^{16–20} Pore persistence when the pulse is switched off has been described and analyzed in Ref. 16. Histograms of the fractional pore area are not distinguishable for configurations Bi most likely because the average value of d_{b-b} does not vary much between the Bi configurations. In contrast, the histograms shown in the left panel of Fig. 4(c) are somewhat more discriminant for configurations Ai because the average d_{b-b} value varies much more among the Ai configurations. Be this as it may, the pore area is suggestive to be more sensitive to symmetry rather than the proximity effect.

Next, we analyze the effect of symmetry and proximity effects on the strain energy distribution of the interior and exterior of the cell and viscoelastic membrane [Figs. 5(a) and 5(b)] for the different configurations shown in Fig. 1. First, there is a general pattern in these graphs in the switch on state, i.e., a narrow peak during a few tens of microseconds followed by a broad plateau. Second, it is noticeable that in the switch off (postpulse) state, a second peak is observed with a time scale which can range from 150 to 200 μs . This observation does

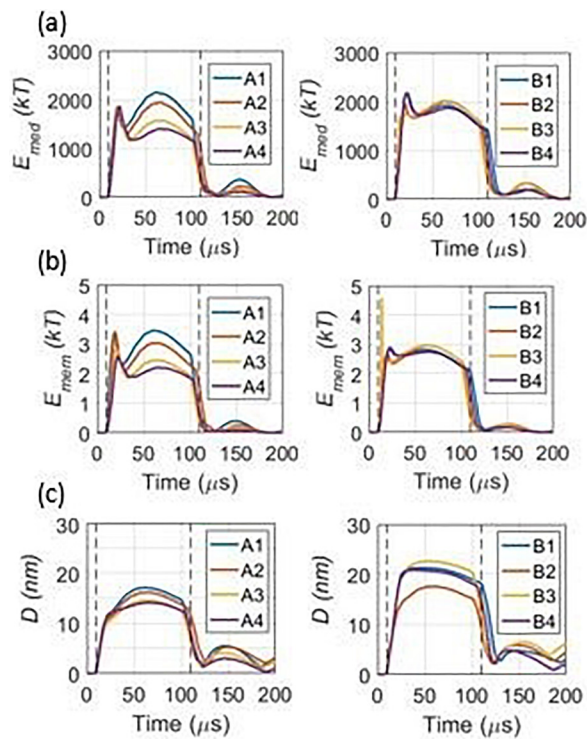


FIG. 5. Simulation results highlighting trends of the strain energy in 7-cell configurations vs time when the different configurations are excited by pulse 1. The dashed lines indicate the beginning and end of the pulse. (a) Strain energy for the interior and exterior of the cell, (b) strain energy for the viscoelastic membrane, and (c) the maximum value of the membrane displacement for the different configurations studied. Physiological conditions ($T = 310\text{ K}$).

not arise from the dominance of the mechanical relaxation process over the electrical charge relaxation since it was also observed in our earlier study dealing with elastic deformation of cells after removal of the electric stimulus.¹ The incomplete shape recovery in the switch off appears to be consistent with the power-law dynamics of cell deformation discussed in Ref. 14. The switch off signal is likely observable in currently AFM-based, scanning probe and confocal fluorescence microscopy experiments under *in vivo* experiments.¹⁷ Figure 5(c) shows the maximum value of the membrane displacement from its original position.

Particular attention is now paid to explore the mechanical response to a bipolar pulse stimulus. It is worth noting that these calculations are performed for configurations A3* and B2 which have an identical average value of d_{b-b} of $3\ \mu\text{m}$ [the star in A3* means that it is neither a A3 nor a A4 configuration since the average d_{b-b} value lies in between the value for A3 ($2.5\ \mu\text{m}$) and that for A4 ($5\ \mu\text{m}$)]. Interestingly, there is a rather clear peak corresponding to the zero-crossing of voltage excitation when the electrical stimulus is oriented along the y-axis. Additionally, it is interesting to note that this switch on peak signal can be larger by a factor of 8 than the corresponding peak signal when the electrical stimulus is oriented along the x-axis that. In the right panel of Fig. 6, we show the corresponding behavior for the B2 configuration. We also point out that the “off” state associated with bipolar pulse stimuli is clearly visible for pulse 2 and 3 excitations of the assemblies containing random distributions of cells.^{23–25}

To summarize, we present explicit evidence of collective behavior of cell assemblies by analyzing their electromechanical response. The

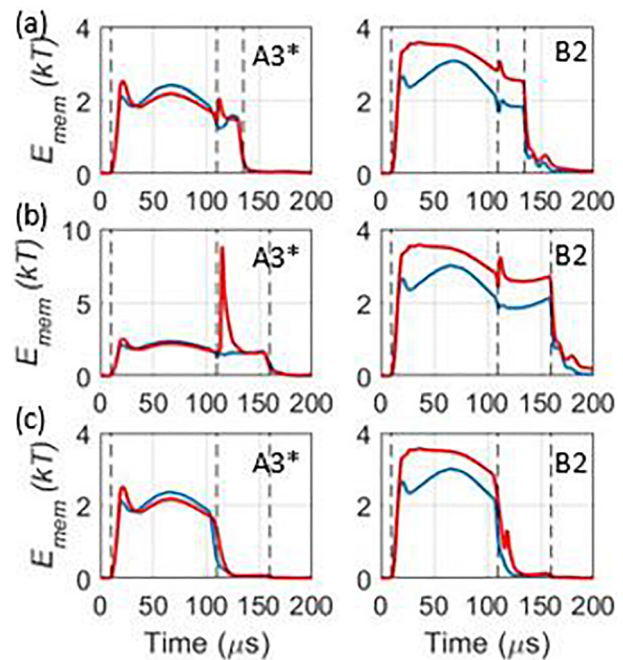


FIG. 6. Strain energy of the membrane as a function of time when configurations A3* and B2 are excited vertically (along the z-axis, blue line) and horizontally (along the y-axis, red line) by (a) pulse 2, (b) pulse 3, and (c) pulse 4, respectively. T is defined by physiological conditions ($T = 310\text{ K}$). The dashed lines indicate the beginning and end of the pulse.

studied heterogeneous configurations present a case in which the local enhancement of the electric field, deformation of the cell, strain energy, and relative area occupied by the pores are sensitive to multiple phenomena that can be difficult to deconvolve. The other remarkable aspect is that we report a switch off (postpulse) phenomenon for several kinds of electrical stimuli observed in different cell configurations. Within our framework, it is possible to obtain also some insight into the parameters affecting the temporal dynamics of the local enhancement of the electric field, the surface charge density, the polarization distribution, the relative deformation, the strain energy, and the pore area extent within the cell membrane. Here, we are interested in cellular hardware (structure and electromechanical properties), but we have had little to say about cellular software (information processing capabilities). A comprehensive study of how they interplay to control cell form and function in tissues, i.e., how the mechanical signals are transmitted and potentially transduced into intracellular biochemical signals, is useful because it can open newer doors to be used for 3D engineered tissues.

See the [supplementary material](#) for the list of the parameter values for our electrodeformation and electroporation model [Fig. S1 (Multimedia view)] describing the temporal evolution of the TMP for configurations A1 and a short discussion of the intercellular boundary-boundary distance histograms for configurations A1–A4 and B1–B4 (Fig. S2).

D.S. would like to thank Université de Brest for supporting this research through its Ph.D. program. The Lab-STICC is the Unité Mixte de Recherche CNRS 6285.

REFERENCES

- D. Shamoony, J. Dermol-Cerne, L. Rems, M. Rebersek, T. Kotnik, S. Lasquellec, C. Brosseau, and D. Miklavčič, "Assessing the electro-deformation and electro-permeabilization of biological cells using a three dimensional finite element model," *Appl. Phys. Lett.* **114**, 063701(1)–063701(5) (2019).
- T. Murovec, D. C. Sweeney, E. Latouche, R. V. Davalos, and C. Brosseau, "Modeling of transmembrane potential in realistic multicellular structures before electroporation," *Biophys. J.* **111**, 2286–2295 (2016).
- M. E. Mezeme, G. Pucihar, M. Pavlin, C. Brosseau, and D. Miklavčič, "A numerical analysis of multicellular environment for modeling tissue electroporation," *Appl. Phys. Lett.* **100**, 143701(1)–143701(4) (2012); M. E. Mezeme, M. Kranjc, F. Bajd, I. Sersa, C. Brosseau, and D. Miklavčič, "Assessing how electroporation affects the effective conductivity tensor of biological tissues," *ibid.* **101**, 213702(1)–213702(4) (2012).
- K. A. DeBruin and W. Krassowska, "Modeling electroporation in a single cell. I. Effects of field strength and rest potential," *Biophys. J.* **77**, 1213–1224 (1999); K. A. DeBruin and W. Krassowska, "Modeling electroporation in a double cell. II. Effects of ionic concentrations," *ibid.* **77**, 1225–1233 (1999); J. C. Neu and W. Krassowska, "Asymptotic model of electroporation," *Phys. Rev. E* **59**, 3471–3482 (1999).
- B. Varga, C. Fazakas, I. Wilhelm, I. A. Krizbai, Z. Szegletes, G. Váró, and A. G. Végh, "Elasto-mechanical properties of living cells," *Biochem. Biophys. Rep.* **7**, 303–308 (2016).
- M.-A. Meyers, P.-Y. Chen, A. Y.-M. Lin, and Y. Seki, "Biological materials: Structure and mechanical properties," *Prog. Mater. Sci.* **53**, 1–206 (2008).
- D. Shamoony, S. Lasquellec, and C. Brosseau, "Perspective: Towards understanding the multiscale description of cells and tissue by electro-mechanobiology," *J. Appl. Phys.* **123**, 240902(1)–240902(18) (2018).
- N. Wang, J. P. Butler, and D. E. Ingber, "Mechanotransduction across the cell surface and through the cytoskeleton," *Science* **260**, 1124 (1993).
- L. Mescia, M. A. Chiapperino, P. Bia, C. M. Lamacchia, J. Gielis, and D. Caratelli, "Design of electroporation process in irregularly shaped multicellular systems," *Electronics* **8**, 37(1)–37(17) (2019).
- K. E. Kasza, A. C. Rowat, J. Liu, T. E. Angelini, C. P. Brangwynne, G. H. Koenderink, and D. A. Weitz, "The cell as a material," *Curr. Opin. Cell Biol.* **19**, 101 (2007).
- D. E. Ingber, "Tensegrity I. Cell structure and hierarchical systems biology," *J. Cell Sci.* **116**, 1157 (2003); D. E. Ingber, N. Wang, and D. Stamenovic, "Tensegrity, cellular biophysics, and the mechanics of living systems," *Rep. Prog. Phys.* **77**, 046603 (2014).
- A. R. Dunn and A. Price, "Energetics and forces in living cells," *Phys. Today* **68**(2), 27 (2015).
- A. M. Handorf, Y. Zhou, M. A. Halanski, and W.-J. Li, "Tissue stiffness dictates development, homeostasis, and disease progression," *Organogenesis* **11**, 1–15 (2015).
- N. Bonakdar, R. Gerum, M. Kuhn, M. Spörrer, A. Lippert, W. Schneider, K. E. Aifantis, and B. Fabry, *Nat. Mater.* **15**, 1090–1094 (2016).
- COMSOL Multiphysics Version 5.2.
- Z. Q. Levine and P. T. Vernier, "Life cycle of an electropore: Field-dependent and field-independent steps in pore creation and annihilation," *J. Membr. Biol.* **236**, 27–36 (2010); A. G. Pakhomov, J. F. Kolb, J. A. White, R. P. Joshi, S. Ziao, and K. H. Schoenbach, "Long-lasting membrane permeabilization in mammalian cells by nanosecond pulsed electric field (nsPEF)," *Bioelectromagnetics* **28**, 655–663 (2007); A. G. Pakomov, E. Gianulis, P. T. Vernier, I. Semenov, S. Xiao, and O. Pakhomova, "Multiple nanosecond electric pulses increase the number but not the size of long-lived nanopores in the cell membrane," *Biochim. Biophys. Acta* **1848**, 958–966 (2015).
- G. W. Brodland, V. Conte, P. G. Cranston, J. Veldhuis, S. Narasimhan, M. S. Hutson, A. Jacinto, F. Ulrich, B. Baum, and M. Miodownik, "Video force microscopy reveals the mechanics of ventral furrow invagination in *Drosophila*," *Proc. Natl. Acad. Sci. U. S. A.* **107**, 22111–22116 (2010).
- E. Goldberg, C. Suarez, M. Alfonso, J. Marchese, A. Soba, and G. Marshall, *Bioelectrochemistry* **124**, 28–39 (2018).
- J. Eyckmans, T. Boudou, X. Yu, and C. S. Chen, "A hitchhiker's guide to mechanobiology," *Dev. Cell* **21**, 35–47 (2011).
- R. S. Son, T. R. Gowrishankar, K. C. Smith, and J. C. Weaver, "Modeling a conventional electroporation pulse train: Decreased pore number, cumulative calcium transport and an example of electrosensitization," *IEEE Trans. Biomed. Eng.* **63**, 571 (2016).
- M. E. Gurtin, *An Introduction to Continuum Mechanics* (Academic Press, 1982).
- R. Pethig, *Dielectric and Electronic Properties of Biological Materials* (Wiley, New York, 1979); C. Gabriel, "Dielectric properties of biological materials," in *Bioengineering and Biophysical Aspects of Electromagnetic Fields*, edited by F. S. Barnes and B. Grenebaum (CRC Press, New York, 2006); K. R. Foster and H. P. Schwan, *Crit. Rev. Biomed. Eng.* **17**, 25 (1989); G. Pucihar, D. Miklavčič, and T. Kotnik, "A time-dependent numerical model of transmembrane voltage inducement and electroporation of irregularly shaped cells," *IEEE Trans. Biomed. Eng.* **56**, 1491–1501 (2009); H. Isambert, "Understanding the electroporation of cells and artificial bilayer membranes," *Phys. Rev. Lett.* **80**, 3404 (1998).
- D. P. Tieleman, H. Leontiadou, A. E. Mark, and S.-J. Marrink, "Simulation of pore formation in lipid bilayers by mechanical stress and electric fields," *J. Am. Chem. Soc.* **125**, 6832–6838 (2003).
- L. Yu and Y. Sheng, "Effect of object 3D shape on the viscoelastic testing in optical tweezers," *Opt. Express* **23**, 6020–6028 (2015); T. Klöppel and W. A. Wall, "A novel two-layer, coupled finite element approach for modeling the nonlinear elastic and viscoelastic behavior of human erythrocytes," *Biomech. Model. Mechanobiol.* **10**, 445–459 (2011).
- L. Rems, M. Ušaj, M. Kandušer, M. Reberšek, D. Miklavčič, and G. Pucihar, "Cell electrofusion using nanosecond electric pulses," *Sci. Rep.* **3**, 3382 (2013).

Supplementary Material of: A multiphysics analysis of the strain energy in multicellular environments, by D. Shamoon, S. Lasquellec, and C. Brosseau*

The Supplementary Material contains the list of the parameter values for our electrodeformation and electroporation model, a figure (Fig. S1) describing the temporal evolution of the TMP for configurations A1, and a short discussion of the intercellular boundary-boundary distance histograms for configurations A1-A4 and B1-B4 with a figure (Fig. S2).

Table S1: Parameter values for the electrodeformation and electroporation model. References: ^a[1], ^b[18,24], ^c[4,18,25].

Electric pulse parameters	
Pulse duration parameter t_0	100 μs
Transition time	1 μs
Applied voltage	5 $\text{kVcm}^{-1} \times 50 \mu\text{m} = 25 \text{ V}$
Total simulation time	200 μs
Electrical properties	
Relative permittivity of the cytoplasm ^a	60
Conductivity of the cytoplasm ^a	0.42 Sm^{-1}
Relative permittivity of the suspension/extracellular matrix ^a	80
Conductivity of the suspension/extracellular matrix ^a	0.012 Sm^{-1}
Relative cell membrane permittivity ^a ϵ_m	8.85
Initial cell membrane conductivity ^a	10^{-6} Sm^{-1}
Resting transmembrane potential ^a U_{res}	-50 mV
Structural properties	
Thickness of the cell membrane ^a d_m	5 nm
Uniform density (all regions) ^b	1050 kgm^{-3}
Young's modulus (int/ext of cell) ^b	1000 Pa
Poisson ratio (int/ext of cell) ^b	0.4
Young's modulus (cell membrane) ^b	500 Pa
Poisson ratio (cell membrane) ^b	0.49
Shear modulus (cell membrane) ^b	1500 Pa
Viscous relaxation time (cell membrane) ^b	0.1 s
Pore density model parameters	
Electrical conductivity of a single pore ^a σ_p	0.114 Sm^{-1}
Electroporation threshold ^c V_{ep}	258 mV
Initial pore density ^c N_0	$1.5 \times 10^9 \text{ m}^{-2}$
Pore radius ^c r_p	0.75 nm
Creation rate coefficient ^c α	$1 \times 10^9 \text{ m}^{-2}\text{s}^{-1}$
Pore creation rate ^c q	2.46

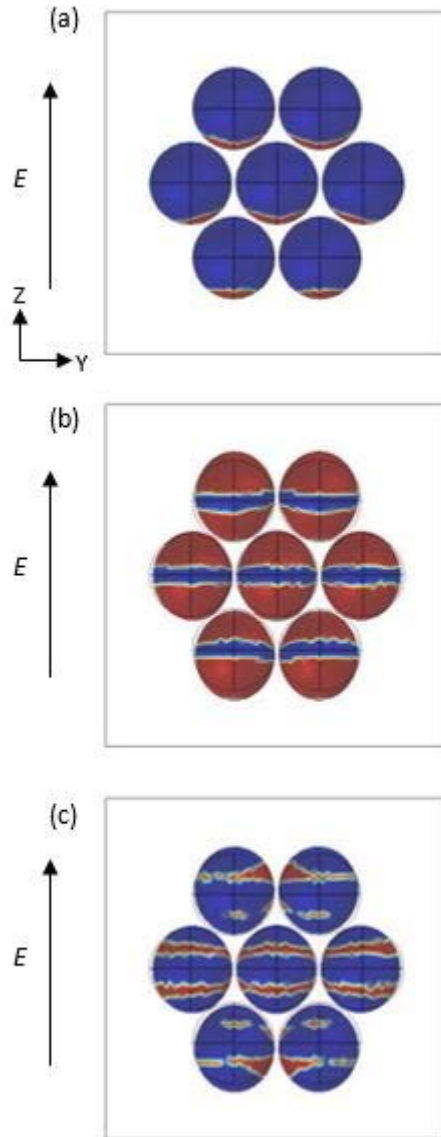


Fig. S1: The 3D plots represent the regions for configuration A1 corresponding to $TMP \geq V_{ep} = 0.258$ V (shown in red, otherwise blue) when pulse 1: (a) rises, (b) is maintained on, and (c) falls (see video Fig. S1 (Multimedia view)).

In this study we consider two series of configurations: a first one with a discrete distribution of the intercellular boundary-boundary distance d_{b-b} values and same cell radius leading to symmetric and regular configurations (A_i , with $i=1,2,3,4$ in Fig. 1), and the other one with a relatively broad distribution of d_{b-b} values (left panel of Fig. S2) thanks to the radius distribution yielding asymmetric and irregular configurations (B_i , with $i=1,2,3,4$ as can be seen in Fig.1). In the A_1 - A_4 configurations, the intercellular boundary distance is respectively x , $2x$, $4x$, $8x$ (where $x=0.625 \mu\text{m}$) and the cell radius is set to $6 \mu\text{m}$. If we look at

the right panel of Fig. S2, it can be seen that the symmetry-breaking B1-B4 configurations are arranged in such a way as to allow the d_{b-b} values to be randomly distributed.

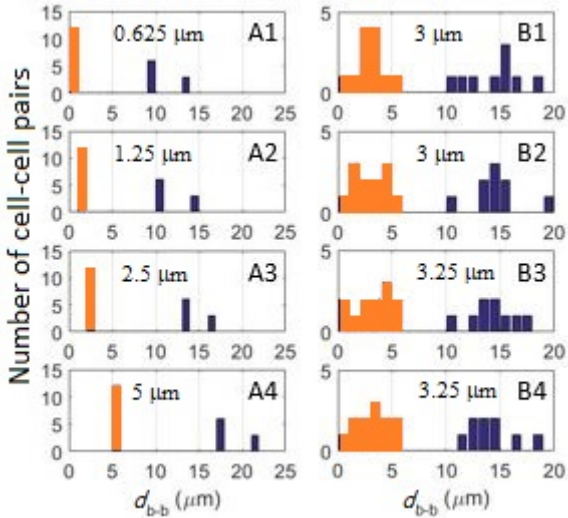


Fig. S2: Proximity histograms for configurations A1-A4 and B1-B4, where d_{b-b} is the intercellular boundary-boundary distance. In these plots, the number indicates the average value of d_{b-b} for the color histogram (orange) corresponding to the lowest d_{b-b} values.

4.1.2 Large number of deforming cells (unpublished work)

The case of N-spherical-cell assemblies is further considered by using larger values of N. An algorithm designed to build a random distribution of non-penetrating N-spherical-cell assembly is used (see Appendix A). Our initial motivation was to consider hundreds or thousands of such assemblies in the same spirit as was done for the statistical analysis of random checkerboards i.e. to represent average properties of cell assembly realizations. But, at present, it represents a challenging task since each simulation runs for about one and a half hour or more. It is reminded that in the same spirit, 5-15 such random assemblies have been previously considered by Mezeme et al. (2012) [22-a] for non-deformable cells. For deformable cells of large number, the analysis is computationally more expensive than that discussed in Chapter 3.

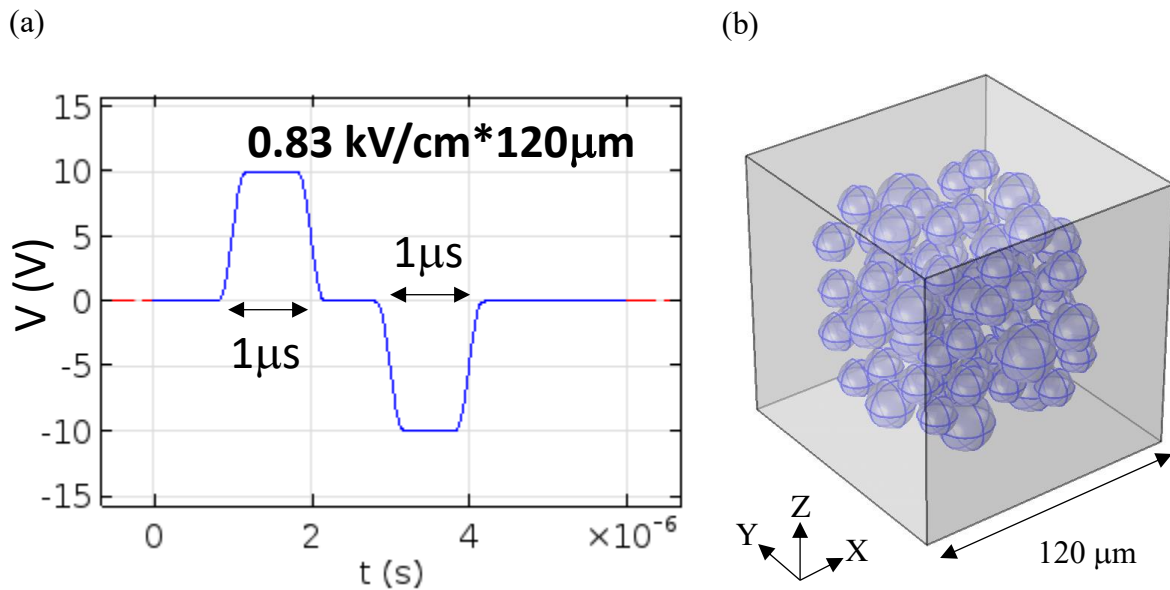


Fig.4.10: Electrical pulse and model geometry of 76 spherical cells (of radii 8, 10, 12 μm) for time-dependent analysis.

In this preliminary test, we consider a single assembly. When the post-simulation analysis protocol will be fully automated, its execution will be made straightforward. Thus the number of assemblies can be increased to formulate average ED and EP behaviors. The

algorithm takes the cube dimensions and number of cells with specified dimensions as inputs and returns the positions of each cell as output. The assembly of cells considered here has 76 cells corresponding to a filling fraction of 0.1338. This assembly is electrically stimulated with the voltage pulse depicted in Fig.4.10. Conductivity of cytoplasm is set to 0.12 Sm^{-1} , while that of suspension media is 0.53 Sm^{-1} . Elastic behavior of cells considered with Young's modulus set to 1000 Pa.

4.1.2.1 ED behavior

The analysis for ED is conducted as before and membrane displacements are obtained. Figure 4.11 shows two snapshots corresponding to the instant times during the end of each pulse polarity.

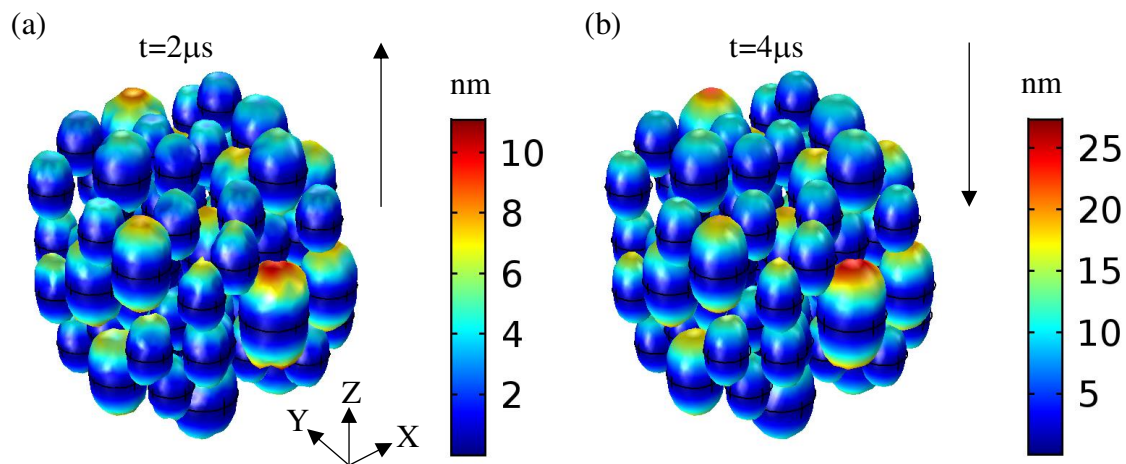


Fig. 4.11: Snapshots of total membrane displacement in nm during the end of each pulse polarity. Arrow depicts the direction of electric field. Pulse and configuration as in Fig.4.10.

It can be observed that the local deformation has more than doubled to 27 nm by the end of second pulse as compared to its value at the end of the first one, i.e. 11 nm. By extracting the maximum value of the total membrane displacement from all cell membranes, we find that it mainly increases rapidly during the rise of the pulse polarities and tends to remain constant after the pulse has gone till the end of simulation ($t = 6 \mu\text{s}$). Since, an elastic model is used, it

is expected to further reduce if longer simulation times are used. Figure 4.12 clearly shows that the maximum value of membrane displacement is calculated as 27 nm.

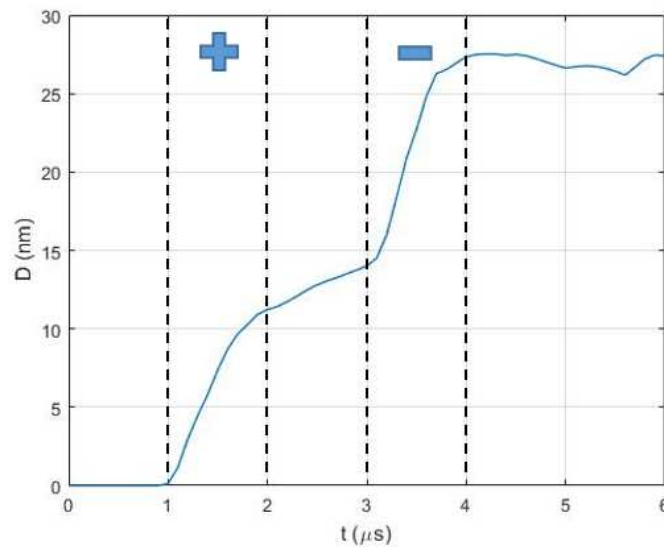


Fig.4.12: Maximum value of the total displacement (anywhere on the membranes) as a function of time. The dashed regions with '+' and '-' indicate pulse polarities. Pulse and configuration as in Fig.4.10.

Strain energy is obtained (Fig.4.13) which confirms the trend illustrated in Fig.4.12 and indicates that the system has still not relaxed mechanically after 6 μs (the end of simulated time). Even though a slight relaxation follows each drop of pulse polarities, the strain in the system persists at least for the duration of the whole simulation.

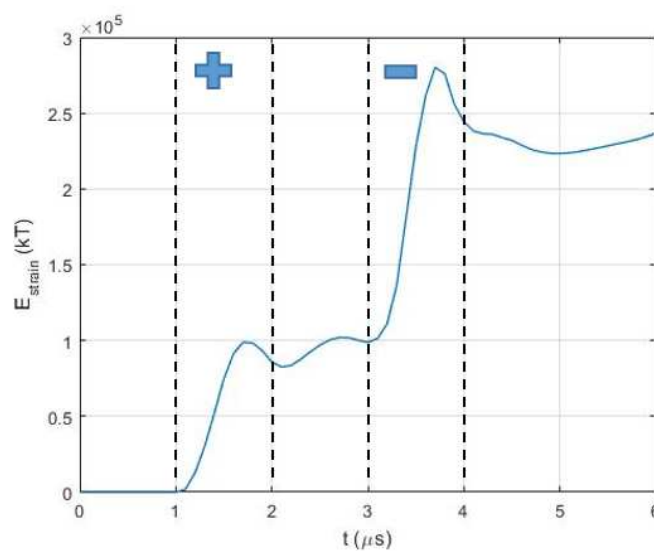


Fig. 4.13: Strain energy for the 76 cell configuration as a function of time. The dashed regions with '+' and '-' indicate pulse polarities. Pulse and configuration as in Fig.4.10.

However, it must be noted that in the event of a net translation of the cell, the strain will remain non-zero even after a complete mechanical relaxation to original shape since the strain is calculated according to the original position of the membrane.

4.1.2.2 EP behavior

EP behavior is now examined for the assembly of cells with $N=76$. The number of generated pores is very small (only about 50 (i.e. 162-112), see Fig.4.14). It is recalled that the number of pores in our previous works i.e. Shamooun et al. (2019-a, b) [47, 49] was calculated to reach 10^5 before becoming constant for the remaining duration of the simulation. Here, the small number is due to the weakness of electric field pulse-strength (0.83 kV/cm). This is further confirmed by running complementary sets of simulations for pulse-strengths 1 kV/cm and 1.2 kV/cm for which the number of pores reached 26,000 and then to 10^5 , respectively. Accordingly, the maximum membrane displacements increase to 47 nm and 102 nm. It is also noted that the formation of the pores increases at the end of positive pulse polarity rather than at the beginning. We expect that this observation is related with the membrane charging time which in this particular case is in the range of 0.74-1.1 μs owing to the cell-radii distribution between 8-12 μm .

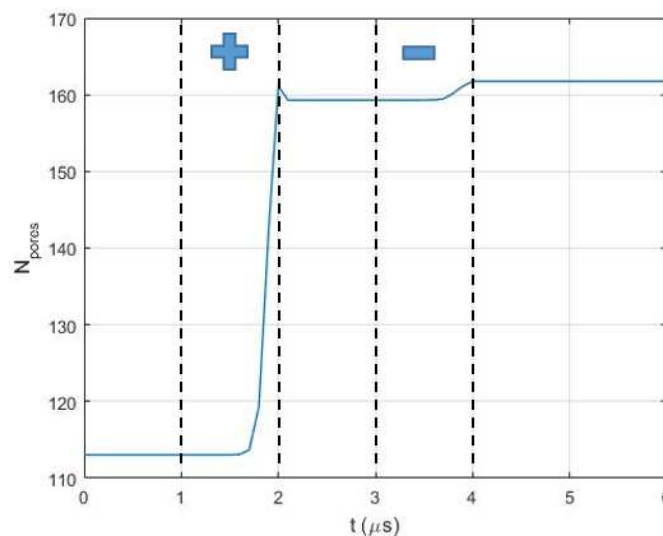


Fig.4.14: Number of pores of fixed radius as a function of time. The dashed regions with '+' and '-' indicate pulse polarities. Pulse and configuration as in Fig.4.10.

This analysis of ED and EP for N-cell assemblies provides evidence that neighboring cells and changing pulse parameters have significant but complex effects on these two related processes that may be distinguishable by experimental techniques. Many more realizations are needed to get the general features of the ED and EP behavior for that. However, these preliminary tests can serve as a guide to understand the effects of neighbor's proximity and non-symmetric effects of the configuration. While a time-dependent analysis predicts how the system evolves in time, a frequency analysis gives important insights also as to how one can use frequency tuning as a force modulation technique among neighboring cells interplaying with the material dispersive properties.

4.2 Frequency analyses

Force modulation by varying the frequency of the exogenous applied field is analyzed in the context of neighboring cells. This is a first step analysis since ED and EP are not incorporated in it, however our results form a necessary stage for developing the model further. All regions of the biological media are assigned dispersive complex relative permittivity (i.e. frequency-dependent). The analysis is performed within quasi-static approximation i.e. the wavelength of the ac field is considered to be much larger than the smallest spatial feature in the geometry of the model.

Firstly, we present the frequency analysis for a single cell of radius $R = 5 \mu\text{m}$ put in a cube of sides $2.5 \cdot R = 12.5 \mu\text{m}$, thus representing a cell suspension with a filling fraction of 0.2608. The complex relative permittivity is set to $\epsilon_{complex} = \epsilon_{static} - i\left(\frac{\sigma}{\epsilon_0 \omega}\right)$ where the static (long-wavelength) relative permittivity for interior, exterior and membrane of the cell are 60, 80 and 8.5 respectively. The conductivities are set to 0.42 S/m, 0.01 S/m and 1×10^{-6} S/m respectively. An applied field strength of 1 kV/cm is given in the frequency range of 10^3 to 10^9 Hz. The results shown in Fig.4.15 show potential difference across the membrane and surface

charge density over it. Over the full frequency range the TMP ranges between ± 0.6 V while the surface charge density ranges between ± 0.18 fC/ μm^2 . It is interesting to observe that the extrema of these two quantities on the poles occur in different frequency ranges i.e. at the topmost point of the cell, *TMP* is highest in the range of 10^3 - 10^4 Hz while the surface charge density is highest around the MHz range.

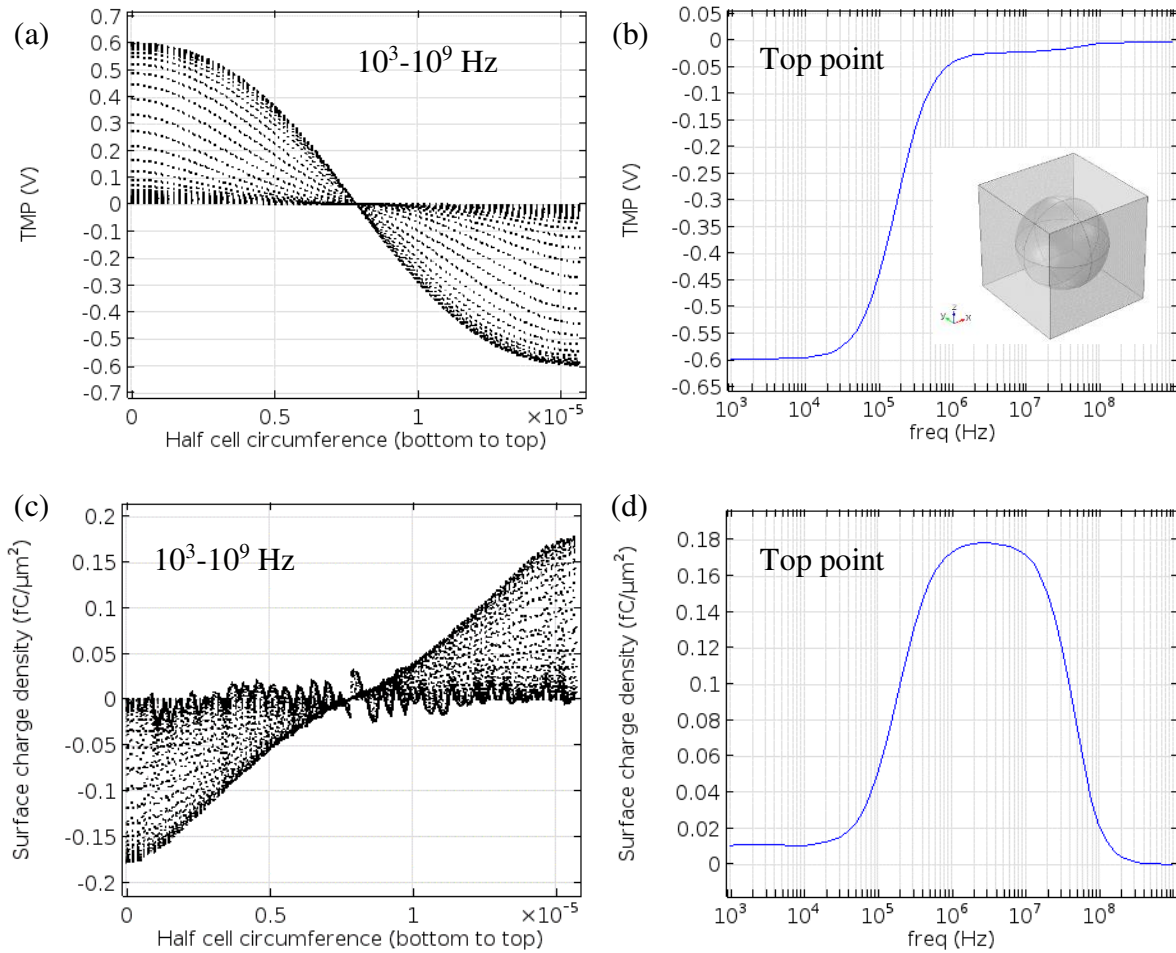


Fig.4.15: (a) *TMP* over half the cell circumference from bottom to top, (b) *TMP* at the topmost point on the cell, (inset) Model geometry; ac field is applied along z axis (c) Surface charge density over half the cell circumference from bottom to top, (d) Surface charge density at the topmost point on the cell

The average force on upper and lower halves of the cell is presented in Fig.4.16 along with results of the effective dielectric behavior. On a single cell, the net total electric force is zero while the two poles experience an equal stretching force (of the order 10^{-5} N in lower frequency range and then drop to 10^{-9} N towards the higher frequency range) in opposite

directions. The real part of effective relative permittivity can be seen relaxing first beyond 50 kHz and then for the second time beyond 50 MHz corresponding to low frequency and high frequency β -relaxation process.

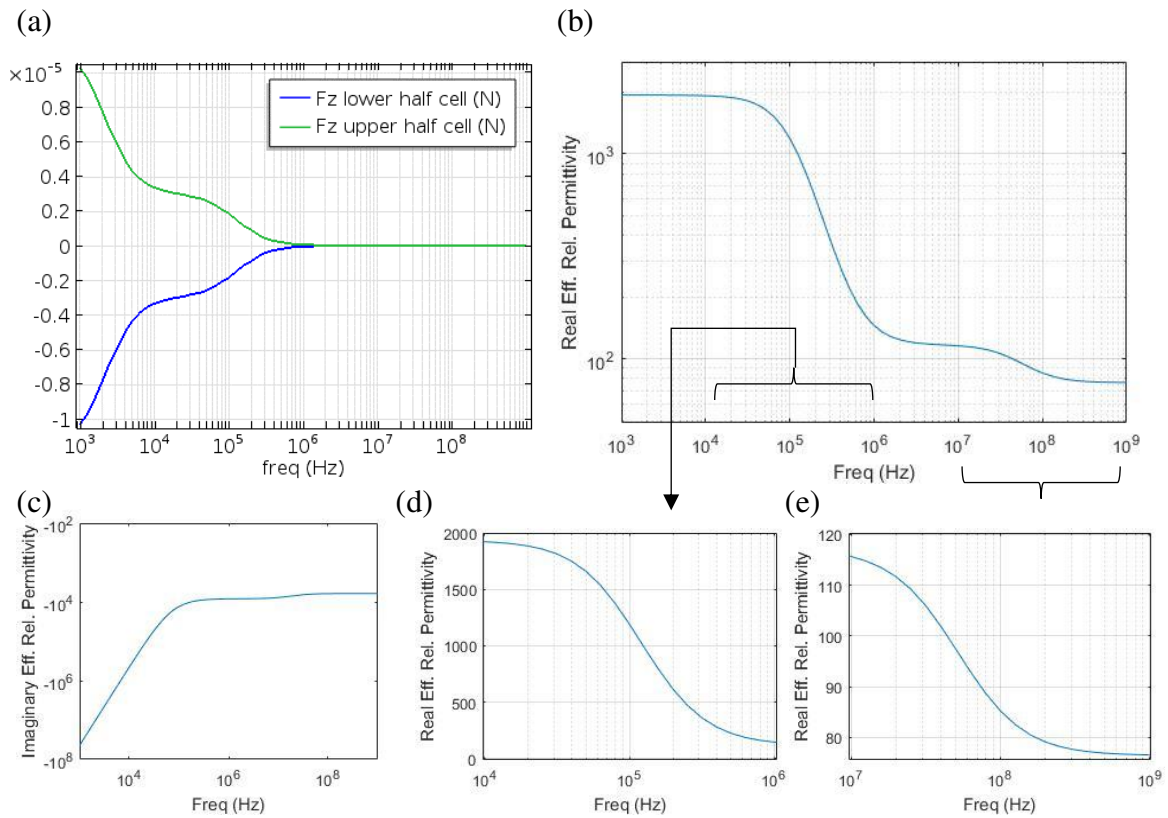


Fig.4.16: (a) Net electrical force over upper and lower halves of the cell surface calculated by surface integration of *MST*, (b) Real part of the effective relative permittivity, (c) Imaginary part of effective relative permittivity, (d-e) Zoomed regions from (b).

The results for neighboring cells are organized in the following sections which consistently show that the inter-cellular electrical forces can be modulated at the local as well as at the global level. These results are in good agreement with the previous work realized by Murovec & Brosseau (2015) [26]. This new addition considers two different lines of investigation. One focusses on two neighboring cells among which one can be found at different relative orientations with respect to the other cell and field direction. Two separate sets of parameters and material properties are used in this case. It is observed that the frequency modulation leads to force reversal on the cell. The other focusses on a cell which is well

surrounded by its nearest neighbors. The effect of introducing second nearest neighbors is examined on the net force experienced by the central cell within the applied frequency modulation analysis. A gradual increase of filling fraction up to 0.29 is implemented.

4.2.1 Effect of relative orientation among two cells on total force

Under an ac applied field, the total electrical force experienced by a cell in proximity to an identical neighbor is examined. The position of the neighboring cell is changed around the reference cell which is positioned in the center of the cubic domain. It is reminded that two sets parameters and properties are used in this analysis. The first set is identical to that used for single cell and mentioned before (Section 4.1.1). Second set of properties consists of the conductivity for interior, exterior and membrane of the cell that is set to 0.75 S/m, 0.056 S/m and 3×10^{-7} respectively. The relative permittivity for the respective regions is set to 75, 80 and 3. Figure 4.17 shows a typical geometry of the model used.

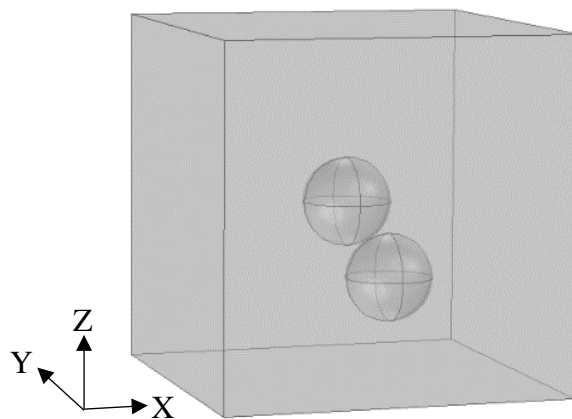


Fig.4.17: Two cells of radius $10 \mu\text{m}$ are separated by 500 nm . The applied ac field is along z axis. Side of the cube is $80 \mu\text{m}$. The position of the off-center cell is revolved around the central cell keeping the same separation.

The central cell is identified as cell 1 and the off-center cell as cell 2. The orientation of cell 2 is defined in terms of angle θ with respect to the field direction along $+z$. Cell 2 is on top of cell 1 when $\theta = 0$. The total electric force as well as the force on polar halves of both

cells are studied as the position of cell 2 is revolved around cell 1. For $\theta = 0$, the forces are plotted in Fig.4.18. It is observed that the average force on the polar halves is in the order of 10^{-5} N during low frequency near 10^3 Hz which drops to half in the next around 10^4 Hz and further drops to 10^{-9} N beyond the range following 10^6 Hz. Both cells experience a net force along z axis in the order of 10^{-7} N which further drops to zero close to 10^5 Hz and then the force reversal is observed till 10^6 Hz after which the magnitude is in the order of 10^{-9} N. The results are illustrated in Fig.4.18.

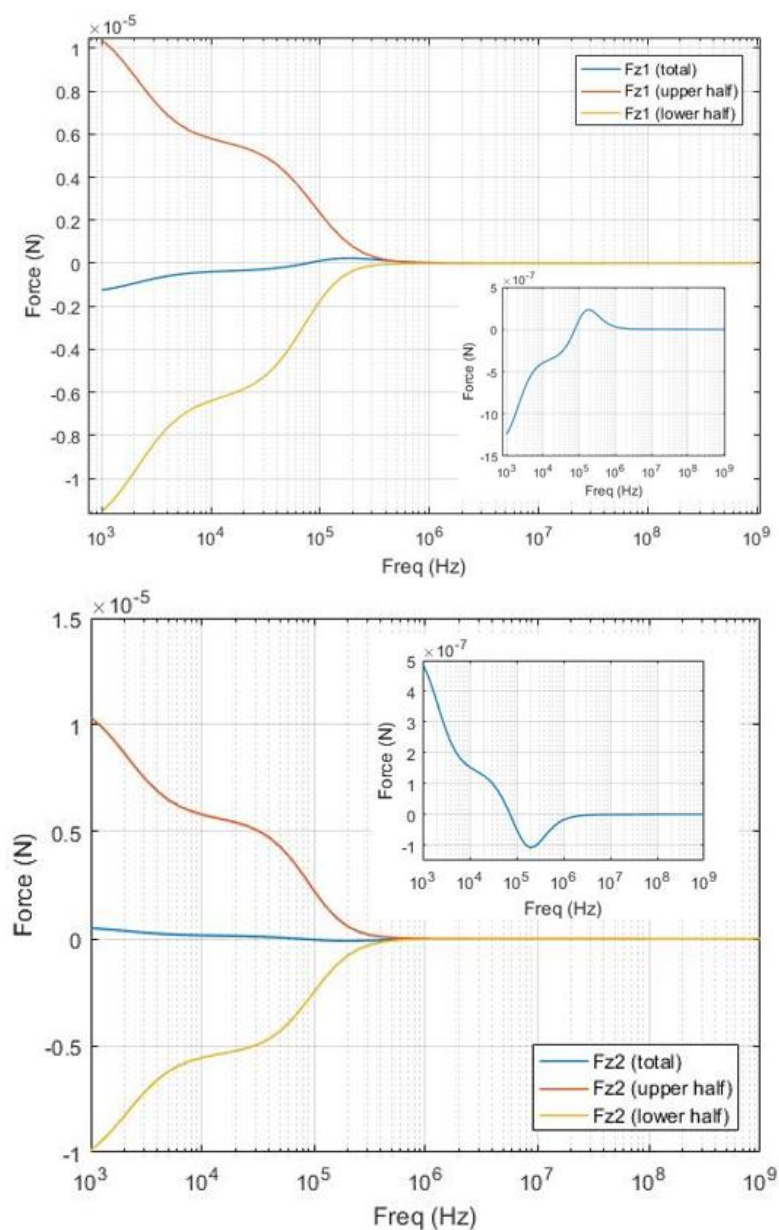


Fig.4.18: Electric force, z component (total and averaged on polar halves) on two neighboring cells as a function of frequency when the angle of orientation for cell 2 is $\theta = 0$. (a) For cell 1 and (b) for cell 2.

When the angle of orientation of cell 2 is varied from 0 to 90 degrees, significant changes in the net force experienced by the two cells are recorded which are displayed in Fig.4.19. It is worth noting that the forces are not necessarily equal and opposite.

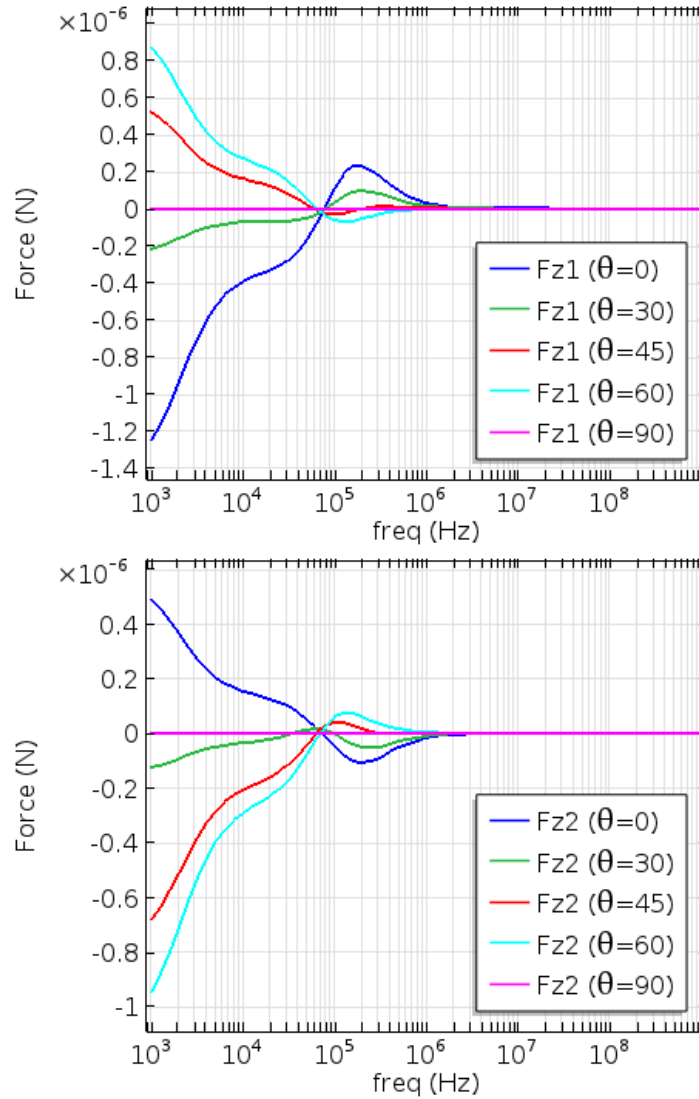


Fig.4.19: Net electric force on two cell configuration as a function of frequency. The angle of orientation of cell 2 is marked in the legend.

For the second set of parameters which were also used in Shamooun et al. (2018) [28], we show the total magnitude of the force and its direction for the two cell configuration in Fig.4.20.

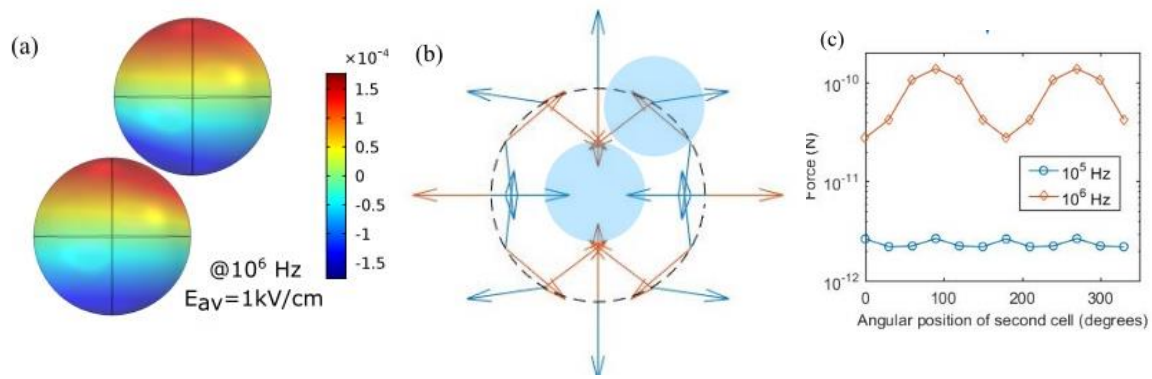


Fig.4.20: Total electric forces between two cells under an applied ac field. (Adapted from Fig.15 of Shamoan et al (2018) [28]). (a) Surface charge distribution (in C/m^2) over two spherical cells of radii $10 \mu m$ each, separated by a distance of 500 nm when an average ac field magnitude of 1 kV/cm with frequency of 10^6 Hz is applied vertically, (b) the direction of total electric force on the second cell at specific angular positions is depicted by arrows for frequency of 10^5 Hz (blue) and 10^6 Hz (red), and (c) a comparison of force magnitudes for the two cases shown in (b).

One can notice that the proximity effect redistributes the surface polarization charges depending upon the direction of the applied field and relative position of the two cells. The two frequencies at 10^5 Hz and 10^6 Hz show remarkable differences in the total force magnitude and orientation. Colored arrows label the frequency and illustrate the change of direction while the dashed line represents the trajectory along which the cell 2 is positioned at specific points corresponding to the angle of orientation. The length of the arrows is a guide to the eyes. More than one order of magnitude difference can be seen clearly as the angular position of cell 2 is varied. However, the second set of parameters lead to a very different order of magnitudes than the first one discussed above.

The change in the order of magnitude of the electrical force is particularly important in cell manipulation techniques. The effect of varying the separation between the two cells is also analyzed. Four simple combinations of the property values labeled as 1(a, b) and 2(a, b) are shown in the inset of Fig.4.21.

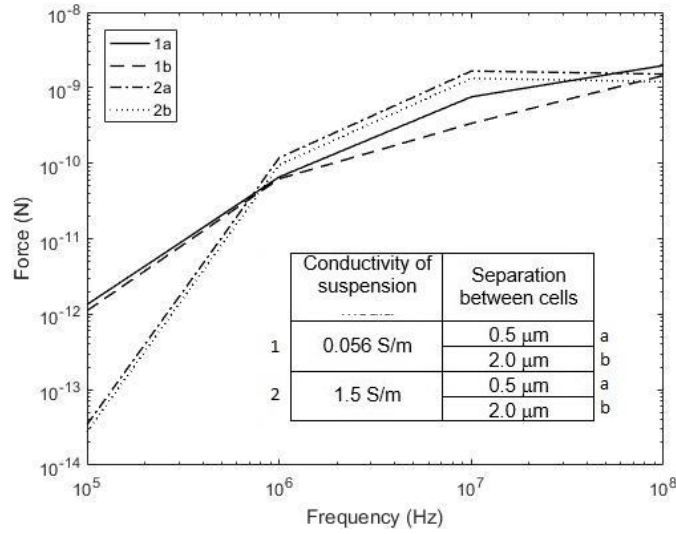


Fig.4.21: Order of magnitude differences in total force on the off-center cell inclined 30° from the vertical from lower side around an identical neighbor cell in the center. The whole system is under an applied average ac electric field of 1 kV/cm strength. The conductivity of suspension media and separation of the cells are varied as shown in the inset table and the legends are marked accordingly.

The geometry for this model consists of the same two-cell configuration when the off-center cell is inclined at 30° from the vertical about the center (same as shown in Fig.4.17). The results show that when frequency is below 10^5 Hz, the force increases by an order of magnitude for a smaller conductivity medium as compared to the case of larger conductivity medium while the separation distance does not have much effect except that the force is slightly intense when cells are closer. As frequency is close to 10^6 Hz, the orders of force magnitude increase to 10^{-10} N for both media. With further increase in frequency, the higher conductivity medium leads to a faster increase in the force than the lower conductivity medium. Additionally, the force is more sensitive to the separation of the cells at higher frequency as shown by the increased separation among the marked lines corresponding to the combinations ‘a’ and ‘b’ of each ‘1’ and ‘2’.

4.2.2 Effect of introducing next-nearest neighbors

A series of geometries is constructed with increasing the number of cells as $N = \{15, 19, 23, 27, 35, 43\}$ in order to have a gradual increase in the filling fraction. The cells are

positioned by direct placement. The multicellular configurations (Fig.4.22) contain cells of two sizes (5 and 10 μm). The first configuration has five larger cells and ten smaller ones so that the central cell is well surrounded by its nearest neighbors. For introducing next-nearest neighbors, only smaller size cells are added in the next configurations as they can fill more space. The obtained filling fractions are in the range 0.18-0.29. In this analysis, the net force components on the central cell are analyzed as a function of frequency and filling fraction.

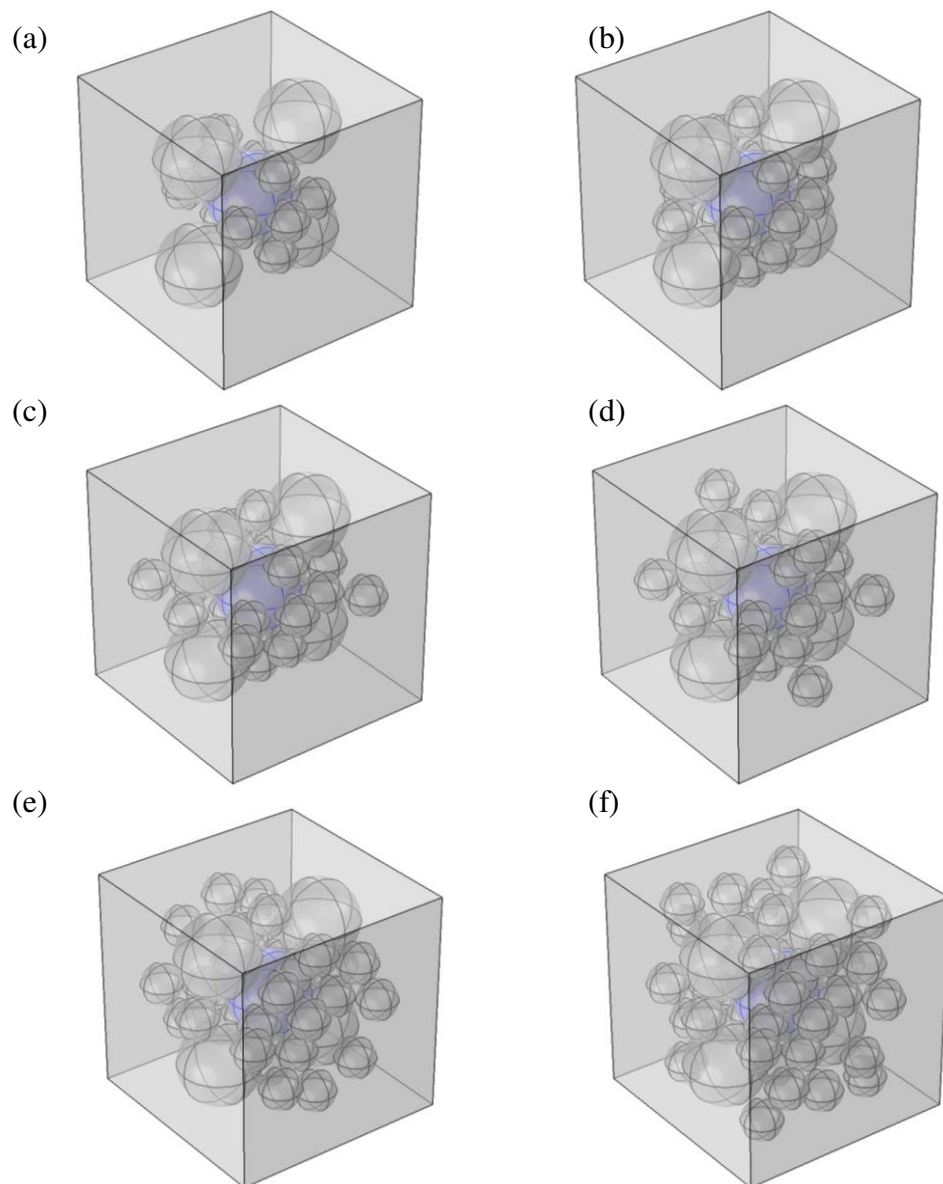


Fig.4.22: Multicellular model geometry with filling fractions (a) 0.18, (b) 0.2, (c) 0.216, (d) 0.23, (e) 0.26 and (f) 0.29. Cube size is 55 μm . Two cell radii - 5 and 10 μm .

The force components which are shown in Fig.4.23 reveal that the net force magnitudes significantly change (within the order of 10^{-8} N) on the central cell with similar force reversal trends as discussed before.

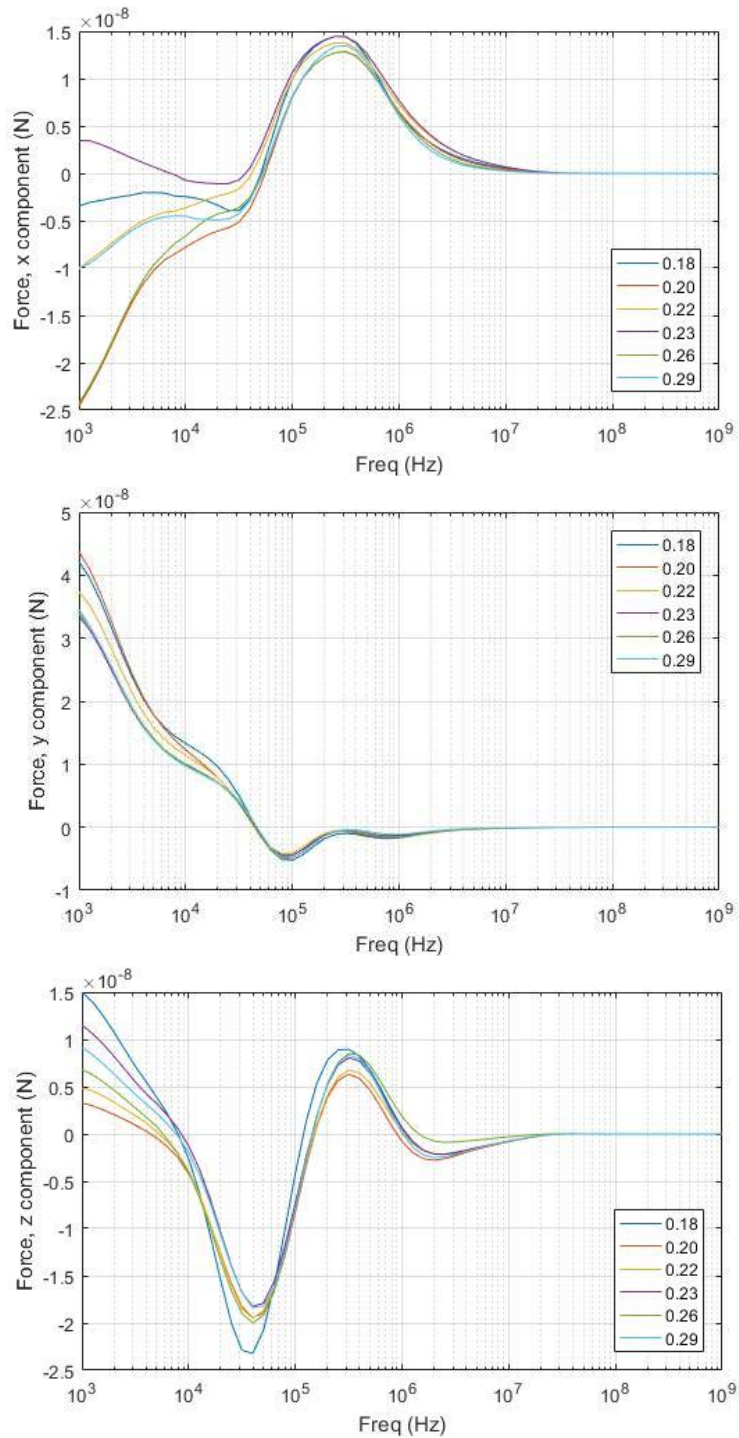


Fig.4.23: Net electric force components for the central cell in a suspension with varying filling fraction due to increase in number of the cells.

We observe that when frequency is changed, the surface charge redistribution becomes more prominent close to the proximity regions at 10^7 Hz as presented in Fig.4.24.

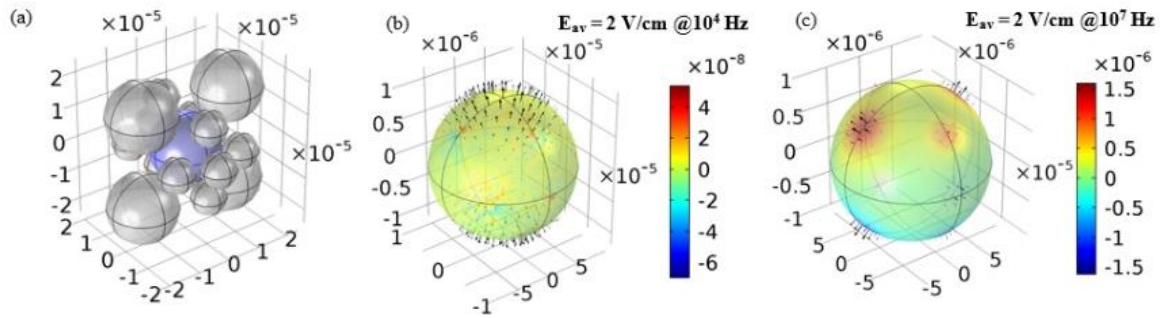


Fig.4.24: Local electric stress distribution on a cell surrounded by other cells under an applied ac field. [Adapted from Fig.16 of Shamooun et al (2018) [28]] (a) Model geometry consists of a random distribution of two-size spheres (radii 10 and 5 μm). The central (blue) sphere is chosen (as reference) for examining the local force distribution on its surface. *MST* is depicted by arrows and surface charge density (in C/m^2) is depicted by color for frequency of (b) 10^4 Hz and (c) 10^7 Hz

At 10^4 Hz, the central cell experiences mainly a bi-directional electrical stress with less prominence around the proximity regions. But, as the frequency is changed to 10^7 Hz, the electrical stress gets concentrated around the proximity regions. In particular, for the larger red-spot covering a surface area of $9.3849 \mu\text{m}^2$, the *MST* was surface integrated to reveal a small force of 1.25 fN for an applied field strength of 2 V/cm but this force scales up to 1.25 nN for an applied field strength of 2 kV/cm.

Considering the frequency analysis of this work, the reader's attention is brought to a previous work by Murovec & Brosseau (2015) [26] in which frequency modulation of electric field excitation of neighboring biological cells showed a similar variation of the local electrical stress distribution. Our results are consistent with that work but calculated for new cell configurations. Consider another previous work by Murovec & Brosseau (2014) [25-b] that is closely related but had a slightly different scenario. In that work, the spheres are modelled as conducting bodies only (not core-shell), which are maintained at fixed potentials (slightly different in magnitude) and the total force is calculated which is shown to possess a repulsion-to-attraction transition with respect to inter-cellular gap distance. The difference in the two

situations is hereby noted. First, cells are not maintained at constant potential here, they are under the applied field, and there is a gradual variation of electric potential around the cell membrane. Hence, it is not the same situation but the possibility of redirection of the force remains due to the same reasons i.e. redistribution of the surface charges. In summary, the force reversal can be observed with inter-cellular distance variation and also with frequency variation without necessarily varying the former.

5. Conclusion and Perspectives

This work aimed at developing simple numerical models for describing ED and EP of biological cell assemblies submitted to an electric field excitation. Experimentally relevant field excitations and experimentally determined material properties are used as inputs for the models. This work is distinguished from the archival literature in that it considers non-symmetric randomized deformable cell assemblies. In summary, this study reveals some of the subtle interactions of cell electrostatics and mechanics for assemblies of cells in specific configurations, which involve a complex interplay of the effects of the electric field, cell surface charge, *TMP*, pore density, and characteristics of the delivered pulse. The experimentally measurable quantities like electric voltage across the cell membrane (*TMP*) and electrical force distribution (*MST*) over the cell membrane are calculated in this study which fall well within the reported estimates in the literature (respectively, -40 mV-1.2 V and 10-70 pN/ μm^2). This work is also distinguished by the use of deformation analysis predicting up to 66 % of strain for cell membrane and ~5 kT for its strain energy under an applied electric pulse. Both ED and EP are shown to be affected by the proximity of cells owing to the local electric field enhancement. We present explicit evidence of collective behavior of cell assemblies by analyzing their electromechanical response both in dc and ac excitations.

Together, these observations suggest that the spatial organization of the polarization charges can play an important role in electro-deformation and EP of biological cells and that this organization can be controlled to facilitate EP. Our model can also be extended in directions such as linking to various device configurations with microfluidics and transport of dilute species from the cell exterior to its interior or vice-versa. This will render these extended models more appropriate for experimental validation. Here, we studied cellular hardware (structure and electromechanical properties), but we had little to say about cellular software (information processing capabilities). A comprehensive study of how they interplay to control

cell form and function in tissues, i.e., how the mechanical signals are transmitted and potentially transduced into intracellular biochemical signals, is useful because it can open newer doors to be used for 3D engineered tissues.

Several trade-offs are involved in construction of a 3D Multiphysics model involving Multiscale non-symmetric arbitrary shapes of cells. Multiscale aspects can be dealt by considering the distinct phases as homogeneous entities in a defined regions of space while the heterogeneity amounts to the number of such distinct phases. Multiphysics aspects can be dealt with by making a clear distinction between the time scales of various events involved that can lead to decoupling of involved equations wherever possible. A single multiscale theoretical model or experimental platform which would include subcellular, cellular and tissue details or have a control over these aspects is still lacking (i.e. from 1 nm to 10 mm as shown in Fig.1.1). Moreover, biochemical reactions during regular biological processes which eventually impact physical responses were not considered in this report. A hybrid continuum approach can be envisioned for such an analysis that takes into account coarse-grained biomolecular details and reactions sourced from a database and considering as well as hundreds of cells up to large length scales.

Considering the modelling of more physical processes, one can further relax the assumption of homogeneous conductivity for interior and exterior of the cells by including the local ionic concentrations that can contribute to the local charge distribution. The membrane conductivity is experimentally measured by ‘voltage clamp’ techniques which maintain a fixed transmembrane potential that can be varied by an external battery. The ionic currents through the membrane are measured using this technique. The frequently monitored ions are K^+ , Na^+ , Cl^- , Ca^{2+} . In context of the model developed in this work, the ‘external battery’ is however not directly applied across the membrane but farther away that indirectly induces the variation of *TMP*. Since, these ions flow through the membrane in and out of the cells by various means

such as voltage-gated ion-channels (or the nano-pores that have been discussed in this work), it would be worth exploring how the local concentrations are affected by application of external fields. Goldberg et al. (2018) [50] have incorporated multiple ionic species in a multiphysics simulation approach to EP. Apart from these, the ion specificity for ion-channels and pore dynamics add further complexity to the scenario. On the other hand, fluid flow in general can also exert pressure on the membrane leading to an additional contribution apart from the *MST*. Hence, modelling of ionic concentrations, pore radii distribution dynamics and fluid flow can be very interesting to give results much closer to the experimental devices used for the purpose.

Membrane mechanics has been conventionally modelled with Helfrich's energy function [51] that uses terms corresponding to surface curvature and bending moduli. This energy function permits a rough estimate of the equilibrium shape of a cell. The general free energy of the membrane can accommodate contributions from Helfrich's energy and more terms such as those accounting for surface tension and occurrence of pores. The strain energy results presented in this work (~ 5 kT) for viscoelastic membrane are of the same order of magnitude as those reported for pore formation (~ 15 - 20 kT) in the literature. Thus, an energy formalism can also be considered to study the electromechanical response of multicellular configurations by their calculation on the defined membranes.

References

- [1] Lim, C. T., Zhou, E. H., & Quek, S. T. (2006). Mechanical models for living cells—a review. *Journal of Biomechanics*, 39(2), 195-216.
- [2] Moeendarbary, E., & Harris, A. R. (2014). Cell mechanics: principles, practices, and prospects. *Wiley Interdisciplinary Reviews: Systems Biology and Medicine*, 6(5), 371-388.
- [3] Sugimura, K., Lenne, P. F., & Graner, F. (2016). Measuring forces and stresses in situ in living tissues. *Development*, 143(2), 186-196.
- [4] Ebrahimi, A. P. (2009). Mechanical properties of normal and diseased cerebrovascular system. *Journal of Vascular and Interventional Neurology*, 2(2), 155.
- [5] Stamenovic, D., Suki, B., Fabry, B., Wang, N., Fredberg, J. J., & Buy, J. E. (2004). Rheology of airway smooth muscle cells is associated with cytoskeletal contractile stress. *Journal of Applied Physiology*, 96(5), 1600-1605.
- [6] Wang, N., Tolic-Nørrelykke, I. M., Chen, J., Mijailovich, S. M., Butler, J. P., Fredberg, J. J., & Stamenovic, D. (2002). Cell prestress. I. Stiffness and prestress are closely associated in adherent contractile cells. *American Journal of Physiology-Cell Physiology*, 282(3), C606-C616.
- [7] Saw, T. B., Doostmohammadi, A., Nier, V., Kocgozlu, L., Thampi, S., Toyama, Y., Marcq, P., Lim, C. T., Yeomans, J. M. & Ladoux, B. (2017). Topological defects in epithelia govern cell death and extrusion. *Nature*, 544(7649), 212.
- [8] Roca-Cusachs, P., Conte, V., & Trepats, X. (2017). Quantifying forces in cell biology. *Nature cell biology*, 19(7), 742.
- [9] Petridou, N. I., Spiró, Z., & Heisenberg, C. P. (2017). Multiscale force sensing in development. *Nature cell biology*, 19(6), 581.

- [10] Son, R. S., Smith, K. C., Gowrishankar, T. R., Vernier, P. T., & Weaver, J. C. (2014). Basic features of a cell electroporation model: illustrative behavior for two very different pulses. *The Journal of Membrane Biology*, 247(12), 1209-1228.
- [11] Zhang, H., & Liu, K. K. (2008). Optical tweezers for single cells. *Journal of the Royal Society Interface*, 5(24), 671-690.
- [12] Guo, F., Mao, Z., Chen, Y., Xie, Z., Lata, J. P., Li, P., Ren, L., Liu, J., Yang, J., Dao, M., Suresh, S., & Huang, T. J. (2016). Three-dimensional manipulation of single cells using surface acoustic waves. *Proceedings of the National Academy of Sciences*, 113(6), 1522-1527.
- [13] Molnar, C., & Gair, J. (2015). *Concepts of Biology: 1st Canadian Edition*.
- [14] Scheurich, P., Zimmermann, U., Mischel, M., & Lamprecht, I. (1980). Membrane fusion and deformation of red blood cells by electric fields. *Zeitschrift für Naturforschung C*, 35(11-12), 1081-1085.
- [15] Abidor, I. G., Arakelyan, V. B., Chernomordik, L. V., Chizmadzhev, Y. A., Pastushenko, V. F., & Tarasevich, M. R. (1979). Electrical breakdown of bilayer lipid membranes. *Bioelectrochemistry and Bioenergetics*, 6, 37-52.
- [16] Marszalek, P., & Tsong, T. Y. (1995). Cell fission and formation of mini cell bodies by high frequency alternating electric field. *Biophysical Journal*, 68(4), 1218-1221.
- [17] Sengel, J. T., & Wallace, M. I. (2016). Imaging the dynamics of individual electropores. *Proceedings of the National Academy of Sciences*, 113(19), 5281-5286.
- [18] Robinson, K. R. (1985). The responses of cells to electrical fields: a review. *Journal of Cell Biology*, 101(6), 2023-2027.
- [19] Robinson, K. R., & Messerli, M. A. (2003). Left/right, up/down: the role of endogenous electrical fields as directional signals in development, repair and invasion. *Bioessays*, 25(8), 759-766.

[20] Joshi, R. P., Hu, Q., Schoenbach, K. H., & Hjalmarson, H. P. (2002). Theoretical predictions of electromechanical deformation of cells subjected to high voltages for membrane electroporation. *Physical Review E*, 65(2), 021913.

[21] Riske, K. A., & Dimova, R. (2005). Electro-deformation and poration of giant vesicles viewed with high temporal resolution. *Biophysical Journal*, 88(2), 1143-1155.

[22-a] Mezeme, M. E., Kranjc, M., Bajd, F., Serša, I., Brosseau, C., & Miklavčič, D. (2012). Assessing how electroporation affects the effective conductivity tensor of biological tissues. *Applied Physics Letters*, 101(21), 213702.

[22-b] Mezeme, M. E., Pucihar, G., Pavlin, M., Brosseau, C., & Miklavčič, D. (2012). A numerical analysis of multicellular environment for modeling tissue electroporation. *Applied Physics Letters*, 100(14), 143701.

[23] Mezeme, M. E., & Brosseau, C. (2013). Engineering nanostructures with enhanced thermoplasmonic properties for biosensing and selective targeting applications. *Physical Review E*, 87(1), 012722.

[24] Murovec, T., & Brosseau, C. (2013). Electrostatics of two charged conducting ellipsoids. *Applied Physics Letters*, 102(8), 084105.

[25-a] Murovec, T., & Brosseau, C. (2014). Does like attract like? *Applied Physics Letters*, 105(5), 054101.

[25-b] Murovec, T., & Brosseau, C. (2014). Numerical simulation of the sign switching of the electrostatic force between charged conducting particles from repulsive to attractive. *Journal of Applied Physics*, 116(21), 214902.

[26] Murovec, T., & Brosseau, C. (2015). Spectral fingerprint of electrostatic forces between biological cells. *Physical Review E*, 92(4), 042717.

- [27] Murovec, T., Sweeney, D. C., Latouche, E., Davalos, R. V., & Brosseau, C. (2016). Modeling of transmembrane potential in realistic multicellular structures before electroporation. *Biophysical Journal*, 111(10), 2286-2295.
- [28] Shamoony, D., Lasquelles, S., & Brosseau, C. (2018). Perspective: Towards understanding the multiscale description of cells and tissues by electromechanobiology. *Journal of Applied Physics*, 123(24), 240902.
- [29] Prodan, E., Prodan, C., & Miller Jr, J. H. (2008). The dielectric response of spherical live cells in suspension: an analytic solution. *Biophysical Journal*, 95(9), 4174-4182.
- [30] Biasio, A. D., Ambrosone, L., & Cametti, C. (2010). The dielectric behavior of nonspherical biological cell suspensions: an analytic approach. *Biophysical Journal*, 99(1), 163-174.
- [31] Schwan, H. P. and Takashima, S. (1991) *Bulletin of the Institute for Chemical Research, Kyoto University*, 69(4): 459-475.
- [32] MacQueen, L. A., Buschmann, M. D., & Wertheimer, M. R. (2010). Mechanical properties of mammalian cells in suspension measured by electro-deformation. *Journal of Micromechanics and Microengineering*, 20(6), 065007.
- [33] Kuznetsova, T. G., Starodubtseva, M. N., Yegorenkov, N. I., Chizhik, S. A., & Zhdanov, R. I. (2007). Atomic force microscopy probing of cell elasticity. *Micron*, 38(8), 824-833.
- [34] Varga, B., Fazakas, C., Wilhelm, I., Krizbai, I. A., Szegletes, Z., Váró, G., & Vég, A. G. (2016). Elasto-mechanical properties of living cells. *Biochemistry and Biophysics Reports*, 7, 303-308.
- [35] Napotnik, T. B., & Miklavčič, D. (2018). In vitro electroporation detection methods—An overview. *Bioelectrochemistry*, 120, 166-182.

- [36] Marszalek, P., Liu, D. S., & Tsong, T. Y. (1990). Schwan equation and transmembrane potential induced by alternating electric field. *Biophysical Journal*, 58(4), 1053-1058.
- [37] Kotnik, T., & Miklavčič, D. (2000). Analytical description of transmembrane voltage induced by electric fields on spheroidal cells. *Biophysical Journal*, 79(2), 670-679.
- [38] Gowrishankar, T. R., & Weaver, J. C. (2003). An approach to electrical modeling of single and multiple cells. *Proceedings of the National Academy of Sciences*, 100(6), 3203-3208.
- [39] Neu, J. C., & Krassowska, W. (1999). Asymptotic model of electroporation. *Physical Review E*, 59(3), 3471.
- [40] Qiang, Y., Liu, J., Yang, F., Dieujuste, D., & Du, E. (2018). Modeling erythrocyte electrodeformation in response to amplitude modulated electric waveforms. *Scientific Reports*, 8(1), 10224.
- [41] Reddy, J. N. (1993). *An introduction to the Finite Element Method*. New York.
- [42] Thomas, J. W. (1995). *Introduction to Finite Differences*. In *Numerical Partial Differential Equations: Finite Difference Methods* (pp. 5-39). Springer, New York, NY.
- [43] Kythe, P. K. (1995). *An introduction to boundary element methods* (Vol. 4). CRC press.
- [44] Kharab, A., & Guenther, R. B. (2011). *An introduction to numerical methods: a MATLAB approach*. Chapman and Hall/CRC.
- [45] Shamoan, D., Lasquellec, S., & Brosseau, C. (2017). Low-order statistics of effective permittivity and electric field fluctuations in two-phase heterostructures. *Journal of Applied Physics*, 122(4), 044106.

[46] Brosseau, C. (2006). Modelling and simulation of dielectric heterostructures: a physical survey from an historical perspective. *Journal of Physics D: Applied Physics*, 39(7), 1277.

[47] Shamoon, D., Dermol-Černe, J., Rems, L., Reberšek, M., Kotnik, T., Lasquelles, S., Brosseau, C., & Miklavčič, D. (2019). Assessing the electro-deformation and electro-poration of biological cells using a three-dimensional finite element model. *Applied Physics Letters*, 114(6), 063701.

[47-a] Pilkey, W. D. (1994). *Formulas for stress, strain, and structural matrices* (Vol. 5). New York: Wiley.

[48] DeBruin, K. A., & Krassowska, W. (1999). Modeling electroporation in a single cell. I. Effects of field strength and rest potential. *Biophysical Journal*, 77(3), 1213-1224.

[49] Shamoon, D., Lasquelles, S., & Brosseau, C. (2019). A multiphysics analysis of the strain energy in multicellular environments. *Applied Physics Letters*, 115(4), 043701.

[50] Goldberg, E., Suárez, C., Alfonso, M., Marchese, J., Soba, A., & Marshall, G. (2018). Cell membrane electroporation modeling: A multiphysics approach. *Bioelectrochemistry*, 124, 28-39.

[51] Guckenberger, A., & Gekle, S. (2017). Theory and algorithms to compute Helfrich bending forces: A review. *Journal of Physics: Condensed Matter*, 29(20), 203001.

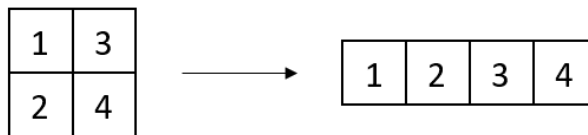
Appendix A: Geometry conception using algorithms

A1. Random 2D checkerboard generation

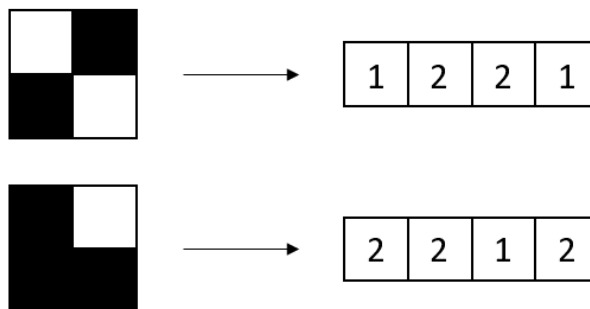
The algorithmic concepts for generating hundreds to thousands of realizations of two phase media in the form of 2D checkerboard (sizes 4x4 and beyond) are presented below. The goal is to obtain all or if not all, then a very high number of realizations for a given filling fraction of the checkerboard. A MATLAB script was written by the author for this goal. It must be borne in mind that these realizations become the source from which a desired number of realizations are then randomly sampled for electrical steady-state analysis.

Assignment of material phase

First, all the small squares of the model from 1 to NxN (here shown for 2x2) are labelled



Arrays are filled with 1s (white) and 2s (black) corresponding to the two phases (ϵ_1 and ϵ_2) using an algorithm based on Monte Carlo method.



The last step is repeated many times ensuring non-repeatability of the sequence and storing all unique sequences. The program stops if the maximum possible number or a sufficiently high number of configurations is reached.

Algorithm highlights

- The aim is to generate sequences of $N \times N$ elements using 2 digits (1s and 2s representing the ID of first and second material) ensuring a fixed filling fraction
- First, Monte Carlo method is used to generate a Gaussian distribution of a large number of sequences (which may contain repeated sequences) centered at the desired filling fraction
- Then, the sequences corresponding to the desired filling fraction are chosen and the unique ones from among them are extracted
- For extremely large number of sequences it is reasonable to generate only up to 10^5 unique sequences

A2. Randomly distributed spherical N-Cells generation

Numerical generation of randomly distributed N objects in 3D space is not trivial since objects can overlap which is not a desired feature in this work. Random distribution of non-overlapping N -cells was generated by using a user-developed MATLAB function (courtesy: Melvin and Laboratory of Biocybernetics, Slovenia)

Algorithm highlights

- The primary inputs such as number of cells, filling fraction and cube dimensions are set
- An average radius for cell distribution is calculated based on the primary inputs
- Non-overlapping condition is enforced by requiring the new random center coordinates to be rejected if the distance between the new and any of the old ones is less than twice the average radius

Titre : Analyse multi-échelle et multi-physique de la déformation d'arrangements cellulaires soumis à un champ électrique : Application à l'électroporation

Mots clés : Électrodéformation, Électroporation, Cellule Biologique, Modélisation par Éléments Finis, Arrangements Cellulaires, Analyse Multi-physique et Multi-échelle

Résumé : Dans cette thèse, nous avons étudié la déformation d'arrangements cellulaires soumis à un champ électrique par simulation numérique. Grâce à la méthode des éléments finis, les phénomènes d'électrodéformation et d'électroporation ont été examinés sur les membranes de N-cellules en modifiant les caractéristiques des tensions appliquées. Les effets de proximité et de symétrie ont fait l'objet d'une étude.

Notre approche permet de prévoir le comportement de cellules en suspension ou dans un tissu soumis à un champ électrique. Les résultats numériques sont en accord avec ceux expérimentaux de la littérature. Notre analyse multi-échelle et multi-physique apporte de nouvelles perspectives dans la compréhension de l'électrodéformation d'un tissu biologique.

Title : Multiscale and Multiphysics analysis of the deformation of cellular arrangements under an electric-field excitation : Application to Electroporation

Keywords : Electrodeformation, Electroporation, Biological Cell, Finite Element Modeling, Cellular Arrangements, Multiphysics and Multiscale Analysis

Abstract : This thesis concerns the numerical analysis of electric field induced physical processes arising in biological cell membranes in N-cell assemblies with various applied voltage characteristics using finite element modeling. The study allows us to explore how the electrodeformation and electroporation phenomena are affected by cell-cell proximity and asymmetry in the N-cell assembly.

It is shown that the presented approach has a significant scope for predicting the behavior of cells in suspension or tissue under an electric stimulus. The results are in good agreement with existing literature. Additionally, we propose new results which open up new perspectives towards Multiscale and Multiphysics analysis of cell assemblies, modelling a biological tissue.